ELECTROMAGNETIC ANALYSIS OF PLANAR LAYERED STRUCTURES

A Thesis
Presented to
The Academic Faculty

by

Fatma Çalışkan

In Partial Fulfillment
of the Requirements for the Degree
Doctor of Philosophy

School of Electrical and Computer Engineering
Georgia Institute of Technology
May 2004

ELECTROMAGNETIC ANALYSIS OF PLANAR LAYERED STRUCTURES

Approved by:

Professor Andrew F. Peterson, Advisor

Professor Gregory D. Durgin

Professor Madhavan Swaminathan

Professor Robert Roper

Professor Emmanouil M. Tentzeris

Date Approved: 6 May 2004

To my mother, father and Zeynep, for their endless love,

To Erdem, for his patience and support,

ACKNOWLEDGEMENTS

I am most grateful to my advisor, Dr. Andrew F. Peterson who guided me throughout my thesis. He has taught me to find my own path in my research and to present my findings in the most accurate and efficient way.

I would like to thank Dr. Madhavan Swaminathan, Dr. Emmanouil M. Tentzeris, Dr. Gregory D. Durgin and Dr. Robert Roper for reading and commenting on the thesis and for the honor they gave me by presiding as the jury.

I would like to express my deepest gratitude to Dr. M. İrşadi Aksun and Dr. Levent Gürel for their supervision and encouragement in all steps of my master thesis. I would also like to thank Dr. Erdem Yazgan and Dr. Adnan Köksal for supporting me during my undergraduate studies.

Many thanks to Çiğdem, Deniz, Dilay, Erdem (Ofli), Ertem, Lale and Noyan for their friendship and support. I also would like to thank all my friends in Atlanta who always remind me that there is a life outside the office, especially Altan, Çağatay, Demet, Elçin, Kardelen, Seçil, Sermet, Sinem and Ümit. Sincere thanks are also extended to my office-mates Andy, Christoph, David, Gi Ho, Rickard, Sharib, Thorsten and Wajih. I also thank all my friends for their moral support.

I wish to thank to Erdem (Ertan) for his patience, support and kindness in these five long years. This thesis cannot happen without his help.

It is a pleasure to express my special thanks to my family, especially to my mother, father and Zeynep, for their endless love and patience. I am here because of their support and encouragement, and I hope I make them proud.

TABLE OF CONTENTS

LIST OF TABLES

LIST OF FIGURES

SUMMARY

The electrical design of microelectronic devices and their packaging is complicated because of non-ideal attributes of the actual circuit realization. Electromagnetic modeling offers the possibility of accurately predicting the electrical performance of devices and reducing the cost associated with the design process. The proposed research concerns extensions of electromagnetic modeling techniques and their application to microelectronic package design. The method of moments (MoM) is utilized as a technique in modeling and analyzing these designs. Recently, an alternate approach called the locally corrected Nyström method (LCN) has been applied to solve integral equations in electromagnetics. Recent research suggests that the LCN is well-suited for higher-order implementations and does not require cell-to-cell current continuity in the underlying representation. Thus it may offer advantages over the MoM, especially for problems involving complex 3-D structures. If cell-to-cell continuity is not required, nonconforming meshes may offer simpler geometrical modeling. In this proposal, we consider applying the above techniques to problems in package designs, which often involve multilayer structures, solid or perforated ground planes, embedded passive devices such as capacitors and spiral inductors, and interconnects in horizontal or vertical directions. Several examples will be used to illustrate the modeling.

CHAPTER I

INTRODUCTION

The electrical design of microelectronic devices and their packaging is complicated because of non-ideal attributes of the actual circuit realization. Electromagnetic modeling offers the possibility of accurately predicting the electrical performance of devices and reducing the cost associated with the design process. The proposed research concerns extensions of electromagnetic modeling techniques and their application to microelectronic package design.

Microstrip structures are used in microwave and millimeter wave integrated circuits (MMICs) and microelectronic packages. Different methods have been employed to analyze these structures, such as the quasi-static methods [47, 9, 48], equivalent waveguide models [25, 35] and segmentation approaches [12, 20]. These techniques are numerically efficient, but the results are not adequately accurate.

Advances in high speed digital computers have led to the development of more sophisticated numerical methods to solve large electromagnetic problems of practical interest which, by classical techniques, would be virtually impossible. The basic techniques that are used in electromagnetic problems are mainly the method of moments (MoM) [23, 22], finite element methods (FEM) [27] and the finite difference time domain (FDTD) methods [32], all of which transform integral, differential or integro-differential equations into algebraic equations.

The method of moments is very popular for the solution of open field problems, particularly for printed geometries in planar stratified media. It is presently recognized as the most powerful approach for the analysis of printed antenna configurations and for the characterization of radiation and coupling phenomena in printed circuit discontinuities. A large number of applications of the MoM can be found in the literature. Rautio and Harrington proposed an electromagnetic analysis of arbitrary microstrip circuits contained in

a rectangular conducting box [45]. The microstrip circuit metallization is subdivided into small rectangular subsections. An explicit surface current distribution exists in each subsection. The fields due to current in an individual subsection are represented by a sum of homogeneous rectangular waveguide modes. Mosig applied the Mixed Potential Integral Equation (MPIE) to analyze microstrip structures [40]. The scalar and vector potential Green's functions are calculated by using stratified media theory and are expressed as Sommerfeld integrals. Naishadham and Nuteson describe an efficient implementation, based on reducing the computation time by utilizing symmetries in Green's functions and the problem formulation, to analyze microstrip structures [41]. Efficiency is enhanced by utilizing near-field and far-field approximations of the Green's functions. For moderate distances between source and observation points, Sommerfeld-type integrals can be used to calculate the Green's functions, but the computation of the functions is expensive. To avoid this problem, the closed-form microstrip Green's functions developed by Chow et al. [14] can be used, where the integrals are approximated as a summation of contributions from the quasidynamic images (for the near-field approximation), the surface-wave poles (for the far-field approximation), and complex images (calculated using Prony's method in terms of complex exponentials). Park et al. [43] introduced an efficient technique to analyze microstrip structures with a substrate and a superstrate using closed-form spatial domain Green's functions which are calculated using the Generalized Pencil of Function (GPOF) method [46]. Eleftheriades and Mosig presented the characterization of multiport planar microwave circuits with MoM using two different excitation models, the delta-gap voltage and the impressed-current models [16].

The main advantages of MoM are its accuracy, versatility and the ability to compute near-zone and far-zone parameters. The basic idea of the MoM is to reduce an integral equation to a matrix equation, and to solve the matrix equation by a known technique.

The Nyström method for the solution of integral equations was first proposed in 1930 [42]. The essence of the approach is replacing the integral operator with a suitable quadrature rule. The integral equation is enforced at nodes (sample points) of the rule, and leads to a linear system of equations for the samples of the unknown function at the node points.

The drawback of the classical Nyström method is that it cannot be used directly for integral equations with singular kernels [7]. Only recently, the method has been extended to treat the singular integral equations arising in electromagnetic radiation and scattering problems [11, 33, 34]. The extended method is known as the locally-corrected Nyström (LCN) method. In this method, by computing convolutions of the kernel with a suitable set of basis functions, it is possible to determine how to adjust the quadrature rule so that it is just as accurate near the singularity as far from it. The beauty of the method is that these quadrature rule modifications are required only in the vicinity of the singularity, hence the name local corrections. Reference [11] provides an in-depth discussion of the LCN method for application of two-dimensional and three-dimensional electromagnetic scattering problems. It is emphasized in [11, 33, 34] that the Nyström method is well-suited for higher-order implementation, since a higher-order result can be obtained by the relatively simple expedient of upgrading the quadrature rule. Furthermore, obtaining higher-order results with MoM is very expensive because of the integrations that must be performed to high accuracy. Thus the LCN approach may offer a much more efficient alternative when high accuracy is desired.

The LCN discretization does not typically impose cell-to-cell current continuity. For problems involving complex 3-D structures, nonconforming meshes may offer simpler geometrical modeling. Therefore, a second potential advantage of the LCN approach is the possibility of using simpler geometrical models than those required by the MoM procedure. In addition, the LCN can easily provide a representation that varies in quadrature order from cell to cell, offering enhanced accuracy in needed regions.

Possible advantages of the LCN method are :

- Simple and efficient mechanism for discretizing integral equations even if they have singular kernels
- Nonconforming mesh models
- Application of adaptive methods for LCN using h-refinement (re-meshing model) or p-refinement (changing order of basis)

- Avoid complex MoM integrations for off-diagonal matrix entries

In this thesis, we consider applying the above techniques to problems in package designs, which often involve multilayer structures, solid or perforated ground planes, embedded passive devices such as capacitors and spiral inductors, and interconnects in horizontal or vertical directions. Several examples will be used to illustrate the modeling.

The organization of this thesis is as follows: In Chapter 2, a method to obtain Green's functions in the spectral and spatial domains is presented. Green's functions incorporate planar layered media within the integral equations. These equations are also explained in Chapter 2 and they will be used in MoM and LCN formulations in subsequent chapters. The GPOF method is used to evaluate Green's functions to avoid the direct calculation of Sommerfeld integrals. The details of the MoM formulations in the spatial domain are given in Chapter 3, along with a variety of numerical examples. The LCN method is applied to MPIE for layered media in Chapter 4. The basic LCN discretization is developed and preliminary test cases are shown for validation. One of the original contribution of this work is the use of LCN for the analysis of layered media structures. A major contribution is presented in the need for mixed-order representations for proper electric charge modeling. An additional contribution is the demonstration that the LCN approach can be used with nonconforming cell models. In Chapter 5, the extension of the LCN approach to printed circuit applications is attempted. Unfortunately, difficulties arise when using the mixed-order LCN approach of Chapter 4 with narrow microstrip lines. These difficulties are explored in Chapter 5. Chapter 6 proposes a possible remedy to the aforementioned difficulties, in the form of an alternative representation for narrow strips. Chapter 7 summarizes the research, and several appendices provide ancillary aspects of the investigation.

CHAPTER II

MPIE IN PLANARLY LAYERED MEDIA

The first step of the MoM and LCN formulations is to write an integral equation describing the electromagnetic problem. Two of the most popular forms of the integral equations are the electric field integral equation (EFIE) and the magnetic field integral equation (MFIE). The EFIE enforces the boundary condition on the tangential components of the electric field, while the MFIE enforces the boundary condition on the tangential components of the magnetic field. The EFIE can be applied to analyze thin structures such as strips, plates or scatterers, but its implementation is more complicated than the MFIE because of the differential operators occurring in the equation. On the other hand, the MFIE cannot be applied to analyze infinitesimally thin structures. In this thesis, the mixed potential integral equation (MPIE) for printed geometries is used as a special case of the EFIE. These integral equations require related Green's functions, either of the vector and scalar potentials (for a MPIE formulation) or of the electric fields (for a traditional EFIE formulation). The Green's function of a wave equation is the solution of the wave equation for a point source. When the solution to the wave equation due to a point source is known, the solution due to a general source can be obtained by the principle of linear superposition [13]. This is a result of the linearity of the wave equation, and the fact that a general source is just a linear superposition of point sources.

2.1 Green's Functions

Green's functions play an important role in integral equations for electromagnetic problems. For planar multilayer geometries, they reduce the dimension of the problem by incorporating the layer information, such as the dielectric constants, thicknesses and the number of layers, through satisfying the boundary conditions at the interfaces between the layers. Therefore, the efficient calculation of Green's functions is quite important for the characterization of

such geometries.

Green's functions of the vector and scalar potentials in the spectral and spatial domains are obtained for horizontal and vertical electric dipole sources placed in multilayer planar media, where the layers are assumed to extend to infinity in transverse directions. The spatial-domain Green's functions are obtained from the spectral-domain Green's functions via the Hankel transformation, in which the spectral-domain Green's functions are known in closed forms for layered media [13, 15]. This transformation, also known as a Sommerfeld integral, contains an oscillatory integrand over an infinite domain whose evaluation is computationally very expensive [29].

To obtain the spatial-domain Green's functions analytically, Green's functions in the spectral domain are approximated in terms of complex exponentials, whose Hankel transforms can be analytically obtained via the Sommerfeld identity [14]. One way to perform this approximation is to use Prony's method, in which the number of samples required must be twice the number of complex exponentials [37]. It is obvious that this leads to difficulty in sampling rapid variations of the spectral-domain Green's functions, unless a large number of exponentials is used. Although a technique known as the least-square Prony method improves the ability to account for the rapid changes with a moderate number of exponentials [2], it still requires several trial and error iterations because of its noise sensitivity, which makes the technique inefficient and less robust. Another exponential approximation technique is the generalized pencil of function (GPOF) method [24], which is more robust and less noise sensitive when compared to the original and least-square Prony methods, and also provides a good measure for choosing the number of exponentials required in the approximation. The GPOF method is summarized in Appendix A. However, the GPOF procedure still requires a study of the spectral-domain behavior of the Green's function in advance, in order to decide on the approximation parameters such as the number of sampling points and the maximum value of the sampling range. In addition, one would need to take thousands of samples in order to be able to approximate a slowly converging function with rapid changes, because both the Prony and the GPOF methods require uniform sampling of the function.

Recently, a new approach based on a two-level approximation has been proposed to overcome the previously mentioned difficulties, and it has been demonstrated that the new approach is very robust and computationally much more efficient than the original one and its variants [1]. The two-level approach divides the range of approximation into two parts, the first one covering the region where the function to be approximated has rapid transitions, the second covering the region where the function is smooth. Therefore, it is no longer necessary to take thousands of samples to account for a rapid transition that occurs in a small part of the entire range, resulting in a significant reduction in the number of data points to be processed, which, in turn, translates into a substantial saving in the computation time.

The two-level approach can be extended to a three-level approach, which divides the range of approximation into three parts. Because the spectral-domain Green's functions might have fast variations locally, and the GPOF method requires uniform sampling along the range of approximation, the use of the multi-level approach prevents taking thousands of samples. On the other hand, using the three-level approach is not necessary for smooth functions where the two-level or one-level approach is sufficient.

Consider the planar multilayered medium shown in Figure 2.1 where it is assumed that the layers extend to infinity in the transverse directions. The source (a horizontal electric dipole (HED) or vertical electric dipole (VED)), is embedded in region i and the observation point can be located in an arbitrary layer. Each layer can have different electric and magnetic properties $(\epsilon_{r_i}, \mu_{r_i})$ and thickness (d_i). Perfect electric conducting planes and half-spaces are also regarded as layers in this formulation. The spectral-domain expressions for the Green's functions are presented in Appendix B.

The exponential approximation process used to construct spatial-domain Green's functions begins by sampling the spectral-domain Green's function to be approximated. The GPOF method is used to obtain the exponential approximation

$$\tilde{G} \cong \frac{1}{j2k_{z_i}} \left\{ \sum_{n_1=1}^{N_1} a_{n_1} e^{-\alpha_{n_1} k_{z_i}} + \sum_{n_2=1}^{N_2} a_{n_2} e^{-\alpha_{n_2} k_{z_i}} + \sum_{n_3=1}^{N_3} a_{n_3} e^{-\alpha_{n_3} k_{z_i}} \right\} \tag{1}$$

where a_n's and α_n's denote the coefficients and exponents of the complex exponentials.

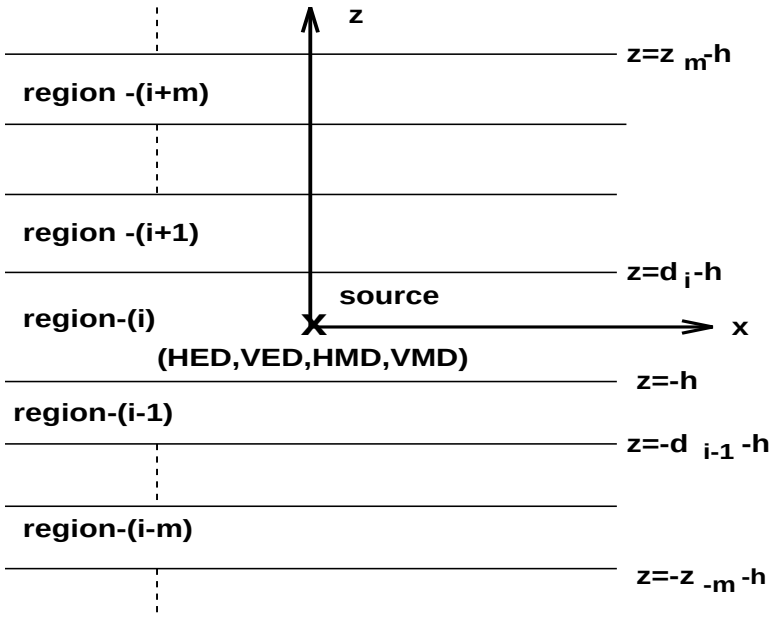

Figure 1: Sources embedded in a multilayer medium.

Since the principal goal of this section is to introduce a robust and efficient technique to obtain the spatial-domain Green's functions in closed-form for planar layered media, it would be useful to first provide the definition of the spatial-domain Green's functions

$$G = \frac{1}{4\pi} \int_{SIP} dk_\rho \, k_\rho H_0^{(2)} (k_\rho \rho) \, \tilde{G} (k_\rho) \tag{2}$$

where G and $\tilde{G}$ are the Green's functions in the spatial and spectral domains, respectively, $H_0^{(2)}$ is the Hankel function of the second kind, and SIP is the Sommerfeld integration path defined in Figures 2.2 and 2.3 for two-level and three-level approximations, respectively.

Using the Sommerfeld identity

$$\frac{e^{-jkr}}{r} = \frac{1}{2j} \int_{SIP} dk_\rho \, k_\rho H_0^{(2)} (k_\rho \rho) \, \frac{e^{-jk_z|z|}}{k_z} \tag{3}$$

the exponential approximation of the spectral domain Green's functions can be transformed to the spatial domain as

$$G \cong \sum_{n_1=1}^{N_1} a_{n_1} \frac{e^{-jk_i r_{n_1}}}{r_{n_1}} + \sum_{n_2=1}^{N_2} a_{n_2} \frac{e^{-jk_i r_{n_2}}}{r_{n_2}} + \sum_{n_3=1}^{N_3} a_{n_3} \frac{e^{-jk_i r_{n_3}}}{r_{n_3}} \tag{4}$$

where $r_{n_1} = \sqrt{\rho^2 - \alpha_{n_1}^2}$, $r_{n_2} = \sqrt{\rho^2 - \alpha_{n_2}^2}$, $r_{n_3} = \sqrt{\rho^2 - \alpha_{n_3}^2}$, $\rho = \sqrt{x^2 + y^2}$, and the a_n's and α_n's are complex numbers. Using the GPOF method and the closed-form spectral-domains Green's functions, the Sommerfeld integrals are evaluated analytically.

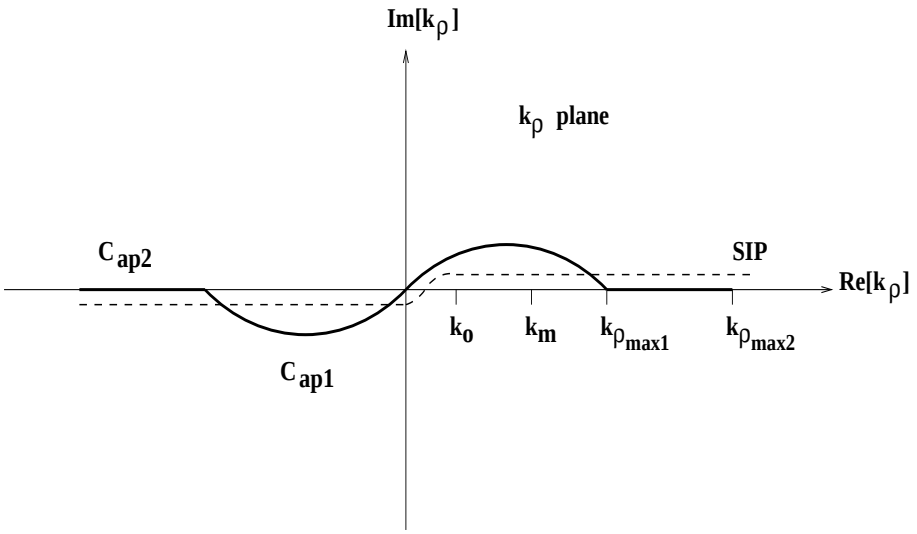

Figure 2: Definition of the Sommerfeld integration path, and the paths C_{ap1} and C_{ap2} used in two-level approximations.

In the two-level approach, a path formed by the paths C_{ap1} and C_{ap2} is employed, as depicted in Figure 2.2, and the paths C_{ap1} and C_{ap2} are defined by the following parametric equations:

$$\text{For } C_{ap2}: \quad k_{z_i} = -jk_i\left[T_{01}+t\right] \qquad 0 \le t \le T_{02} \tag{5}$$

$$\text{For } C_{ap1}: \quad k_{z_i} = k_i\left[-jt+\left(1-\frac{t}{T_{01}}\right)\right] \qquad 0 \le t \le T_{01} \tag{6}$$

where t is the parametric variable sampled uniformly in the corresponding ranges, T_{01} and T_{02}. T_{01} must be large enough to capture the asymptotic behavior of the Green's function. The remaining function is easily captured in the second part of the approximation by using a small number of sampling points. In the three-level approach, a similar path is formed by the paths C_{ap1}, C_{ap2} and C_{ap3} which are defined by the following parametric equations:

$$\text{For } C_{ap3}: \quad k_{z_i} = -jk_i\left[T_{01}+T_{02}+t\right] \qquad 0 \le t \le T_{03} \tag{7}$$

$$\text{For } C_{ap2}: \quad k_{z_i} = -jk_i\left[T_{01}+t\right] \qquad 0 \le t \le T_{02} \tag{8}$$

$$\text{For } C_{ap1}: \quad k_{z_i} = k_i\left[-jt+\left(1-\frac{t}{T_{01}}\right)\right] \qquad 0 \le t \le T_{01} \tag{9}$$

The spectral-domain Green's functions are first derived in the source layer, then by using an iterative algorithm applied to each transverse electric (TE) and transverse magnetic

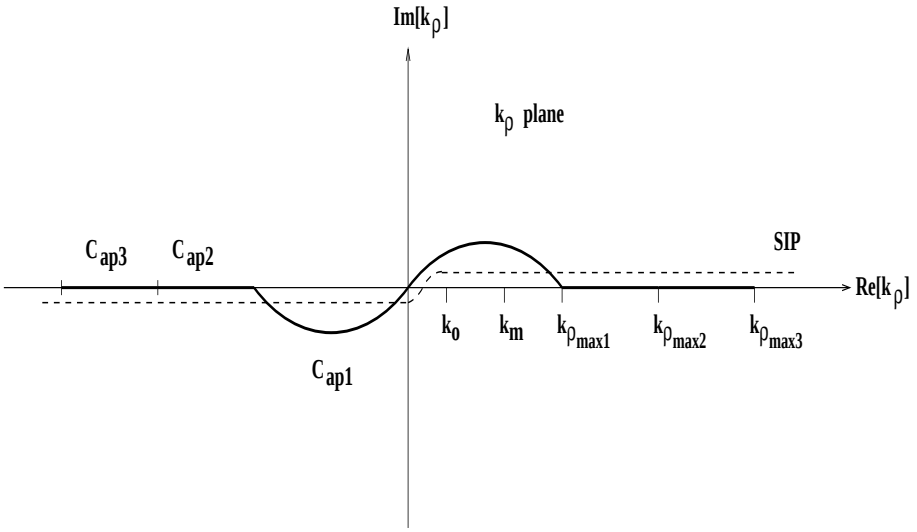

Figure 3: Definition of the Sommerfeld integration path, and the paths C_{ap1}, C_{ap2} and C_{ap3} used in three-level approximations.

(TM) component they are obtained in the observation layer. Then, the spectral-domain Green's functions are approximated in terms of complex exponentials via the GPOF method after the direct terms have been extracted.

All of the Green's functions, presented herein, are for vector and scalar potentials that are not defined uniquely in stratified media [15]. In other words, different sets of Green's functions for the vector and scalar potentials can be chosen to satisfy the same boundary conditions [38, 39]. The following notation for the Green's function is commonly used and referred to as the traditional form for the vector potentials:

$$\overrightarrow{\overleftarrow{G}}_A = (\hat{x}\hat{x} + \hat{y}\hat{y})G_{xx} + \hat{z}\hat{x}G_{zx} + \hat{z}\hat{y}G_{zy} + \hat{z}\hat{z}G_{zz} \tag{10}$$

The notation $G_x^{q_e}$ and $G_z^{q_e}$ are used for the scalar potentials.

2.2 Formulation of the Mixed Potential Integral Equation in 3-D

Consider a planar conducting structure in a multilayer environment. The tangential components of the scattered electric field on the plane of the patch and on the vertical strips can be written in terms of the surface current density, **J**, and the associated Green's functions

of the vector and scalar potentials as follows:

$$E_x^s = -jwG_{xx}^A * J_x + \frac{1}{jw}\frac{\partial}{\partial x}\left(G^{q_e} * \nabla \cdot \mathbf{J}\right) \tag{11}$$

$$E_y^s = -jwG_{yy}^A * J_y + \frac{1}{jw}\frac{\partial}{\partial y}\left(G^{q_e} * \nabla \cdot \mathbf{J}\right) \tag{12}$$

$$E_z^s = -jwG_{zx}^A * J_x - jwG_{zy}^A * J_y - jwG_{zz}^A * J_z + \frac{1}{jw}\frac{\partial}{\partial z}\left(G^{q_e} * \nabla \cdot \mathbf{J}\right) \tag{13}$$

where $*$ denotes convolution and $G_{xx}^A = G_{yy}^A$. The fields E_x^s, E_y^s and E_z^s represent the scattered electric field components along the x-, y- and z-directions, respectively. The term G_{ij}^A represents the i-directed vector potential at $\mathbf{r}$ due to a j-directed electric dipole of unit strength located at $\mathbf{r}'$, while G^{q_e} represents the scalar potential by a unit point charge associated with an electric dipole. Since the traditional form of the Green's functions are employed in the formulation, the Green's function of the scalar potential is not unique for horizontal and vertical electric dipoles as stated previously. The term involving the Green's function of the scalar potential can be explicitly written as

$$G^{q_e} * \nabla \cdot \mathbf{J} = G_x^{q_e} * \frac{\partial J_x}{\partial x} + G_y^{q_e} * \frac{\partial J_y}{\partial y} + G_z^{q_e} * \frac{\partial J_z}{\partial z} \tag{14}$$

where $G_x^{q_e}\left(= G_y^{q_e}\right)$ and $G_z^{q_e}$ denote the Green's functions of the scalar potential for a horizontal and vertical electric dipole, respectively.

The total electric field in region i is the summation of the scattered electric fields and the incident electric field

$$\boldsymbol{E}^t = \hat{x}E_x^s + \hat{y}E_y^s + \hat{z}E_z^s + \boldsymbol{E}^i \tag{15}$$

Boundary conditions for the tangential electric fields are applied on the conductors as

$$(\boldsymbol{E}^t)_{tan} = 0 \tag{16}$$

Imposing Eq. (16) on Eq. (15) results in the following mixed potential integral equation (MPIE):

$$(\hat{x}E_x^s + \hat{y}E_y^s + \hat{z}E_z^s)_{tan} = -(\boldsymbol{E}^i)_{tan} \tag{17}$$

This equation can be solved in principle to determine the currents and electromagnetic fields throughout the multilayer structure.

CHAPTER III

METHOD OF MOMENTS

The Hankel transforms of the spectral-domain Green's functions are oscillatory and slowly convergent in nature. Therefore, the use of the spatial-domain MoM was not popular until the recent introduction of an efficient algorithm to approximate the spatial-domain Green's functions in closed form [14, 3]. This closed-form approximation of the spatial-domain Green's functions not only improves the calculation of the Green's functions, but also results in an analytical evaluation of the MoM matrix entries [6]. Therefore, the computational efficiency of the spatial-domain MoM in the solution of the MPIE has been improved without sacrificing the accuracy in the results. In this chapter, the solution of the MPIE using the MoM procedure is explained, based on the formulations of the references [6, 5, 30, 28]. In Section 3.1, the MoM procedure is described in detail. The application of the MoM to printed geometries in the spatial domain is presented in Section 3.2. The analytical calculation of the integrals is illustrated in Section 3.3, while the calculation of S-parameters using de-embedding is explained in Section 3.4.

3.1 MoM

The method of moments is a procedure for converting a continuous equation into a discrete matrix equation. Although the MoM in this thesis is applied for the solution of a specific integral equation, the general framework of the MoM is presented here for the sake of completeness. For this purpose, the following operator equation is considered:

$$L(f) = g \tag{18}$$

where g represents a known source, and L denotes a linear operator operating on an unknown function f, that has to be determined. The first step in the application of the MoM for the solution of Eq. (18) is to expand the unknown function by a set of known basis functions

with unknown coefficients as

$$f = \sum_n \alpha_n f_n \tag{19}$$

where f_n represents the basis function spanning the domain of the operator L, and α_n is the corresponding unknown coefficient. Using the representation of f in Eq. (19) and the linearity property of L, the following equation is obtained :

$$\sum_n \alpha_n L(f_n) = g \tag{20}$$

The second step in MoM is to introduce a set of weighting functions, or testing functions, w_1, w_2, $w_3, ...$ in the range space of L, and to take their inner products with both sides of Eq. (20), resulting in

$$\begin{aligned} < w_1, g > &= \sum_n \alpha_n < w_1, L(f_n) > \\ < w_2, g > &= \sum_n \alpha_n < w_2, L(f_n) > \\ &\vdots \end{aligned} \tag{21}$$

These equations can be written in matrix form as

$$[g_m] = [l_{mn}][\alpha_n] \tag{22}$$

where

$$[g_m] = \begin{bmatrix} < w_1, g > \\ < w_2, g > \\ \vdots \end{bmatrix}$$

$$[l_{mn}] = \begin{bmatrix} < w_1, L(f_1) > & < w_1, L(f_2) > \dots \\ < w_2, L(f_1) > & < w_2, L(f_2) > \dots \\ \dots\dots\dots\dots\dots\dots\dots\dots\dots\dots\dots\dots \end{bmatrix}$$

$$[\alpha_n] = \begin{bmatrix} \alpha_1 \\ \alpha_2 \\ \vdots \end{bmatrix} \tag{23}$$

If the matrix $[l]$ is nonsingular, then the solution for f is obtained from Eq. (19) using

$$[\alpha_n] = [l_{mn}]^{-1}[g_m] \tag{24}$$

If the matrix $[l]$ is of infinite order, then its inversion can not be performed unless $[l]$ is diagonal. If the sets f_n and w_n are finite, the matrix is of finite order, and can be inverted by standard procedures.

The solution depends on the set of basis functions, which must be linearly independent and should be chosen such that some linear combination with the form of Eq. (19) can approximate f reasonably well. The solution also depends on the set of testing functions $w_1, w_2, \ldots$, which should be linearly independent and should best represent the properties of g. Some additional factors which affect the choice of f_n and w_n are (1) the accuracy of solution desired, (2) the ease of evaluation of the matrix elements, (3) the size of the matrix that can be inverted, and (4) the realization of a well-conditioned matrix $[l]$ [23].

The name "method of moments" derives from the original terminology that $\int x^n f(x)\,dx$ is the nth moment of f. When x^n is replaced by an arbitrary w_n, we continue to call the integral a moment of f. The method is also known as "method of weighted residuals," a name that derives from the following interpretation. If Eq. (20) represents an approximate equality, then the difference between the exact and approximate $L(f)$ is

$$g - \sum_n \alpha_n L(f_n) = r \tag{25}$$

which is called the residual r. The inner products $< w_n, r >$ are called the weighted residuals. Eq. (21) is obtained simply by setting all weighted residuals to zero.

3.2 Formulation of the Spatial Domain MoM

The method of moments converts an integral equation to a matrix equation through the expansion of the unknown function in terms of known basis functions and the enforcement of the equation using the testing functions. Therefore, one needs to choose the basis and testing functions judiciously to minimize the error in average sense. In the study, the basis and testing functions are chosen from the same set of functions, a process known as Galerkin's method.

The surface current density **J** is expanded in terms of sub-domain basis functions as

$$J_x(x,\, y) = \sum_m I_x^m B_x^m(x,\, y) \tag{26}$$

$$J_y(x,\, y) = \sum_n I_y^n B_y^n(x,\, y) \tag{27}$$

$$J_z(x,\, y,\, z) = \sum_l I_z^l B_z^l(x,\, y,\, z) \tag{28}$$

where B_x^m, B_y^n and B_z^l are the basis functions with the unknown coefficients I_x^m, I_y^n and I_z^l, defined at m-th and n-th position on the subdivided horizontal conductor and at l-th position on the subdivided vertical conductor. In this thesis, rooftop functions are chosen as the basis functions to represent x-, y-, and z-components of the current density as shown in Figure 4.

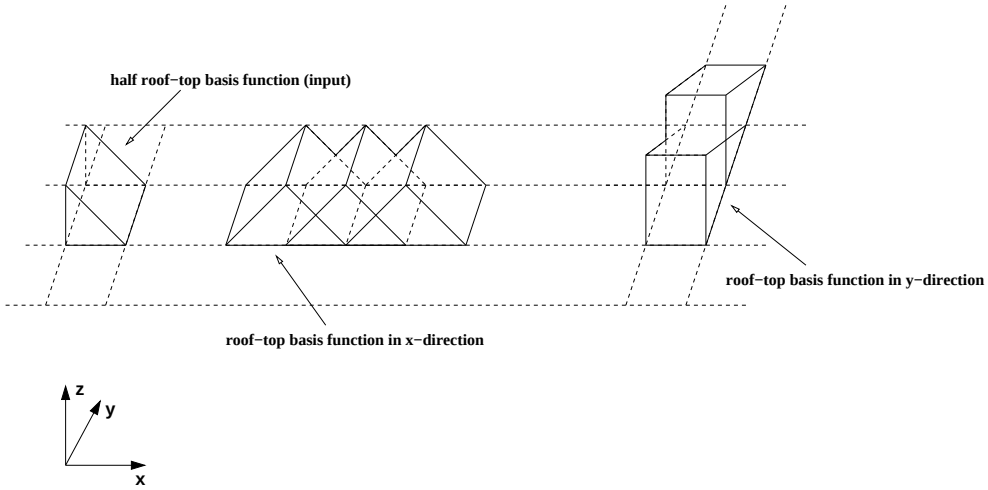

Figure 4: Rooftop basis functions in x- and y-dimensions

After substituting Eqs. (26)-(28) into Eq. (17) and applying the testing procedure of the MoM to the equation using the testing functions $T_x^{m'}$, $T_y^{n'}$ and $T_z^{l'}$, the following equation is obtained

$$\left\langle \boldsymbol{T}(x,y,z)\ ,\ \hat{x}E_x^s + \hat{y}E_y^s + \hat{z}E_z^s \right\rangle = -\left\langle \boldsymbol{T}(x,y,z)\ ,\ \boldsymbol{E^i} \right\rangle \tag{29}$$

which leads to a matrix equation for the unknown coefficients of the basis functions as

$$\begin{bmatrix} Z_{xx} & Z_{xy} & Z_{xz} \\ Z_{yx} & Z_{yy} & Z_{yz} \\ Z_{zx} & Z_{zy} & Z_{zz} \end{bmatrix} \begin{bmatrix} I_x \\ I_y \\ I_z \end{bmatrix} = \begin{bmatrix} V_x \\ V_y \\ V_z \end{bmatrix} \tag{30}$$

where the Zs denote the mutual impedances between the testing and basis functions, and the Vs represent the excitation voltages due to the current source(s). The matrix entries corresponding to the horizontal and the vertical metallizations are written as

$$Z_{xx} = -j\omega \left\langle T_x^{m'},\, G_{xx}^A * B_x^m \right\rangle + \frac{1}{j\omega} \left\langle T_x^{m'},\, \frac{\partial}{\partial x} \left[G_x^{q_e} * \frac{\partial B_x^m}{\partial x} \right] \right\rangle \tag{31}$$

$$Z_{xy} = \frac{1}{j\omega} \left\langle T_x^{m'},\, \frac{\partial}{\partial x} \left[G_y^{q_e} * \frac{\partial B_y^n}{\partial y} \right] \right\rangle \tag{32}$$

$$Z_{yx} = \frac{1}{j\omega} \left\langle T_y^{n'},\, \frac{\partial}{\partial y} \left[G_x^{q_e} * \frac{\partial B_x^m}{\partial x} \right] \right\rangle \tag{33}$$

$$Z_{yy} = -j\omega \left\langle T_y^{n'},\, G_{yy}^A * B_y^n \right\rangle + \frac{1}{j\omega} \left\langle T_y^{n'},\, \frac{\partial}{\partial y} \left[G_y^{q_e} * \frac{\partial B_y^n}{\partial y} \right] \right\rangle \tag{34}$$

$$Z_{zx} = -j\omega \left\langle T_z^{l'},\, G_{zx}^A * B_x^m \right\rangle + \frac{1}{j\omega} \left\langle T_z^{l'},\, \frac{\partial}{\partial z} \left[G_x^{q_e} * \frac{\partial B_x^m}{\partial x} \right] \right\rangle \tag{35}$$

$$Z_{xz} = \frac{1}{j\omega} \left\langle T_x^{m'},\, \frac{\partial}{\partial x} \left[G_z^{q_e} * \frac{\partial B_z^l}{\partial z} \right] \right\rangle \tag{36}$$

$$Z_{zy} = -j\omega \left\langle T_z^{l'},\, G_{zy}^A * B_y^n \right\rangle + \frac{1}{j\omega} \left\langle T_z^{l'},\, \frac{\partial}{\partial z} \left[G_y^{q_e} * \frac{\partial B_y^n}{\partial y} \right] \right\rangle \tag{37}$$

$$Z_{yz} = \frac{1}{j\omega} \left\langle T_y^{n'},\, \frac{\partial}{\partial y} \left[G_z^{q_e} * \frac{\partial B_z^l}{\partial z} \right] \right\rangle \tag{38}$$

$$Z_{zz} = -j\omega \left\langle T_z^{l'},\, G_{zz}^A * B_z^l \right\rangle + \frac{1}{j\omega} \left\langle T_z^{l'},\, \frac{\partial}{\partial z} \left[G_z^{q_e} * \frac{\partial B_z^l}{\partial z} \right] \right\rangle \tag{39}$$

where $<,>$ and $*$ denote inner product and convolution operators, respectively, defined as follows:

$$\langle f(x,\, y),\, g(x,\, y) \rangle = \iint dx\, dy\, f(x,\, y) \cdot g(x,\, y) \tag{40}$$

$$f(x,\, y) * g(x,\, y) = \iint dx'\, dy'\, f(x - x',\, y - y') \cdot g(x',\, y') \tag{41}$$

Using the closed-form Green's functions with the MoM improves the computational efficiency of the MoM for simple geometries which have only horizontal conductors. The next step is to develop an accurate and efficient EM simulator to analyze general geometries. The application of the MoM with the closed-form Green's functions to a geometry with vertical metallization is not as straightforward as the application of MoM to only horizontal geometries [30].

The z and z' parameters in the equations of the spectral-domain Green's functions have to be constant when sampling the functions over the range of approximation to obtain the exponential approximation of the functions. Therefore, obtaining spatial-domain Green's functions for horizontal conductors is not a problem. On the other hand, the inner product integrals in Eqs. (35)-(39) have integrations over z and/or z' for vertical conductors. Vertical conductors typically represent vias between layers of metallizations and are of interest.

In order to obtain spatial-domain Green's functions for vertical conductors, the spectral-domain Green's functions can be written explicitly in terms of the amplitudes of the up- and down-going waves in the functions (see Appendix B). The exponential functions of z and z' can then be factored out from the spectral-domain equations. As an example, $\tilde{G}^A_{zx}$ is written as

$$\begin{aligned}
\tilde{G}^A_{zx} \quad = \quad & -\frac{\mu_i}{2jk_{z_i}}\frac{k_x k_{z_i}}{k_\rho^2}\Bigg\{\left(\tilde{R}^{i,i+1}_{TE}M^{TE}_i + \tilde{R}^{i,i+1}_{TM}M^{TM}_i\right)e^{-jk_{z_i}(2d_i-z'-z)} \\
& + \left(\tilde{R}^{i,i+1}_{TE}\tilde{R}^{i,i-1}_{TE}M^{TE}_i - \tilde{R}^{i,i+1}_{TM}\tilde{R}^{i,i-1}_{TM}M^{TM}_i\right)e^{-jk_{z_i}(2d_i+z'-z)} \\
& + \left(\tilde{R}^{i,i-1}_{TM}\tilde{R}^{i,i+1}_{TM}M^{TM}_i - \tilde{R}^{i,i-1}_{TE}\tilde{R}^{i,i+1}_{TE}M^{TE}_i\right)e^{-jk_{z_i}(2d_i+z-z')} \\
& + \left(-\tilde{R}^{i,i-1}_{TE}M^{TE}_i - \tilde{R}^{i,i-1}_{TM}M^{TM}_i\right)e^{-jk_{z_i}(z'+z)}\Bigg\} \qquad (42)
\end{aligned}$$

after substituting the amplitudes of the up- and down-going waves. Integrals over z and z' are performed analytically in the spectral domain, prior to applying the exponential approximation process using the GPOF method. The remaining step is to calculate the spatial-domain equation using the Sommerfeld identity in Eq. (3) via the spectral-domain equation.

To explain the solution procedure, the first part of Z_{zx} is written as

$$\begin{aligned}
\left\langle T^{l'}_z,\, G^A_{zx} * B^m_x \right\rangle \quad = \quad & \iint dz\, dy\, T^{l'}_z(y,\, z) \\
& \cdot \iint dx'\, dy'\, G^A_{zx}(x-x',\, y-y',\, z,\, z')B^m_x(x',\, y') \qquad (43)
\end{aligned}$$

where z' is constant. When the spatial-domain Green's function is replaced by the spectral-domain Green's function using Eq. (2), and using the separability of the testing function, $T^{l'}_z(y,\, z) = T^{l'}_z(y)\, T^{l'}_z(z)$, the following expression is obtained

$$\left\langle T^{l'}_z,\, G^A_{zx} * B^m_x \right\rangle \quad = \quad \iint dz\, dy\, T^{l'}_z(y)\, T^{l'}_z(z)$$

$$\cdot \iint dx'\, dy' \left\{ \frac{1}{4\pi} \int_{SIP} dk_\rho\, k_\rho H_0^{(2)}\left(k_\rho|\rho-\rho'|\right) \tilde{G}_{zx}^{A}\left(k_\rho,\, z\right) \right\} B_x^m(x',\, y') \tag{44}$$

After changing the order of integrations, the following function, F_{zx}^{A}, is defined as

$$\begin{aligned} F_{zx}^{A} &\overset{\text{def}}{=} \int dz\, T_z^{l'}(z) \frac{1}{4\pi} \int_{SIP} dk_\rho\, k_\rho H_0^{(2)}\left(k_\rho|\rho-\rho'|\right) \frac{\tilde{G}_{zx}^{A}\left(k_\rho,\, z\right)}{-jk_x} \\ &\cong \frac{1}{4\pi} \int_{SIP} dk_\rho\, k_\rho H_0^{(2)}\left(k_\rho|\rho-\rho'|\right) \cdot \text{GPOF}\left\{ \int dz\, T_z^{l'}(z) \frac{\tilde{G}_{zx}^{A}\left(k_\rho,\, z\right)}{-jk_x} \right\} \end{aligned} \tag{45}$$

The next step is to apply the exponential approximation to the argument of the GPOF$\{\cdot\}$ without the $-jk_x$ term, to obtain

$$\left\langle T_z^{l'},\, G_{zx}^{A} * B_x^m \right\rangle = -\int dy\, T_z^{l'}(y) \iint dx'\, dy'\, B_x^m(x',\, y') \frac{\partial}{\partial x'} F_{zx}^{A} \tag{46}$$

When the chain rule is applied to the inner integrand

$$\frac{\partial}{\partial x'} \left[B_x^m\left(x',\, y'\right) F_{zx}^{A} \right] = \frac{\partial}{\partial x'} B_x^m\left(x',\, y'\right) F_{zx}^{A} + B_x^m\left(x',\, y'\right) \frac{\partial}{\partial x'} F_{zx}^{A} \tag{47}$$

the inner product expression is replaced by

$$\begin{aligned} \left\langle T_z^{l'},\, G_{zx}^{A} * B_x^m \right\rangle &= -\int dy\, T_z^{l'}(y) \int dy' \left[B_x^m\left(x',\, y'\right) F_{zx}^{A} \right] \Big|_{x' \in \Omega_B} \\ &\quad + \int dy\, T_z^{l'}(y) \iint dx'\, dy'\, F_{zx}^{A} \frac{\partial}{\partial x'} B_x^m\left(x',\, y'\right) \end{aligned} \tag{48}$$

where Ω_B is the boundary of the domain of the basis function. After substituting $x - x' = u$ and $y - y' = v$, the inner product (48) is written as

$$\begin{aligned} \left\langle T_z^{l'},\, G_{zx}^{A} * B_x^m \right\rangle &= \int dv\, F_{zx}^{A} \int dy \left[T_z^{l'}(y) B_x^m\left(x-u,\, y-v\right) \right] \Big|_{x' \in \Omega_B} \\ &\quad + \iint du\, dv\, F_{zx}^{A} \int dy\, T_z^{l'}(y) \frac{\partial}{\partial x'} B_x^m\left(x-u,\, y-v\right) \end{aligned} \tag{49}$$

where $x = x_i$, the x-coordinate of the vertical metallization. The first term in Eq. (49) is zero for the rooftop basis functions. On the other hand, the term must be evaluated for the half-rooftop basis functions. The other inner products in Eqs. (35)-(39) can be evaluated in similar fashion and are presented in Appendix C.

3.3 Analytical Calculation of the Integrations

A closed-form evaluation of the various integrals can be explained using the first inner product of Eq. (31), which can be written as:

$$\left\langle T_x^{m'},\, G_{xx}^{A} * B_x^m \right\rangle = \int\int dy dx\, T_x^{m'}(x,y) \int\int dy' dx'\, G_{xx}^{A}(x-x', y-y') B_x^m(x',y')$$

$$
\begin{aligned}
&= \int\int dvdu\, G^A_{xx}(u,v) \int\int dydx\, T_x^{m'}(x,y) B_x^m(x-u,y-v) \\
&= \int\int dvdu\, G^A_{xx}(u,v)\, [T_x^{m'} \otimes B_x^m] \qquad (50)
\end{aligned}
$$

where $\otimes$ is a correlation function integral used for the inner double integral (which can be evaluated analytically). The Green's function is approximated as

$$
G^A_{xx}(u,v) \cong \sum_{n=1}^{N} a_n \frac{e^{-jk_i r_n}}{r_n} \qquad (51)
$$

where $r_n = \sqrt{u^2+v^2-\alpha_n^2} = \sqrt{u^2+v^2+c_n^2}$, and α_n and c_n are defined in the preceding chapter. After the evaluation of the correlation integral, the outer double integral must be evaluated to calculate the matrix entries. The analytical evaluation of the MoM matrix entries is explained in [6]. The integrals reduce to the form

$$
\int\int dvdu \frac{e^{-jk_i r_n}}{r_n}\, u^k v^l \quad for \quad k = 0,\ldots,3, \quad l = 0,1 \qquad (52)
$$

When $k = l = 0$ in Eq. (52), the exponential term can be approximated by a Taylor's series, and the resulting integrand is an analytically integrable function [22]. For nonzero k and l, the integrals in Eq. (52) can be calculated analytically using the Taylor's series expansion of the exponential term and the integral identities in [6, 36]. The convergence of the Taylor's series expansion for each r_n has to be examined for the same number of terms. As a result, for different basis and testing function pairs, the expansion is performed around different center points R_c. Error analysis shows that fifth order Taylor's series is enough to obtain analytic and numeric integrations in good agreement [5]. Using the fifth order Taylor series expansion around R_c, $e^{-jk_i r_n}$ can be approximated as

$$
e^{-jk_i r_n} \approx e^{-jk_i R_c}(\beta_0 + \beta_1 r_n + \beta_2 r_n^2 + \beta_3 r_n^3 + \beta_4 r_n^4 + \beta_5 r_n^5) \qquad (53)
$$

where

$$
\begin{aligned}
\beta_0 &= 1 + jk_i R_c - \frac{k_i^2 R_c^2}{2} - j\frac{k_i^3 R_c^3}{6} + \frac{k_i^4 R_c^4}{24} + j\frac{k_i^5 R_c^5}{120} \\
\beta_1 &= -jk_i + k_i^2 R_c + j\frac{k_i^3 R_c^2}{2} - \frac{k_i^4 R_c^3}{6} - j\frac{k_i^5 R_c^4}{24} \\
\beta_2 &= -\frac{k_i^2}{2} - j\frac{k_i^3 R_c}{2} + \frac{k_i^4 R_c^2}{4} + j\frac{k_i^5 R_c^3}{12} \\
\beta_3 &= j\frac{k_i^3}{6} - \frac{k_i^4 R_c}{6} - j\frac{k_i^5 R_c^2}{12}
\end{aligned}
$$

$$\beta_4 = \frac{k_i^4}{24} + j\frac{k_i^5 R_c}{24}$$
$$\beta_5 = -j\frac{k_i^5}{120}$$

When c_n becomes large enough, the approximation starts to fail, so a parameter is calculated as

$$c_{th} = 10\sqrt{h_x^2 + h_y^2} \tag{54}$$

where th corresponds to threshold, and h_x and h_y are cell sizes in x- and y-directions, respectively. When c is smaller than c_{th}, the approximation can be written as

$$R_c = \sqrt{u_{mid}^2 + v_{mid}^2 + c_n^2} \tag{55}$$
$$\frac{e^{-jk_i r_n}}{r_n} \approx \frac{e^{-jk_i R_c}}{r_n}(\beta_0 + \beta_1 r_n + \beta_2 r_n^2 + \beta_3 r_n^3 + \beta_4 r_n^4 + \beta_5 r_n^5) \tag{56}$$

When c is larger than c_{th}, the approximation can be written as

$$R_c = \frac{u_{mid}^2 + v_{mid}^2}{2\sqrt{u_{mid}^2 + v_{mid}^2 + c_n^2}} \tag{57}$$
$$r'_n = \frac{u^2 + v^2}{2\sqrt{u_{mid}^2 + v_{mid}^2 + c_n^2}} \tag{58}$$
$$\frac{e^{-jk_i r_n}}{r_n} \approx \frac{e^{-jk_i(\sqrt{u_{mid}^2+v_{mid}^2+c_n^2}-R_c)}}{\sqrt{u_{mid}^2 + v_{mid}^2 + c_n^2}} e^{-jk_i R_c} \cdot (\beta_0 + \beta_1 r'_n + \beta_2 {r'_n}^2 + \beta_3 {r'_n}^3 + \beta_4 {r'_n}^4 + \beta_5 {r'_n}^5) \tag{59}$$

where the β's are calculated with respect to each c_n and R_c, and u_{mid} and v_{mid} are the middle points of the integration regions in the $u-$ and $v-$dimensions, respectively.

Although the matrix-fill time has been significantly reduced with this approach, further improvement can be still achieved; the Taylor's series expansion in this formulation is applied for every exponential function in the closed-form Green's function expression and the analytic integration is performed for every exponential. This repetition can be avoided by approximating the overall summation by a polynomial in the least square sense

$$\sum_{n=1}^{N} a_n \frac{e^{-jk_i r_n}}{r_n} \approx \frac{\beta_0}{r} + \beta_1 + \beta_2 r + \beta_3 r^2 + \beta_4 r^3 + \beta_5 r^4 \tag{60}$$

where $r = \sqrt{u^2 + v^2}$. As the polynomial is a function of r only, the analytical integrations are performed only once. Since the polynomial approximation can not be applied for the

matrix entries which contain singularities, it is used in the calculation of all the matrix entries except for the self and adjacent terms.

3.4 Calculation of S-parameters

There are two commonly used excitation models, the delta-gap voltage source and the impressed-current source. The delta-gap voltage model assumes ideal voltage sources exciting each port of the circuit, and neglects the direct radiation from these ideal sources. The impressed-current model assigns known excitation currents to each port, and uses the electromagnetic fields of these currents as the actual excitation. Note that the EM simulation technique presented in this thesis uses impressed-current sources to characterize an N-port circuit [16]. From the MoM matrix, the impedance or the admittance matrix associated with the ports can be calculated directly. Additional processing is necessary to extract the S-parameters associated with the ports.

In the impressed-current model, it is assumed that each port is defined by a single cell. Half-subsectional currents are impressed at each port. Figure 5 depicts one of the ports of the circuit illuminated by a current source of unity magnitude. The impressed current is placed in the infinitesimal gap between the ground plane and the microstrip transmission line [16].

Because there exists fringing, reactive and evanescent fields in the vicinity of the source and load terminals, circuit parameters, such as input impedance and S-parameters, are obtained by removing these higher order effects from the calculations, a process called de-embedding [44]. The main idea is to extend the length of the feed-lines so that incident and reflected waves can be extracted using ideal transmission line theory.

The formulation will be presented here for a two-port network. For a two-port, non-reciprocal, nonsymmetric network, the following procedure is applied to calculate the S-parameters [46, 28]. First, the port transmission lines must have a length of at least 1 to 2 wavelengths so that any near-field effects of the source can be easily separated from a well-defined standing wave on each line. One of the ports is excited and the current densities on the conductors, including the port transmission lines, are obtained. The GPOF method

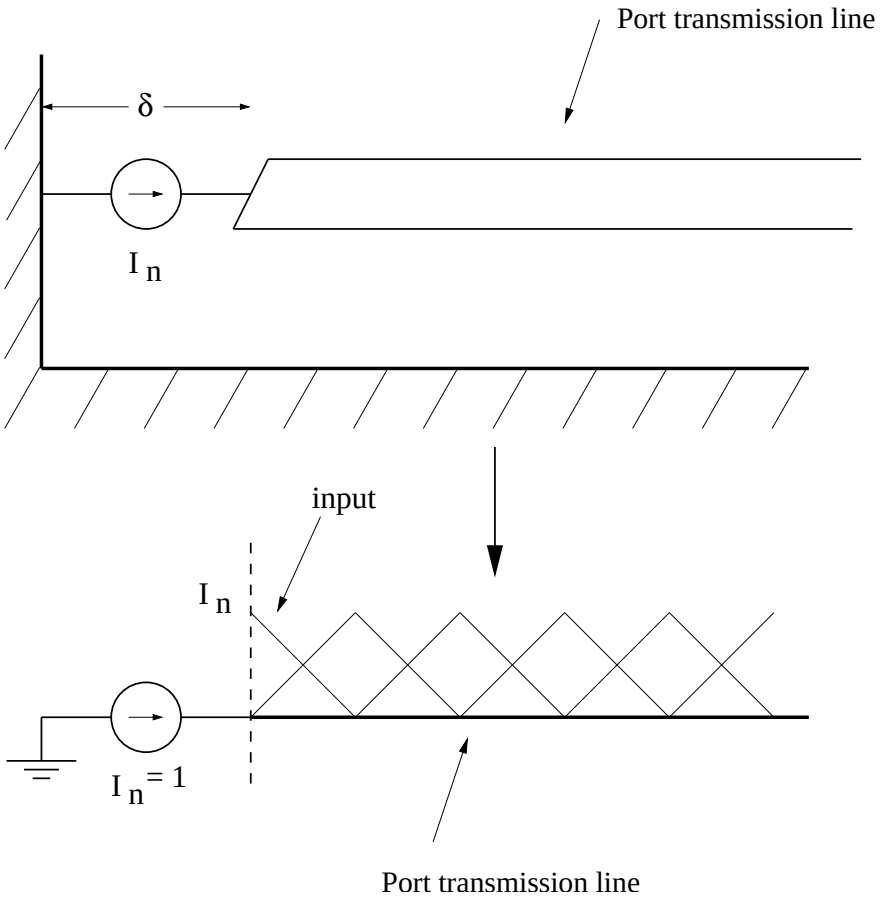

Figure 5: Impressed-current source model for port n

is used to approximate the current distribution on each port transmission line by a sum of complex exponentials as

$$I(x) \approx \sum_{i=1}^{N} I_i e^{(\alpha_i + j\beta_i)x} \tag{61}$$

where α_i and β_i correspond to the attenuation and propagation constants of the i^{th} mode of the current, respectively, and x is the distance along the port transmission line.

This approximation is equivalent to numerically separating the incident, reflected, evanescent, and the higher order propagating waves at the reference plane. If the port transmission lines are sufficiently long, evanescent and higher-order modes will be negligible. Then, the current can be expressed by only two exponentials with complex coefficients corresponding to the incident and reflected waves at the corresponding ports. (In the numerical experiments carried out in this study, it was found that the α_i's are small compared to the β_i's, and the propagation constants corresponding to the incident and reflected waves are identical except their sign difference, as expected.) Thus, the current distributions are expressed as

$$I_1(x) = I_{11}^{+} e^{-j\beta_1 x} + I_{11}^{-} e^{+j\beta_1 x} \tag{62}$$

$$I_2(x) = I_{21}^{+} e^{-j\beta_2 x} + I_{21}^{-} e^{+j\beta_2 x} \tag{63}$$

where I_{ij} is the current wave coefficient on the i^{th} port transmission line when port j is excited. The equations can be related to each other by using the S-parameter matrix

$$\begin{bmatrix} -I_{11}^{-} \\ I_{21}^{-} \end{bmatrix} = \begin{bmatrix} S_{11} & S_{12} \\ S_{21} & S_{22} \end{bmatrix} \begin{bmatrix} I_{11}^{+} \\ -I_{21}^{+} \end{bmatrix} \tag{64}$$

Next, port 2 is excited and the current distribution on the entire structure is again obtained. The current densities on the port are expressed as

$$I_1(x) = I_{12}^{+} e^{-j\beta_1 x} + I_{12}^{-} e^{+j\beta_1 x} \tag{65}$$

$$I_2(x) = I_{22}^{+} e^{-j\beta_2 x} + I_{22}^{-} e^{+j\beta_2 x} \tag{66}$$

The current wave coefficients can similarly be related using the S-parameter matrix

$$\begin{bmatrix} -I_{12}^{-} \\ I_{22}^{-} \end{bmatrix} = \begin{bmatrix} S_{11} & S_{12} \\ S_{21} & S_{22} \end{bmatrix} \begin{bmatrix} I_{12}^{+} \\ -I_{22}^{+} \end{bmatrix} \tag{67}$$

By combining (62) and (65), for a general two-port network, a matrix relation, which is used to find the S-parameters, can be written in the form

$$\begin{bmatrix} I_{11}^{+} & I_{12}^{+} & 0 & 0 \\ 0 & 0 & I_{11}^{+} & I_{12}^{+} \\ I_{21}^{+} & I_{22}^{+} & 0 & 0 \\ 0 & 0 & I_{21}^{+} & I_{22}^{+} \end{bmatrix} \begin{bmatrix} S_{11} \\ S_{12} \\ S_{21} \\ S_{22} \end{bmatrix} = \begin{bmatrix} -I_{11}^{-} \\ -I_{12}^{-} \\ -I_{21}^{-} \\ -I_{22}^{-} \end{bmatrix} \tag{68}$$

The S-parameters are calculated from the coefficients of these exponentials and transferred to the desired reference planes [46]. These S-parameters are inherently normalized and referenced to the characteristic impedances of the port transmission lines. Note that the propagation constants on the transmission lines are also found as the by-product of this method, which also enables us to extract the effective permittivity at each frequency of operation.

However, in some cases, it might be numerically difficult to extract the propagation constant and the unknown coefficients of the exponentials with sufficient precision from the same current samples by direct application of the GPOF method. This situation occurs in MIC structures where the electrical length of the port transmission line is very small. In such cases, one can find the propagation constant from a sufficiently long test transmission line, which has the same cross section as the original port transmission line, and then use this propagation constant to fit the current on the original line with complex exponentials through a linear least-squares algorithm [31]. Finally, the S-parameters obtained are converted to the S-parameters with the reference impedance of 50 Ω.

The characteristic impedances of the port transmission lines are calculated by using the following equation which is based on a quasi-TEM approach [17]

$$Z_c = \frac{1}{2\pi}\sqrt{\frac{\mu_0}{\epsilon_0 \epsilon_{eff}}} \ln\left(f_1 \frac{h}{w} + \sqrt{1 + \left(2\frac{h}{w}\right)^2}\right) \tag{69}$$

where $f_1 = 6 + (2\pi - 6)exp[-(30.666h/w)^{0.7528}]$, h is the thickness of the substrate and w is the width of the transmission line.

To calculate the S-parameters of a general N-port network with different characteristic impedances Z_{0_i} at port i, the following pseudo code, which fills the matrices in Eq. (68), is

given here for convenience [28]

$$
\begin{aligned}
&A \leftarrow 0 \\
&n \leftarrow \text{number of ports} \\
&for \quad i = 0, 1, 2, \cdots, n-1 \\
&begin \\
&\quad for \quad l = 0, 1, 2, \cdots, n-1 \\
&\quad begin \\
&\qquad for \quad m = 0, 1, 2, \cdots, n-1 \\
&\qquad begin \\
&\qquad\quad A_{i*n+m,\, l+m*n} \leftarrow I_{il}^{+} * sqrt(Z_{0_l}) \\
&\qquad end \\
&\qquad B_{i*n+l} \leftarrow -I_{il}^{-} * sqrt(Z_{0_l}) \\
&\quad end \\
&end
\end{aligned}
$$

Then, the S-parameters are found from $\mathbf{S} = \mathbf{A}^{-1}\mathbf{B}$.

3.5 Interdigital MIC Capacitor

For the examples, a general microstrip geometry in a layered medium is assumed where all layers and the ground plane extend to infinity in the horizontal plane, and the conductors are lossless and thin.

As an example to demonstrate the MoM solution, and verify the validity of the GPOF-based approximation of the Green's function, consider an interdigital MIC capacitor as shown in Figure 6 [28]. An interdigital lumped MIC capacitor is a good example of a non-resonant structure which has very small dimensions with respect to the guided wavelength. The bottom layer is a ground plane. The dielectric constant of the substrate, ϵ_r, is 12.9. The substrate thickness, h, is 200 μm. The capacitor is placed on top of the substrate and the top layer is free space.

The arrows on the port transmission lines in Figure 6 show the reference planes used in the calculation and in the de-embedding of the circuit parameters. The S-parameters provided here are normalized with respect to 50 Ω reference impedance.

The geometry is a symmetric structure so $S_{11} = S_{22}$ and $S_{12} = S_{21}$. S_{11} and S_{12}

of the capacitor are obtained using the MoM approach and compared to the results of a commercial software package called "em" by Sonnet Software, Inc [49]. Figures 7 and 8 are the magnitudes and phases of the S-parameters, respectively. The results are in good agreement with each other. The results exhibit less agreement as frequency is increased since the same geometrical model is used over the entire band. Sonnet "em" assumes a

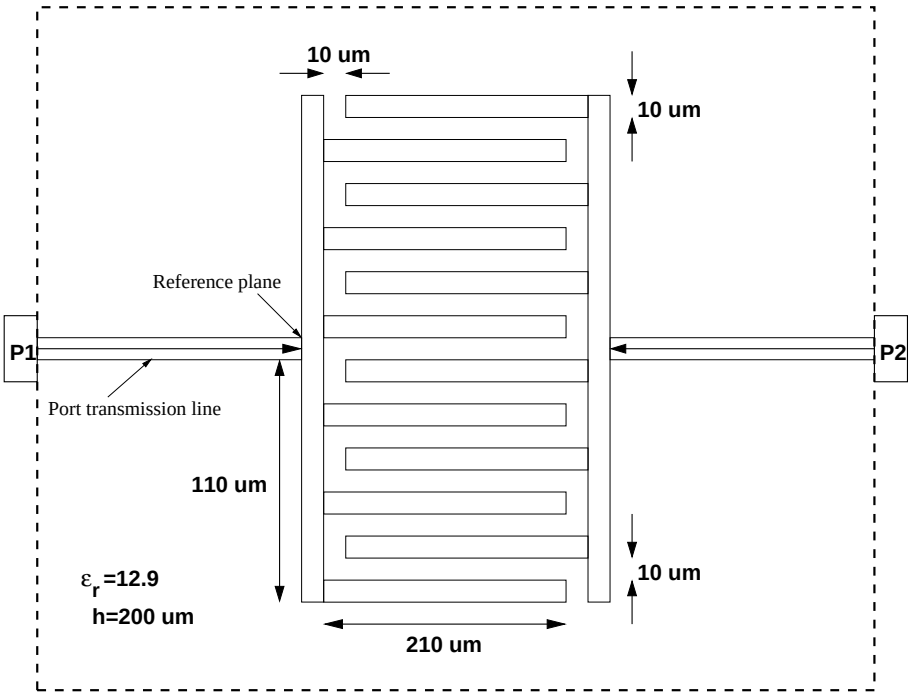

Figure 6: Geometry of the interdigital MIC capacitor

closed region, there may be some validation loss in one model as frequency is increased.

3.6 MIC Bandpass Filter

An interdigital MIC capacitor is a simple structure compared to filters since filters typically exhibit a resonance frequency, making it more difficult to obtain correct and accurate results. Therefore, as another example, consider an MIC bandpass filter as shown in Figure 9 [8]. The layer structure is similar to the capacitor example. The bottom layer is a ground plane. The dielectric constant of the substrate, ϵ_r, is 9.9. The substrate thickness, h, is 15 mil. The filter is placed on top of the substrate and the upper semi-infinite layer is free space. The dimensions are shown on the figure.

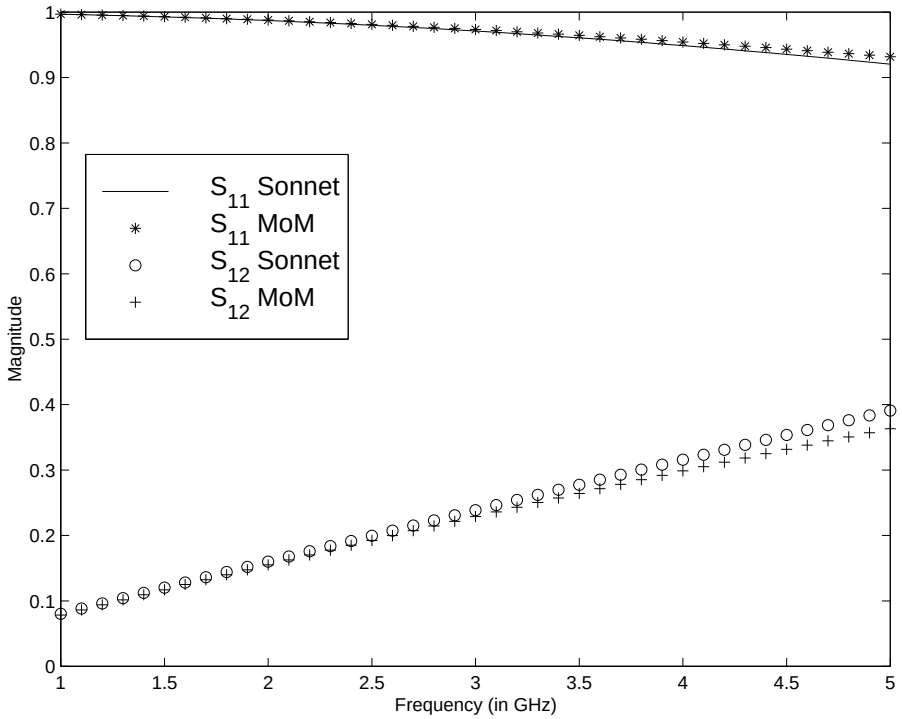

Figure 7: Magnitudes of S_{11} and S_{12} of the MIC capacitor shown in Figure 6

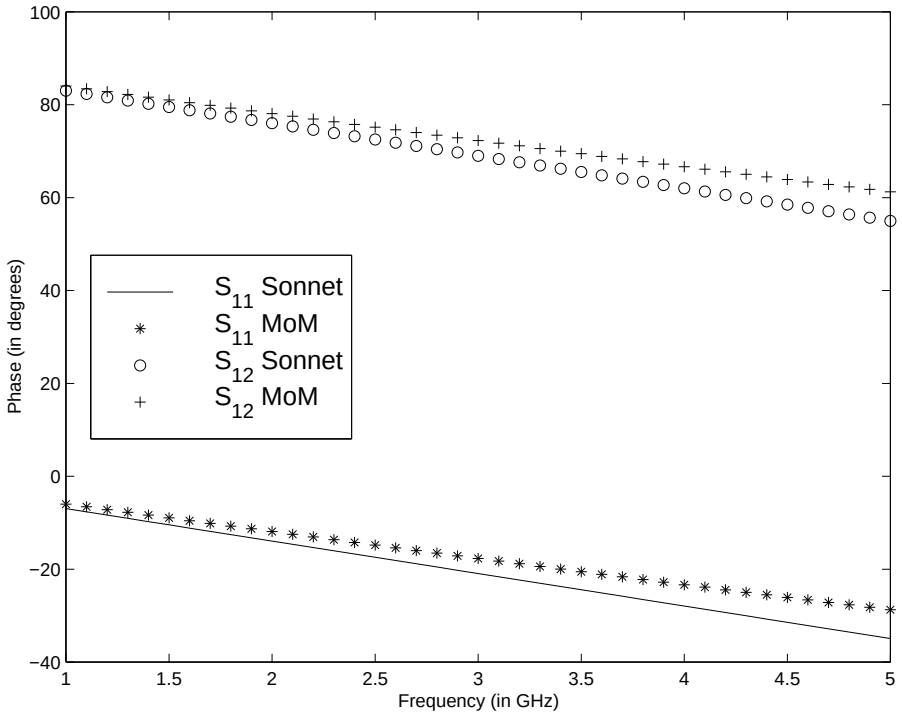

Figure 8: Phases of S_{11} and S_{12} of the MIC capacitor shown in Figure 6

The geometry is a symmetric structure so $S_{11} = S_{22}$ and $S_{12} = S_{21}$. S_{11} and S_{12} of the filter are obtained using the MoM approach and compared to the results of the commercial software package "em" by Sonnet. Figures 10 and 11 show the magnitudes of S_{11} and S_{12}, respectively. Figures 12 and 13 show the phases of S_{11} and S_{12}, respectively. The results are in good agreement with each other.

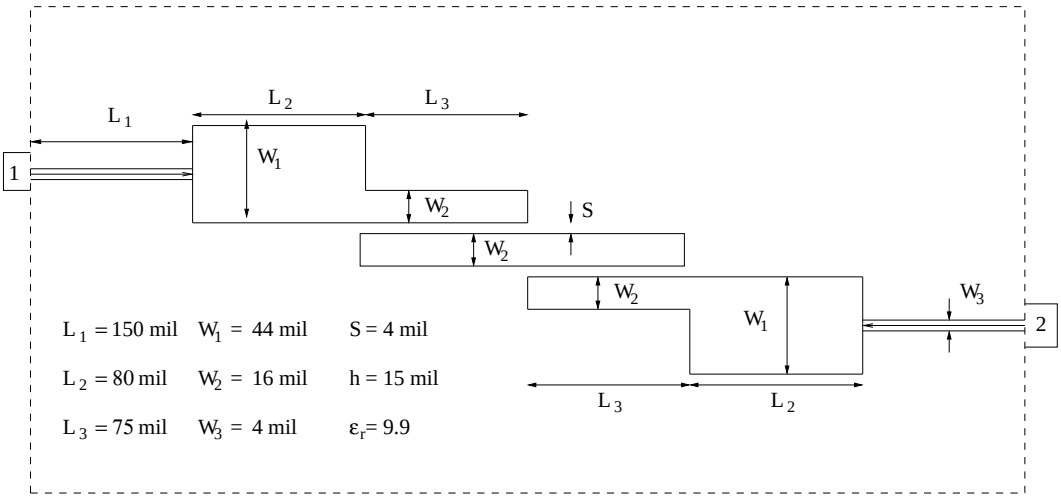

Figure 9: Geometry of the bandpass filter

3.7 Microstrip Single-Stub Filter

Another example is a microstrip single-stub filter as shown in Figure 14 [16]. The bottom layer is a ground plane. The dielectric constant of the substrate, ϵ_r, is 2.33. The substrate thickness, h, is 1.57 mm. The microstrip lines are placed on top of the substrate and the upper (semi-infinite) layer is free space.

The geometry is a symmetric structure so $S_{11} = S_{22}$ and $S_{12} = S_{21}$. S_{11} and S_{12} of the stub filter are obtained using the MoM approach and compared to the results of the commercial software package "em" by Sonnet. Figures 15 and 16 show the magnitudes of S_{11} and S_{12}, respectively. Figures 17 and 18 show the phases of S_{11} and S_{12}, respectively. The results are in good agreement with each other, except near $f = 2.1$ GHz where there is a deviation between the results of the MoM and Sonnet. Sonnet "em" gives questionable results at that frequency and reports that it is unable to calculate the characteristic impedance and effective permittivity. This is likely related to the fact that "em" surrounds

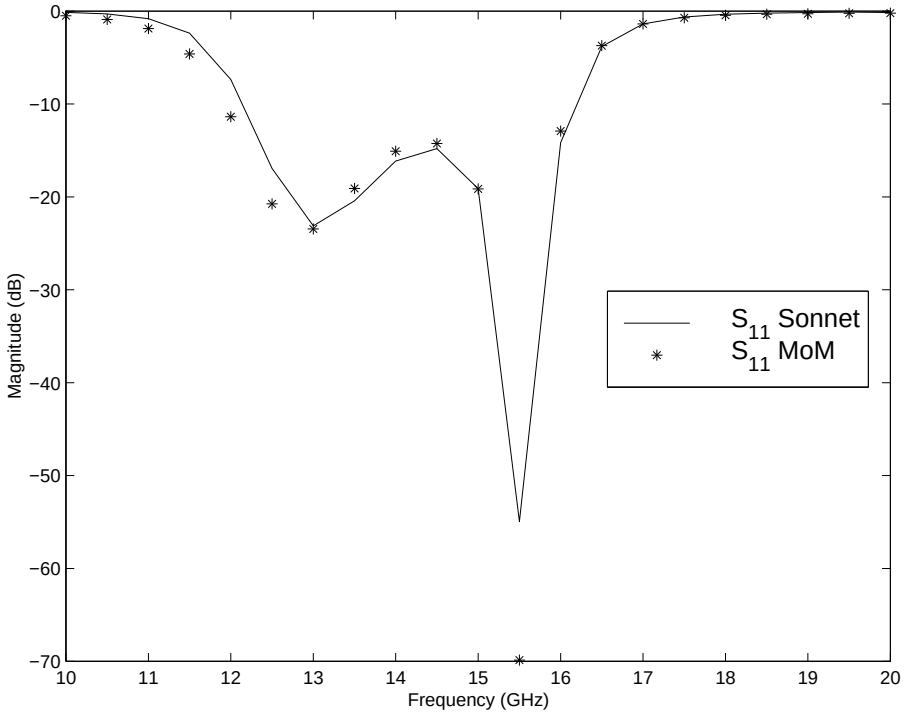

Figure 10: Magnitude of S_{11} of the bandpass filter shown in Figure 9

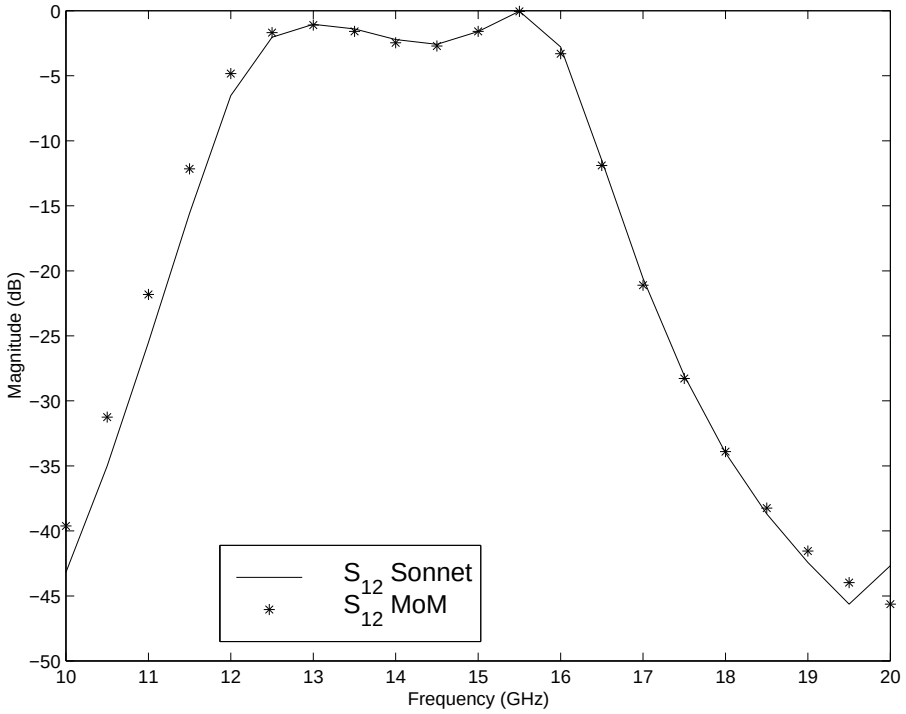

Figure 11: Magnitude of S_{12} of the bandpass filter shown in Figure 9

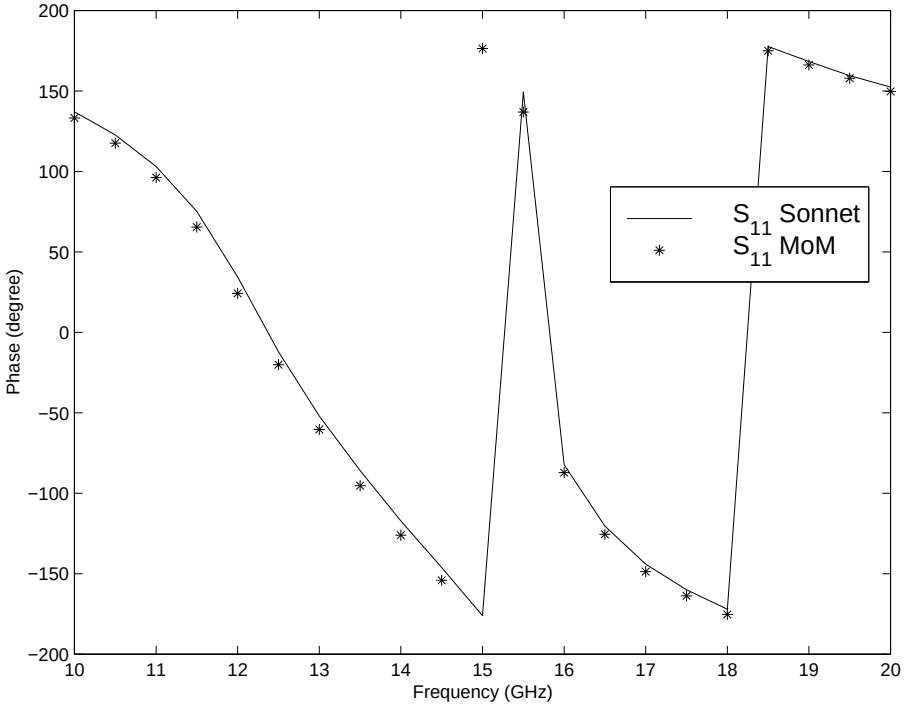

Figure 12: Phase of S_{11} of the bandpass filter shown in Figure 9

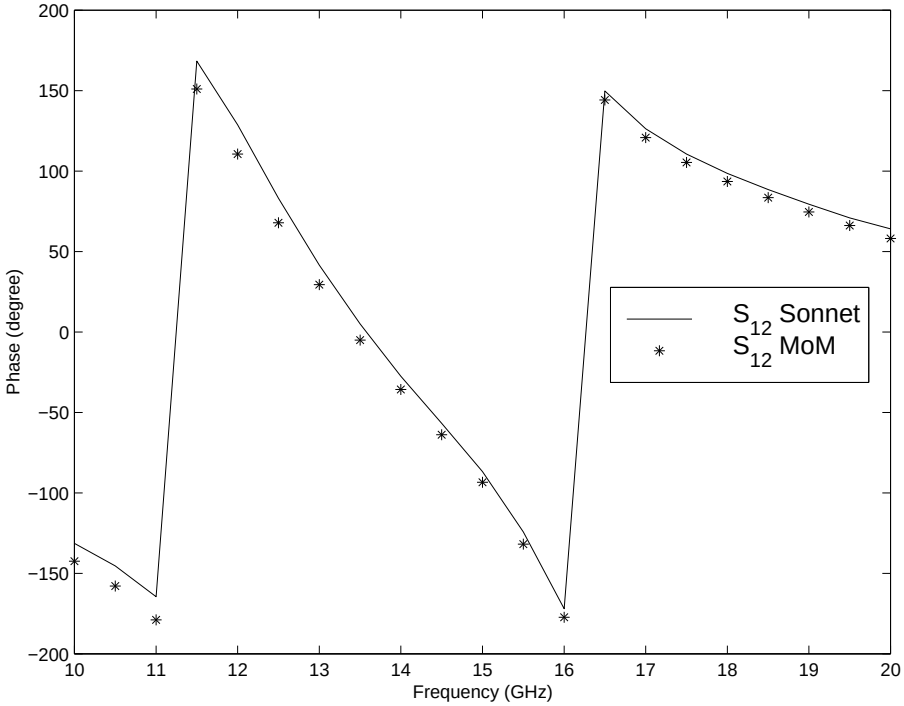

Figure 13: Phase of S_{12} of the bandpass filter shown in Figure 9

the structure with a closed conducting box; this frequency is probably a resonant frequency of that box.

3.8 Short Circuited Microstrip Line

The previous examples involve only horizontal conductors. The next example, a microstrip line connected to ground through a shorting pin (via), has both horizontal and vertical conductors as shown in Figure 19. The via is modelled as a rectangular strip. The bottom layer is a ground plane. The dielectric constant of the substrate, ϵ_r, is 4.0. The substrate thickness, h, is 0.02032 cm. The microstrip line is placed on top of the substrate and the top layer is free space. The via is placed between the microstrip line and ground plane.

The S-parameters S_{11} and S_{12} of the line are obtained using the MoM approach and compared to the results of the commercial software package "em" by Sonnet. Figure 20 shows the magnitudes of S_{11} and S_{12}, while Figure 21 shows the phases of S_{11} and S_{12}. The short-circuited line exhibits a theoretical reflection coefficient of unity magnitude, as indicated by the numerical solution in Figure 20. There is generally good agreement between the results of the MoM code and the commercial software package for both magnitude and phase of the S-parameters.

3.9 Spiral MIC Inductor

Consider a short circuited spiral MIC inductor as shown in Figure 22. The structure contains one vertical conducting via to connect the inner end of the microstrip spiral to the ground plane that forms the bottom layer. The dielectric constant of the substrate, ϵ_r, is 12.9. The substrate thickness, h, is 100 μm. The microstrip lines are placed on top of the substrate and the upper semi-infinite layer is free space.

The S-parameter S_{11} for the inductor is obtained using the MoM approach and compared to the results of the commercial software package "em" by Sonnet. Figure 23 shows the magnitude of S_{11}, while Figure 24 shows the phase of S_{11}. There is generally good agreement between the results. Since the S-parameter S_{11} is the same as the reflection coefficient Γ,

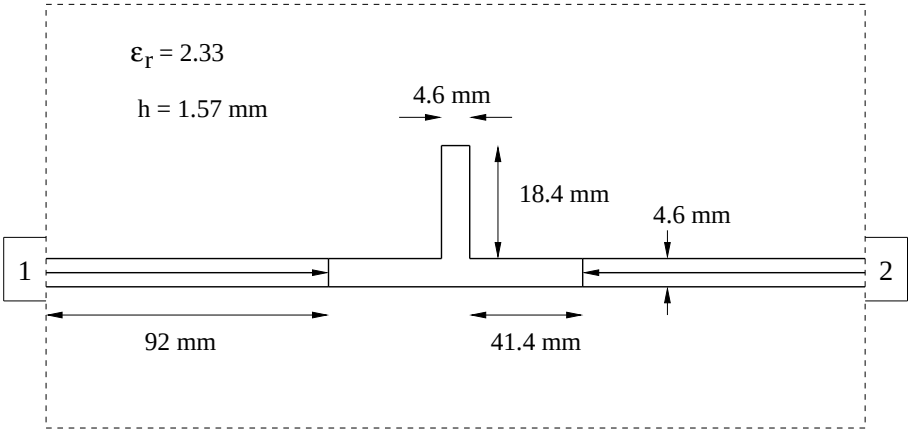

Figure 14: Geometry of the single-stub filter

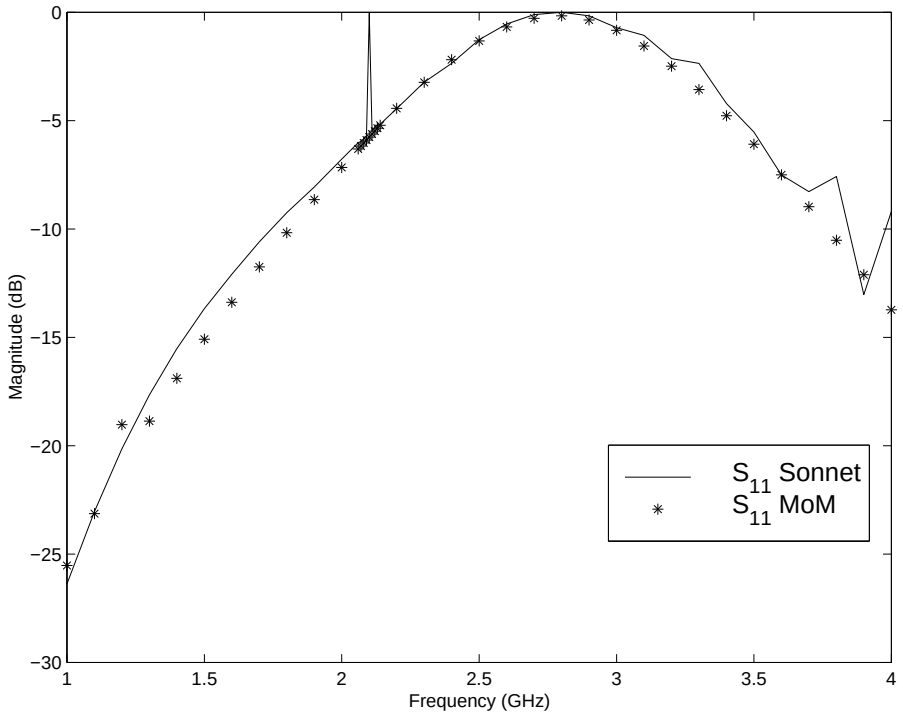

Figure 15: Magnitude of S_{11} of the single-stub filter shown in Figure 14

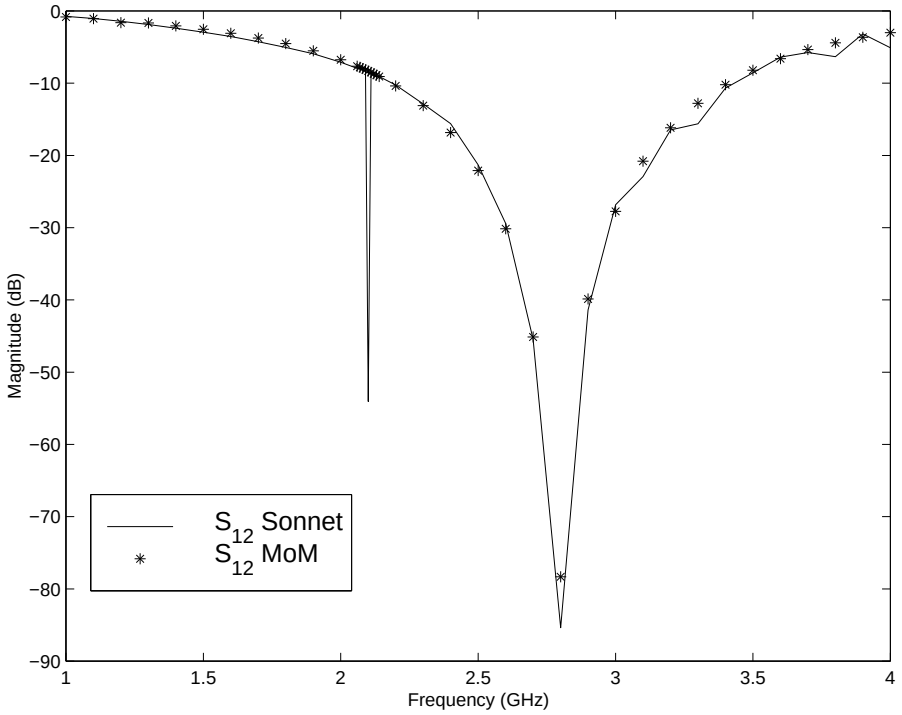

Figure 16: Magnitude of S_{12} of the single-stub filter shown in Figure 14

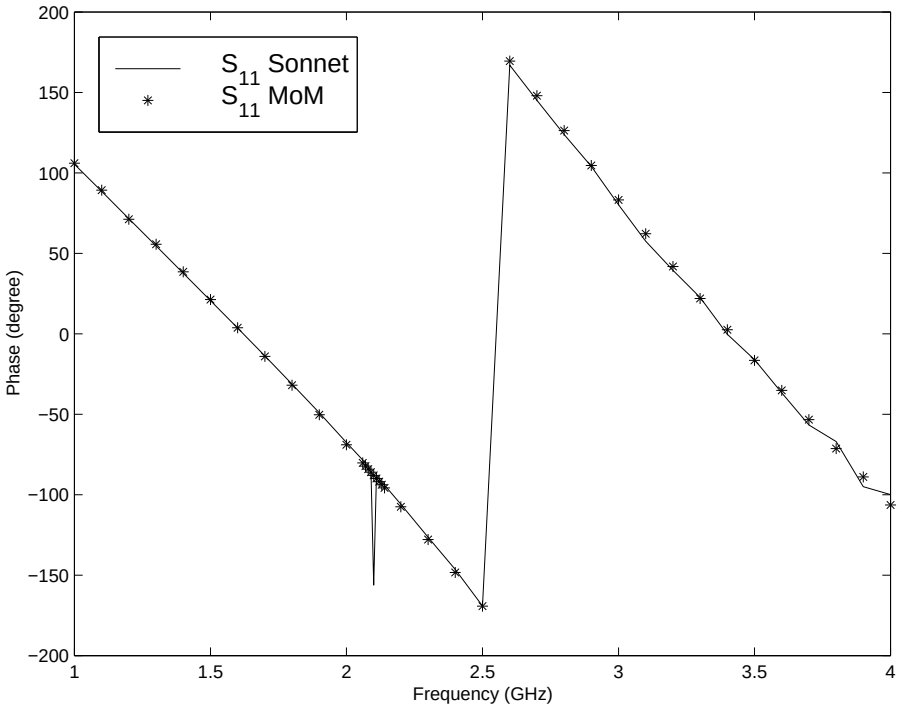

Figure 17: Phase of S_{11} of the single-stub filter shown in Figure 14

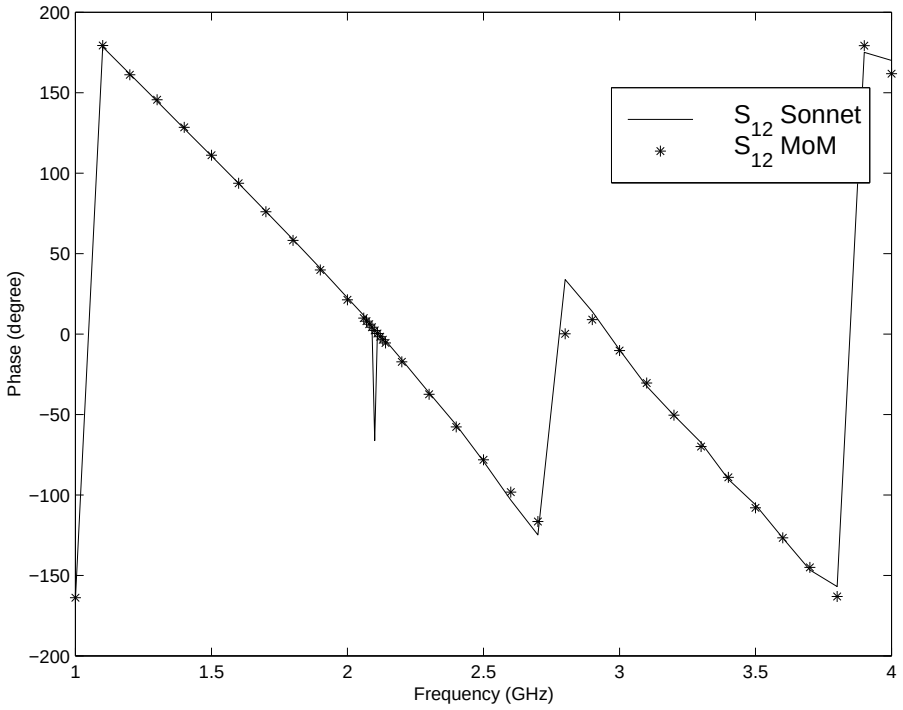

Figure 18: Phase of S_{12} of the single-stub filter shown in Figure 14

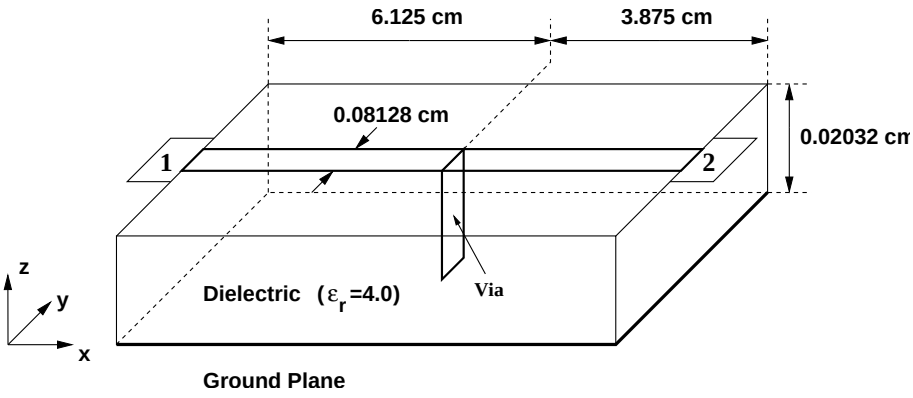

Figure 19: Geometry of the short circuited microstrip line

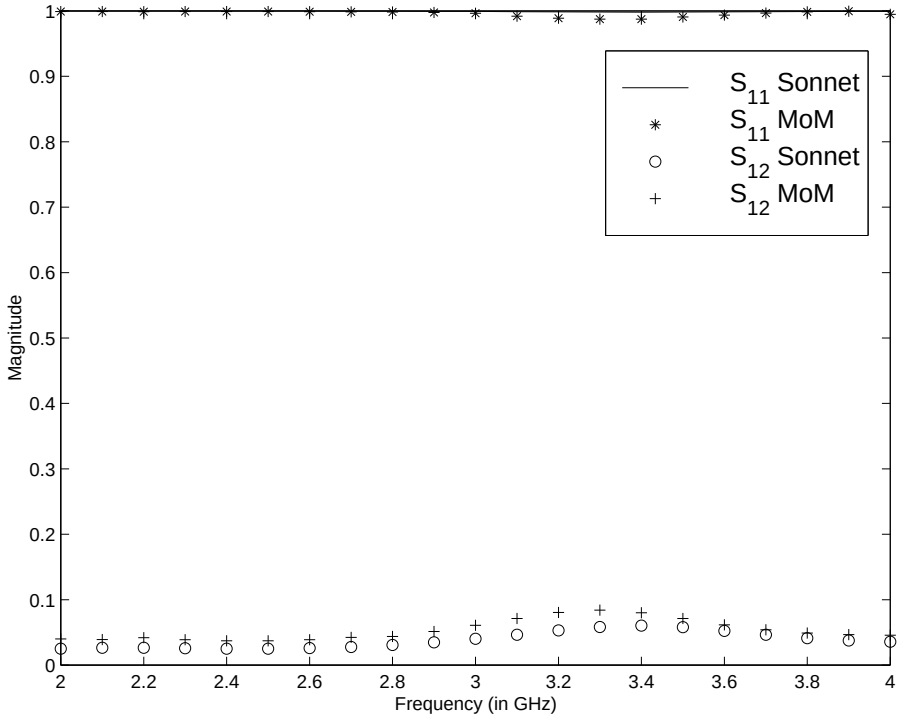

Figure 20: Magnitudes of S_{11} and S_{12} of the short circuited microstrip line shown in Figure 19

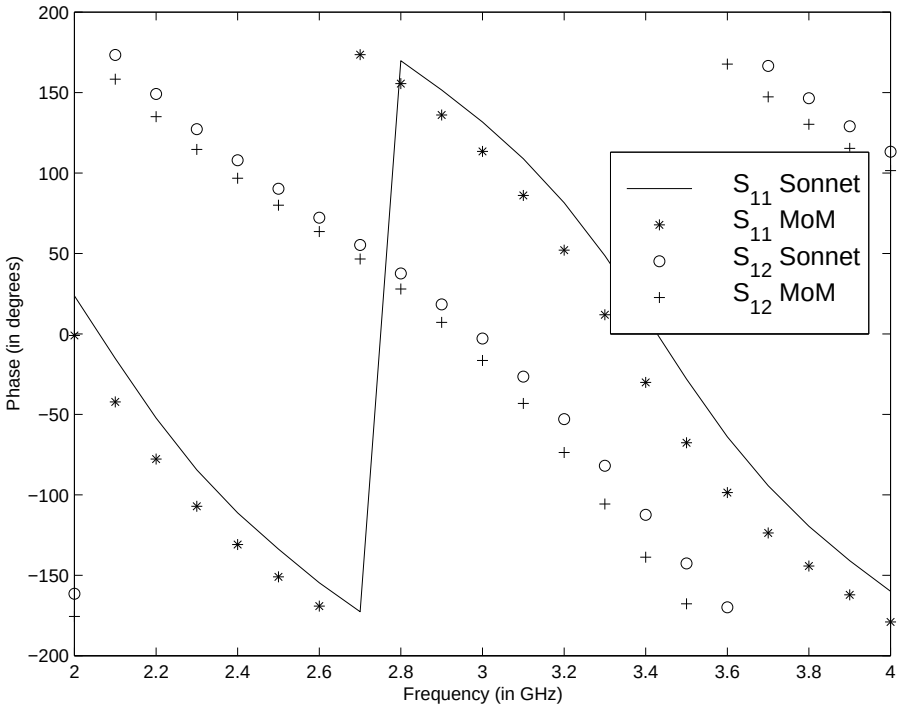

Figure 21: Phases of S_{11} and S_{12} of the short circuited microstrip line shown in Figure 19

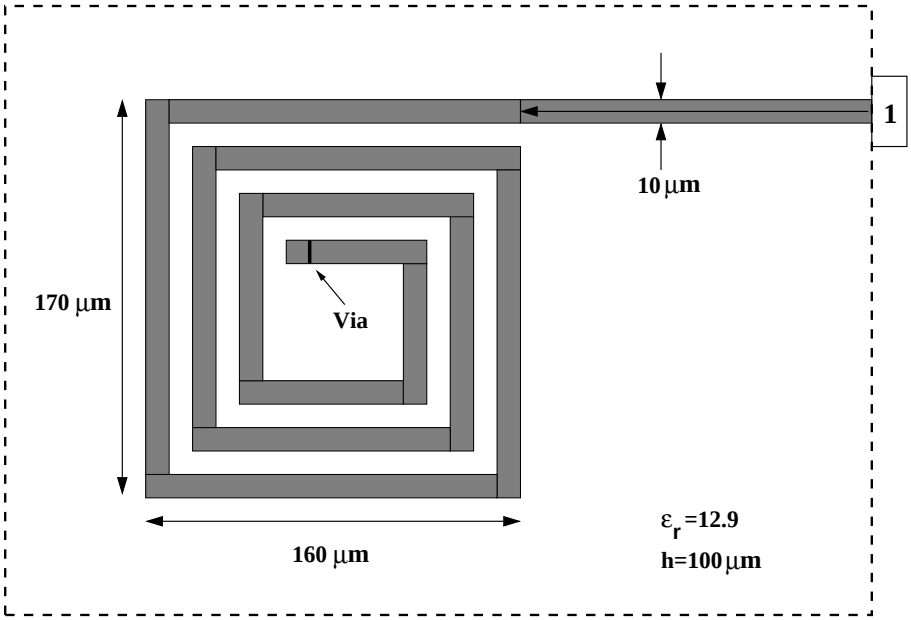

Figure 22: Geometry of the spiral MIC inductor

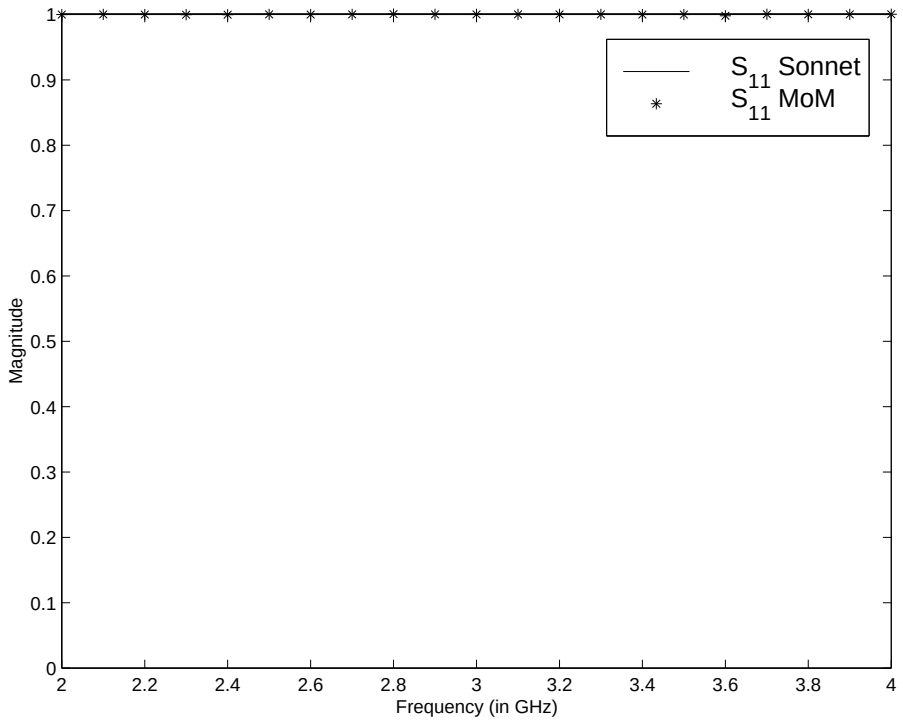

Figure 23: Magnitude of S_{11} of the spiral MIC inductor shown in Figure 22

the input impedance of the spiral inductor can be calculated using

$$Z_{in} = Z_0 \frac{1+\Gamma}{1-\Gamma} \tag{70}$$

Figures 25 and 26 show the magnitude and the phase of the inductor's input impedance. As expected for an inductor, the magnitude of the impedance exhibits a linear growth with frequency and the phase of the impedance is equal to 90^o through the frequency range. As can be seen from the figures, the results of the MoM analysis agree very well with the results from the commercial software package.

In the preceding examples, the via is modelled by a vertical strip. Consequently, the model may not be sufficiently accurate to represent a solid shorting pin as the frequency increases. A rectangular cylinder can be easily constructed from four vertical strips and may comprise a more realistic model for MoM analysis with the closed-form Green's functions.

3.10 Summary

This chapter describes an MoM formulation for solving the MPIE. The examples provided in Sections 3.5 - 3.9 validate the implementation of the Green's functions presented in Chapter 2, and the implementation of the S-parameter extraction procedure described in Section 3.4. These and other MoM examples will also serve as a point of comparison with the LCN results obtained in subsequent chapters.

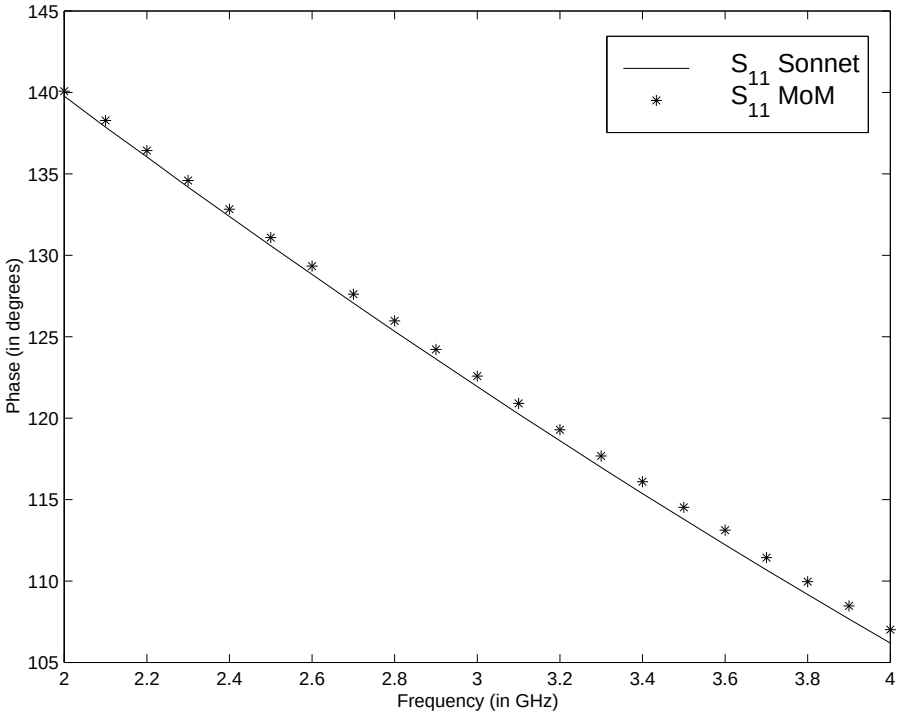

Figure 24: Phase of S_{11} of the spiral MIC inductor shown in Figure 22

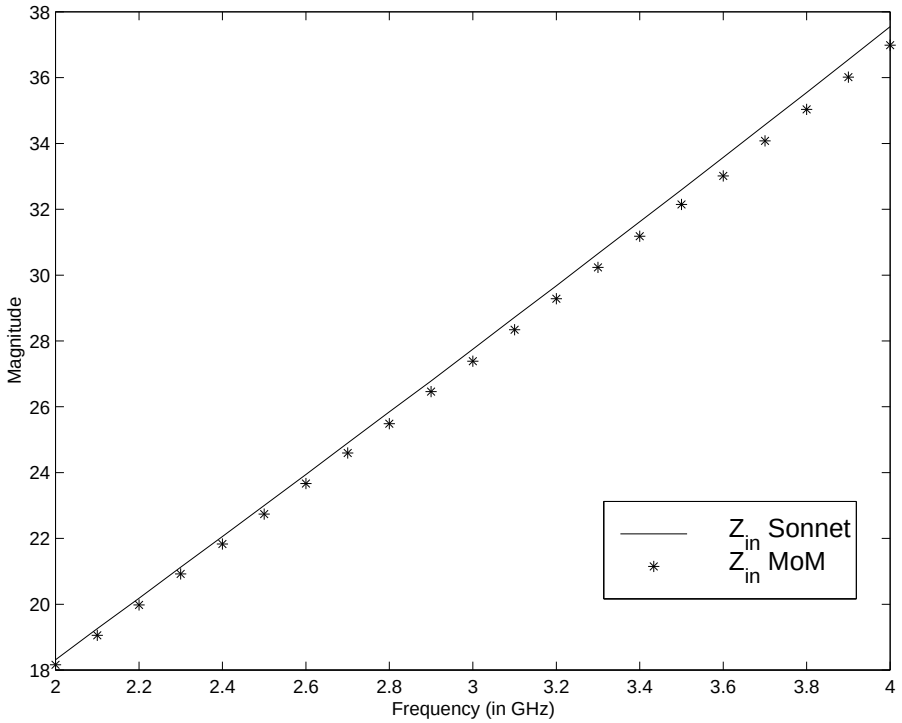

Figure 25: Magnitude of the input impedance of the spiral MIC inductor shown in Figure 22

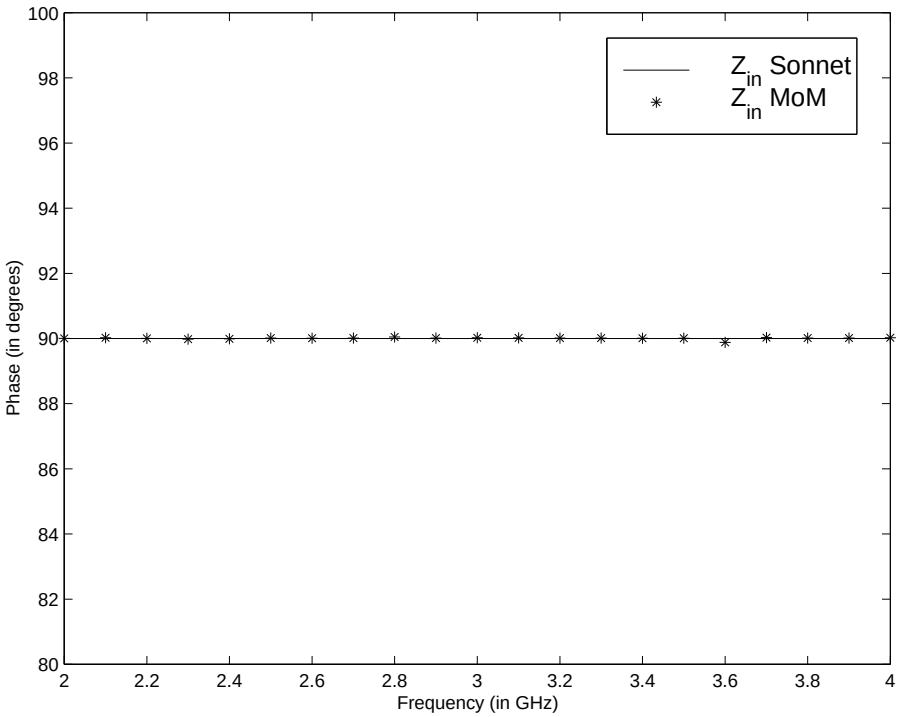

Figure 26: Phase of the input impedance of the spiral MIC inductor shown in Figure 22

CHAPTER IV

THE LOCALLY-CORRECTED NYSTRÖM METHOD

While the MoM discretization procedure is widely used in electromagnetics, recent research suggests that an alternative procedure known as the locally-corrected Nyström (LCN) method may offer improved computational efficiency and a more systematic means of incorporating higher-order representations (and better accuracy). As a part of the proposed research, the LCN method will be investigated as an alternative to the MoM for solving Eq. (17).

The LCN formulation is described and implemented using the MPIE and the layered-medium Green's functions from Chapter 2. Results for plane-wave scattering from plates in free space are used to validate the numerical implementation. Extensions of the LCN approach for printed circuit analysis are discussed in Chapters 5 and 6.

The LCN implementation described in this chapter is the first use of the LCN procedure for planar layered structures. In the course of the investigation, it was determined that the LCN procedure did not work well with polynomial-complete expansions [11] for solving vector integral equations such as the MPIE. As a consequence, mixed-order quadrature rules were introduced for use with LCN. This modification, original with this study, appears to greatly improve the accuracy of the LCN procedure for vector electromagnetics problems.

An additional issue to be explored in this investigation is the use of the LCN method with nonconforming models. Traditional MoM discretizations usually require a conforming-cell model of the conductor surface, where cell boundaries are aligned so that basis functions can straddle two cells. A conforming model is more difficult to generate than a nonconforming model. The LCN approach does not require basis functions to overlap cells, so it can be used with nonconforming models. In Section 4.7, the relative accuracy of the LCN results will be investigated for conforming and nonconforming cells.

4.1 The Classical Nyström Method

The traditional Nyström method is a simple and efficient method for discretization of integral equations with non-singular kernels [42]. The key point of the method is to replace the integral operator with a suitable quadrature rule. Consider the integral equation

$$\phi(\mathbf{r}) = \int_{\Omega} G(\mathbf{r} - \mathbf{r}')J(\mathbf{r}')\, ds' \tag{71}$$

where $G(\mathbf{r})$ is a non-singular kernel, $J(\mathbf{r})$ is an unknown current density, and $\phi(\mathbf{r})$ is a known forcing function. A quadrature rule is used to approximate the integral with a summation to obtain

$$\phi(\mathbf{r}) = \sum_{n=1}^{N} \alpha_n G(\mathbf{r} - \mathbf{r}'_n)J(\mathbf{r}'_n) \tag{72}$$

A Gauss-Legendre quadrature rule is employed, where $\mathbf{r}'_n$ and α_n are the sample points and weights defined by the quadrature rule, and $J(\mathbf{r}'_n)$ are unknown samples of the current density. Then, enforcing (72) at N sample points leads to a linear system of equations with an m-th row expressed as

$$\phi(\mathbf{r}_m) = \sum_{n=1}^{N} \alpha_n G(\mathbf{r}_m - \mathbf{r}'_n)J(\mathbf{r}'_n) \tag{73}$$

This system provides the solution of $J(\mathbf{r})$ at N discrete points. When $G(\mathbf{r})$ is a non-singular kernel and the geometry is smooth, the accuracy of the method will be related to the quadrature rule and the order of the rule. Therefore, if the quadrature rule is exponentially convergent, the solution of the unknown current may be as well.

4.2 The Locally-Corrected Nyström Method

The classical Nyström method cannot be applied directly to singular kernels, including those that usually occur in electromagnetics. If $G(\mathbf{r}_m - \mathbf{r}'_n)$ is infinite when $\mathbf{r}_m = \mathbf{r}'_n$, then (73) is undefined. To solve this problem, a modified technique known as the locally-corrected Nyström method was recently introduced [11, 33, 34]. The essence of the method is that by computing convolutions of the kernel with a suitable set of basis functions, it is possible to modify the quadrature rule so that it is just as accurate near the singularity as far from it. The beauty of the method is that these quadrature rule modifications are required only in

the vicinity of the singularity, hence the name local corrections. Since quadrature weights and discretized kernel terms always enter into the quadrature rule as product pairs, the local corrections can equivalently be applied to the kernel and one can keep the original quadrature weights. In this sense one is actually synthesizing a new kernel to sample, near the singularity of the original kernel. The corrected matrix representation of the kernel, $\tilde{G}_{m,n}$ can be given as

$$\tilde{G}_{m,n} = \begin{cases} L_{m,n} & \text{when } \mathbf{r}_m \in D_n \\ G_{m,n} = G(\mathbf{r}_m - \mathbf{r}'_n) & \text{otherwise} \end{cases} \tag{74}$$

where D_n is the local correction domain and $L_{m,n}$ is a matrix of local corrections whose entries are calculated within D_n. The idea of the local corrections is to introduce a new quadrature rule that is specialized to the convolutional integral and that is exact for a specific class of functions. Assume that the current density J is expanded into a set of known basis functions $f_k(\mathbf{r}')$ that are distributed over Ω. The entries $L_{m,n}$ can be expressed in terms of the equations

$$\sum_{n=1}^{N} \alpha_n L_{m,n} f_k(\mathbf{r}'_n) = \int_{\Omega} G(\mathbf{r}_m - \mathbf{r}') f_k(\mathbf{r}')\, ds' \tag{75}$$

which is the m-th row of the local correction matrix involving N basis functions $f_k(\mathbf{r}')$. The linear system of equations can then be solved for the m-th row of $L_{m,n}$ using LU factorization. Once $L_{m,n}$ is found, (73)-(75) are combined, leading to the linear system of equations:

$$\phi(\mathbf{r}_m) = \sum_{n=1}^{N} \alpha_n \tilde{G}_{m,n} J(\mathbf{r}'_n) \tag{76}$$

Eq. (76) is used to solve for the unknown current density samples.

4.3 LCN Formulation of the MPIE in 3-D

It is common practice when working with the MPIE to modify Eq. (75) by incorporating an inner product with a testing function. In this situation, Eq. (75) can be rewritten as

$$\left\langle T^m(\mathbf{r})\,,\, \sum_{n=1}^{N} \alpha_n L_{m,n} f_k(\mathbf{r}'_n) \right\rangle = \left\langle T^m(\mathbf{r})\,,\, \int_{\Omega} G(\mathbf{r} - \mathbf{r}') f_k(\mathbf{r}')\, ds' \right\rangle \tag{77}$$

where α_n's and $L_{m,n}$'s are constants, and $f_k(\mathbf{r}'_n)$ is not dependent on $\mathbf{r}$. Therefore, Eq. (77) can be expressed as

$$\sum_{n=1}^{N} \alpha_n L_{m,n} f_k(\mathbf{r}'_n) = \frac{1}{Area(T^m)} \left\langle T^m(\mathbf{r}) \, , \, \int_\Omega G(\mathbf{r}-\mathbf{r}') f_k(\mathbf{r}') \, ds' \right\rangle \tag{78}$$

The tangential components of the scattered electric field on the plane of the patch can be written in terms of the surface current density $\mathbf{J}$, and the associated Green's functions of the vector and scalar potentials as follows:

$$E_x^s = -jwG_{xx}^A * J_x + \frac{1}{jw}\frac{\partial}{\partial x}\left(G^{q_e} * \nabla \cdot \mathbf{J}\right) \tag{79}$$

$$E_y^s = -jwG_{yy}^A * J_y + \frac{1}{jw}\frac{\partial}{\partial y}\left(G^{q_e} * \nabla \cdot \mathbf{J}\right) \tag{80}$$

where the term involving the Green's function of the scalar potential can be explicitly written as

$$G^{q_e} * \nabla \cdot \mathbf{J} = G_x^{q_e} * \frac{\partial J_x}{\partial x} + G_y^{q_e} * \frac{\partial J_y}{\partial y} \tag{81}$$

where

$$G_x^{q_e} = G_y^{q_e} \tag{82}$$

and the scalar potential Green's function in the spatial domain can be written as

$$G^{q_e}(x,x',y,y') \cong \sum_{n=1}^{N^{q_e}} a_n \frac{e^{-jk_i r_n}}{r_n} \tag{83}$$

where $r_n = \sqrt{(x-x')^2+(y-y')^2-\alpha_n^2} = \sqrt{(x-x')^2+(y-y')^2+c_n^2}$ as defined in earlier chapters.

In the LCN formulation, since the current density is unknown, the derivative on the current is shifted onto the scalar potential Green's function using, for example,

$$\frac{\partial}{\partial x}\left(G_x^{q_e} * \frac{\partial J_x}{\partial x}\right) = J_x\left(\frac{\partial^2}{\partial x^2} G_x^{q_e}\right) \tag{84}$$

Eqs. (79) and (80) can be written as

$$\begin{aligned} E_x^s(x,y) \;=\; & -jwG_{xx}^A * J_x + \frac{1}{jw}\iint dx'\,dy' \left(\frac{\partial^2}{\partial x'^2} G_x^{q_e}\right) J_x(x',y') + \\ & \frac{1}{jw}\iint dx'\,dy' \left(\frac{\partial}{\partial x'}\frac{\partial}{\partial y'} G_y^{q_e}\right) J_y(x',y') \end{aligned} \tag{85}$$

$$E_y^s(x,y) = -jwG_{yy}^A * J_y + \frac{1}{jw}\iint dx'\,dy'\left(\frac{\partial}{\partial y'}\frac{\partial}{\partial x'}G_x^{q_e}\right)J_x(x',y') + \frac{1}{jw}\iint dx'\,dy'\left(\frac{\partial^2}{\partial y'^2}G_y^{q_e}\right)J_y(x',y') \quad (86)$$

where

$$\frac{\partial}{\partial x'}G^{q_e} = \sum_{n=1}^{N^{q_e}} a_n(x-x')(jk_i+\frac{1}{r_n})\frac{e^{-jk_ir_n}}{r_n^2} = -\frac{\partial}{\partial x}G^{q_e} \quad (87)$$

$$\frac{\partial}{\partial y'}G^{q_e} = \sum_{n=1}^{N^{q_e}} a_n(y-y')(jk_i+\frac{1}{r_n})\frac{e^{-jk_ir_n}}{r_n^2} = -\frac{\partial}{\partial y}G^{q_e} \quad (88)$$

$$\frac{\partial}{\partial y'}\frac{\partial}{\partial x'}G^{q_e} = -\sum_{n=1}^{N^{q_e}} a_n(x-x')(y-y')(k_i^2r_n^2-3jk_ir_n-3)\frac{e^{-jk_ir_n}}{r_n^5} = \frac{\partial}{\partial x'}\frac{\partial}{\partial y'}G^{q_e} \quad (89)$$

$$\frac{\partial^2}{\partial x'^2}G^{q_e} = -\sum_{n=1}^{N^{q_e}} a_n[(1+jk_ir_n)(r_n^2-3(x-x')^2)+k_i^2r_n^2(x-x')^2]\cdot\frac{e^{-jk_ir_n}}{r_n^5} \quad (90)$$

$$\frac{\partial^2}{\partial y'^2}G^{q_e} = -\sum_{n=1}^{N^{q_e}} a_n[(1+jk_ir_n)(r_n^2-3(y-y')^2)+k_i^2r_n^2(y-y')^2]\cdot\frac{e^{-jk_ir_n}}{r_n^5} \quad (91)$$

Using Eq. (73), Eq. (85) can be written as

$$E_x^s(x,y) = -jw\sum_{n_1=1}^{N_1}\sum_{n_2=1}^{N_2}\alpha_{n_1}\alpha_{n_2}G_{xx}^A(x,y,x'_{n_1},y'_{n_2})J_x(x'_{n_1},y'_{n_2}) + \frac{1}{jw}\sum_{n_1=1}^{N_1}\sum_{n_2=1}^{N_2}\alpha_{n_1}\alpha_{n_2}\frac{\partial^2}{\partial x'^2}G_x^{q_e}(x,y,x'_{n_1},y'_{n_2})J_x(x'_{n_1},y'_{n_2}) + \frac{1}{jw}\sum_{n_3=1}^{N_3}\sum_{n_4=1}^{N_4}\alpha_{n_3}\alpha_{n_4}\frac{\partial}{\partial x'}\frac{\partial}{\partial y'}G_y^{q_e}(x,y,x'_{n_3},y'_{n_4})J_y(x'_{n_3},y'_{n_4}) \quad (92)$$

where $J_x(x',y')$ and $J_y(x',y')$ are unknown current densities. As a result, the integrals are converted to summations and the complexity of the method decreases.

Using Eq. (78), the local correction matrix entries can be written as

$$\sum_{n_1=1}^{N_1}\sum_{n_2=1}^{N_2}\alpha_{n_1}\alpha_{n_2}L_{xx}(x,y,x'_{n_1},y'_{n_2})f_{k_1,k_2}(x'_{n_1},y'_{n_2}) = \frac{1}{Area(T^m)}\cdot\left(-j\omega\left\langle T^m,\, G_{xx}^A * f_{k_1,k_2}\right\rangle + \frac{1}{j\omega}\left\langle T^m,\, \frac{\partial}{\partial x}\left[G_x^{q_e} * \frac{\partial f_{k_1,k_2}}{\partial x}\right]\right\rangle\right) \quad (93)$$

and

$$\sum_{n_3=1}^{N_3}\sum_{n_4=1}^{N_4}\alpha_{n_3}\alpha_{n_4}L_{xy}(x,y,x'_{n_3},y'_{n_4})f_{k_3,k_4}(x'_{n_3},y'_{n_4}) = \frac{1}{Area(T^m)}\cdot \frac{1}{j\omega}\left\langle T^m,\frac{\partial}{\partial x}\left[G_y^{q_e}*\frac{\partial f_{k_3,k_4}}{\partial y}\right]\right\rangle \quad (94)$$

where f_{k_1,k_2} and f_{k_3,k_4} are subdomain basis functions defined over a cell. The basis functions will be discussed in the following section.

4.4 An Implementation Difficulty and Remedy

As recently proposed [11, 33, 34, 18], the local corrections associated with the LCN method employ the polynomials underlying the specific quadrature rule used for the discretization. For smooth surfaces, Legendre polynomials have been employed in conjunction with Gauss-Legendre quadrature. For two-dimensional surfaces, product quadrature rules have been used to define the LCN procedure and basis functions that are the product of Legendre polynomials have been used for the local corrections [18].

Consider a conducting plate in the $x-y$ plane, divided into N cells. A representation for the surface current density can be expressed as

$$\mathbf{J}(x,y) = \sum_{n=1}^{N}\left(\hat{x}\sum_{i=1}^{p}\sum_{j=1}^{q}a_{n,i,j}P_{i-1}(x)P_{j-1}(y)+\hat{y}\sum_{i=1}^{p}\sum_{j=1}^{q}b_{n,i,j}P_{j-1}(x)P_{i-1}(y)\right) \quad (95)$$

where $P_i(u)$ denotes a Legendre polynomial in u of degree i. In previous LCN implementations, the upper limits on indices i and j in Eq. (95) have been set to the same value ($p=q$).

In the initial implementation of LCN used for the present study, polynomial expansions that were complete to equal orders in x and y were employed. Such an approach is suggested by the recent literature [11, 33, 34, 18]. However, poor results were obtained for current density, especially the cross-polarized component (results will be presented in the following section). Since the results in the literature are limited to far-field quantities, this problem was not expected. After a fairly exhaustive process of testing the computer program for bugs, it was decided that the problem might reside with the nature of the polynomial expansion itself.

In connection with MoM analysis, it has been observed that results are generally more accurate for currents on conducting surfaces when the surface charge density representation is itself self-consistent to a single polynomial degree. The surface charge is obtained from the divergence of surface current, a procedure that involves a derivative of the current along the vector direction. The condition for self-consistency is that the equivalent representation for the charge is complete to the same polynomial order in x and y. This condition implies that the current density is not complete to the same degree in x and y, but is one polynomial degree higher along the vector direction than in the perpendicular direction. This suggests that the current density should be represented by mixed-order polynomials.

To investigate the use of mixed-order representations with the LCN procedure, product rules were constructed that differed in degree by one in x and y. Basis functions were constructed from Legendre polynomials to compute the local corrections. These have the form

$$\mathbf{J}(x,y) = \sum_{n=1}^{N}\left(\hat{x}\sum_{i=1}^{p}\sum_{j=1}^{p-1}a_{n,i,j}P_{i-1}(x)P_{j-1}(y) + \hat{y}\sum_{j=1}^{p-1}\sum_{i=1}^{p}b_{n,j,i}P_{j-1}(x)P_{i-1}(y)\right) \quad (96)$$

where the upper limits on index j $(p-1)$ is one less that that of index i (p). For a current of the form of (96), the associated charge density is of degree $p-1$ in both x and y.

As demonstrated in the following section, the use of mixed-order representations with the LCN discretization of the MPIE is quite successful for problems such as square conducting plates.

4.5 1λ *x* 1λ *plate in free space*

As a preliminary test case for the LCN implementation, consider a 1λ x 1λ plate in free space, illuminated by a plane wave. The plane wave incident electric field can be written as

$$\boldsymbol{E}^i = (\cos\theta\cos\phi\hat{x} + \cos\theta\sin\phi\hat{y} - \sin\theta\hat{z})\exp(-j(k_x x + k_y y + k_z z)) \quad (97)$$

where

$$k_x = k_o\sin\theta\cos\phi \quad (98)$$

$$k_y = k_o\sin\theta\sin\phi \quad (99)$$

$$k_z = k_o\cos\theta \quad (100)$$

and where the parameters θ and ϕ are chosen as 0 for this example (the plate is illuminated by a normally-incident uniform plane wave). For validation, the LCN results are compared with the results of the MoM formulation. Figures 27a and 27b show the $x-$ and $y-$components, respectively, of the surface current densities on the plate obtained using MoM. Figures 28a and 28b show the $x-$ and $y-$components, respectively, of the surface current densities on the plate obtained using LCN with 3 by 3 quadrature rules for each cell. These figures show reasonable agreement between the $x-$components of the MoM and LCN approaches. The $y-$components do not agree as well. The $y-$component of the current density obtained using LCN exhibits irregular fluctuations and does not appear to be correct.

Interestingly, similar results have been obtained when using MoM discretizations and representations equivalent to (95) [21]. In that case, the irregular results have been attributed to an inconsistent representation of the underlying charge density [21, 19]. As discussed in the preceding section, it is believed that the charge representation should be in essence complete to the same degree in x and y, meaning that the representation for current density should involve mixed-order polynomial functions. In consequence, most MoM approaches now employ mixed-order basis functions for the surface current, such as the rooftop and RWG basis functions [21, 19].

To investigate the use of mixed-order representations with the LCN procedure, product rules were constructed that differed in degree by one in x and y. Basis functions were constructed from Legendre polynomials to compute the local corrections. Figures 29a and 29b show the resulting surface current for the identical plate as Figures 28a and 28b, obtained using 3 by 2 product quadrature rules. In Figures 29a and 29b, both the co-pol and cross-pol currents appear smooth.

Figures 30a and 30b show an additional LCN result obtained using 4 by 3 quadrature rules, where Eq. (96) was used with $p = 4$ for the local corrections. Figure 31 presents the x-component of the surface current density on the plate along the cuts $x = 0.5\lambda$ and $y = 0.5\lambda$. This figure shows reasonable agreement between the MoM and LCN approaches.

The preceding results do not incorporate the proper condition at the knife edge of

the plate, where the parallel component of the current is infinite. This behavior can be incorporated [18], but appears to be unrelated to the charge modeling issue that resulted in the gross errors in the cross-pol currents.

To summarize, LCN results obtained for currents on surfaces in three dimensions, especially for cross-polarization results, appear incorrect when obtained from the EFIE with polynomial-complete representations. The use of mixed-order representations (as common practice with MoM discretizations) appears to alleviate this difficulty. The observed behavior is consistent with that of [21], and suggests that the problem is due to an inconsistent representation of the underlying surface charge density [19].

After the surface current density is found, the surface charge density can be calculated using the continuity equation

$$\nabla \cdot \mathbf{J} = -j\omega\rho = \frac{\partial J_x}{\partial x} + \frac{\partial J_y}{\partial y} \tag{101}$$

In MoM formulations, rooftop basis functions are incorporated to approximate the current. Therefore, the charge on each cell can be calculated by taking the derivative of rooftop functions (which is constant). In LCN formulations, the current is found at the sample points of the quadrature rule for each cell. As a result, the current cannot be approximated by the summation of basis functions. To resolve this problem, Lagrange's interpolation formula can be used to approximate the current in each cell. For the polynomial complete representation, if the quadrature rule is 3 by 3 on a cell, the current density in the x-direction can be approximated as

$$\begin{aligned} J_x(x,y) \quad = \quad & \frac{(x-x_2)(x-x_3)}{(x_1-x_2)(x_1-x_3)}\left[c_1\frac{(y-y_2)(y-y_3)}{(y_1-y_2)(y_1-y_3)} + c_4\frac{(y-y_1)(y-y_3)}{(y_2-y_1)(y_2-y_3)} + \right. \\ & \left. c_7\frac{(y-y_1)(y-y_2)}{(y_3-y_1)(y_3-y_2)}\right] + \frac{(x-x_1)(x-x_3)}{(x_2-x_1)(x_2-x_3)}\left[c_2\frac{(y-y_2)(y-y_3)}{(y_1-y_2)(y_1-y_3)} + \right. \\ & \left. c_5\frac{(y-y_1)(y-y_3)}{(y_2-y_1)(y_2-y_3)} + c_8\frac{(y-y_1)(y-y_2)}{(y_3-y_1)(y_3-y_2)}\right] + \\ & \frac{(x-x_1)(x-x_2)}{(x_3-x_1)(x_3-x_2)}\left[c_3\frac{(y-y_2)(y-y_3)}{(y_1-y_2)(y_1-y_3)} + c_6\frac{(y-y_1)(y-y_3)}{(y_2-y_1)(y_2-y_3)} + \right. \\ & \left. c_9\frac{(y-y_1)(y-y_2)}{(y_3-y_1)(y_3-y_2)}\right] \end{aligned} \tag{102}$$

where x_1, x_2, x_3, y_1, y_2 and y_3 are sample points of the quadrature rule, and $c_1, \cdots, c_9$ are the current density values at the sample points, as shown on Figure 32. The current density

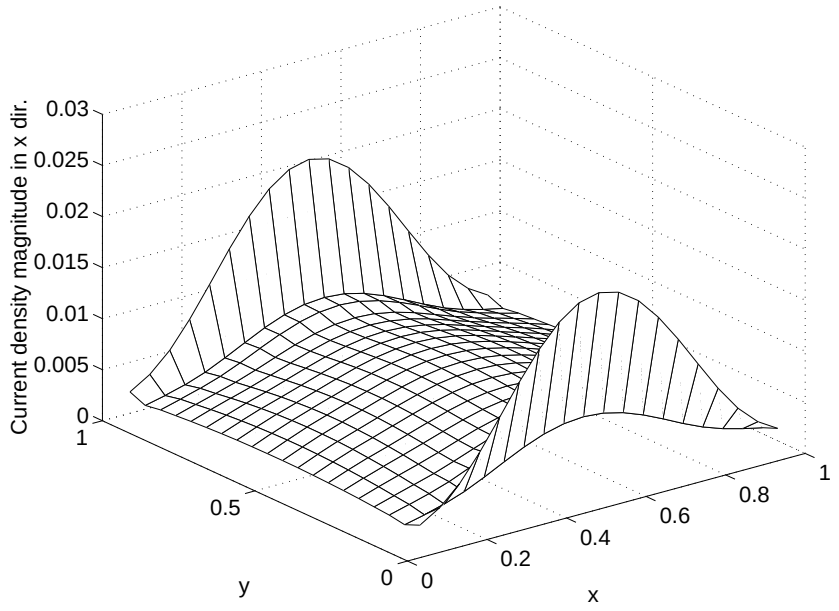

(a)

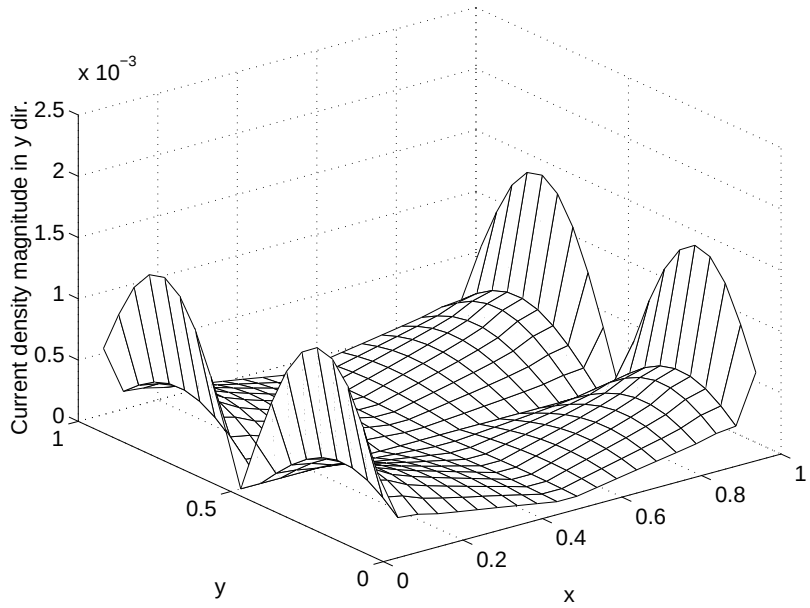

(b)

Figure 27: (a) The co-pol and (b) the cross-pol components of the surface current density on a 1λ x 1λ plate in free space obtained using MoM

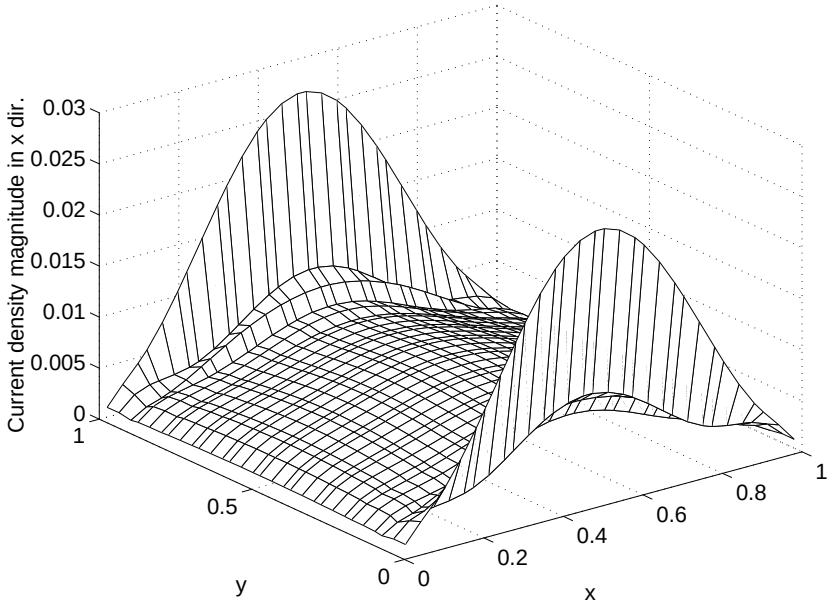

(a)

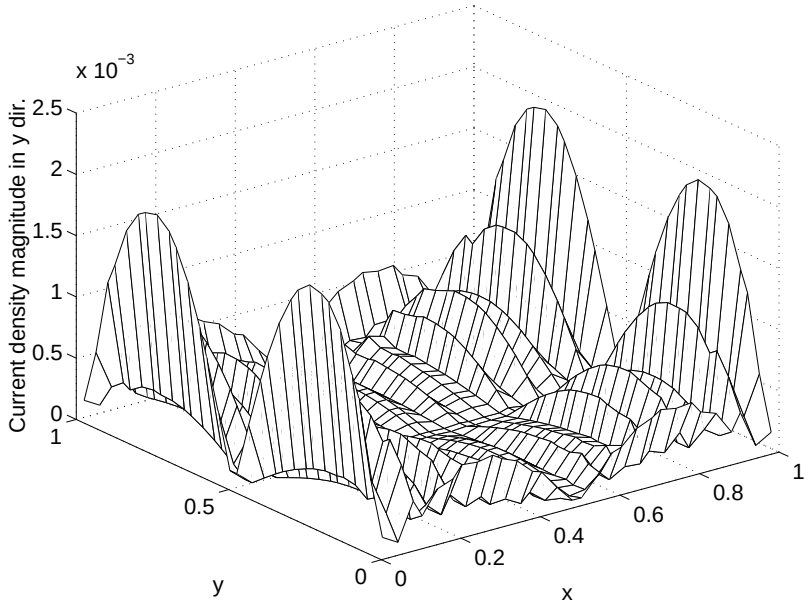

(b)

Figure 28: (a) The co-pol and (b) the cross-pol components of the surface current density on a 1λ x 1λ plate in free space obtained using LCN with 3 by 3 quadrature rules for each cell

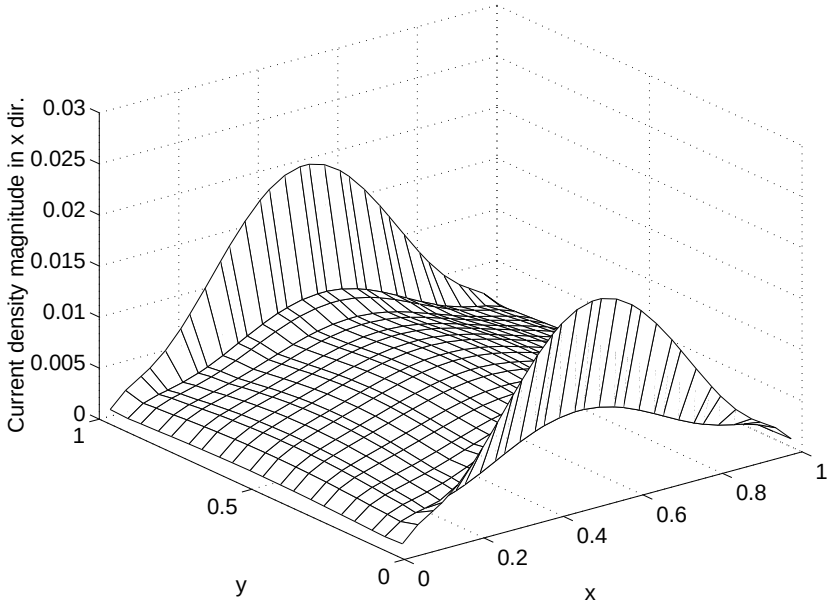

(a)

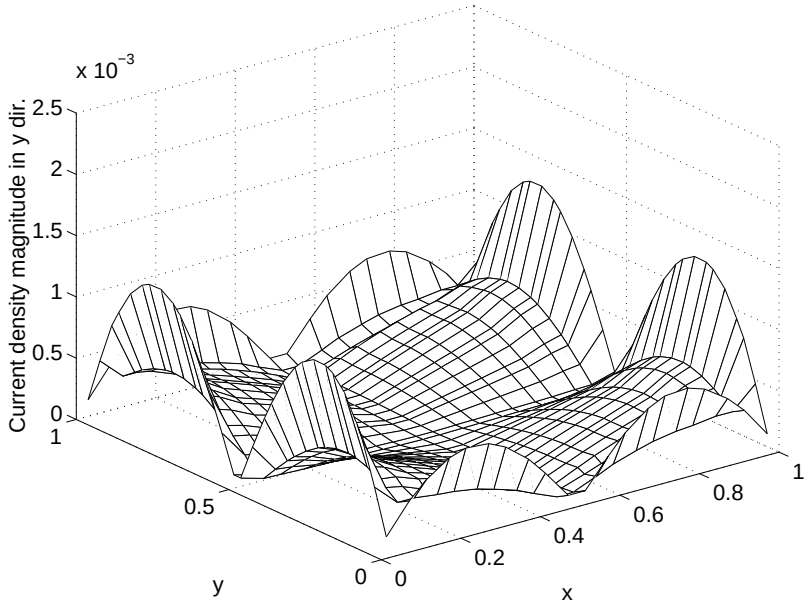

(b)

Figure 29: (a) The co-pol and (b) the cross-pol components of the surface current density on a 1λ x 1λ plate in free space obtained using LCN with 3 by 2 quadrature rules for each cell

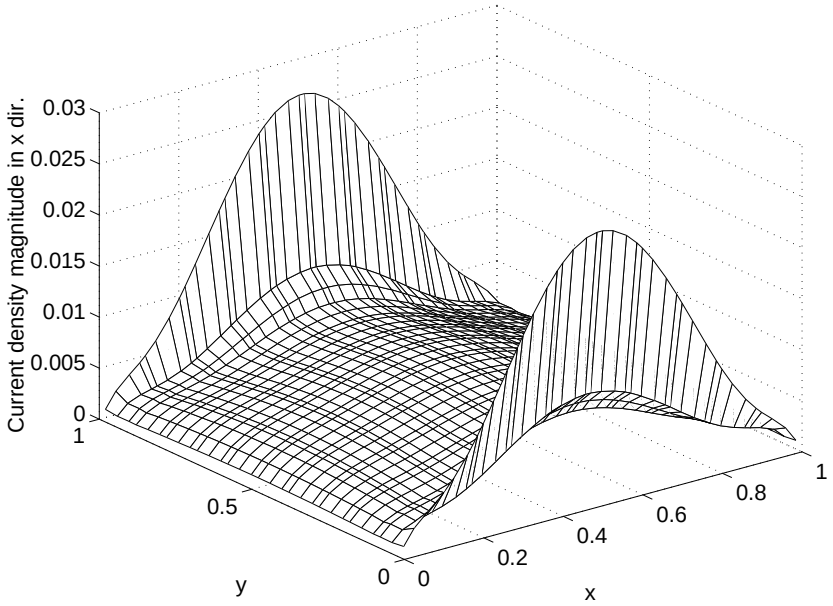

(a)

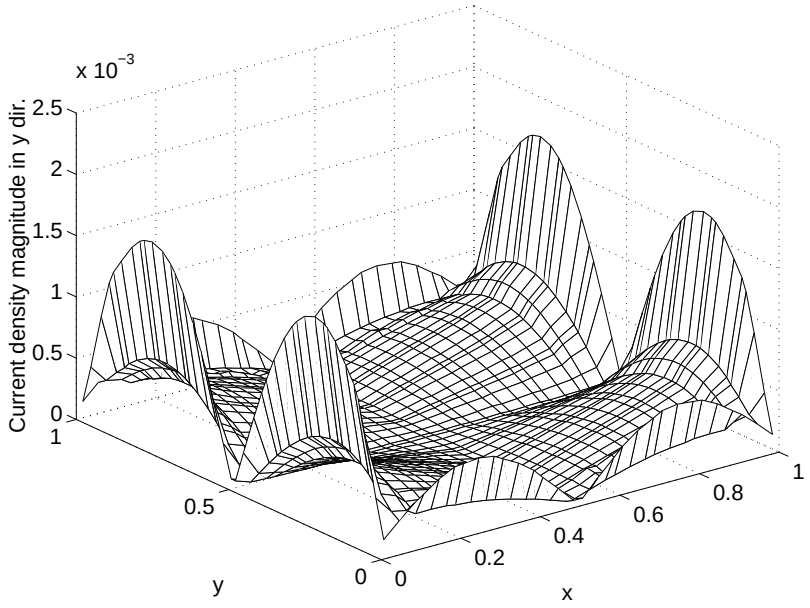

(b)

Figure 30: (a) The co-pol and (b) the cross-pol components of the surface current density on a 1λ x 1λ plate in free space obtained using LCN with 4 by 3 quadrature rules for each cell

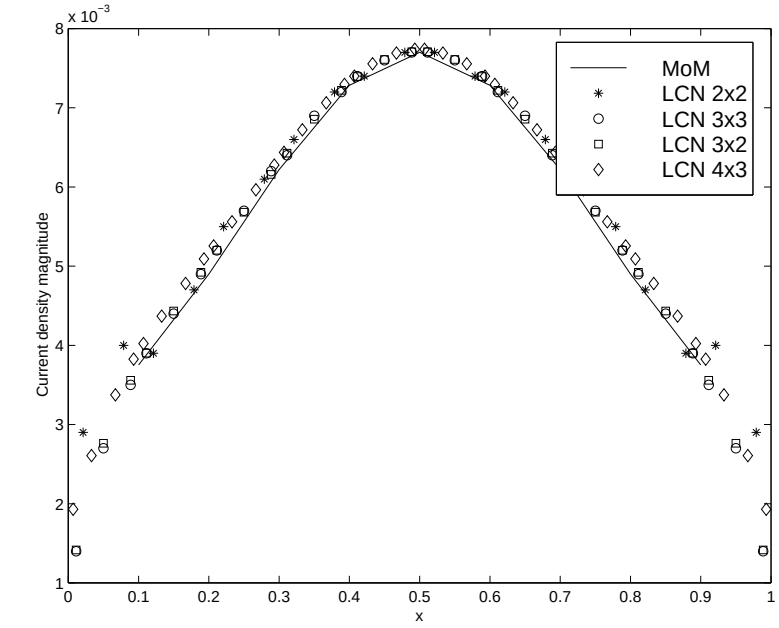

(a)

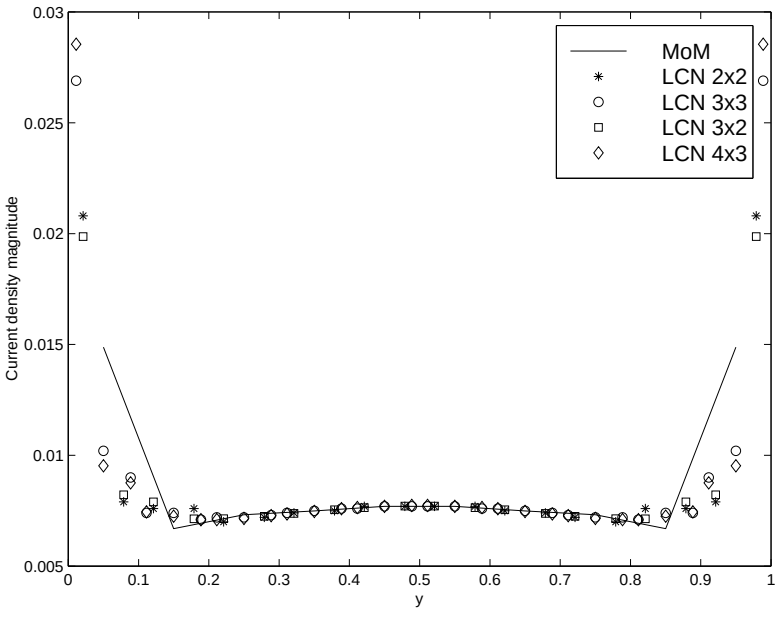

(b)

Figure 31: The x-component of the surface current density on a 1λ x 1λ plate in free space when (a) $y = 0.5\lambda$ (b) $x = 0.5\lambda$

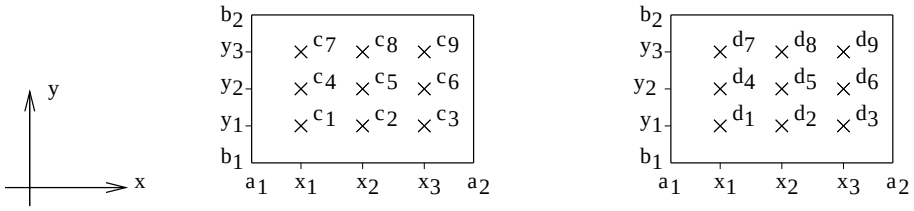

Figure 32: Polynomial complete representation on a cell when the quadrature order is 3 by 3 for the $x-$ and $y-$components of the current density

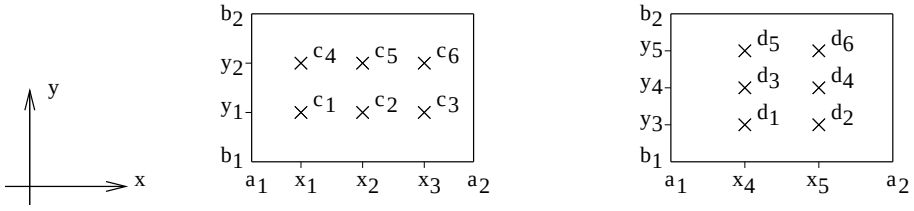

Figure 33: Mixed-order representation on a cell when the quadrature order is 3 by 2 for the $x-$component and 2 by 3 for the $y-$component of the current density

in the $y-$direction can be approximated as

$$\begin{aligned} J_y(x,y) &= \frac{(x-x_2)(x-x_3)}{(x_1-x_2)(x_1-x_3)}\left[d_1\frac{(y-y_2)(y-y_3)}{(y_1-y_2)(y_1-y_3)}+d_4\frac{(y-y_1)(y-y_3)}{(y_2-y_1)(y_2-y_3)}+\right.\\ &\left. d_7\frac{(y-y_1)(y-y_2)}{(y_3-y_1)(y_3-y_2)}\right]+\frac{(x-x_1)(x-x_3)}{(x_2-x_1)(x_2-x_3)}\left[d_2\frac{(y-y_2)(y-y_3)}{(y_1-y_2)(y_1-y_3)}+\right.\\ &\left. d_5\frac{(y-y_1)(y-y_3)}{(y_2-y_1)(y_2-y_3)}+d_8\frac{(y-y_1)(y-y_2)}{(y_3-y_1)(y_3-y_2)}\right]+\\ &\frac{(x-x_1)(x-x_2)}{(x_3-x_1)(x_3-x_2)}\left[d_3\frac{(y-y_2)(y-y_3)}{(y_1-y_2)(y_1-y_3)}+d_6\frac{(y-y_1)(y-y_3)}{(y_2-y_1)(y_2-y_3)}+\right.\\ &\left. d_9\frac{(y-y_1)(y-y_2)}{(y_3-y_1)(y_3-y_2)}\right] \end{aligned} \tag{103}$$

where $d_1,\cdots,d_9$ are the current density values at the sample points, as shown on Figure 32. For the mixed-order representation, if the quadrature rule is 3 by 2, the current density in the $x-$direction can be approximated as

$$\begin{aligned} J_x(x,y) &= \frac{(x-x_2)(x-x_3)}{(x_1-x_2)(x_1-x_3)}\left[c_1\frac{(y-y_2)}{(y_1-y_2)}+c_4\frac{(y-y_1)}{(y_2-y_1)}\right]+\\ &\frac{(x-x_1)(x-x_3)}{(x_2-x_1)(x_2-x_3)}\left[c_2\frac{(y-y_2)}{(y_1-y_2)}+c_5\frac{(y-y_1)}{(y_2-y_1)}\right]+\\ &\frac{(x-x_1)(x-x_2)}{(x_3-x_1)(x_3-x_2)}\left[c_3\frac{(y-y_2)}{(y_1-y_2)}+c_6\frac{(y-y_1)}{(y_2-y_1)}\right] \end{aligned} \tag{104}$$

where x_1, x_2, x_3, y_1 and y_2 are sample points of the quadrature rule, and $c_1, \cdots, c_6$ are the current density values at the sample points, as shown on Figure 33. For the mixed-order representation, if the quadrature rule is 2 by 3, the current density in the $y-$direction can be approximated as

$$\begin{aligned} J_y(x,y) &= \frac{(y-y_4)(y-y_5)}{(y_3-y_4)(y_3-y_5)}\left[d_1\frac{(x-x_5)}{(x_4-x_5)}+d_2\frac{(x-x_4)}{(x_5-x_4)}\right]+ \\ &\quad \frac{(y-y_3)(y-y_5)}{(y_4-y_3)(y_4-y_5)}\left[d_3\frac{(x-x_5)}{(x_4-x_5)}+d_4\frac{(x-x_4)}{(x_5-x_4)}\right]+ \\ &\quad \frac{(y-y_3)(y-y_4)}{(y_5-y_3)(y_5-y_4)}\left[d_5\frac{(x-x_5)}{(x_4-x_5)}+d_6\frac{(x-x_4)}{(x_5-x_4)}\right] \end{aligned} \tag{105}$$

where x_4, x_5, y_3, y_4 and y_5 are sample points of the quadrature rule, and $d_1, \cdots, d_6$ are the current density values at the sample points, as shown on Figure 33.

Using the continuity equation and the approximation of current equations, the charge density on each cell can be calculated by taking the derivative of the current equations. Figures 34a and 34b show the real and imaginary parts of the charge density (scaled by a factor of $-j\omega$) on the plate obtained using MoM. Figures 35a and 35b show the real and imaginary parts of the charge density on the plate obtained using LCN with 3 by 3 quadrature rules for each cell. These figures show reasonable agreement between the MoM and LCN approaches except on the cells at the edges of the plate. The reason is that the $y-$component of the current density obtained using LCN is smaller than the $x-$component. As a result, the effect of the $y-$component on charge density is much less than the $x-$component, except within the cells at the edges of the plate. Figures 36a and 36b show the real and imaginary parts of the charge density on the plate obtained using LCN with 3 by 2 quadrature rules for each cell. Figures 37a and 37b present the real and imaginary parts of the charge density on the plate obtained using LCN with 4 by 3 quadrature rules for each cell. As expected, these figures show reasonable agreement between the MoM and LCN approaches when mixed-order representations are used with the LCN procedure.

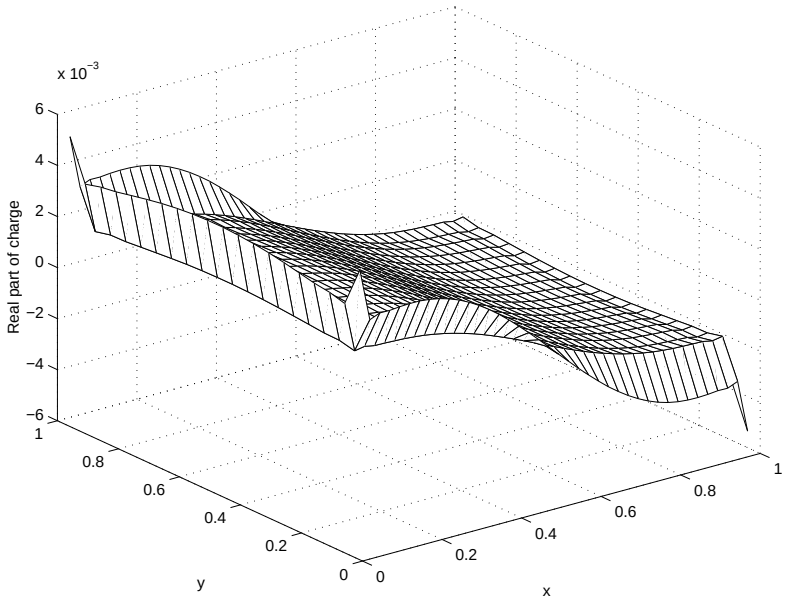

(a)

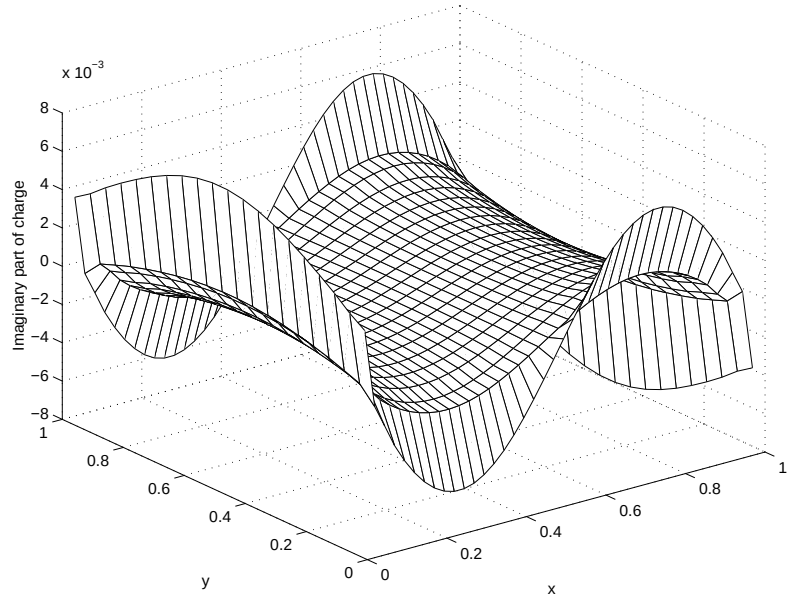

(b)

Figure 34: (a) The real and (b) imaginary parts of the charge density on a 1λ x 1λ plate in free space obtained using MoM

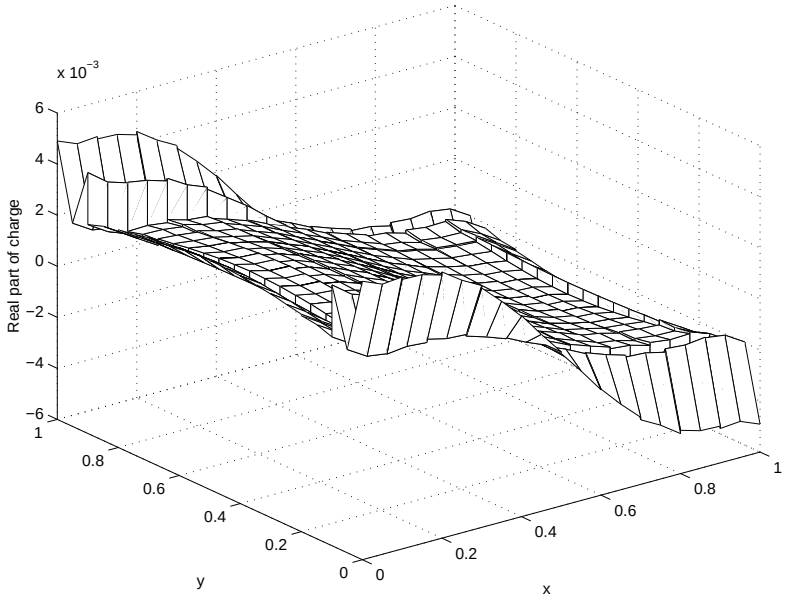

(a)

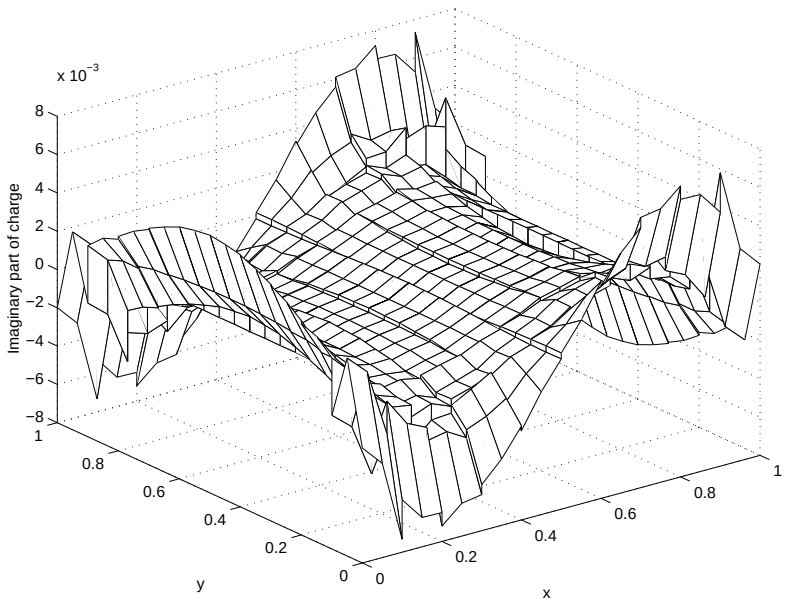

(b)

Figure 35: (a) The real and (b) imaginary parts of the charge density on a 1λ x 1λ plate in free space obtained using LCN with 3 by 3 quadrature rules for each cell

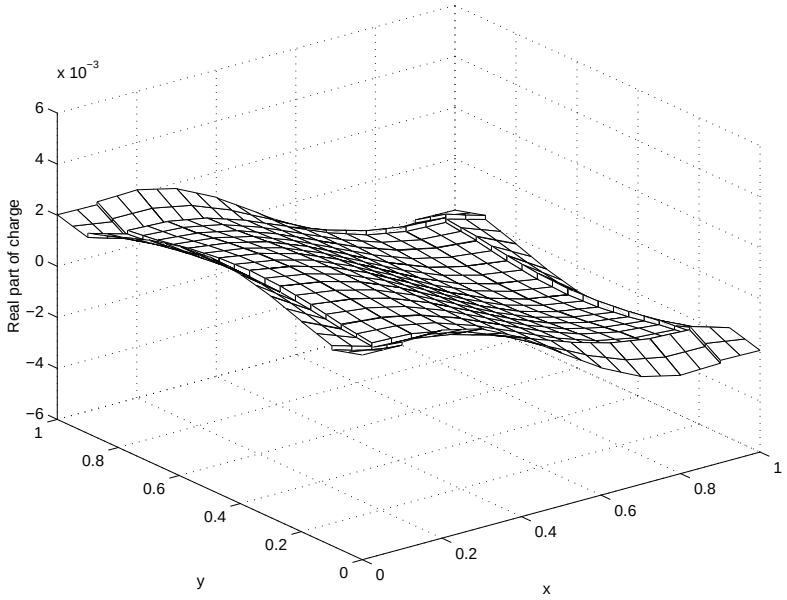

(a)

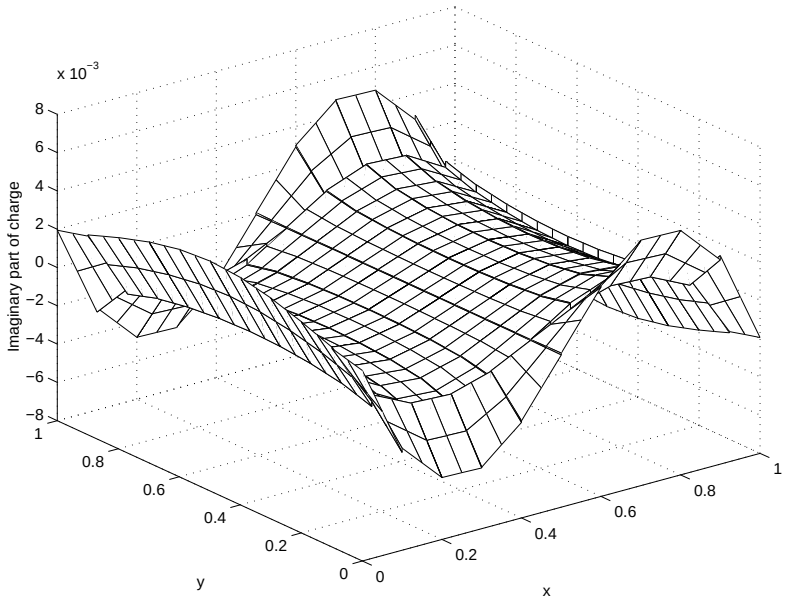

(b)

Figure 36: (a) The real and (b) imaginary parts of the charge density on a 1λ x 1λ plate in free space obtained using LCN with 3 by 2 quadrature rules for each cell

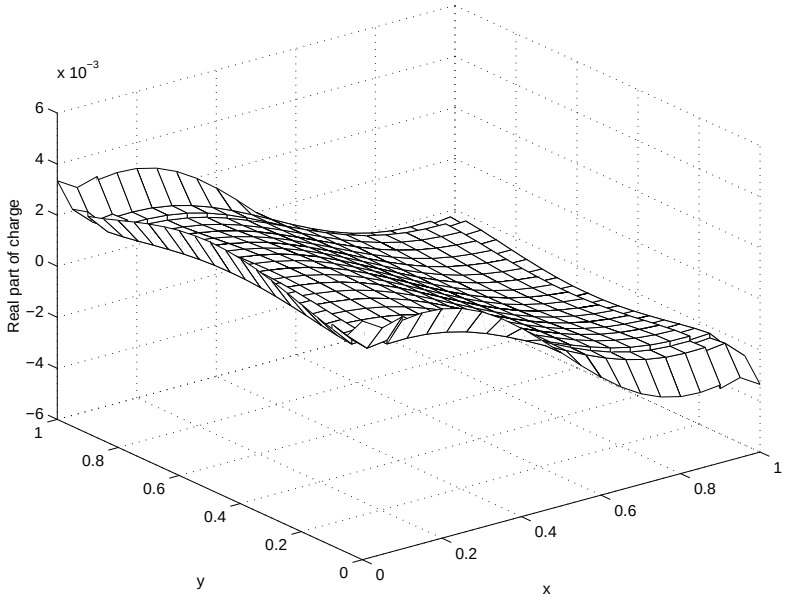

(a)

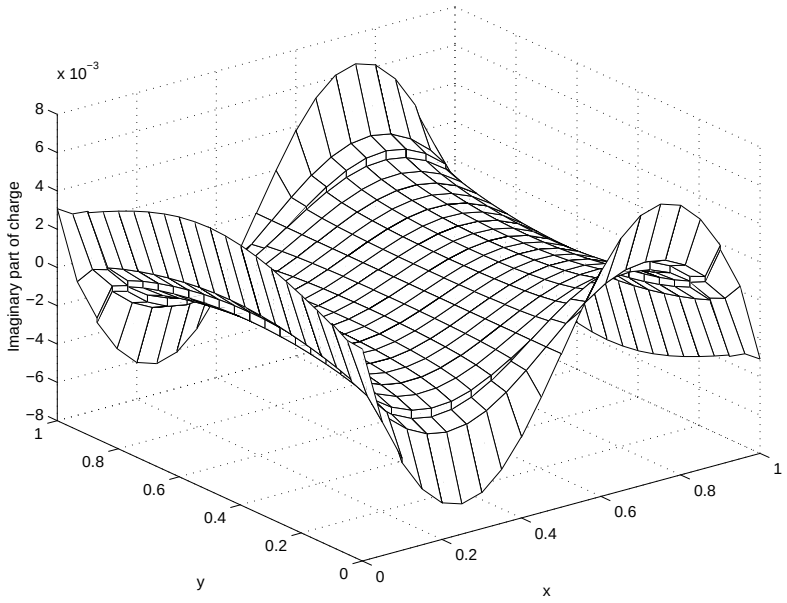

(b)

Figure 37: (a) The real and (b) imaginary parts of the charge density on a 1λ x 1λ plate in free space obtained using LCN with 4 by 3 quadrature rules for each cell

4.6 1λ *x* 1λ *plate over a grounded substrate*

For the next example, consider a 1λ x 1λ plate over a grounded substrate. The dielectric constant of the substrate, ϵ_r, is 2.2. The substrate thickness, h, is 0.1λ. The plate is placed on top of the substrate and the upper medium is free space. Figures 38a and 38b show the $x-$ and $y-$components of the surface current densities on the plate obtained using MoM. Figures 39a and 39b show the $x-$ and $y-$components, respectively, of the surface current densities on the plate obtained using LCN with 3 by 3 quadrature rules for each cell. Figures 40a and 40b depict the $x-$ and $y-$components, respectively, of the surface current densities on the plate obtained using LCN with 3 by 2 quadrature rules for each cell. Figures 41a and 41b show the $x-$ and $y-$components, respectively, of the surface current densities on the plate obtained using LCN with 4 by 3 quadrature rules for each cell. From these figures, it is observed that the LCN procedure with polynomial complete representation does not agree with the MoM and the LCN procedure with mixed-order representation, as expected. In fact, the results of the polynomial-complete representation are highly erratic and completely non-physical in appearance. Figure 42 presents the $x-$component of the surface current density on the plate when $x = 0.5\lambda$ and $y = 0.5\lambda$. This figure shows reasonable agreement between the MoM and LCN approaches when mixed-order representations are used with the LCN procedure.

In summary, the preceding example supports the previous conclusion that a mixed-order representation is necessary with the MPIE.

Figures 43a and 43b show the real and imaginary parts of the charge density (scaled by a factor of $-j\omega$) on the plate obtained using MoM. Figures 44a and 44b show the real and imaginary parts of the charge density on the plate obtained using LCN with 3 by 2 quadrature rules for each cell. Figures 45a and 45b give the real and imaginary parts of the charge density on the plate obtained using LCN with 4 by 3 quadrature rules for each cell. As expected, these figures show reasonable agreement between the MoM and LCN approaches when mixed-order representations are used with the LCN procedure.

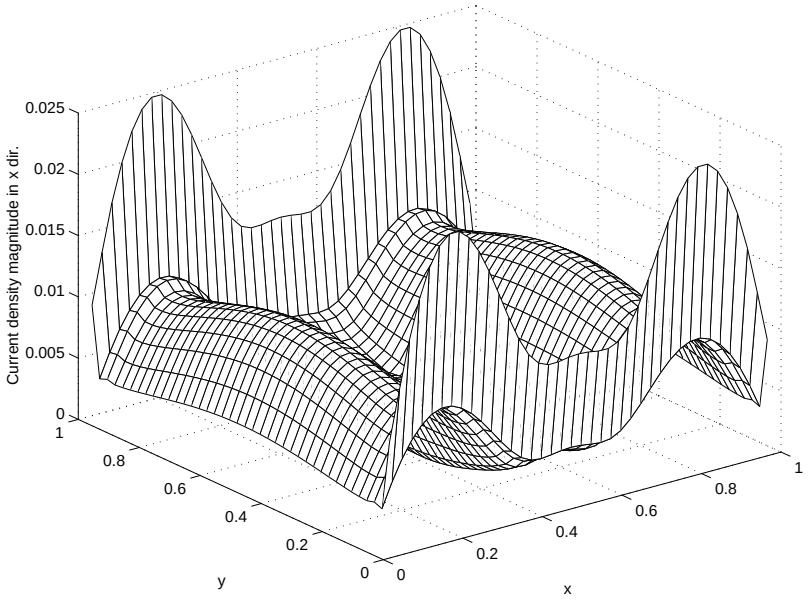

(a)

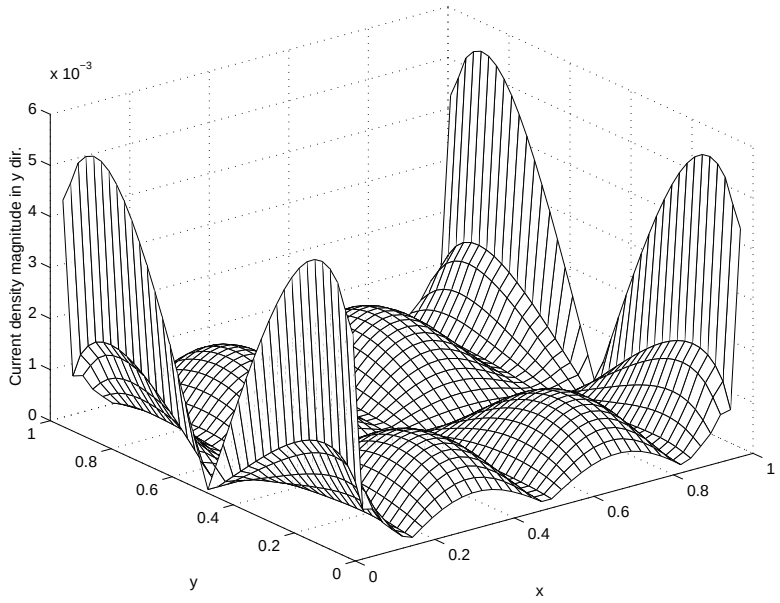

(b)

Figure 38: (a) The co-pol and (b) the cross-pol components of the surface current density on a 1λ x 1λ plate over a grounded substrate obtained using MoM

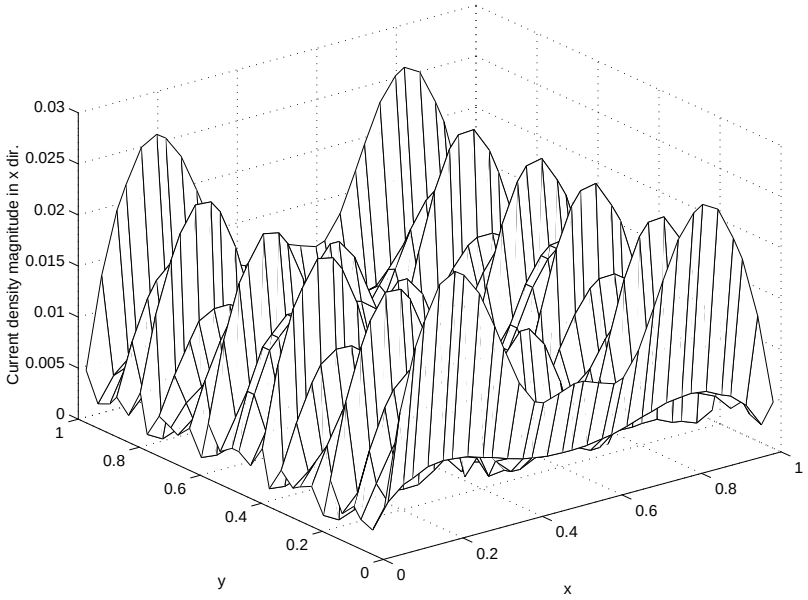

(a)

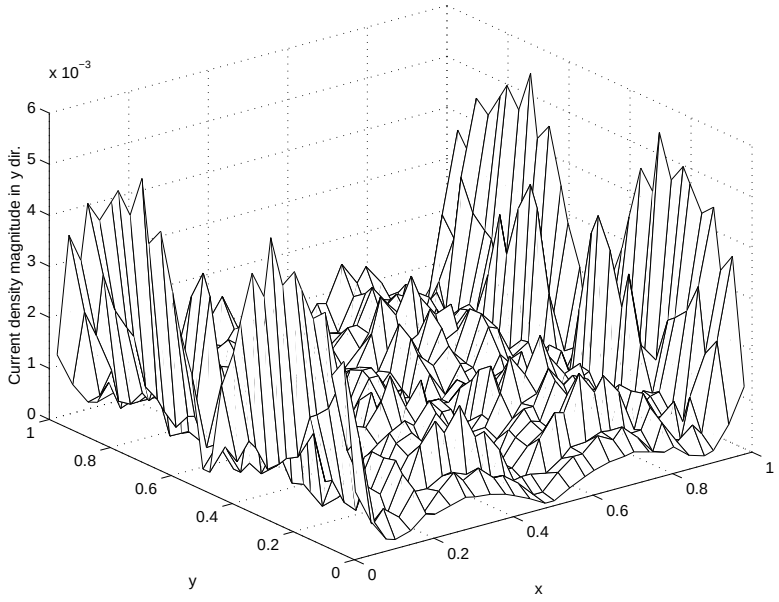

(b)

Figure 39: (a) The co-pol and (b) the cross-pol components of the surface current density on a 1λ x 1λ plate over a grounded substrate obtained using LCN with 3 by 3 quadrature rules for each cell

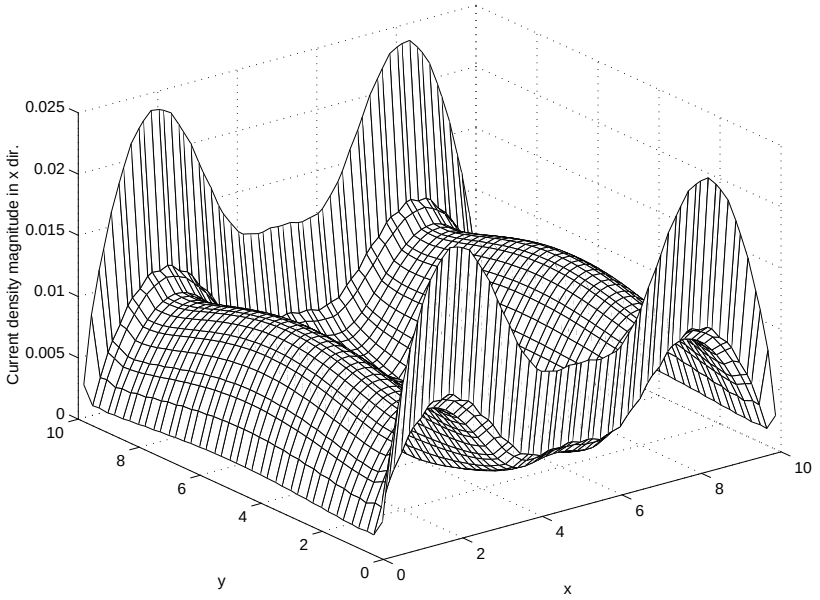

(a)

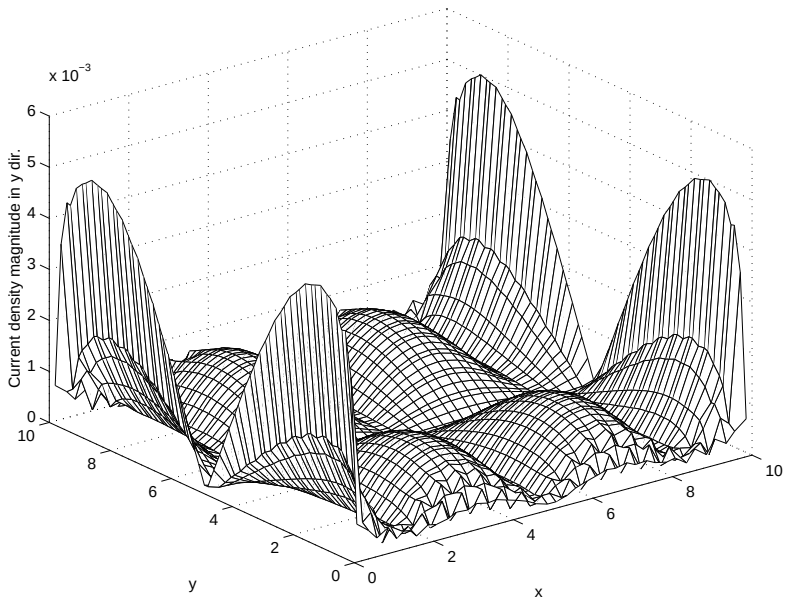

(b)

Figure 40: (a) The co-pol and (b) the cross-pol components of the surface current density on a 1λ x 1λ plate over a grounded substrate obtained using LCN with 3 by 2 quadrature rules for each cell

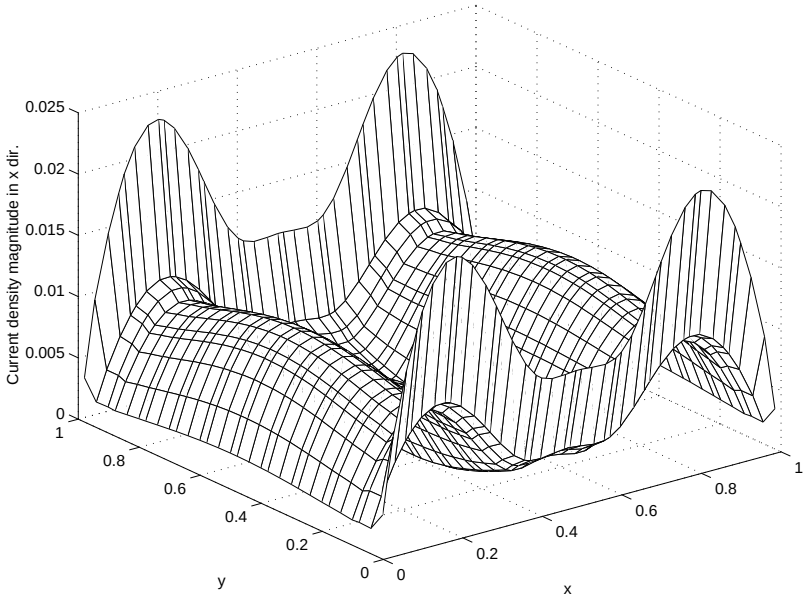

(a)

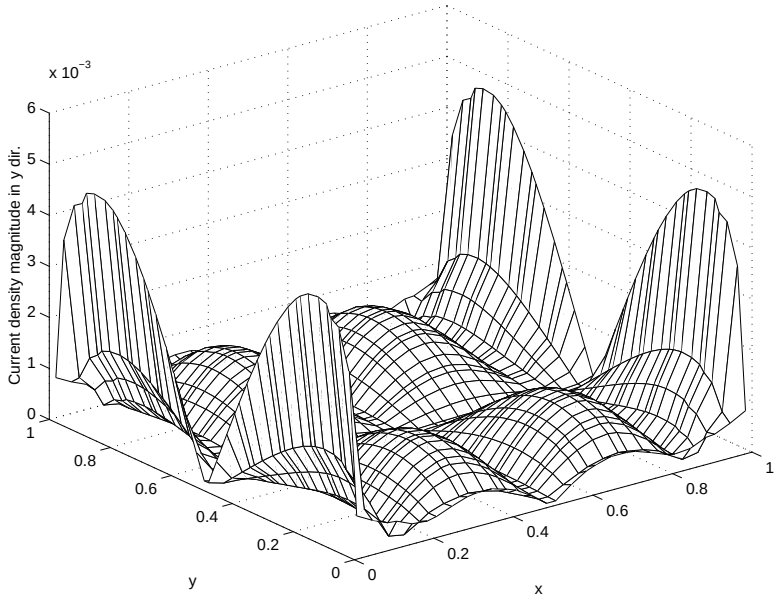

(b)

Figure 41: (a) The co-pol and (b) the cross-pol components of the surface current density on a 1λ x 1λ plate over a grounded substrate obtained using LCN with 4 by 3 quadrature rules for each cell

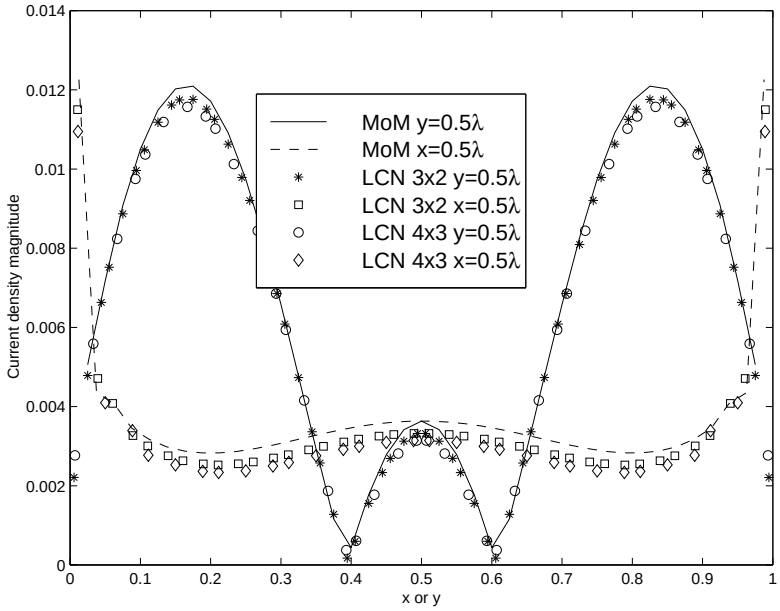

Figure 42: The x-component of the surface current density on a 1λ x 1λ plate over a grounded substrate when $x = 0.5\lambda$ and $y = 0.5\lambda$

4.7 Nonconforming models

The LCN procedure is based upon a purely local representation of the current density, meaning that the representation within a cell is entirely independent of the neighboring cells. This feature of LCN suggests the possibility of analyzing models that are nonconforming. In a nonconforming model, some of the cells have edges whose junctions do not perfectly align with the junctions of neighboring cells. The MoM procedure of Chapter 3 cannot be used with nonconforming models, since the rooftop expansion functions used within that procedure overlap adjacent cells.

Nonconforming models are of interest because of the general difficulty of providing self-consistent conforming models for complex structures. Ideally, model generation for three-dimensional objects can be approached by dividing the structure into simpler parts, and generating models (meshes) for the parts. However, when combining those parts back together, one will generally not obtain a conforming model. The need for a conforming model therefore leads to additional complexity in the modeling procedure.

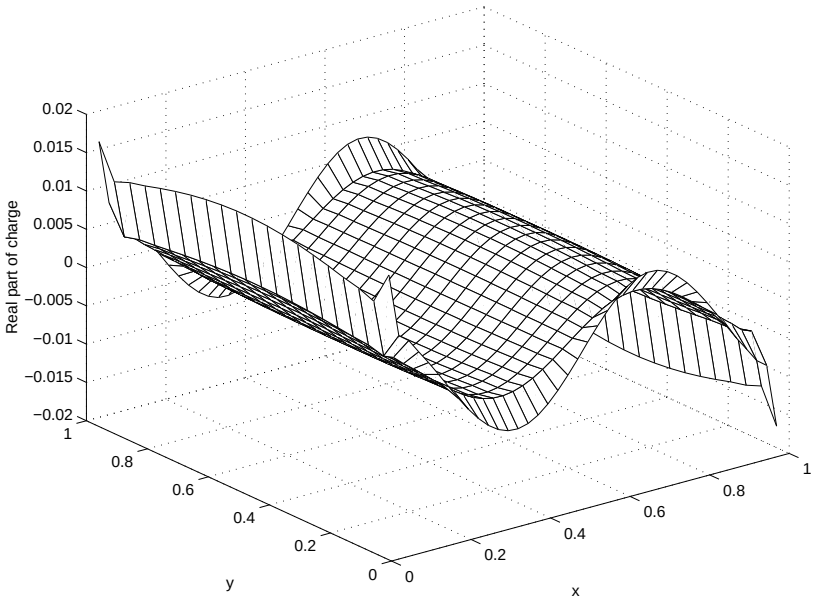

(a)

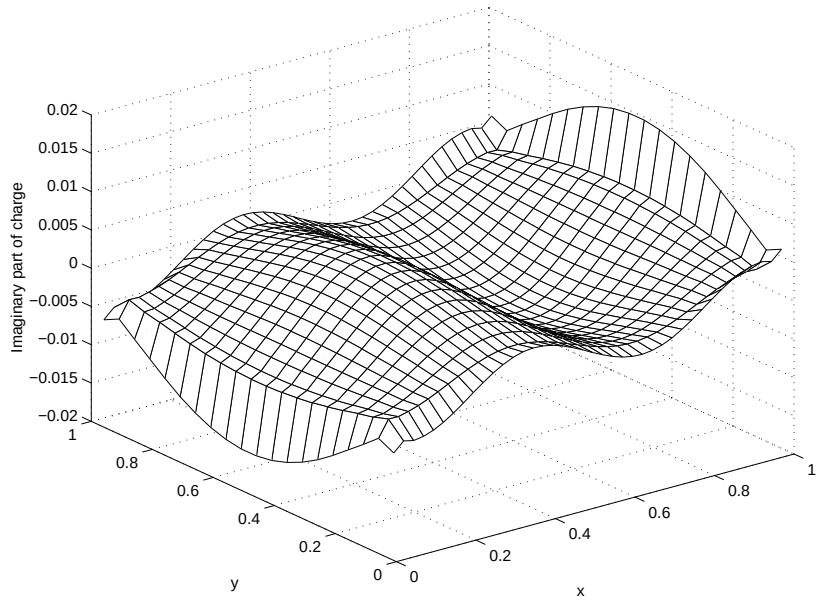

(b)

Figure 43: (a) The real and (b) imaginary parts of the charge density on a 1λ x 1λ plate over a grounded substrate obtained using MoM

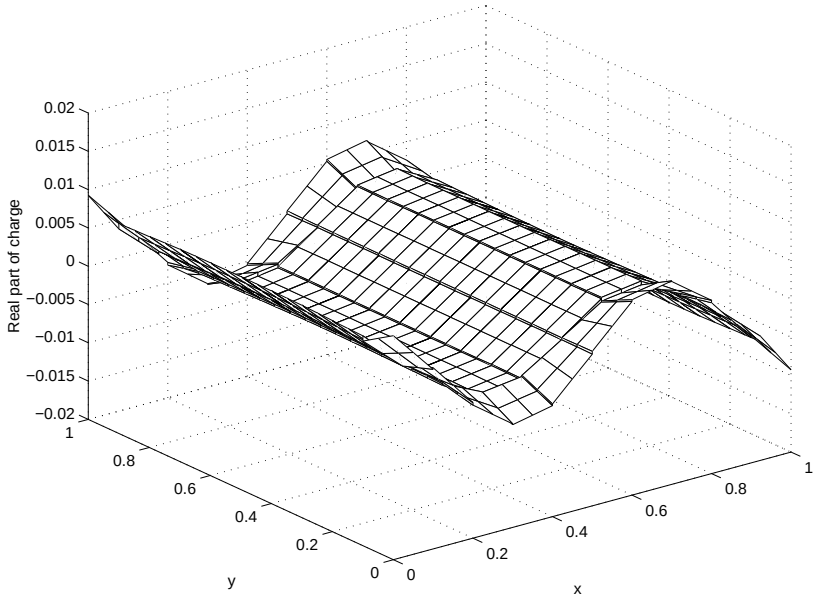

(a)

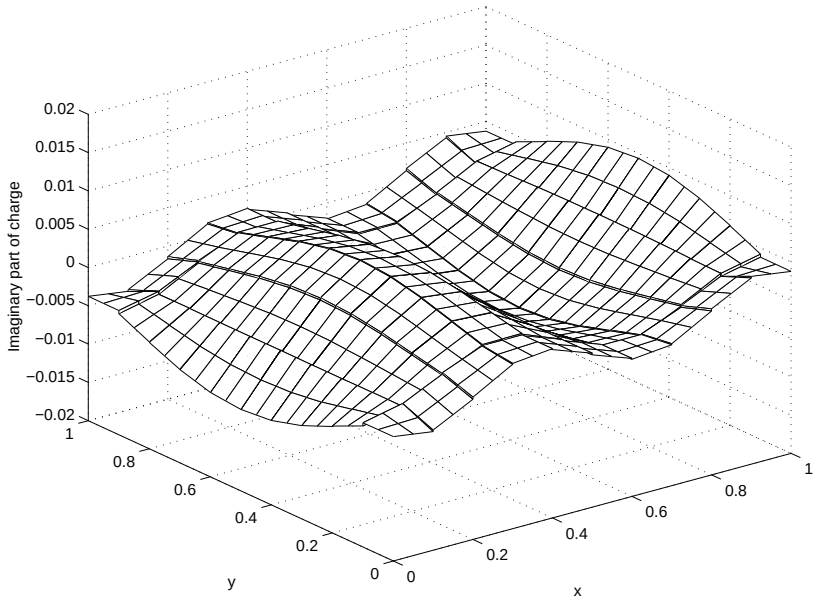

(b)

Figure 44: (a) The real and (b) imaginary parts of the charge density on a 1λ x 1λ plate over a grounded substrate obtained using LCN with 3 by 2 quadrature rules for each cell

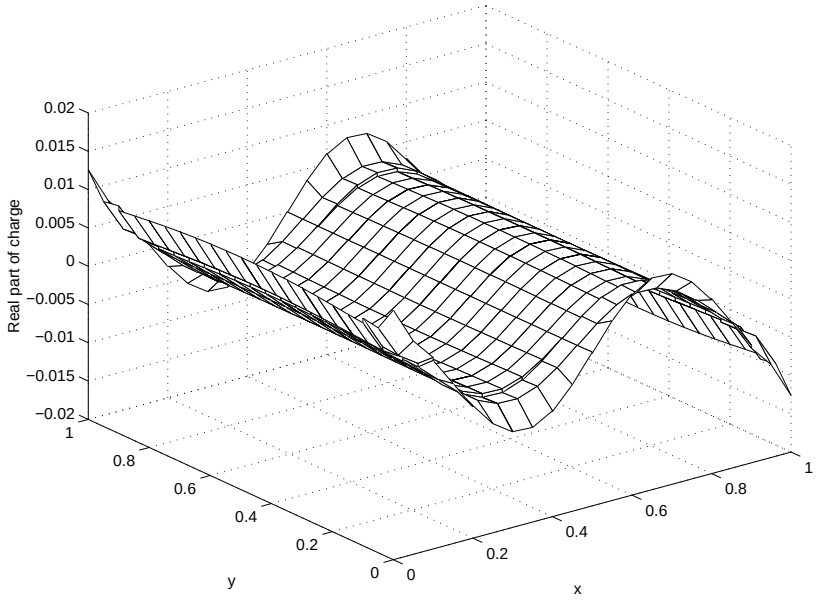

(a)

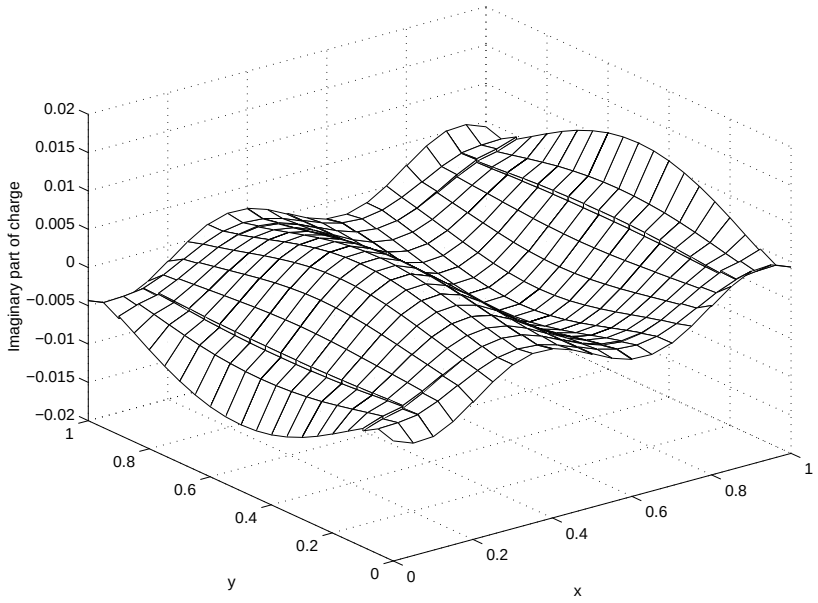

(b)

Figure 45: (a) The real and (b) imaginary parts of the charge density on a 1λ x 1λ plate over a grounded substrate obtained using LCN with 4 by 3 quadrature rules for each cell

In this section, the performance of LCN is studied for several nonconforming models of a flat plate. The results suggest that the LCN procedure can be used to successfully treat structures that are described with nonconforming models.

Consider a 0.3λ x 0.3λ plate in free space illuminated by a normally incident plane wave. For validation, the LCN results to follow are compared with the results of the MoM formulation based on rooftop basis and testing functions. Figure 46 shows the $x-$component of the surface current density on the plate along the cuts $x = 0.15\lambda$ and $y = 0.15\lambda$. This figure shows reasonable agreement between the MoM and LCN approaches, when a conforming mesh is used for both.

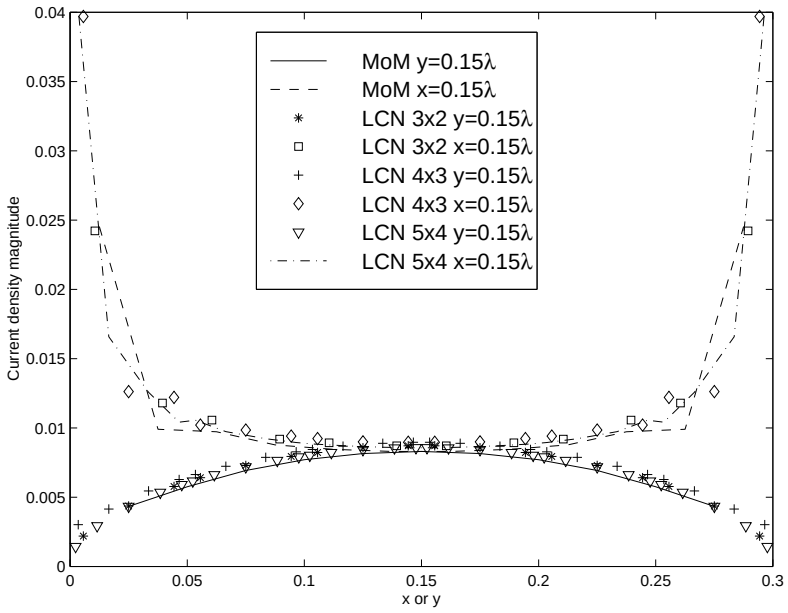

Figure 46: The x-component of the surface current density on a 0.3λ x 0.3λ plate in free space when $x = 0.15\lambda$ and $y = 0.15\lambda$. 36-cell conforming model.

To demonstrate the effects of using nonconforming meshes, additional results for the current density induced on a 0.3λ x 0.3λ plate in free space are presented. Figures 47 and 48 depict the basic structure of the models. As a reference, Figure 49a and Figure 49b display the $x-$ and $y-$components of the current densities on the plate obtained using conforming meshes. For this example and the remaining examples in this paragraph, the

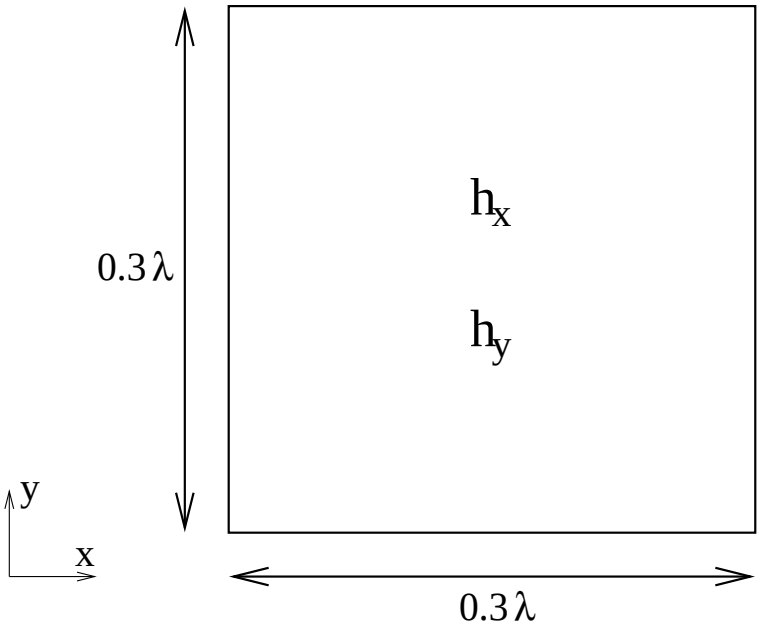

(a)

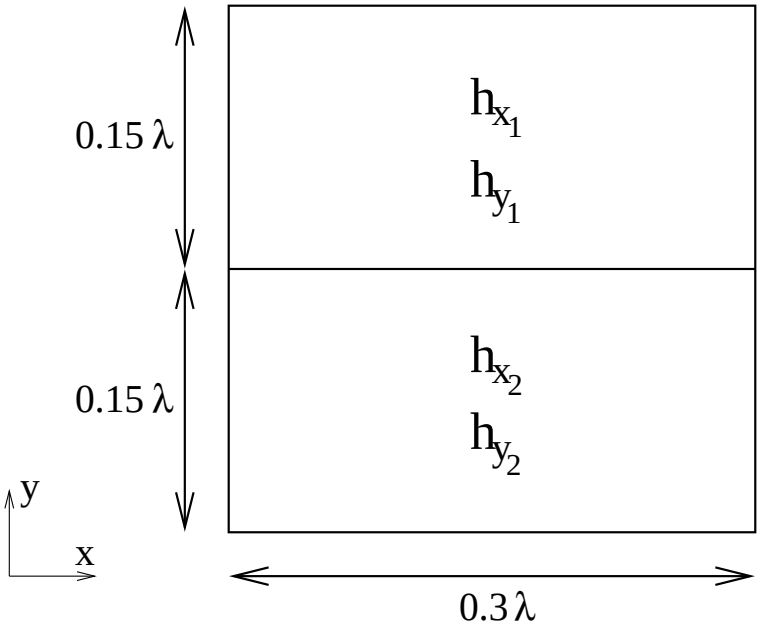

(b)

Figure 47: (a) Conforming meshing model and (b) nonconforming meshing model when the plate is divided into two regions across the $y-$axis

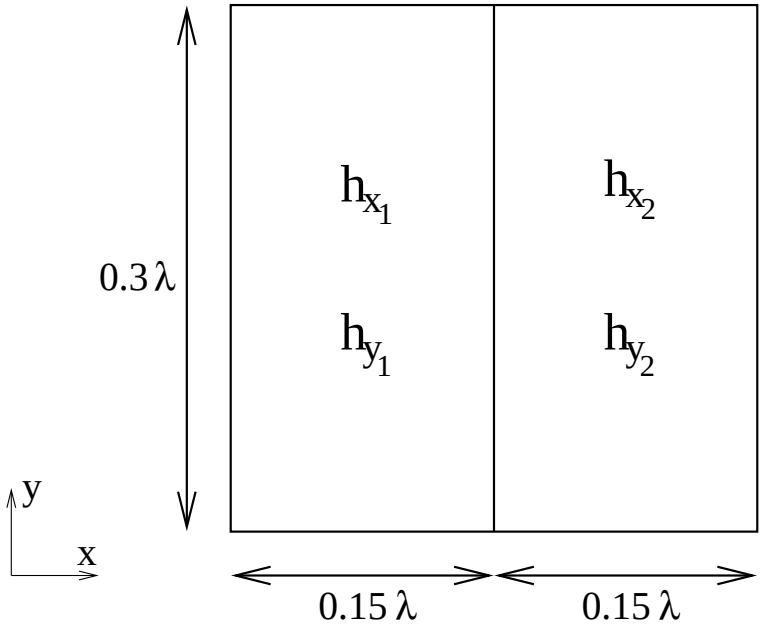

(a)

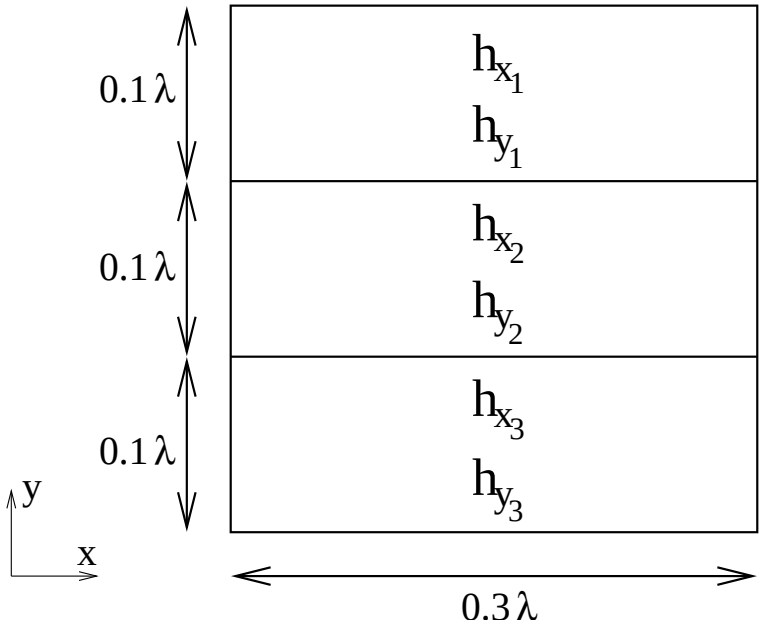

(b)

Figure 48: (a) Nonconforming meshing model when the plate is divided into two regions across the $x-$axis and (b) nonconforming meshing model when the plate is divided into three equal regions across the $y-$axis.

current densities are obtained using LCN with 3 by 2 quadrature rules. In this case, the dimension of each cell in the x and y directions, h_x and h_y (as shown in Figure 47a), are both set to $\lambda/20 = 0.05\lambda$.

In the first example, the plate is divided into two regions across the $y-$axis in which the cell sizes are different, which results in a nonconforming mesh (as shown in Figure 47b). In the first region, where y is less than 1.5λ, the dimension h_{x_1} is set to 0.075λ. The same length in the second region, h_{x_2}, is set to 0.06λ. In both regions, the dimension of each cell along y, denoted as h_{y_1} and h_{y_2} for the first and second regions, respectively, is set to 0.05λ. The $x-$ and $y-$components of the current densities for this example (obtained using LCN with 3 by 2 quadrature rules) are shown in Figure 50a and Figure 50b, respectively. The nonconforming meshing does not detrimentally affect the result.

In the second example, the plate is divided into two regions across the $x-$axis (as shown in Figure 48a). For this example, h_{y_1} and h_{y_2} are set to 0.075λ and 0.06λ, respectively. In both regions, h_{x_1} and h_{x_2} are set to 0.05λ. The surface current densities for this second example (obtained using LCN with 3 by 2 quadrature rules) are given in Figure 51a and Figure 51b for the $x-$ and $y-$components, respectively. When the densities are compared with Figure 49a and Figure 49b, there is a reasonable agreement between the $x-$components of the current density but the $y-$components do not agree well. One might expect that in this configuration, the effect of the nonconforming cells would be greater than in the previous example since the dominant component of the current is flowing directly across the junction between the two regions of the plate. In fact, the difference, while noticeable, is relatively small compared with the magnitude of the dominant current component.

In the third example, the plate is partitioned the same as in the first example (along the $y-$axis), but the size of the cells along the y differ in the two regions. In this example, h_{y_1} and h_{y_2} are set to 0.05λ and 0.025λ, respectively. In addition, h_{x_1} and h_{x_2} are both set to 0.05λ. (The LCN with 3 by 2 quadrature rules is used to obtain the current.) The $x-$ and $y-$components of the current densities are shown in Figure 52a and Figure 52b, respectively. This example also shows that the LCN with nonconforming meshing appears to give the correct results.

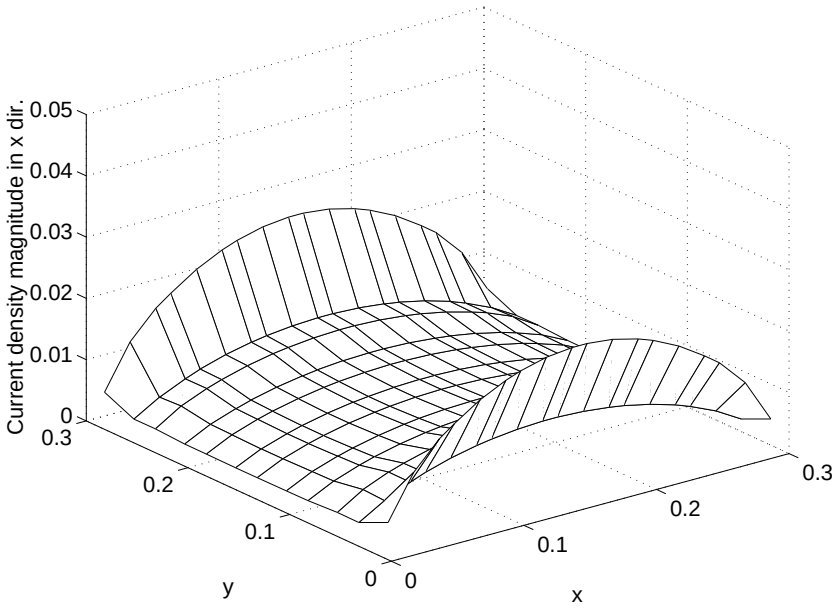

(a)

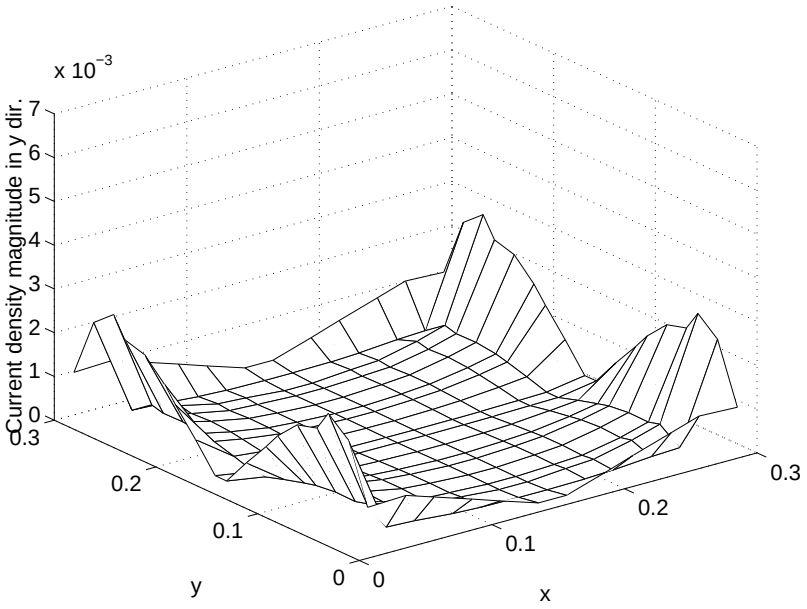

(b)

Figure 49: (a) The x-component and (b) the y-component of the surface current density on a 0.3λ x 0.3λ plate in free space obtained using LCN with 3 by 2 quadrature rules for each cell when $h_x = h_y = \lambda/20 = 0.05\lambda$. Conforming mesh case.

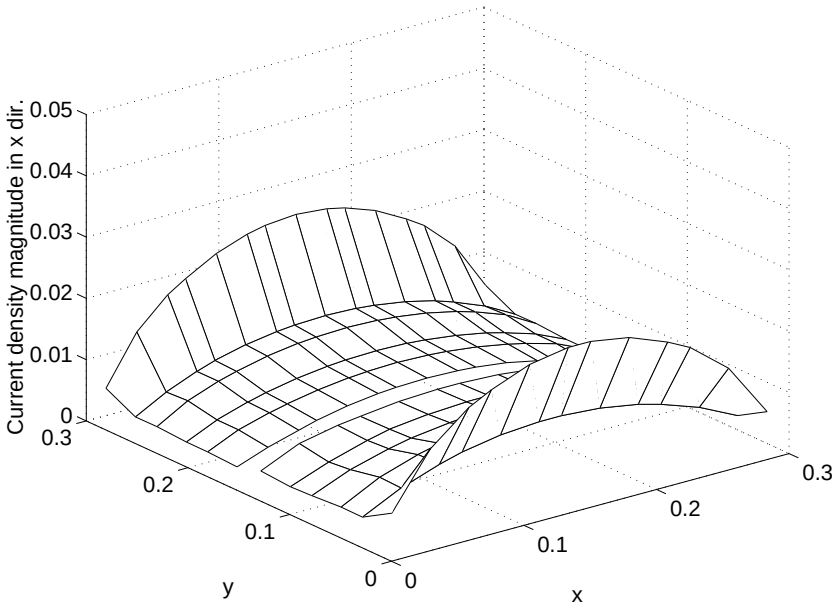

(a)

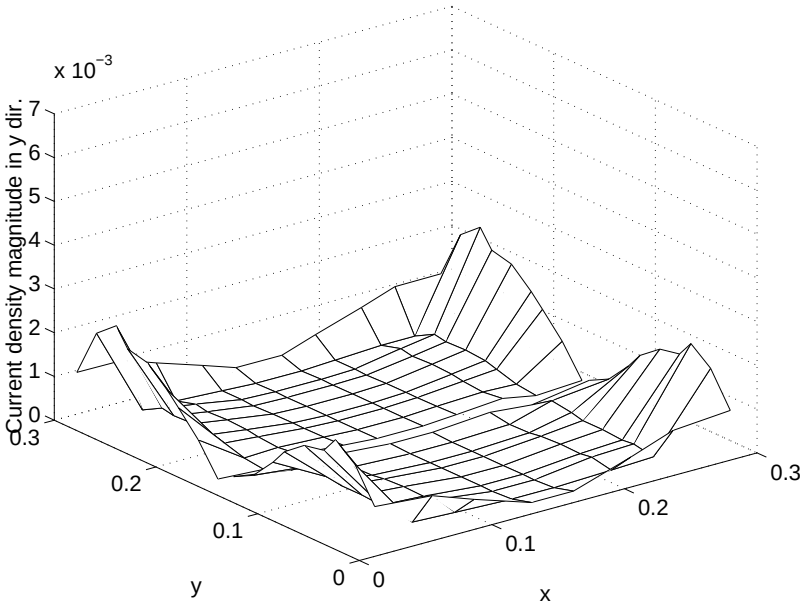

(b)

Figure 50: (a) The x-component and (b) the y-component of the surface current density on a 0.3λ x 0.3λ plate in free space obtained using LCN with 3 by 2 quadrature rules for each cell when $h_{x_1} = 0.075\lambda$, $h_{x_2} = 0.06\lambda$ and $h_{y_1} = h_{y_2} = \lambda/20$. Nonconforming case.

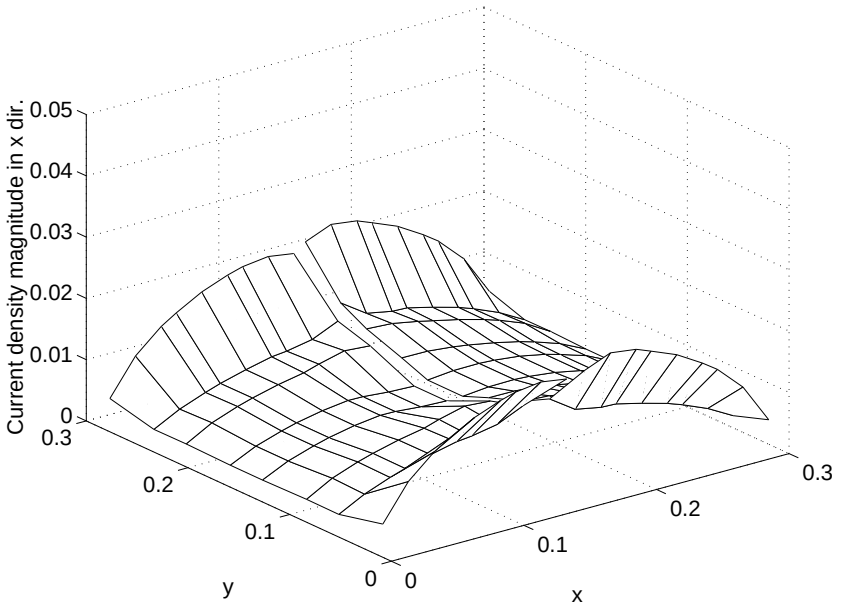

(a)

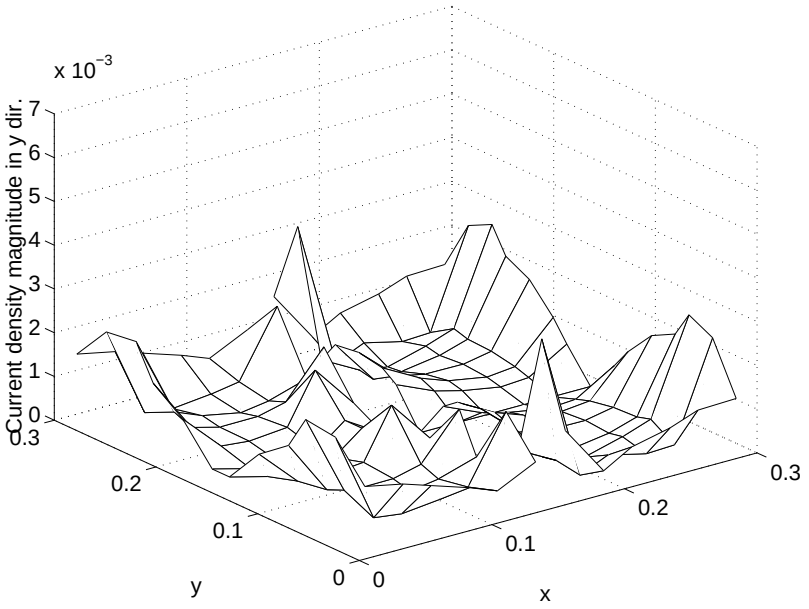

(b)

Figure 51: (a) The x-component and (b) the y-component of the surface current density on a 0.3λ x 0.3λ plate in free space obtained using LCN with 3 by 2 quadrature rules for each cell when $h_{x_1} = h_{x_2} = \lambda/20$, $h_{y_1} = 0.075\lambda$ and $h_{y_2} = 0.06\lambda$. Nonconforming case.

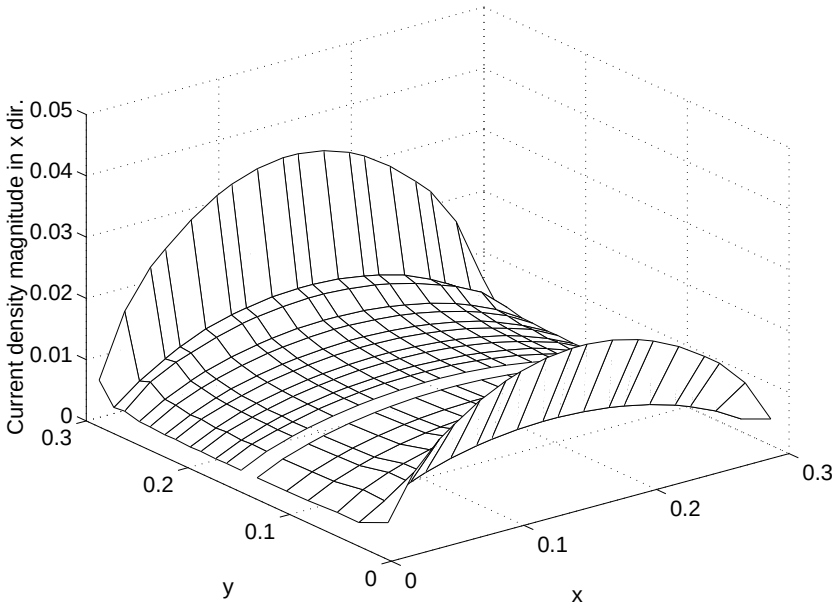

(a)

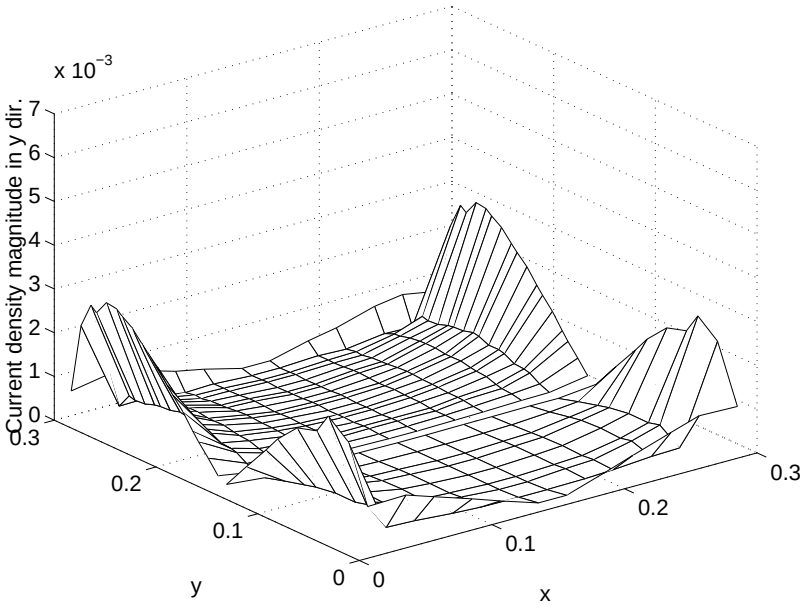

(b)

Figure 52: (a) The x-component and (b) the y-component of the surface current density on a 0.3λ x 0.3λ plate in free space obtained using LCN with 3 by 2 quadrature rules for each cell when $h_{x_1} = h_{x_2} = \lambda/20$, $h_{y_1} = \lambda/20$ and $h_{y_2} = \lambda/40$. Nonconforming case.

As a fourth example, the second example is repeated but with the cell dimension along the $x-$axis different in the two regions. In this case, while h_{x_1} and h_{x_2} are set to 0.025λ and 0.05λ, respectively, h_{y_1} and h_{y_2} are both set to 0.05λ. Figure 53a and Figure 53b present the $x-$ and $y-$components of the current density obtained using LCN with 3 by 2 quadrature rules. These results appear satisfactory except for small fluctuations in the $y-$component.

In the final two examples, the plate is divided into three equal regions along the $y-$axis (as shown in Figure 48b). In the fifth example, while h_{y_1} and h_{y3} in the first and third region are set to 0.025λ, h_{y_2} in the second region is set to 0.05λ. In this example, h_{x_1}, h_{x_2} and h_{x3} are all set to 0.05λ. The $x-$ and $y-$components of the current densities are shown in Figure 54a and Figure 54b. (These current densities are also obtained using the LCN method with 3 by 2 quadrature rules).

In the last example, while the cells are divided equally in the first and third region such that h_{x_1}, h_{y_1}, h_{x3} and h_{y3} are set to 0.05λ, they are divided in the second region so that both h_{x_2} and h_{y_2} are set to 0.025λ. Figure 55a and Figure 55b show the $x-$ and $y-$components of the current densities obtained using LCN with 3 by 2 quadrature rules. The last two examples show reasonable agreement between results obtained with conforming and nonconforming meshes.

The examples described in the paragraph above were also repeated using the LCN method with a 4 by 3 mixed-order representation. The results of that study exhibited an overall accuracy similar to the examples discussed above.

Based on this preliminary study of nonconforming models with the LCN method, it appears feasible to use the LCN procedure with nonconforming meshes. The accuracy of the currents produced by the LCN procedure did not degrade substantially when nonconforming models were employed. In several cases there were noticeable errors in the cross-polarization currents, but those currents and the associated errors are relatively small. Since the example used for this investigation was an electrically-small plate, the presence of the nearby edge singularity also tended to exaggerate the difference between current densities in plots based on different meshes. While an additional investigation of nonconforming meshes remains necessary to quantify the error involved, the preliminary results above support the idea that

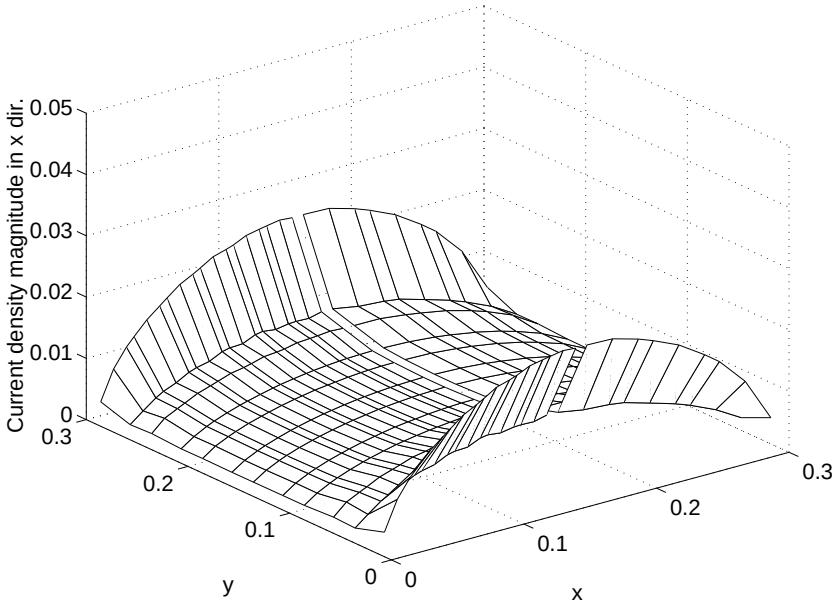

(a)

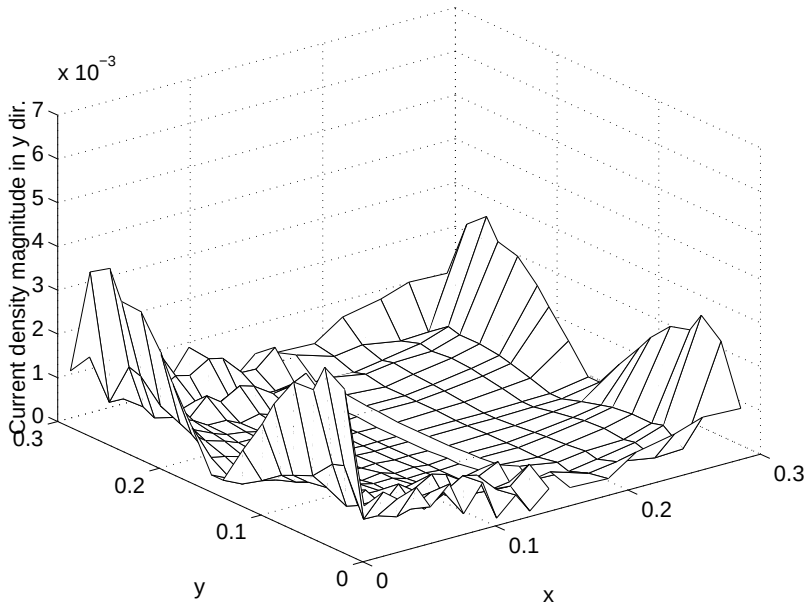

(b)

Figure 53: (a) The x-component and (b) the y-component of the surface current density on a 0.3λ x 0.3λ plate in free space obtained using LCN with 3 by 2 quadrature rules for each cell when $h_{x_1} = \lambda/40$, $h_{x_2} = \lambda/20$ and $h_{y_1} = h_{y_2} = \lambda/20$. Nonconforming case.

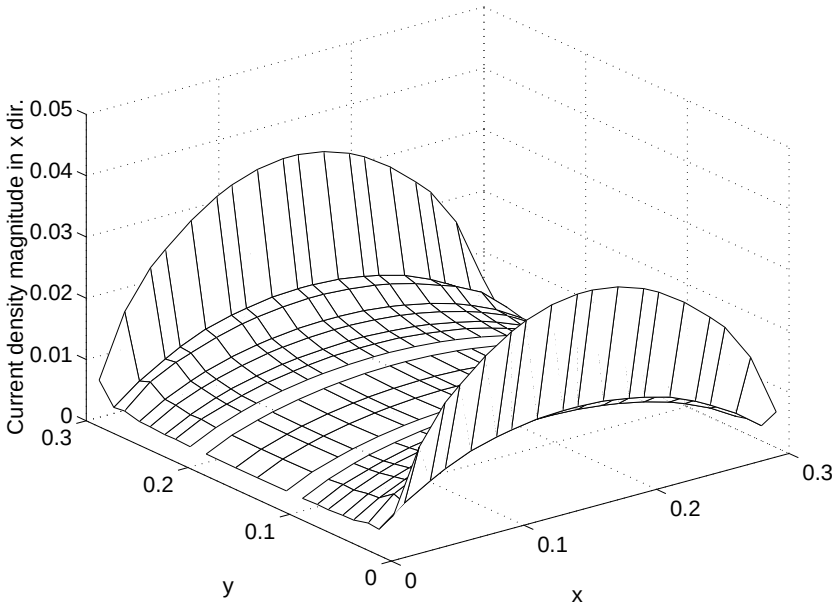

(a)

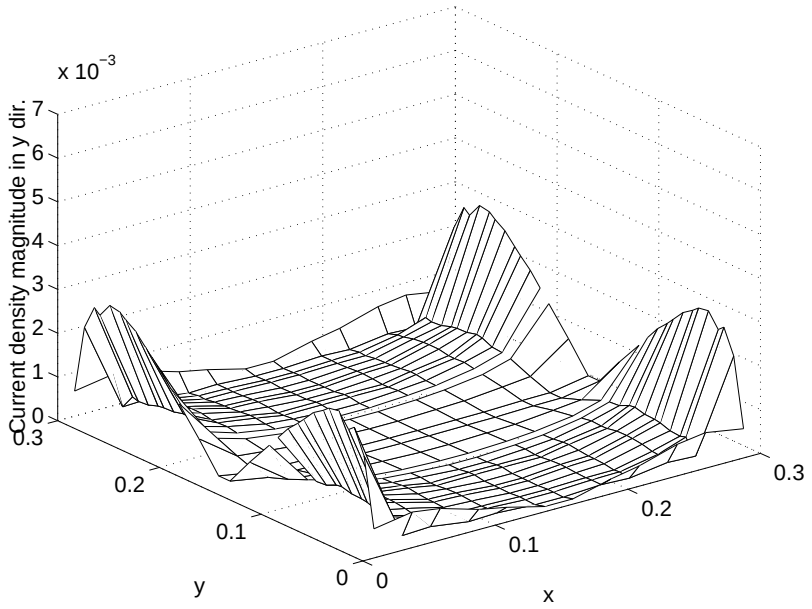

(b)

Figure 54: (a) The x-component and (b) the y-component of the surface current density on a 0.3λ x 0.3λ plate in free space obtained using LCN with 3 by 2 quadrature rules for each cell when $h_{x_1} = h_{x_2} = h_{x3} = \lambda/20$, $h_{y_1} = h_{y3} = \lambda/40$ and $h_{y_2} = \lambda/20$. Nonconforming case.

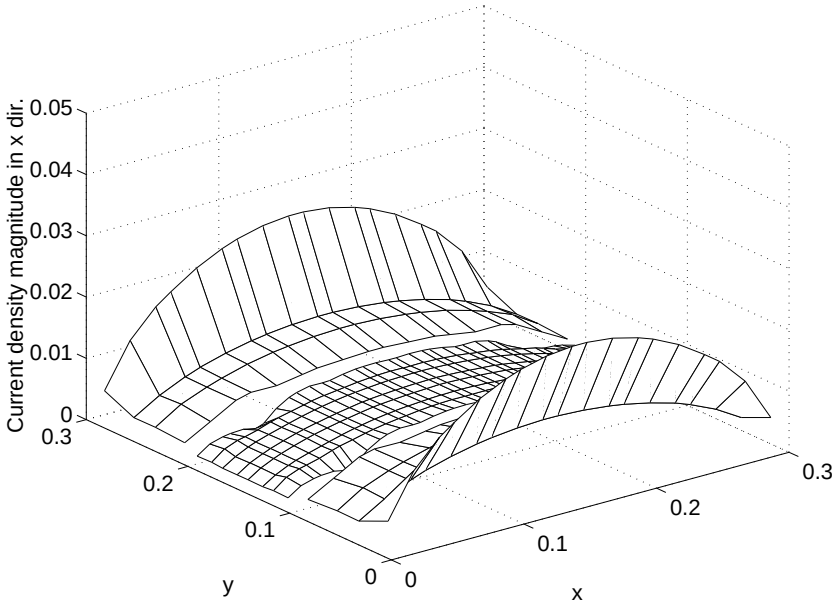

(a)

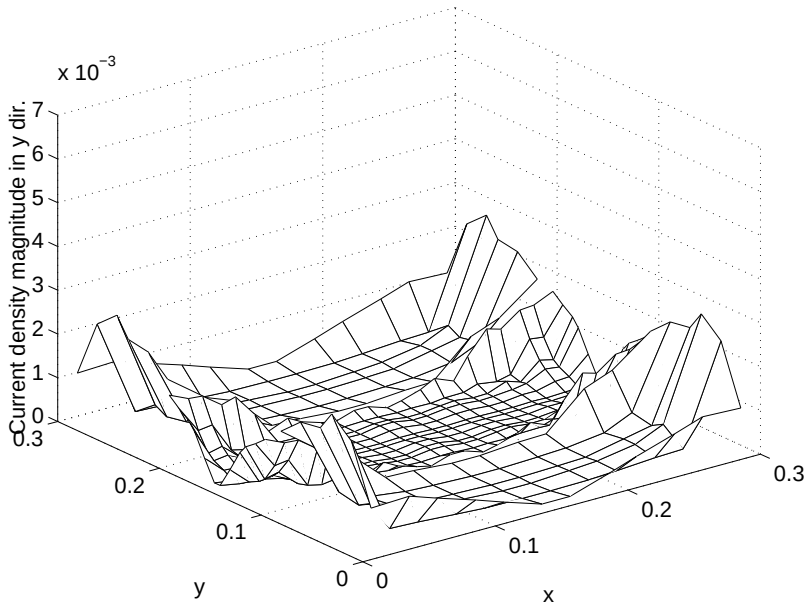

(b)

Figure 55: (a) The x-component and (b) the y-component of the surface current density on a 0.3λ x 0.3λ plate in free space obtained using LCN with 3 by 2 quadrature rules for each cell when $h_{x_1} = h_{x3} = h_{y_1} = h_{y3} = \lambda/20$ and $h_{x_2} = h_{y_2} = \lambda/40$. Nonconforming case.

the LCN procedure can be used successfully with nonconforming models.

4.8 Summary

In this chapter, the LCN procedure was used to provide numerical solutions of the MPIE for planar layered problems, such as a conducting plate in free space or a conducting plate separated from a ground plane by a dielectric substrate. Results based on polynomial-complete representations for the current density on the plates were found to be poor in accuracy, and mixed-order representations for the current were introduced. The mixed-order representations involve the use of mixed-order quadrature rules with the LCN method for widely-spaced matrix entries and the use of mixed-order polynomials as basis functions for the local correction terms. It was shown that the use of mixed-order representations substantially improves the accuracy of the numerical results.

Higher-degree mixed-order representations were also implemented, providing a range of discretizations with order 3 by 2, 4 by 3, and 5 by 4 to choose from.

Finally, a preliminary study of nonconforming meshes was initiated. The results suggest that the LCN procedure is applicable to nonconforming meshes with little degradation of accuracy.

CHAPTER V

THE LCN ANALYSIS OF STRUCTURES USING IMPRESSED-CURRENT SOURCES

An initial objective of the present research was to evaluate the LCN procedure for the electromagnetic analysis of typical structures representing interconnects and microelectronic circuits. In the previous chapter, the LCN approach was applied to simple layered media structures that were excited with uniform plane waves. To analyze circuitry, the plane wave feed must be replaced by an impressed current or voltage source feed. In Sections 5.1 and 5.2, an impressed-current feed model and the associated de-embedding and S-parameter analysis are presented. These features are similar to those used with the MoM analysis discussed in detail in Chapter 3, and their development in this chapter will be brief. Subsequent sections of this chapter present results obtained from several structures using the impressed-current source. Because of difficulties that arose in connection with this modeling, the goal of analyzing a variety of microelectronic structures using the LCN procedure has not been achieved at the present time.

5.1 Impressed-current feed model

The impressed-current model employs the electromagnetic fields of an impressed current source as the excitation function associated with the MPIE. As in the MoM analysis of Chapter 3, ports are defined by a single cell, and half-subsectional currents are impressed at each port, as shown in Figure 56. In Figure 56, a port of the circuit is illuminated by a current source of unity magnitude located in the gap between the ground plane and the microstrip transmission line. This feed model is similar to that used with the MoM approach in Chapter 3. The only difference between the methods is the type of testing functions used to impose the integral equation. The MoM approach of Chapter 3 used roof-top testing functions to average over the excitation fields, while the LCN formulation

samples the fields at discrete points. In the MoM formulation, the current density at the feed port edge was specified as unity, and not treated as an unknown. Within the LCN formulation, the samples of the current density at the quadrature nodes in the port cell are treated as unknowns.

5.2 S-parameter analysis

The calculation of S-parameters within the LCN method is similar to the S-parameter calculation used with the MoM approach. S-parameters are obtained using the de-embedding process explained in Section 3.4. Here some details will be given which are related to the LCN approach.

For a two-port network, the following procedure is applied to calculate the S-parameters. As in the MoM analysis, the port transmission lines are chosen to be at least 1 to 2 wavelengths in length to isolate the near-field effects of the source (evanescent and higher-order modes). One of the ports is excited and the current densities on the conductors, including the port transmission lines, are obtained. Suppose the port transmission line under consideration is aligned with x. The nature of the MoM formulation is such that the roof-top basis functions only support an $x-$component of the current density along a line parallel to x. The mixed-order LCN representations involve both $x-$ and $y-$components of the current densities on each cell along the port transmission lines, with at least a linear transverse behavior for a 3 by 2 quadrature scheme. With LCN, the y-component is ignored for a de-imbedding analysis of a line parallel to x. For a 3 by 2 LCN representation, the $y-$dependence of the $x-$component of the current density is averaged prior to analysis. The GPOF method is used to approximate the current distribution on each port transmission line by a sum of complex exponentials as

$$I(x) \approx \sum_{i=1}^{N} I_i e^{(\alpha_i + j\beta_i)x} \tag{106}$$

where α_i and β_i correspond to the attenuation and propagation constants of the i^{th} mode of the current, respectively, and x is the distance along the port transmission line. The forward and reflected waves are obtained in a manner identical to the procedure described in Chapter 3.

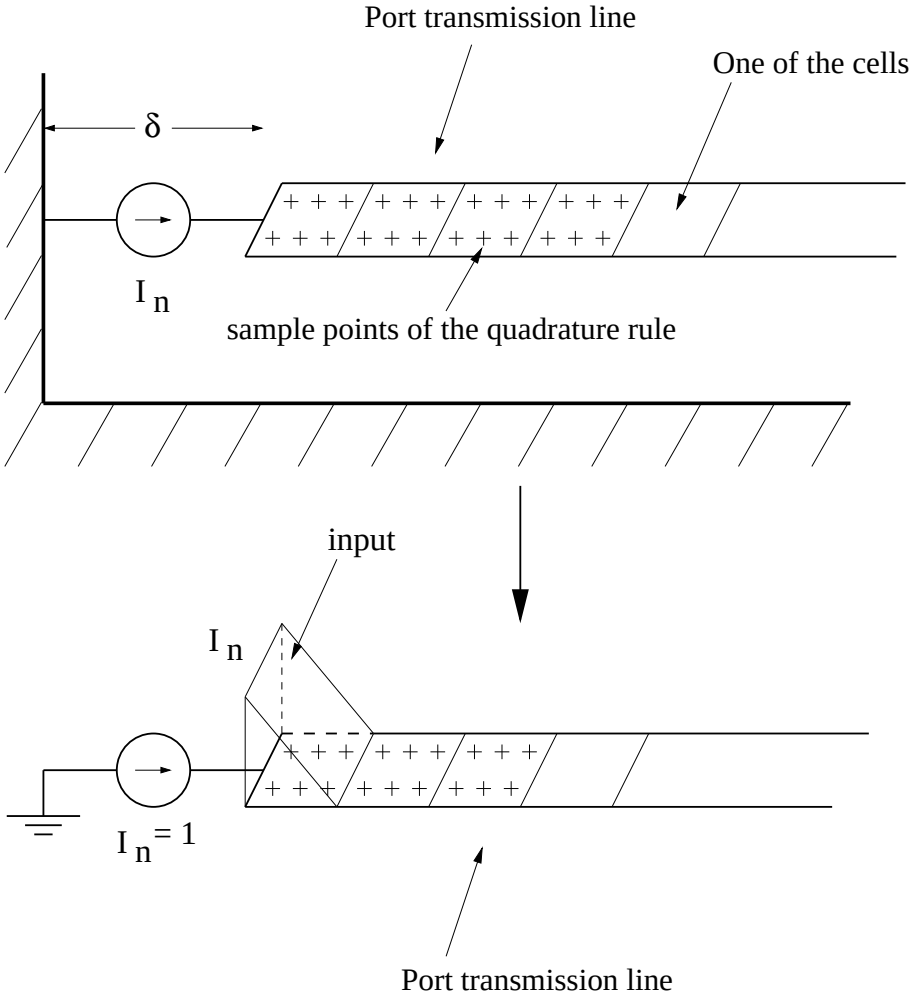

Figure 56: Impressed-current source model for port n (used in the LCN approach)

The LCN representation requires a relatively large number of unknowns to model a port transmission line (12 per cell for a 3 by 2 representation), compared with an average of one per cell for MoM using rooftop basis functions. To reduce the number of unknowns, it is possible with the LCN approach to drop the $y-$component of the current density on the port transmission line. This possibility will be investigated in Section 5.5. An alternative possibility, using a special representation for port transmission lines, is proposed and implemented in Chapter 6.

5.3 Example: Square conducting plate over a grounded substrate

As a preliminary test case for the LCN implementation, consider a 10.0 cm x 10.0 cm plate over a grounded substrate illuminated by an impressed-current source as shown in Figure 4. The current source is a half roof-top function with unity magnitude. The dielectric constant of the substrate, ϵ_r, is 2.2. The substrate thickness, h, is 1 cm. The plate is placed on top of the substrate and the upper medium is free space. For this example, the dimensions of each cell along the x and y axis, h_x and h_y, are both set to 1 cm. Figures 57a and 57b show the magnitude of the $x-$ and $y-$components, respectively, of the surface current densities on the plate obtained using LCN with 3 by 2 quadrature rules at 3 GHz. For validation purposes, the same structure is analyzed using the MoM approach for comparison. In the MoM application, the cell dimensions, h_x and h_y, are both set to 0.5 cm. Figures 58a and 58b show the magnitude of the $x-$ and $y-$components, respectively, of the surface current densities at 3 GHz obtained using MoM. Figure 59 depicts the $x-$component of the surface current density on the plate along the cuts at $x = 5$ cm and $y = 5$ cm, due to impressed-current source at 3 GHz. Figure 60 shows the $y-$component of the surface current density on the plate along cuts at $x = 5$ cm and $y = 5$ cm, also at 3 GHz. These figures show reasonable agreement between the LCN and MoM approaches.

5.4 Example: Microstrip Line

As a second example employing the impressed current feed, consider a microstrip line with the same medium parameters as the previous example. The example is a 1.0 cm x 10.0 cm

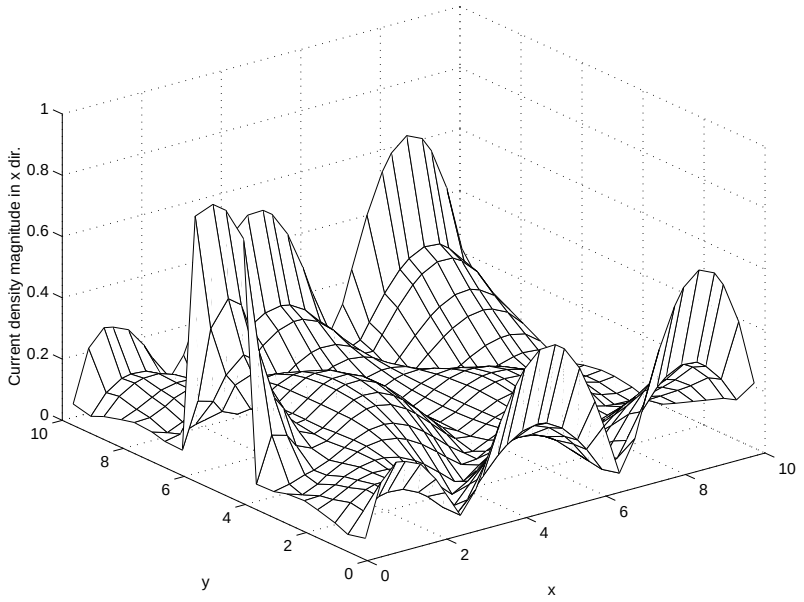

(a)

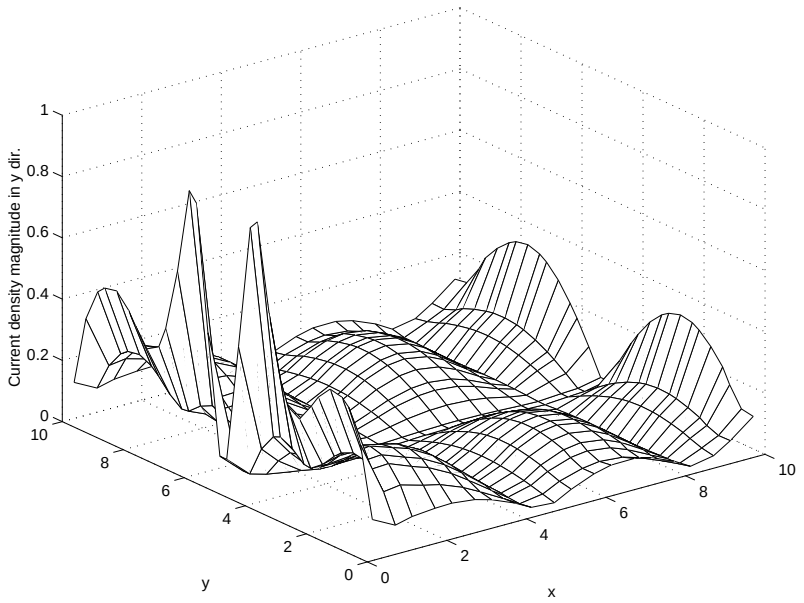

(b)

Figure 57: (a) The co-pol and (b) the cross-pol components of the surface current density on a 10.0 cm x 10.0 cm plate over a grounded substrate excited by an impressed-current source. LCN result obtained with 3 by 2 quadrature rules at 3 GHz.

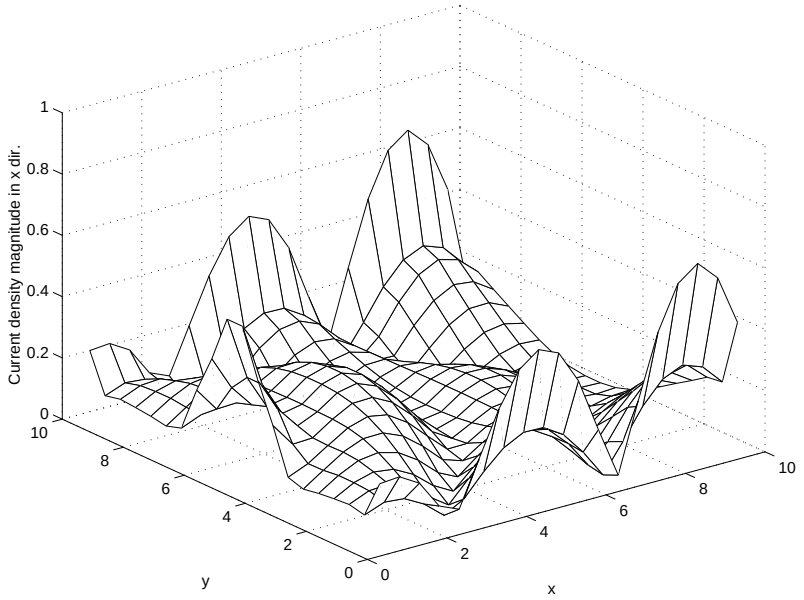

(a)

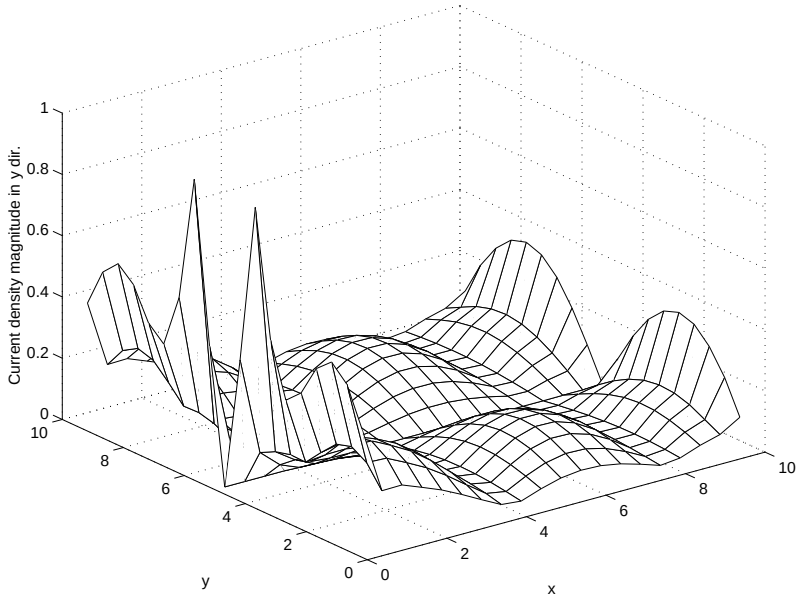

(a)

Figure 58: (a) The co-pol and (b) the cross-pol components of the surface current density on a 10.0 cm x 10.0 cm plate over a grounded substrate excited by an impressed-current source. MoM result obtained at 3 GHz.

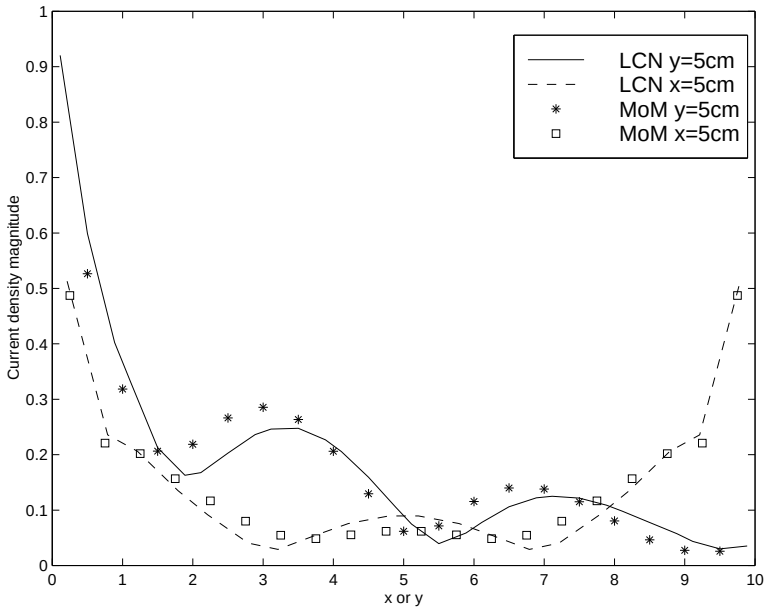

Figure 59: The co-pol component of the surface current density on a 10.0 cm x 10.0 cm plate over a grounded substrate along the cuts $x = 5$ cm and $y = 5$ cm. 3 GHz result.

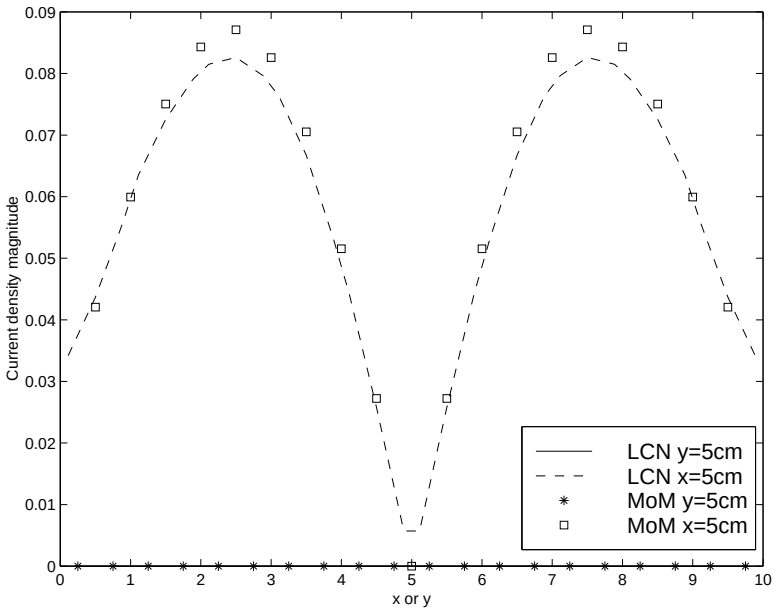

Figure 60: The cross-pol component of the surface current density on a 10.0 cm x 10.0 cm plate over a grounded substrate along the cuts $x = 5$ cm and $y = 5$ cm. 3 GHz result.

strip over a grounded substrate. The line is fed at one end using the impressed current source, and is open-circuited at the other end. For the LCN analysis, the dimensions of each cell in x and y, h_x and h_y, are set to 0.5 cm and 1 cm, respectively. Figures 61a and 61b show the magnitude and phase, respectively, of the $x-$component of the surface current density on the line at 3 GHz obtained using LCN with 3 by 2 quadrature rules. Figure 62 is the magnitude of the $y-$component of the surface current density on the plate obtained using LCN. For comparison, results are also obtained using the MoM approach, with cells of dimension h_x and h_y equal to 0.125 cm and 0.5 cm, respectively. Figures 63a and 63b show the magnitude and the phase of the $x-$component of the surface current density on the microstrip line obtained at 3 GHz using the MoM. Although there are roof-top basis functions representing the $y-$component of the surface current density for this example, they are centered in the middle of the strip and have negligible magnitudes due to the symmetry. Therefore, the $y-$component is not shown. To compare the methods, the magnitude and the phase of the $x-$component of the surface current densities on the microstrip line are plotted as shown in Figure 64a and 64b, respectively.

There is a relatively large difference between the results of the LCN approach and the MoM procedure in this case. In general, this difference in both magnitude and phase is much greater than that observed with the previous example, which involved the 10.0 cm x 10.0 cm plate over the same medium. The plate example employed larger cell dimensions for both the LCN and MoM analysis. Both the LCN and MoM representations for the microstrip line are such that the transverse dependence of the dominant component of the current density is actually constant. Additional study of the microstrip line using smaller cell dimensions did not lead to an obvious explanation for these results.

It should be noted that the LCN representation for the $y-$component of the surface current density yields a nonzero result, in contrast to the MoM procedure (which did not support a $y-$component due to the nature of the basis functions and the specific symmetry arising in this MoM model). An obvious question is what happens if the $y-$component of the surface current density is dropped from the LCN representation? Figures 65a and 65b show the magnitude and the phase of the $x-$component of the surface current density on the

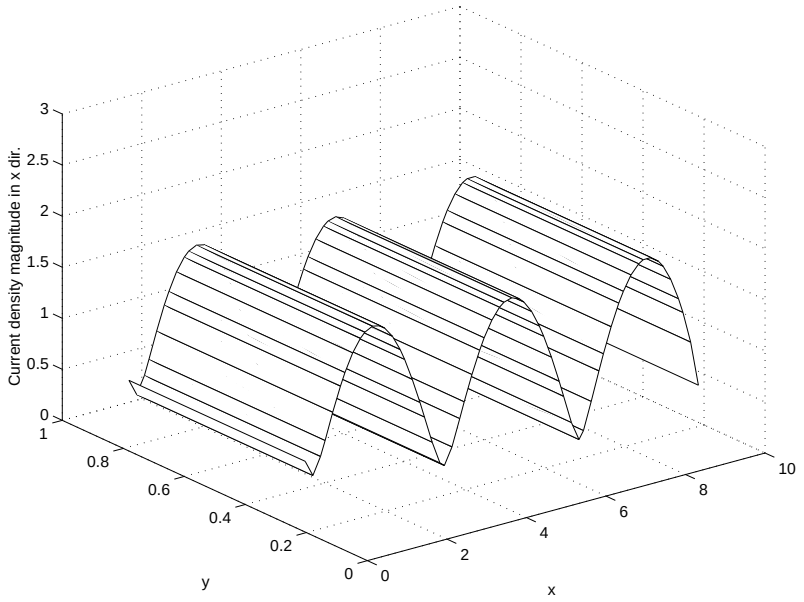

(a)

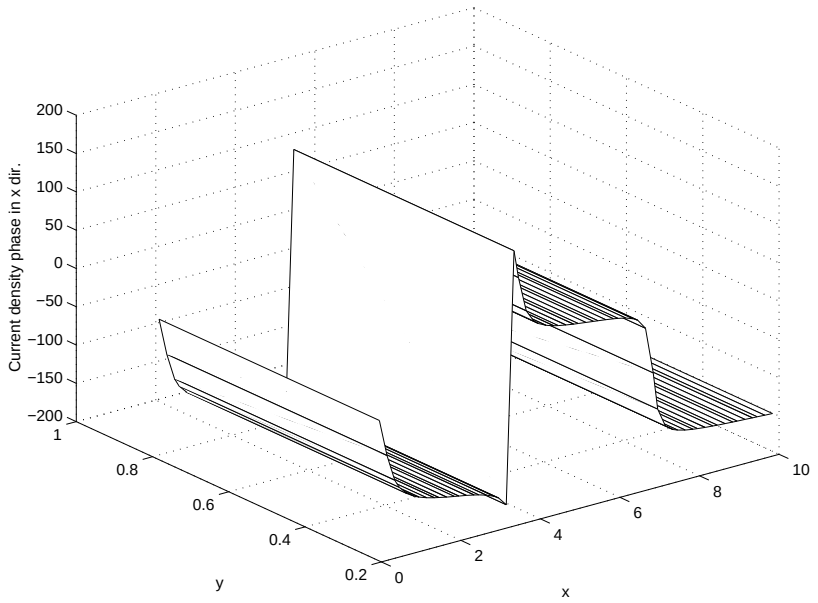

(b)

Figure 61: (a) The magnitude and (b) the phase of the co-pol component of the surface current density on a 1.0 cm x 10.0 cm microstrip line at 3 GHz. An impressed-current source is used with the LCN and 3 by 2 quadrature rules.

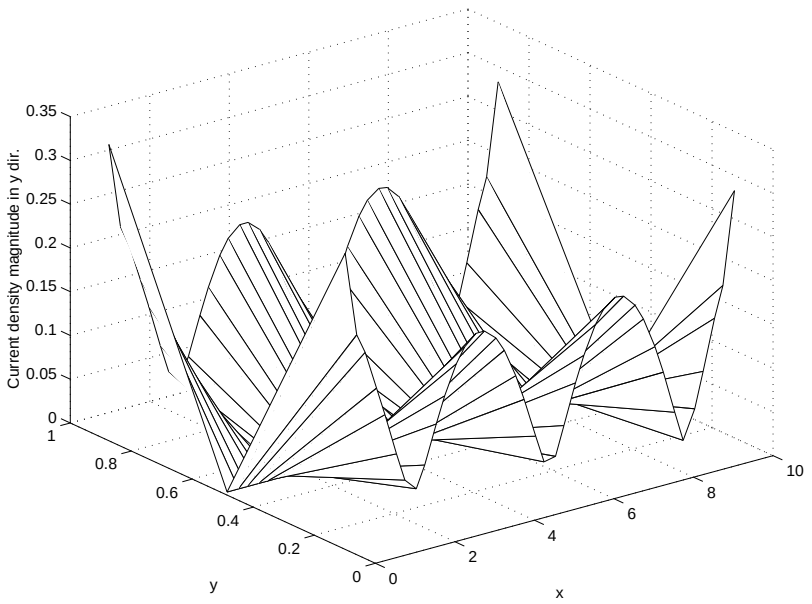

Figure 62: The magnitude of the cross-pol component of the surface current density on a 1.0 cm x 10.0 cm microstrip line at 3 GHz. An impressed-current source is used with the LCN and 3 by 2 quadrature rules.

microstrip line at 3 GHz obtained from the LCN with 3 by 2 quadrature rules when there is no $y-$component of current included in the formulations. To facilitate a comparison, the magnitude and the phase of the $x-$component of the surface current densities on the microstrip line are plotted as shown in Figures 66a and 66b. Under these conditions, there is a good agreement between the LCN and MoM results. Figure 66 suggests that the large difference is tied to the presence or absence of the $y-$component of current on the microstrip line. Since the cross-pol component of current should be relatively small, and is in fact an order of magnitude smaller than the co-pol current, it seems unlikely that it would cause large differences in the co-pol (x) component.

To ensure that the impressed-current source code was not the cause of the problem, the 1.0 cm x 10.0 cm microstrip line was analyzed using a normally-incident uniform plane wave excitation. As in the preceding example, the dielectric constant of the substrate, ϵ_r, is 2.2, and the substrate thickness, h, is 1 cm. The strip is placed on top of the substrate and the upper medium is free space. The dimensions of the cells, h_x and h_y, are 0.5 cm and 1 cm,

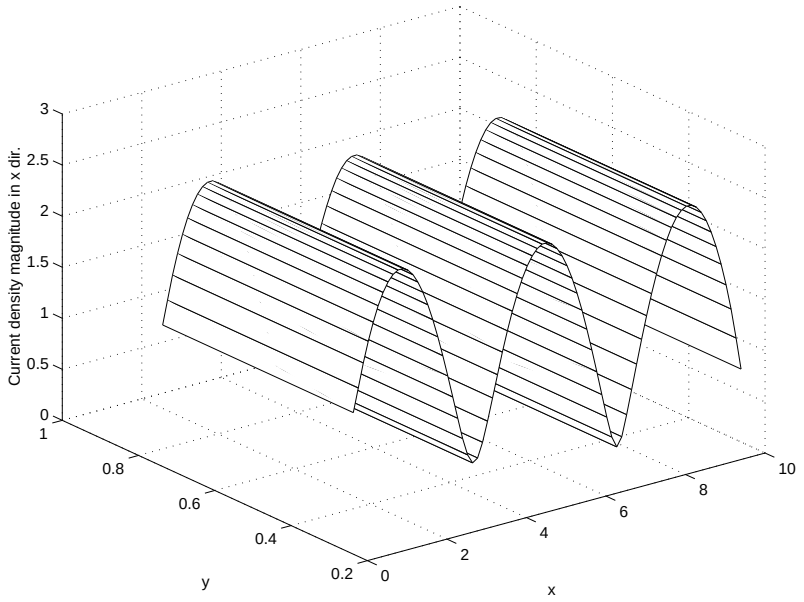

(a)

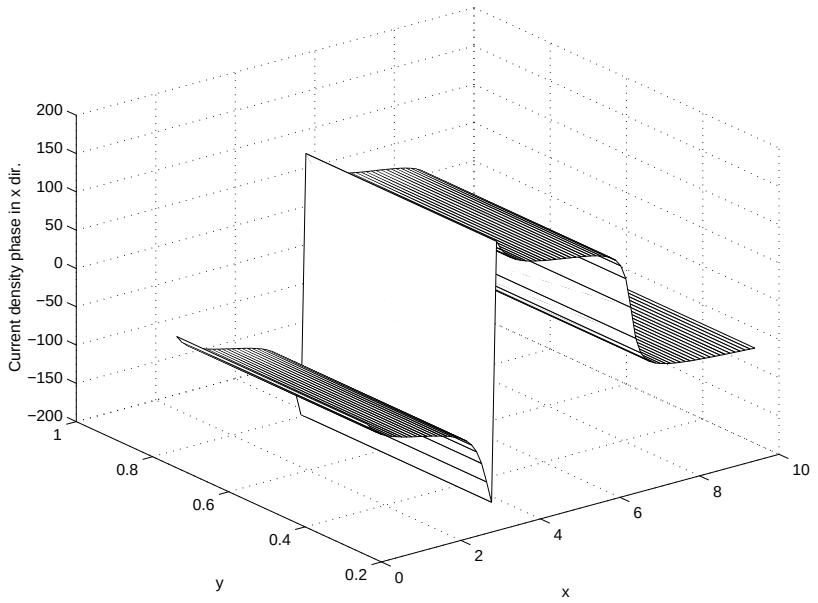

(b)

Figure 63: (a) The magnitude and (b) the phase of the co-pol component of the surface current density on a 1.0 cm x 10.0 cm plate over a grounded substrate illuminated by impressed-current source obtained using MoM at 3 GHz

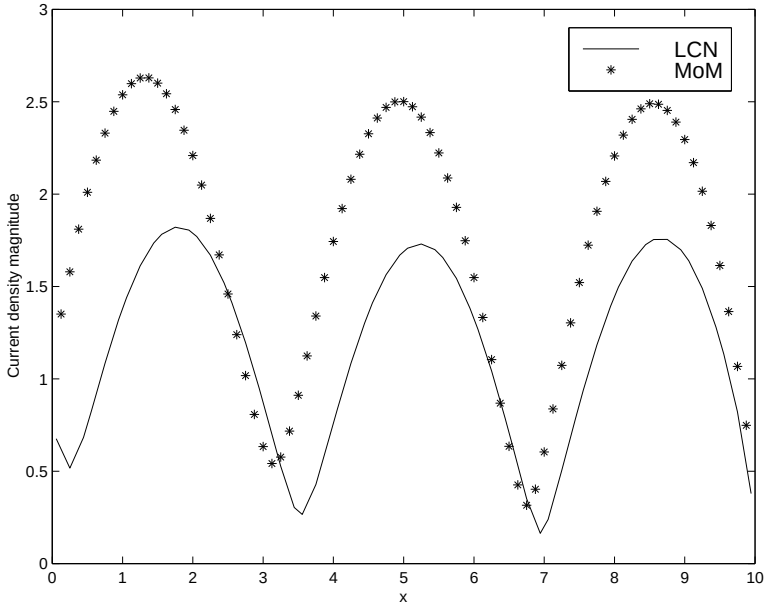

(a)

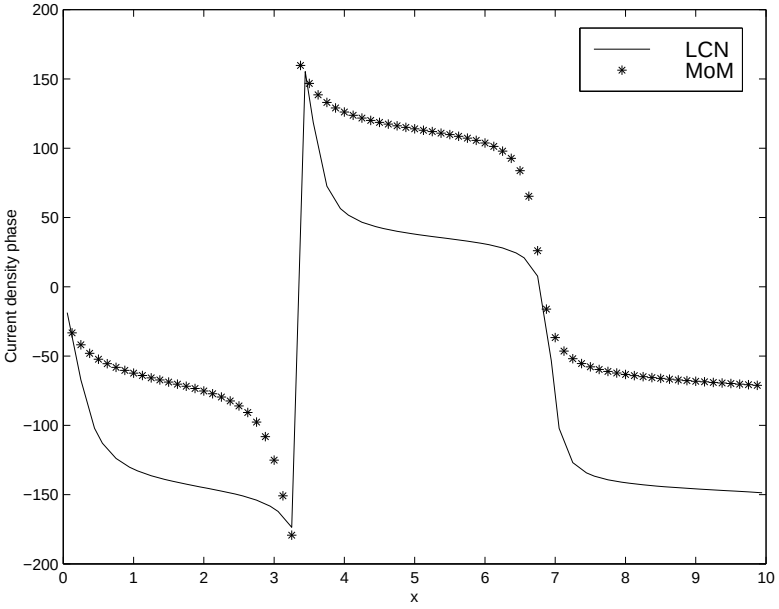

(b)

Figure 64: (a) The magnitude and (b) the phase of the co-pol component of the surface current density on a 1.0 cm x 10.0 cm plate over a grounded substrate illuminated by impressed-current source when $y = 0.5$ cm at 3 GHz

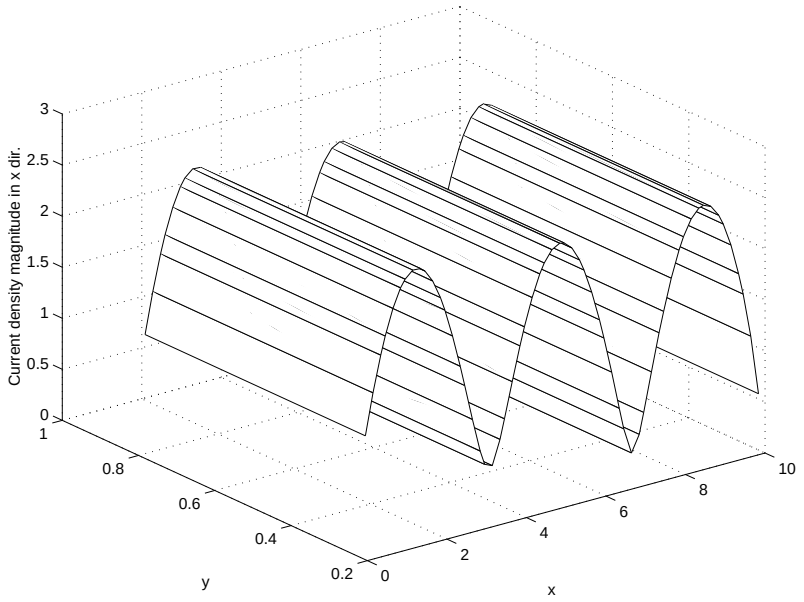

(a)

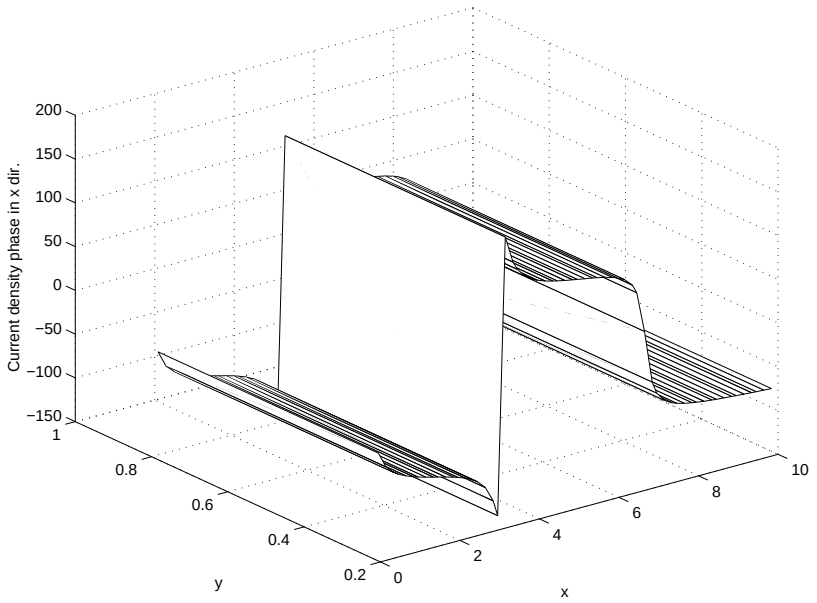

(b)

Figure 65: (a) The magnitude and (b) the phase of the co-pol component of the surface current density on a 1.0 cm x 10.0 cm microstrip line at 3 GHz. Impressed-current source excitation with 3 by 2 LCN, using only the co-pol currents.

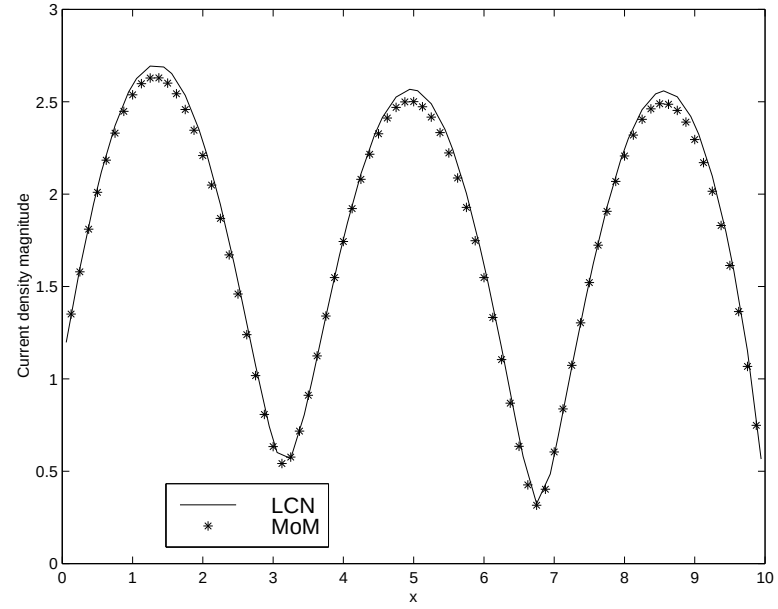

(a)

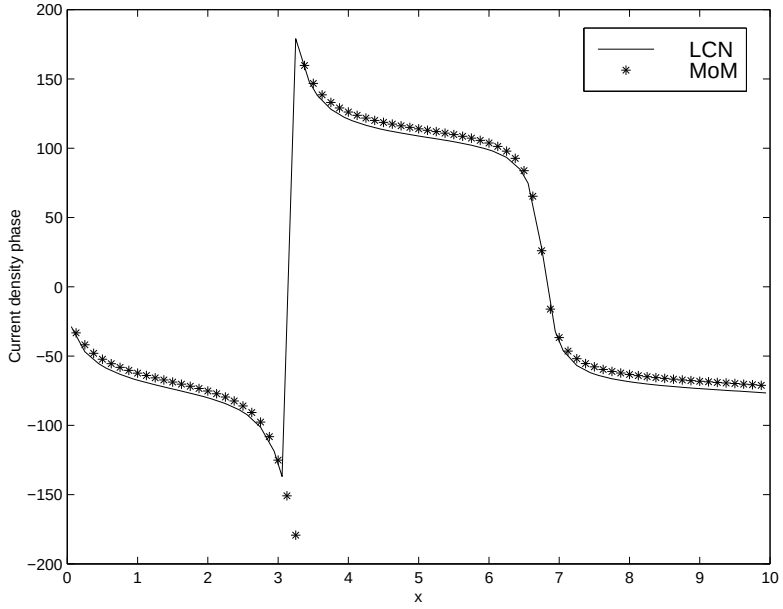

(b)

Figure 66: (a) The magnitude and (b) the phase of the co-pol component of the surface current density at 3 GHz on a 1.0 cm x 10.0 cm microstrip line. Results are plotted along the centerline $y = 0.5$ cm.

respectively. Figures 67a and 67b show the magnitude and phase of the $x-$component of the surface current density on the microstrip line obtained at 3 GHz using the LCN with 3 by 2 quadrature rules. Figure 68 shows the $y-$component of the surface current density for the same example. For additional information, Figures 69a and 69b show the real and imaginary parts of the surface charge density along the microstrip line, obtained using the LCN approach. For validation, the LCN results are compared with the results of the MoM formulation. In the MoM application, the cell dimensions h_x and h_y are set to 0.125 cm and 0.5 cm, respectively. Figures 70a and 70b show the magnitude and the phase of the $x-$component of the surface current density on the microstrip line obtained using MoM at 3 GHz. Figures 71a and 71b show the real and imaginary parts of the charge density on the plate obtained using MoM. To facilitate a comparison, the $x-$component of current at $y = 0.5$ cm is plotted in Figure 72. These figures clearly show that the results of the LCN approach and the MoM approach do not agree for plane wave illumination, and therefore confirm that the difficulty does not lie with the impressed current feed.

This result is unexpected because the 10.0 cm x 10.0 cm plate over the same medium was analyzed in Section 4.6 and the figures show agreement between the LCN and MoM approaches for that problem.

Another issue to address is whether a finer mesh will affect the accuracy of the solutions. For the following example, the cell sizes h_x and h_y are both set to 0.5 cm. Figures 73a and 73b show the magnitude and the phase of the $x-$component of the surface current density on the microstrip line obtained using LCN with 3 by 2 quadrature rules for each cell, respectively at 3 GHz. Figures 74 presents the magnitude and the phase of the $y-$component of the surface current density on the line obtained at 3 GHz using LCN. Figures 75a and 75b give the real and imaginary parts of the charge density on the plate obtained using LCN. These figures demonstrate that using smaller cell sizes doesn't fundamentally change the results from the LCN method. One may also apply smaller cell sizes to the MoM approach. Suppose h_x and h_y are both set to 0.125 cm. Figures 76a and 76b present the magnitude and phase of the $x-$component of the surface current density on the line obtained using MoM at 3 GHz. Figures 77 shows the magnitude of the $y-$component of the surface current

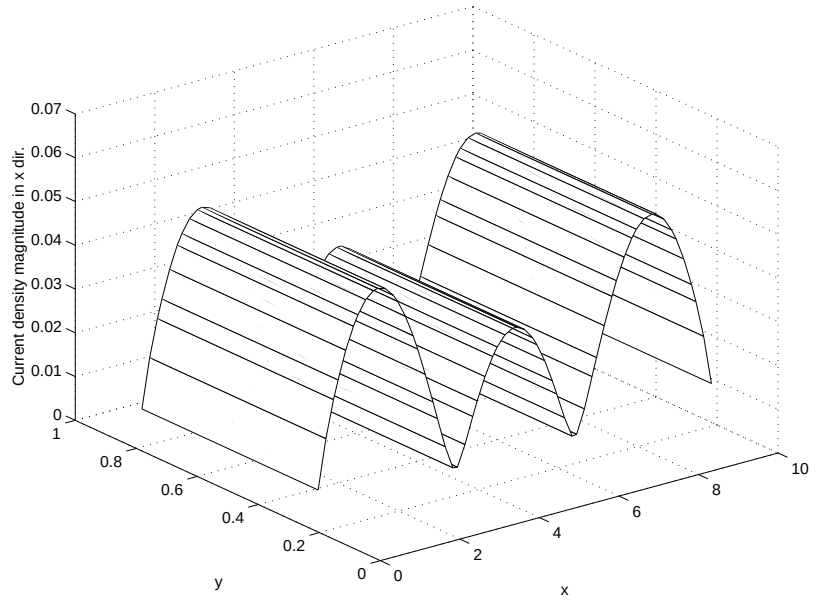

(a)

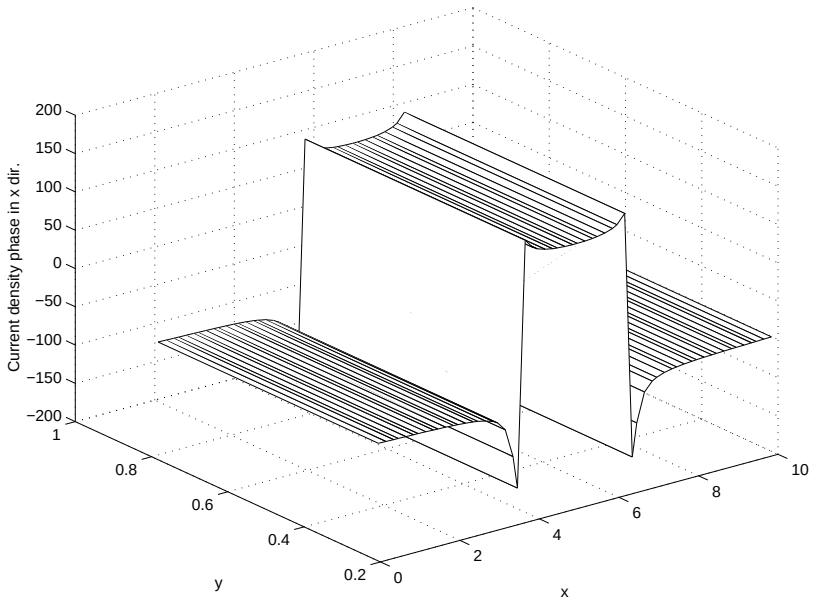

(b)

Figure 67: (a) The magnitude and (b) the phase of the co-pol component of the surface current density on a 1.0 cm x 10.0 cm microstrip line illuminated by a normally-incident uniform plane wave at 3 GHz. 3 by 2 LCN result.

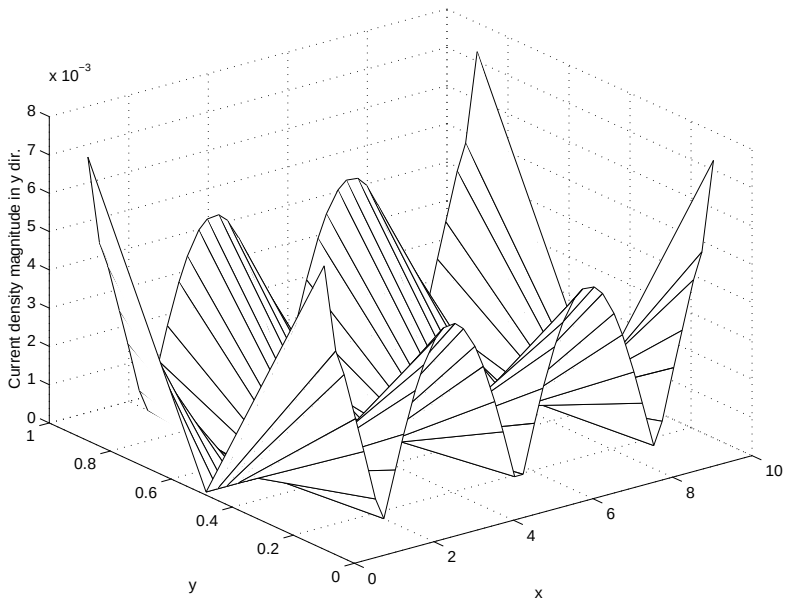

Figure 68: The magnitude of the cross-pol component of the surface current density on a 1.0 cm x 10.0 cm microstrip line illuminated by a normally-incident uniform plane wave at 3 GHz. 3 by 2 LCN result.

density on the line obtained using MoM, respectively at 3 GHz. Figures 78a and 78b give the real and imaginary parts of the charge density on the plate obtained using the MoM. From these results, it appears that the previous cell sizes produce similar results and there is no need to use smaller sizes.

As a final step in the comparison, the LCN procedure is considered without a $y-$component of the current density on the microstrip line. For this comparison, h_x and h_y are set to 0.5 cm and 1 cm, respectively. Figures 79a and 79b show the magnitude and the phase of the $x-$component of the surface current density on the line at 3 GHz obtained using LCN with 3 by 2 quadrature rules. Figures 80a and 80b give the real and imaginary parts of the charge density on the plate obtained using LCN. To compare the MoM result with the LCN result (when there is no $y-$component of the surface current density on the line), the magnitude and the phase of the $x-$component of the surface current density are plotted at the $y = 0.5$ cm cut as shown in Figures 81a and 81b. As in previous cases, there is good agreement between the results when the $y-$component of the current density is suppressed.

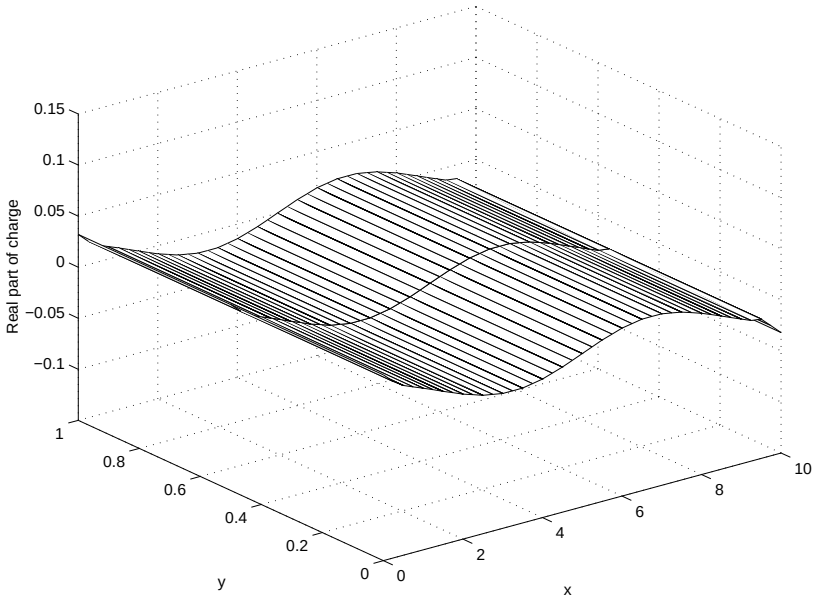

(a)

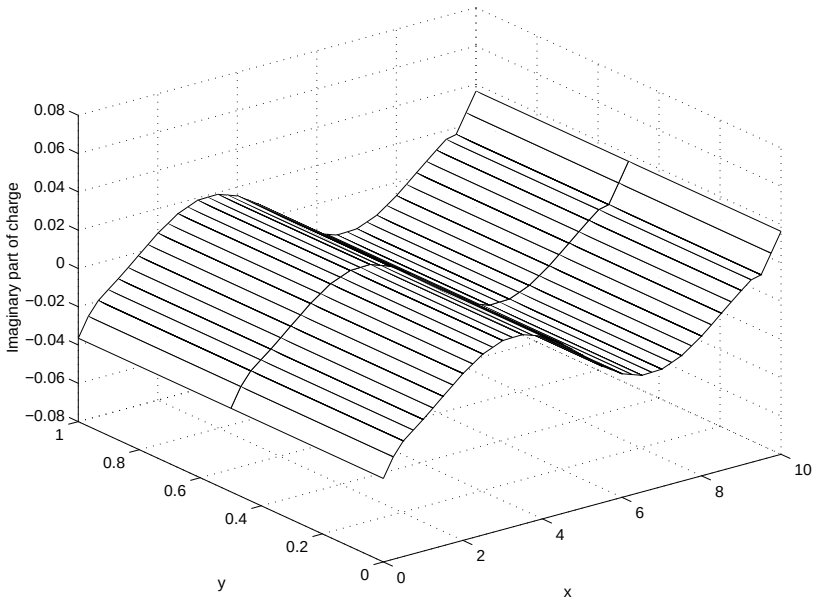

(b)

Figure 69: (a) The real and (b) the imaginary parts of the charge density on a 1.0 cm x 10.0 cm microstrip line illuminated by a normally-incident uniform plane wave at 3 GHz. 3 by 2 LCN result.

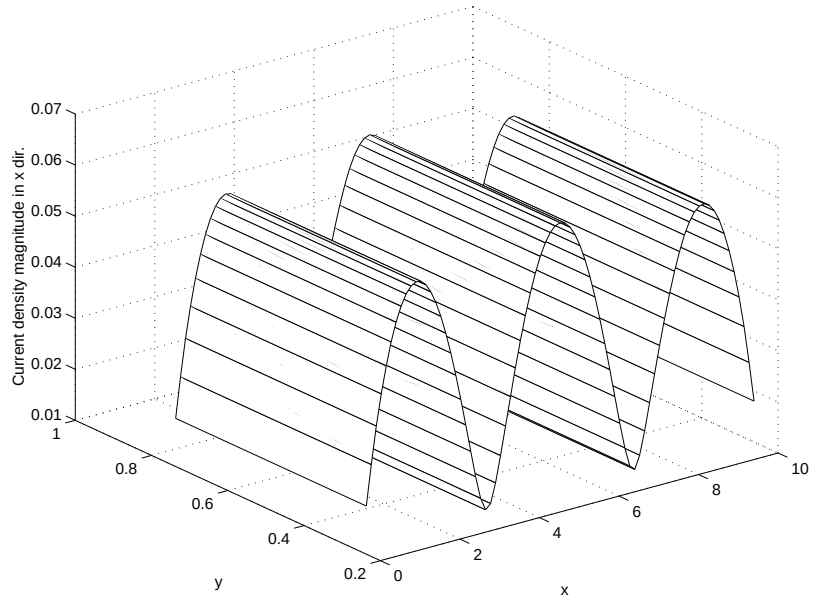

(a)

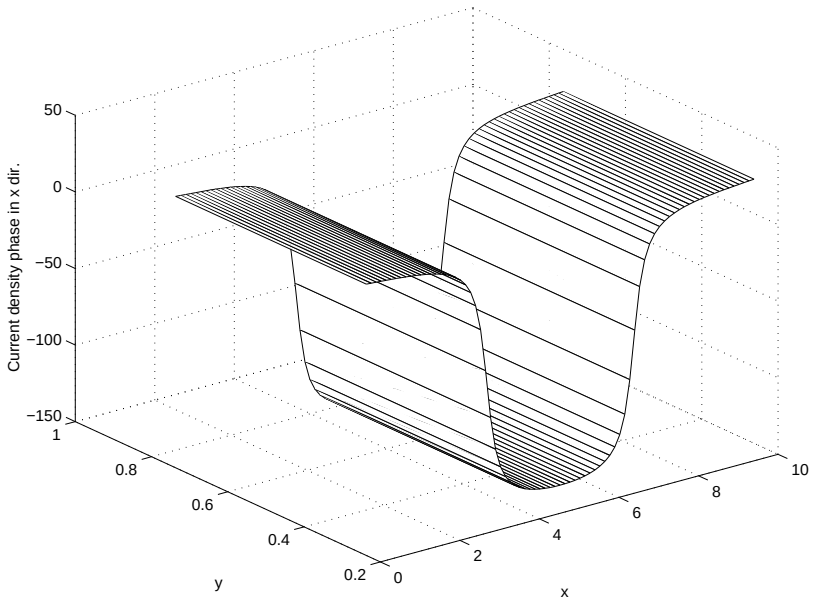

(b)

Figure 70: (a)The magnitude and (b) the phase of the co-pol component of the surface current density on a 1.0 cm x 10.0 cm microstrip line illuminated by a normally-incident uniform plane wave obtained using the MoM at 3 GHz.

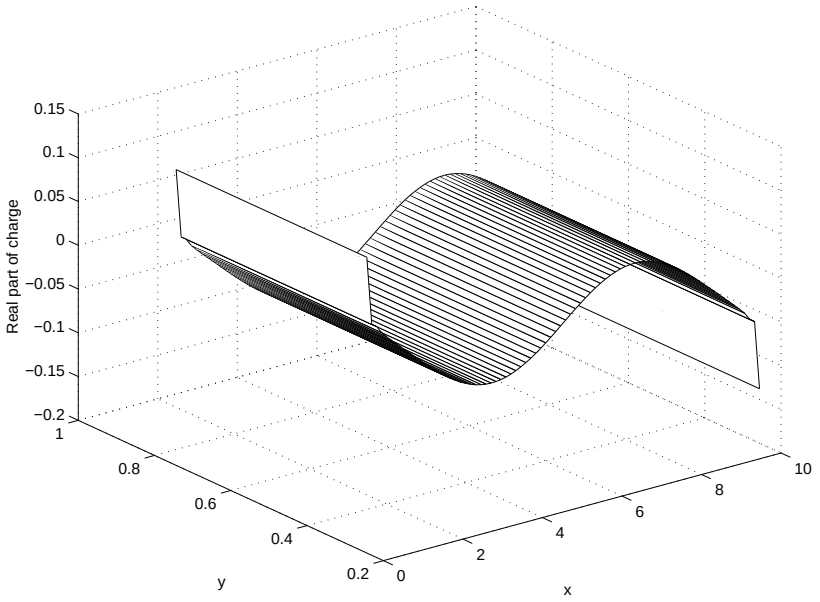

(a)

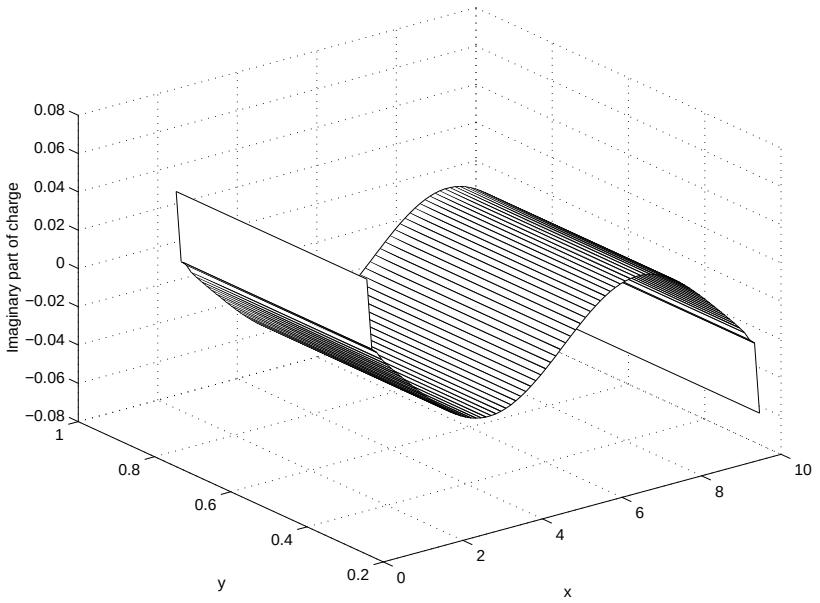

(b)

Figure 71: (a) The real and (b) the imaginary parts of the charge density on a 1.0 cm x 10.0 cm microstrip line illuminated by a normally-incident uniform plane wave obtained using the MoM at 3 GHz.

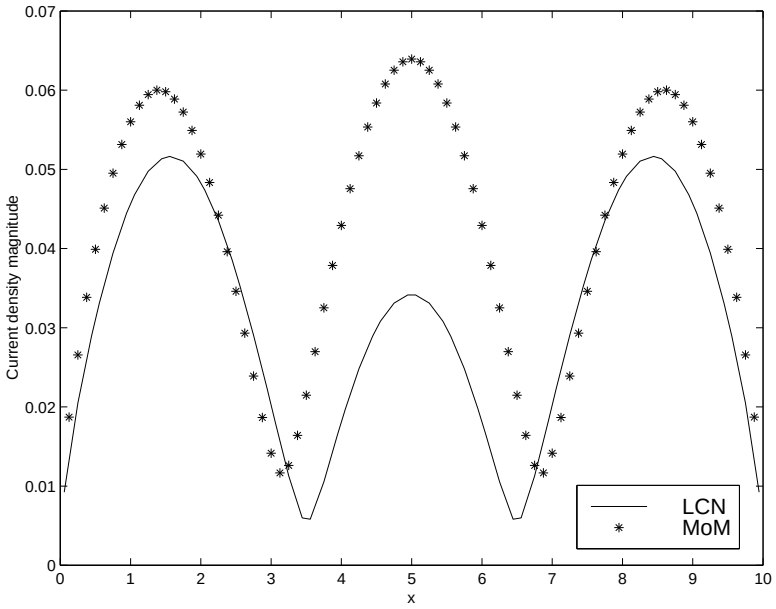

Figure 72: The magnitude of the co-pol component of the surface current density at 3 GHz on a 1.0 cm x 10.0 cm microstrip line illuminated by a normally-incident uniform plane wave when $y = 0.5$ cm.

There is clearly a difference in the results of the MoM and LCN procedures for the example of the microstrip line. The previous results suggest that this difference can be mitigated by omitting the $y-$component of current along an $x-$directed line from the LCN representation. This requirement is rather unusual, since the LCN procedure should adjust the coefficients to zero (or some very small values) if the cross-pol currents are not needed in the solution.

An alternative explanation has to do with the expected behavior of the current density along a microstrip line. In fact, the currents on any structure with a metal edge exhibit an edge singularity. This behavior is evident in the previous plots of the current density on plates. However, a narrow microstrip line may be more susceptible to erratic results due to improperly representing the current near the edge, since the entire structure is electrically close to the edges. A slight error in the coupling between the co-pol and cross-pol currents could lead to gross errors in the overall result, if the errors occur at a location where the

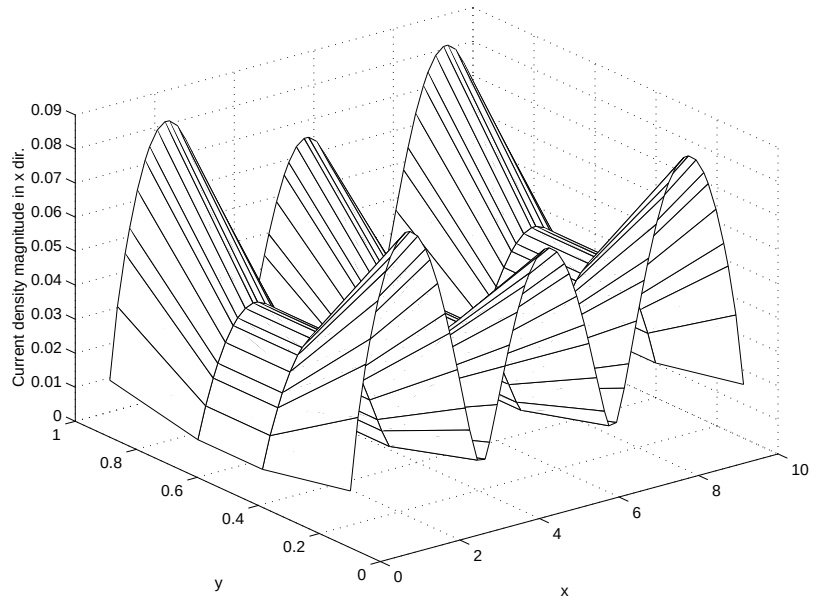

(a)

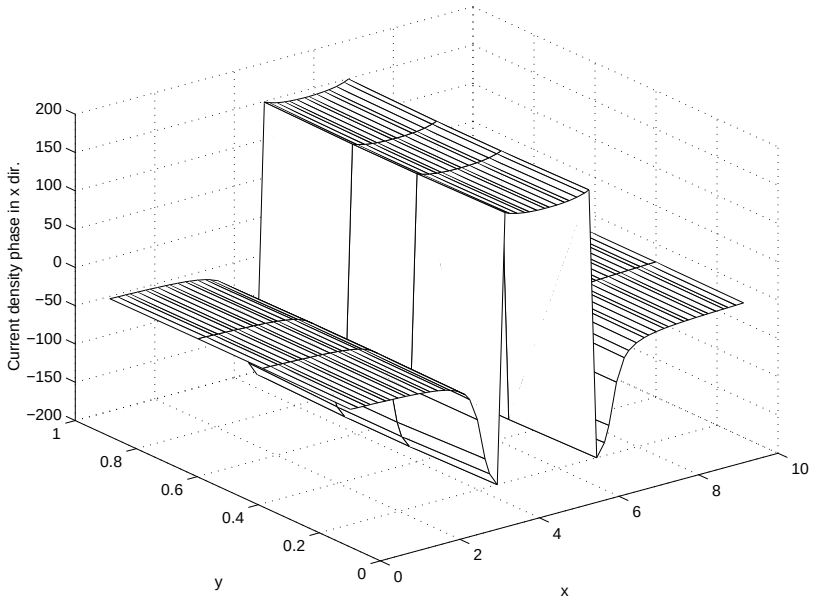

(b)

Figure 73: (a) The magnitude and (b) the phase of the co-pol component of the surface current density on a 1.0 cm x 10.0 cm microstrip line illuminated by a normally-incident uniform plane wave. The LCN result with 3 by 2 quadrature rules at 3 GHz is obtained using a finer mesh than the previous figures.

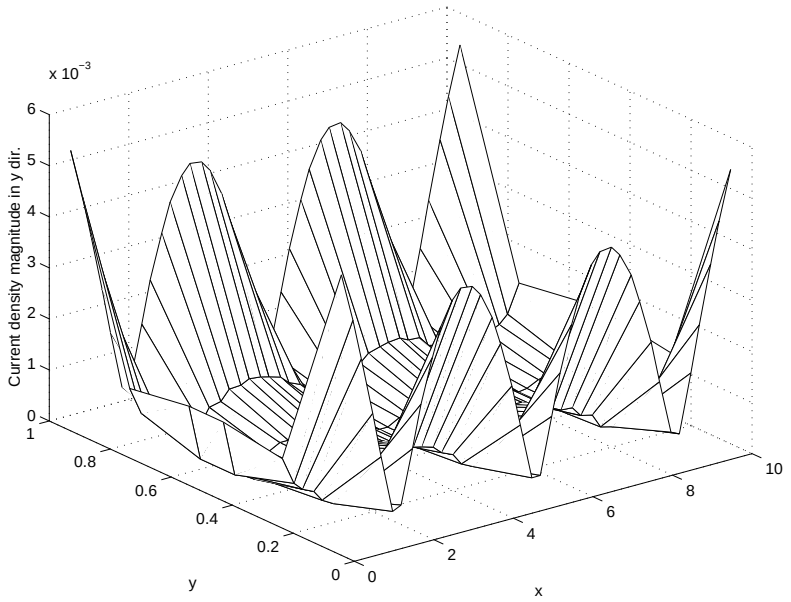

Figure 74: The magnitude of the cross-pol component of the surface current density on a 1.0 cm x 10.0 cm microstrip line illuminated by a normally-incident uniform plane wave. The LCN result at 3 GHz is obtained using 3 by 2 quadrature rules.

co-pol currents are large (such as the edge).

In fact, there has been no attempt made in this investigation to properly model edge singularities, with either the MoM or LCN formulations. Proper modeling of the singularity within the MoM analysis would require a special basis function that explicitly incorporates the singular behavior. With the LCN formulation, quadrature rules of the Gauss-Jacobi type can be incorporated, in conjunction with the use of Jacobi polynomials adjusted for the proper singularity within the local correction calculations. These approaches were avoided in the present investigation as they have been investigated previously by others [18] and they complicate the implementation of the specific approach employed for the matrix entry calculations. Chapter 6 will summarize some additional steps that were considered in an attempt to understand the difficulty outlined above.

5.5 Example: Microstrip Single-Stub Filter

As an additional example, consider a microstrip single-stub filter as shown in Figure 14. The bottom layer is a ground plane. The dielectric constant of the substrate, ϵ_r, is 2.33. The

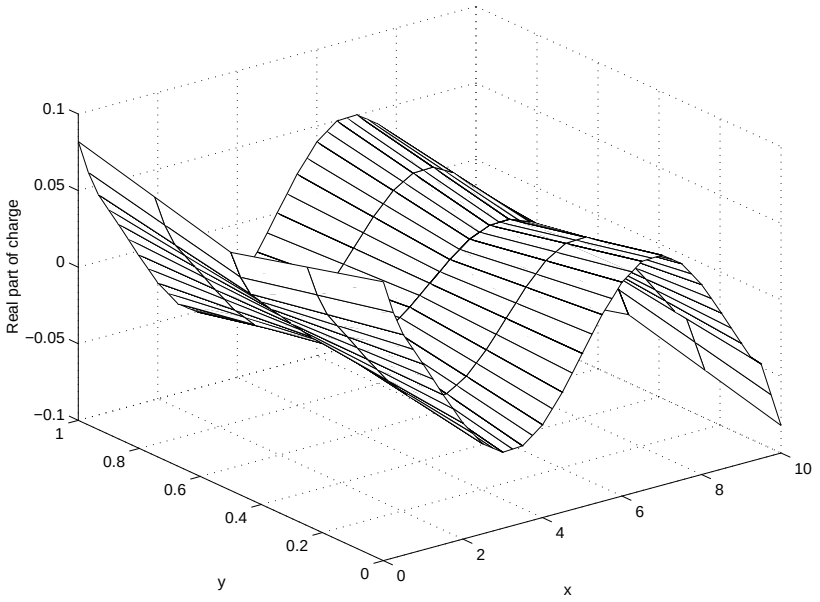

(a)

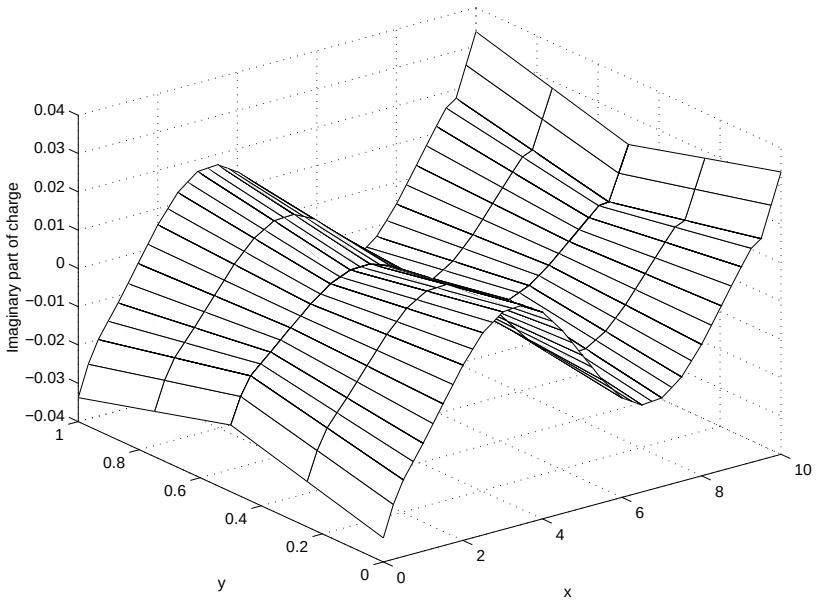

(b)

Figure 75: (a) The real and (b) the imaginary parts of the charge density on a 1.0 cm x 10.0 cm line illuminated by a normally-incident uniform plane wave. The LCN result is obtained at 3 GHz with 3 by 2 quadrature rules.

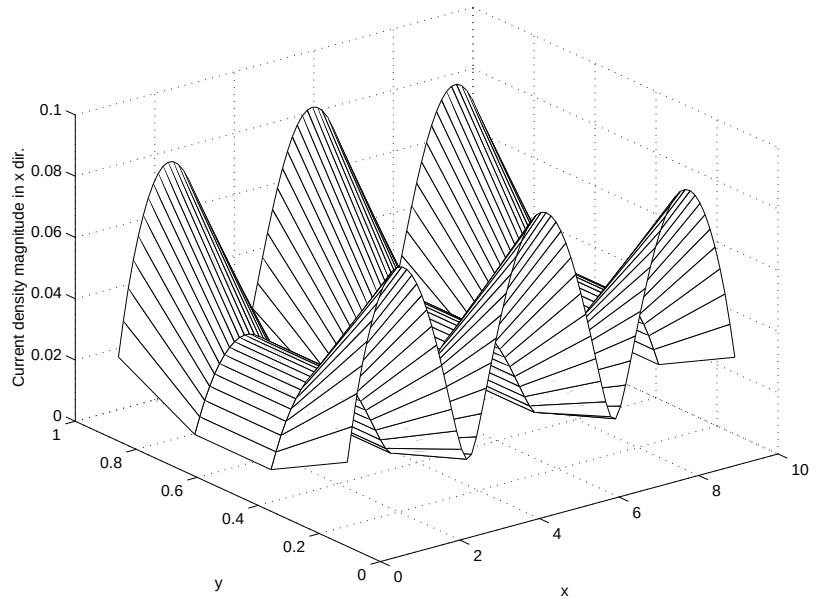

(a)

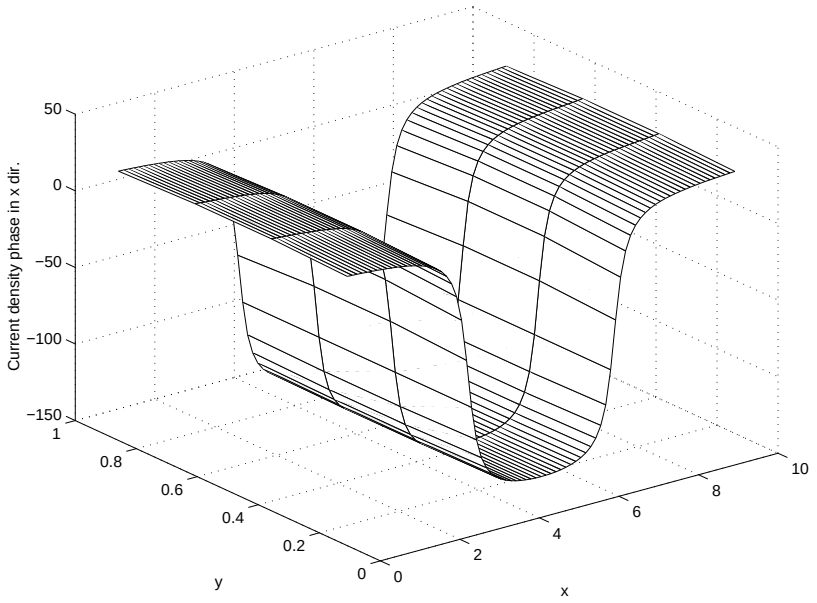

(b)

Figure 76: (a)The magnitude and (b) the phase of the co-pol component of the surface current density on a 1.0 cm x 10.0 cm line illuminated by a normally-incident uniform plane wave. The MoM result at 3 GHz is obtained using smaller cell sizes that the previous MoM example.

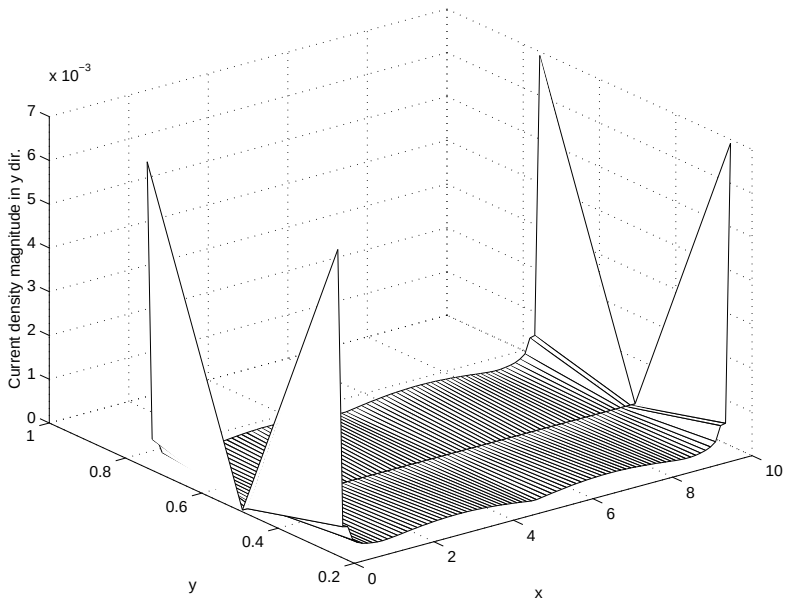

Figure 77: The magnitude of the cross-pol component of the surface current density on a 1.0 cm x 10.0 cm line illuminated by a plane wave. The 3 GHz result is obtained using the MoM.

substrate thickness, h, is 1.57 mm. The microstrip lines are placed on top of the substrate and the upper region is free space. This filter was analyzed in Section 3.7 and the MoM S-parameter results exhibited good agreement with a commercial software product.

The S-parameters S_{11} and S_{12} for the single-stub filter are obtained using the LCN approach and compared to the MoM results. For the LCN analysis, each cell within the filter model has both $x-$ and $y-$components of the current density and since 3 by 2 quadrature rules are used, each cell has 12 unknowns. The S-parameters are calculated from the co-pol currents. It was observed that the numerical values obtained for the propagation constant β on the port transmission line are different from the corresponding β obtained using the MoM formulation. Figures 82 and 83 show the magnitudes of S_{11} and S_{12}, respectively. Figures 84 and 85 show the phases of S_{11} and S_{12}, respectively. While these results exhibit general agreement, there is a clear indication of a difference between them, especially in the phase.

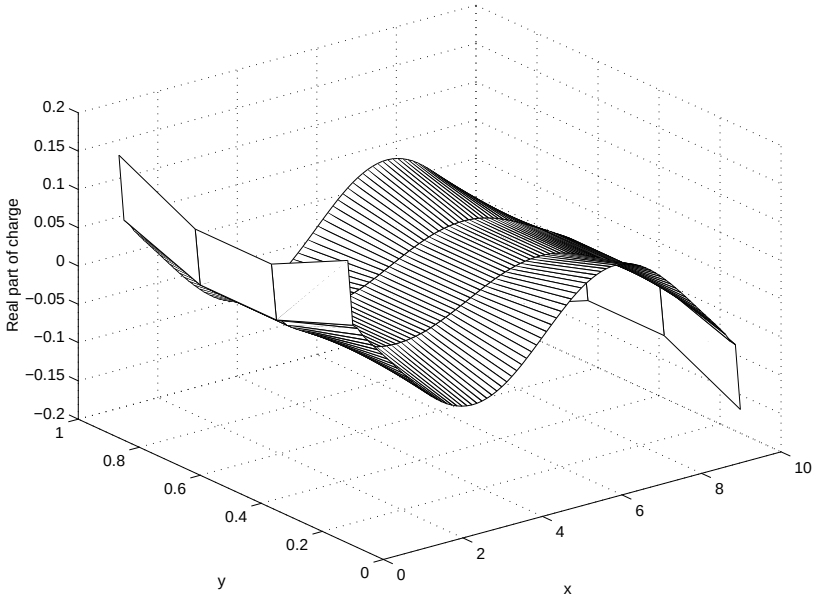

(a)

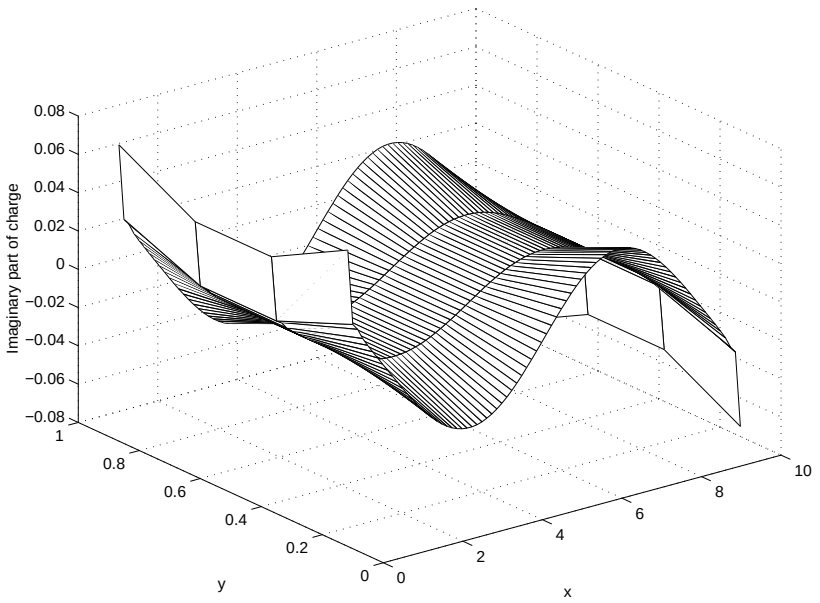

(b)

Figure 78: (a) The real and (b) the imaginary parts of the charge density on a 1.0 cm x 10.0 cm line over a grounded substrate due to uniform plane wave illumination. The 3 GHz MoM result.

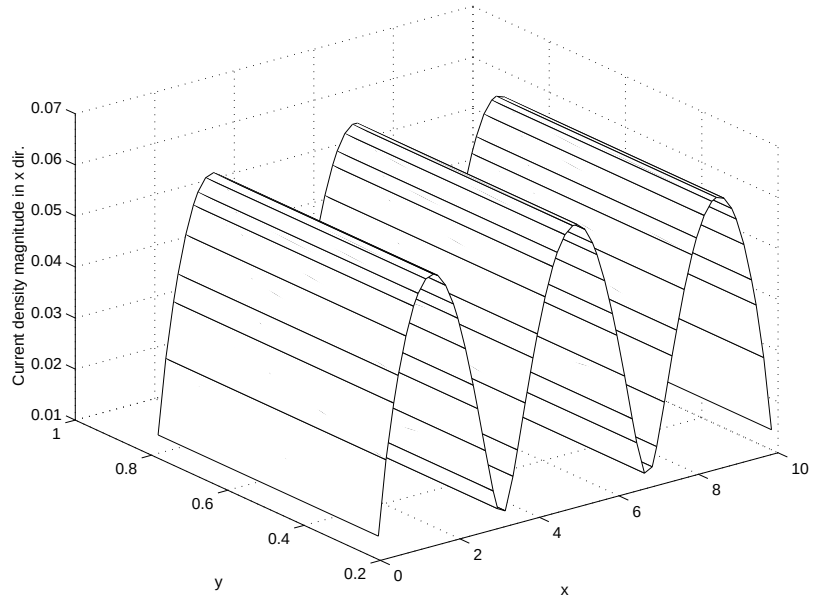

(a)

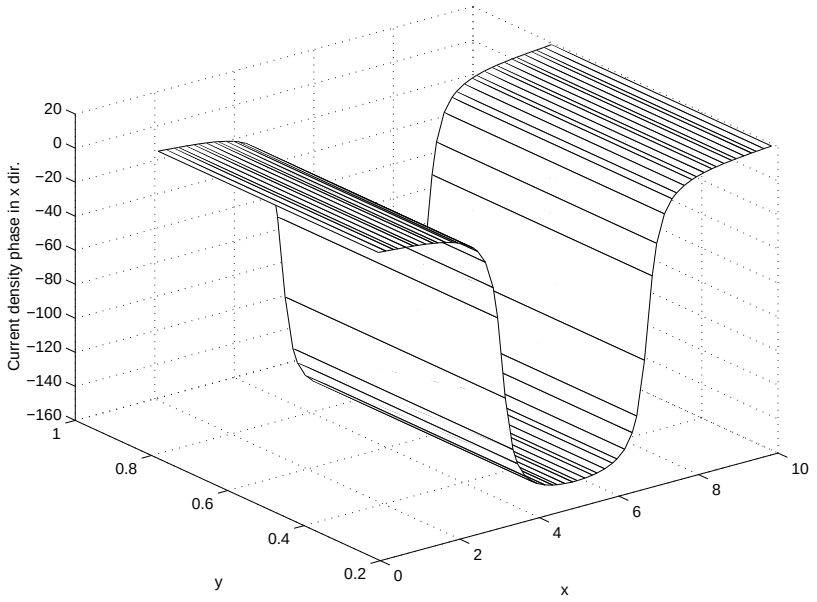

(b)

Figure 79: (a) The magnitude and (b) the phase of the co-pol component of the surface current density on a 1.0 cm x 10.0 cm microstrip line illuminated by a uniform plane wave at 3 GHz. The LCN result with 3 by 2 quadrature rules is obtained with the $y-$component of the current omitted.

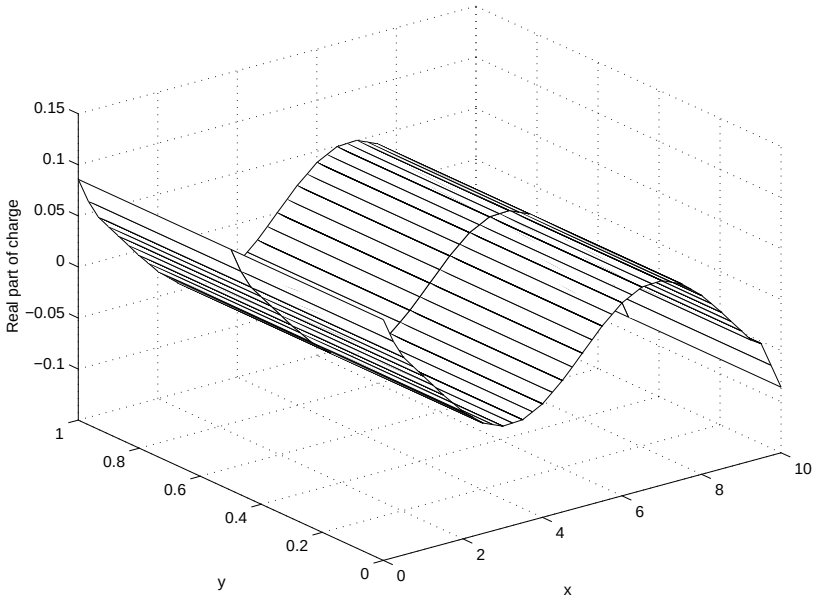

(a)

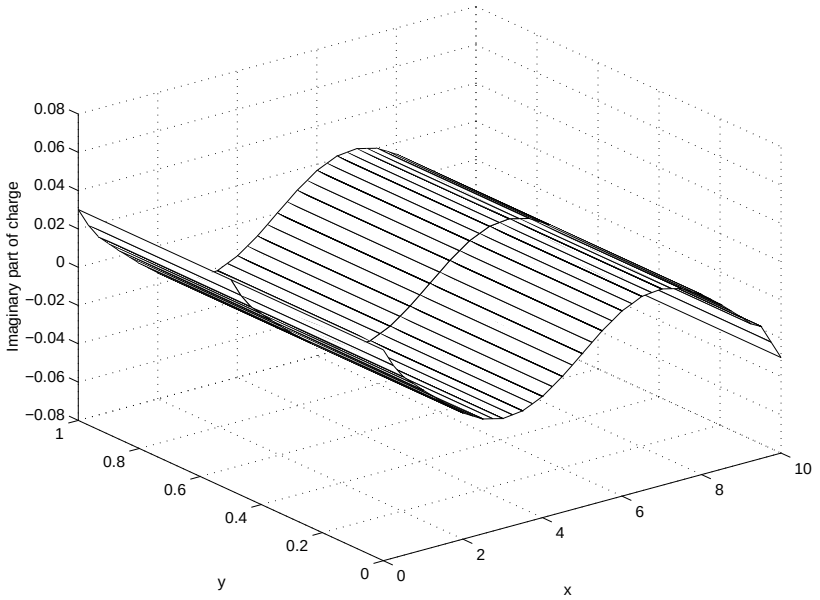

(b)

Figure 80: (a) The real and (b) the imaginary parts of the charge density on a 1.0 cm x 10.0 cm plate over a microstrip line illuminated by a uniform plane wave. The LCN result with 3 by 2 quadrature rules is obtained with the $y-$component of the current omitted.

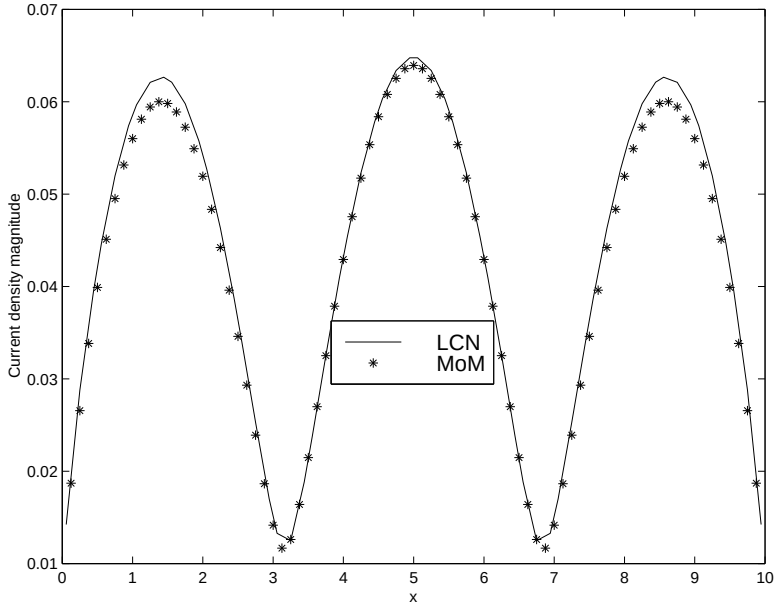

(a)

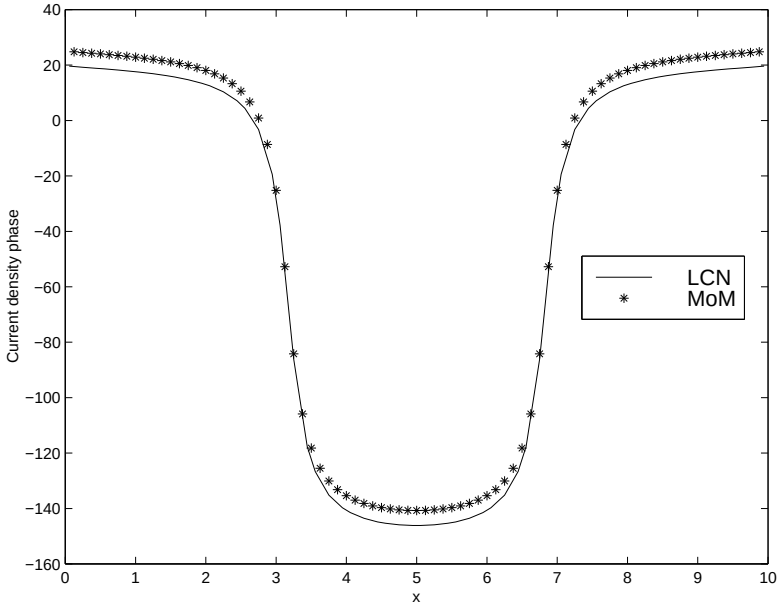

(b)

Figure 81: (a) The magnitude and (b) the phase of the co-pol component of the surface current density on a 1.0 cm x 10.0 cm microstrip line illuminated by a uniform plane wave, along the $y = 0.5$ cm cut.

Figures 86a and 86b show the magnitude and the phase of the $x-$component of the surface current density on the microstrip line obtained using LCN with 3 by 2 quadrature rules at 2.9 GHz. Figures 87a and 87b present the magnitude and the phase of the $x-$component of the surface current density on the microstrip line obtained using MoM at 2.9 GHz. A close inspection of these figures indicates that there is a difference in magnitude of about 50%, and in addition there is a shift in the standing wave pattern on the input side of the filter.

In order to study the behavior of the numerical results when the cross-pol component of the current density is omitted from the LCN analysis, results for the stub filter were generated under those conditions. The S_{11} and S_{12} for the single-stub filter are obtained using the LCN approach and compared to the results of the MoM approach. Since the cross-pol component of the current density has been dropped from the LCN representation, each cell in the model has only 6 unknowns, The results obtained using the LCN procedure under these conditions appear to agree with those obtained using the MoM. In addition, the values obtained for β (the propagation constant on the port transmission line) are similar to those obtained using the MoM formulation. Figures 88 and 89 show the magnitudes of S_{11} and S_{12}, respectively. Figures 90 and 91 show the phases of S_{11} and S_{12}, respectively. It is clear that the agreement in phase is far superior to that observed in the preceding example, although there are still some differences in the magnitudes of the S-parameters.

Figures 92a and 92b show the magnitude and the phase of the $x-$component of the surface current density on the microstrip line obtained using LCN with 3 by 2 quadrature rules for each cell, respectively at 2.9 GHz. The currents produced by the LCN without the cross-pol currents do not exhibit good agreement with either of the previous results.

5.6 Discussion

In this chapter, an attempt was made to extend the mixed-order LCN formulation to several problems excited by impressed-current sources. Problems of interest include various printed circuit structures, which often involve narrow microstrip lines. Unfortunately, it appears that the mixed-order LCN formulation does not work well for that type of problem.

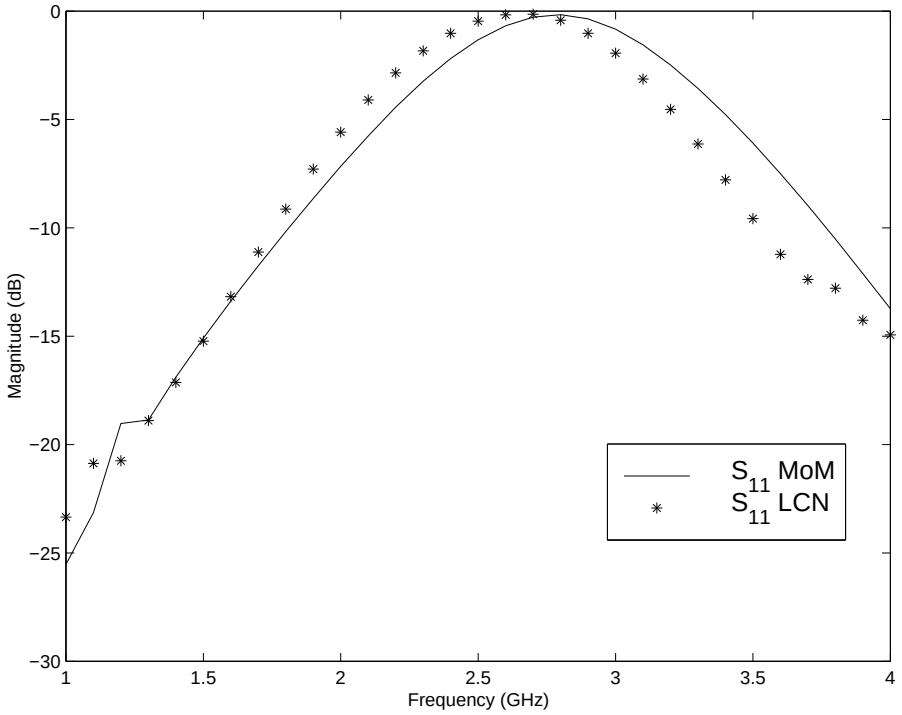

Figure 82: Magnitude of S_{11} for the single-stub filter shown in Figure 14

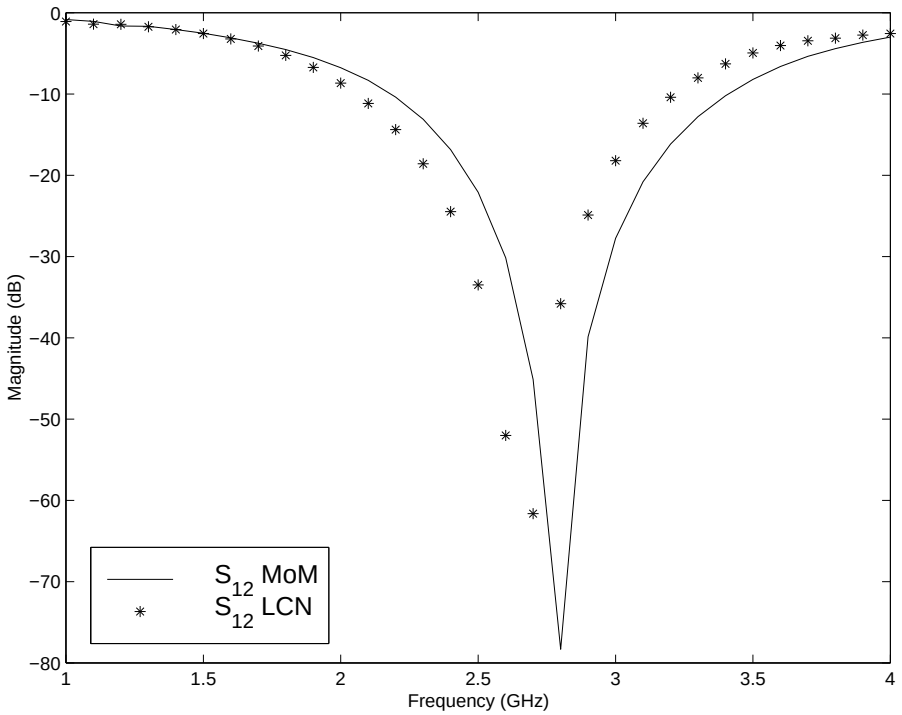

Figure 83: Magnitude of S_{12} for the single-stub filter shown in Figure 14

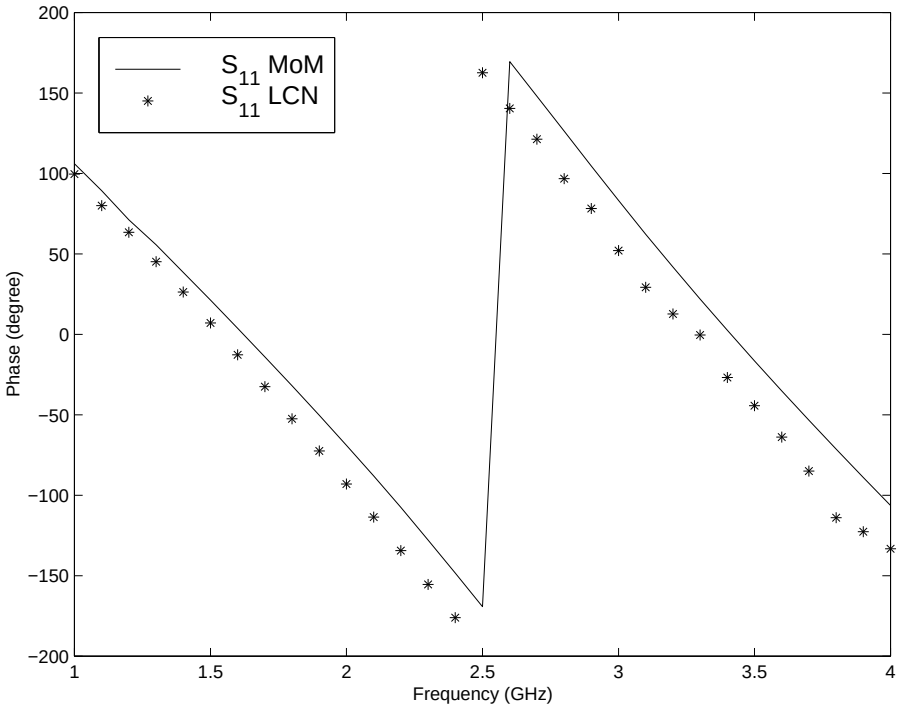

Figure 84: Phase of S_{11} for the single-stub filter shown in Figure 14

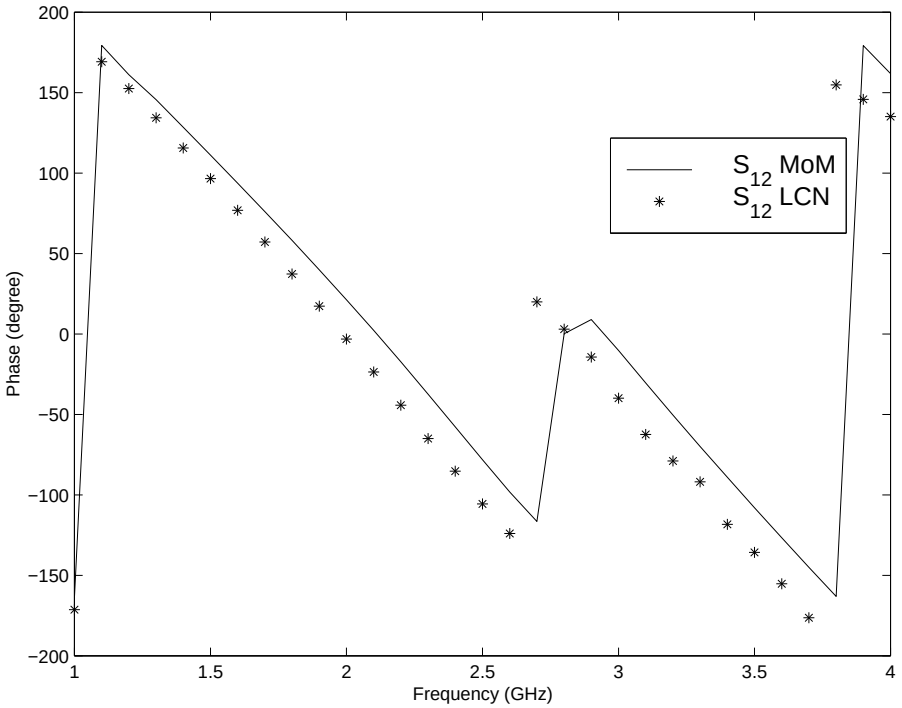

Figure 85: Phase of S_{12} for the single-stub filter shown in Figure 14

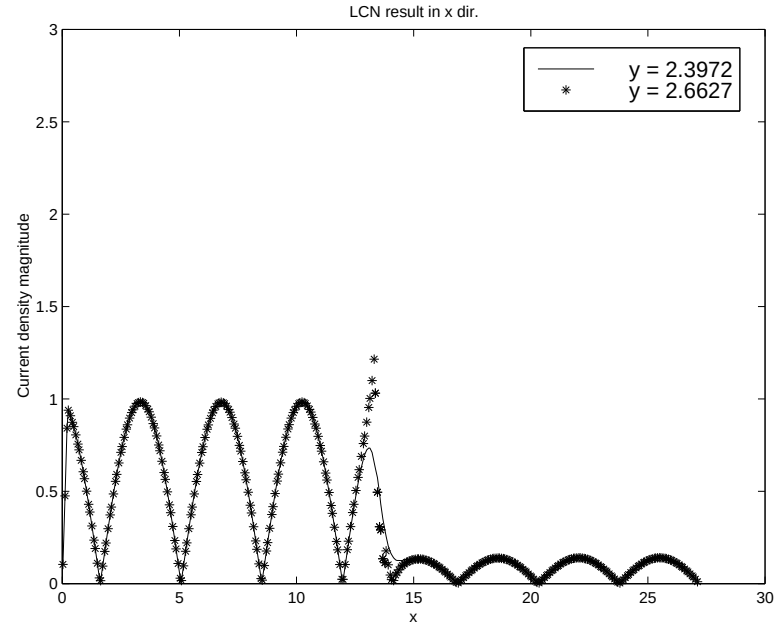

(a)

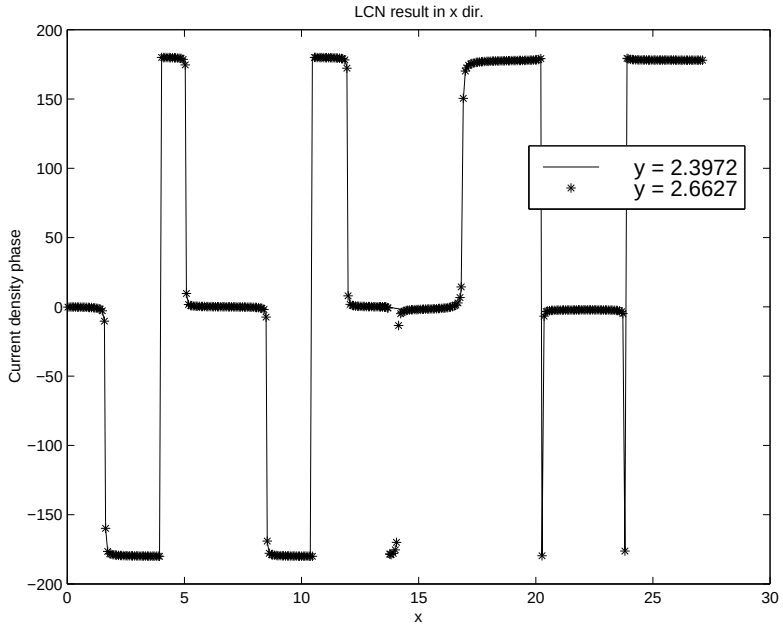

(b)

Figure 86: (a) The magnitude and (b) the phase of the $x-$component of the surface current density on the single-stub filter obtained at 2.9 GHz using LCN.

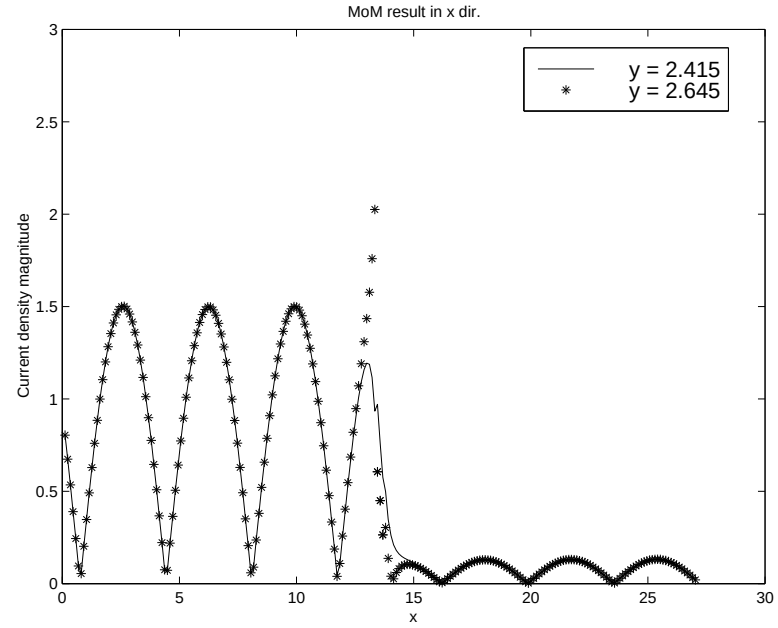

(a)

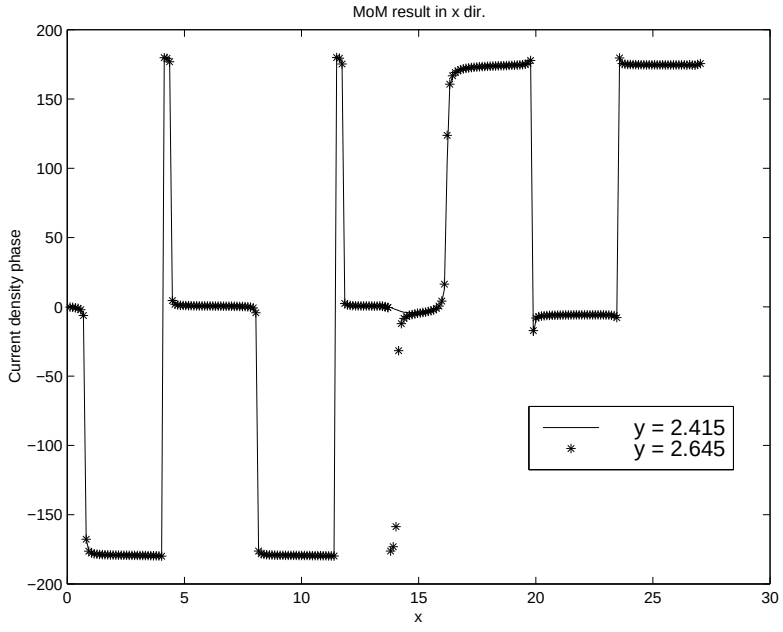

(b)

Figure 87: (a) The magnitude and (b) the phase of the $x-$component of the surface current density on the single-stub filter obtained at 2.9 GHz using the MoM.

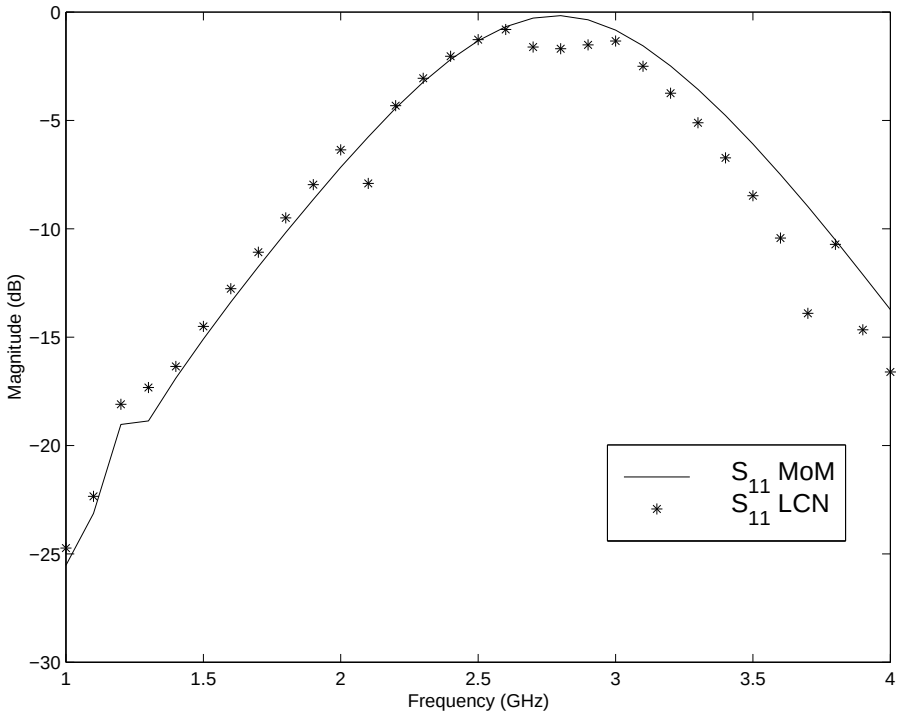

Figure 88: Magnitude of S_{11} of the single-stub filter shown in Figure 14, when cross- pol currents are omitted from the LCN analysis.

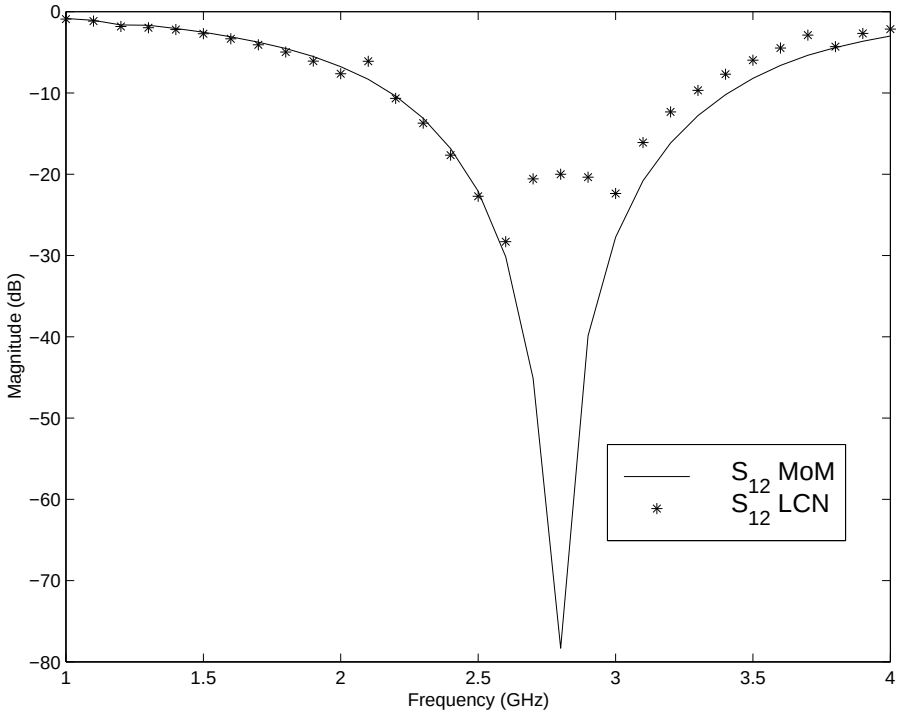

Figure 89: Magnitude of S_{12} of the single-stub filter shown in Figure 14, when cross- pol currents are omitted from the LCN analysis.

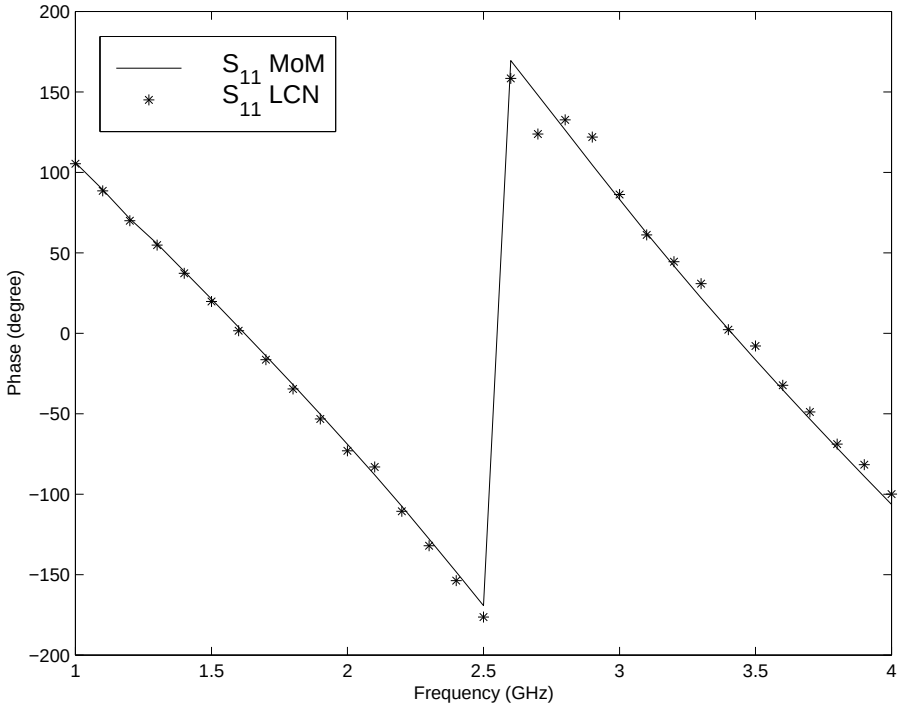

Figure 90: Phase of S_{11} of the single-stub filter shown in Figure 14, when cross- pol currents are omitted from the LCN analysis.

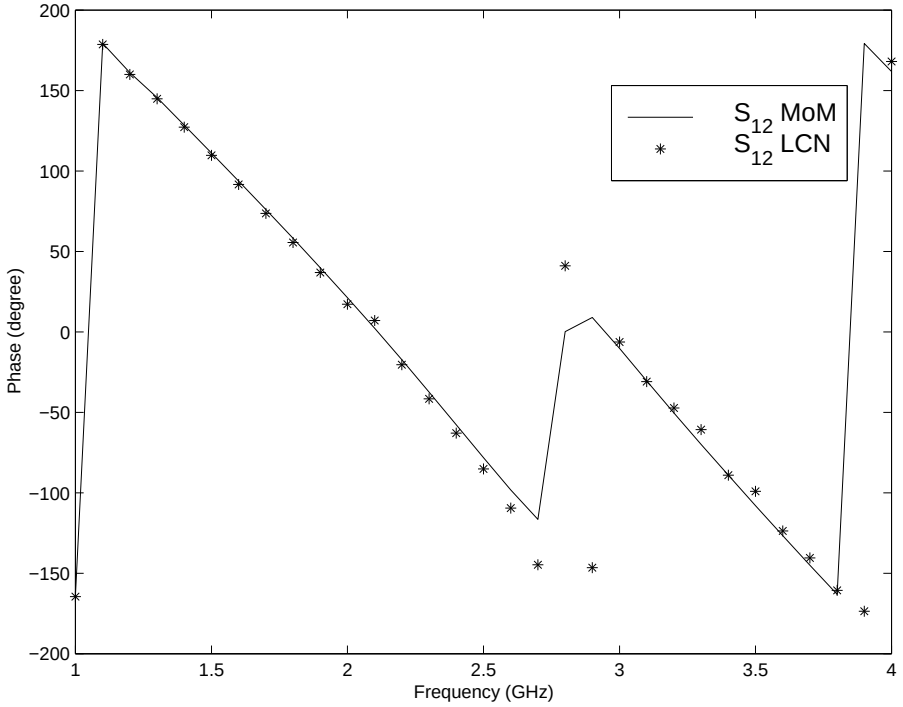

Figure 91: Phase of S_{12} of the single-stub filter shown in Figure 14, when cross- pol currents are omitted from the LCN analysis.

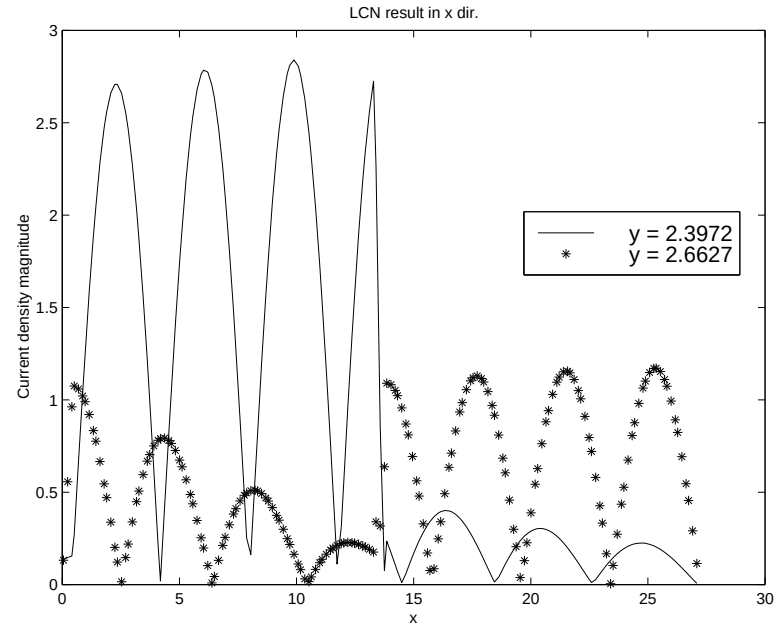

(a)

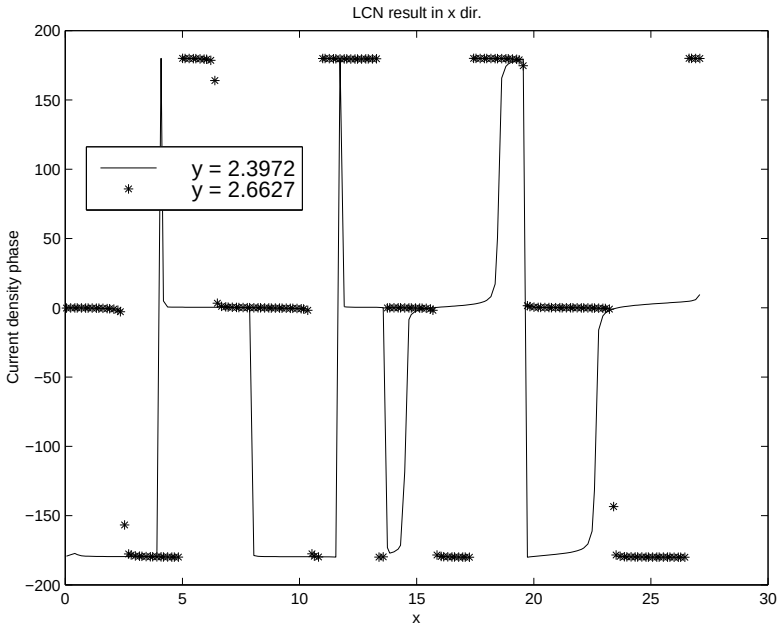

(b)

Figure 92: (a) The magnitude and (b) the phase of the $x-$component of the surface current density on the single-stub filter obtained at 2.9 GHz using LCN with 3 by 2 quadrature rules, with the cross-pol currents omitted from the LCN representation.

A considerable amount of effort was expended in order to determine if the problem was due to a bug in the computer code, or something endemic to the formulation. Results suggest that the difficulties occur for both the impressed-current feed and the plane wave feed models. The erratic results do not improve substantially as smaller cell sizes are employed. They do appear to improve for simple microstrip lines if the cross-pol current is dropped from the LCN representation. However, the currents on the stub filter example did not appear to improve after the cross-pol current was dropped.

Since the difficulty seems to arise for narrow strips, it is postulated that it may be caused by a poor model of the edge singularity associated with the co-pol component of the current on the strip. Neither the MoM approach nor the LCN formulation used in the present investigation incorporate the proper edge singularity, and therefore it is reasonable to conclude that neither approach yields the correct solution near an edge. The 3 by 2 mixed-order representation may be more sensitive to this situation than the simpler roof-top basis function used within the MoM.

An additional downside to the use of the 3 by 2 representation is that it requires a large number of unknowns (12 per cell) for narrow strips, compared to only one per cell for the MoM. Thus a structure consisting largely of strips would require an order of magnitude more unknowns for LCN analysis than MoM analysis. That situation is likely to be unacceptable in practice.

To continue the investigation one step further, the following chapter considers an alternative to the 3 by 2 representation used with the LCN formulation for narrow strips.

CHAPTER VI

AN LCN FORMULATION FOR NARROW STRIPS INCORPORATING THE EDGE SINGULARITY

The previous chapter reported that the LCN approach produced inaccurate results for narrow strips when both components of the current are included in the representation. In addition, the basic 3 by 2 representation (the simplest that appears to work well for other structures) requires twelve unknowns per cell under those conditions (far more than the simplest MoM approaches). On the other hand, when the cross-pol current was dropped from the LCN representation for two of the examples under consideration, the results improved dramatically. (For the third example of the stub filter, the current density did not improve.)

Since printed circuit structures often contain narrow strips, any modeling approach for printed circuit applications must include an accurate, efficient means for incorporating narrow strips. The aim of this chapter is to find a better LCN representation that can be used for treating narrow strips and microstrip lines.

6.1 Example: Conducting Strip in Free Space

For clarity, the microstrip line example of Chapter 5 (which incorporated a ground plane, substrate, and impressed current source feed) will be simplified to the case of a single narrow conducting strip in free space, illuminated by a normally-incident plane wave. A single example will be considered: a strip of length = $L = 4/3\ \lambda$, width = $2h = 4/30\ \lambda$, and infinitesimal thickness in the third dimension. The incident field is a uniform plane wave normally incident to the flat part of the strip with the electric field polarized along the long dimension L of the strip.

There are two modeling difficulties with this problem: First, the current along the strip exhibits a square-root singularity at the knife edges. Second, the charge density exhibits

the same type of singularity at the strip ends. Similar features arise in connection with the microstrip line considered in Chapter 5. Common practice when using MoM procedures is to ignore both singularities. With the MoM formulation of Chapter 3, ignoring the singularities did not lead to any obvious difficulties (although it is quite likely that the numerical results were not highly accurate as a consequence). With the LCN approach of Chapter 5, ignoring the singularities appeared to result in substantial error in the results.

Using the approach of Chapter 3, MoM results were obtained for the conducting strip in free space, using cells of dimension h_x and h_y equal to 1/60 λ and 4/150 λ, respectively. This model has 5 cells across the strip width, and a total of 715 unknowns. This model is adequate to approximate the current crowding effect, and produce a result with a greater current density near the strip edges than in the strip center. Results were also obtained using the LCN approach with the 3 by 2 representation for the current density and a 20-cell model for the strip. With the LCN approach, the cell dimensions h_x and h_y are set to 2/30 λ and 4/30 λ, respectively. The LCN procedure uses a quadratic representation for the current along the vector direction of the basis, but for this model just a constant representation in the y direction. The LCN model requires 12 unknowns per cell to represent both components of the current density, and therefore this 20 by 1 cell model employed 240 unknowns. To compare the LCN and MoM methods, the magnitude and the phase of the $x-$component of the surface current density along the center of the strip are plotted as shown in Figures 93a and 93b. As in the examples of Chapter 5, there is a substantial difference in both the magnitude and phase of the current density.

To investigate the impact of cell size on the results, the previous example is repeated using a 40-cell model, with cell dimensions of h_x equal to 2/30 λ and h_y equal to 2/30 λ. The LCN procedure using the 3 by 2 representation requires 480 unknowns for this model of the strip. The LCN results now exhibit a linear variation across the width of the strip, with a minimum in the center, and are actually sampled slightly off the centerline as dictated by the location of the quadrature points. To compare the LCN and MoM methods, the magnitude and the phase of the co-pol component of the surface current density along the centerline are plotted as shown in Figures 94a and 94b. In this case there is better agreement

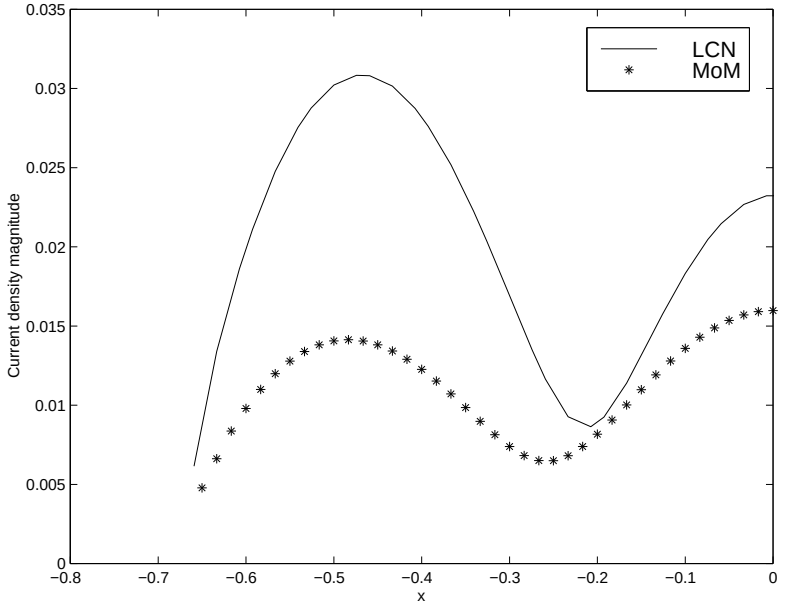

(a)

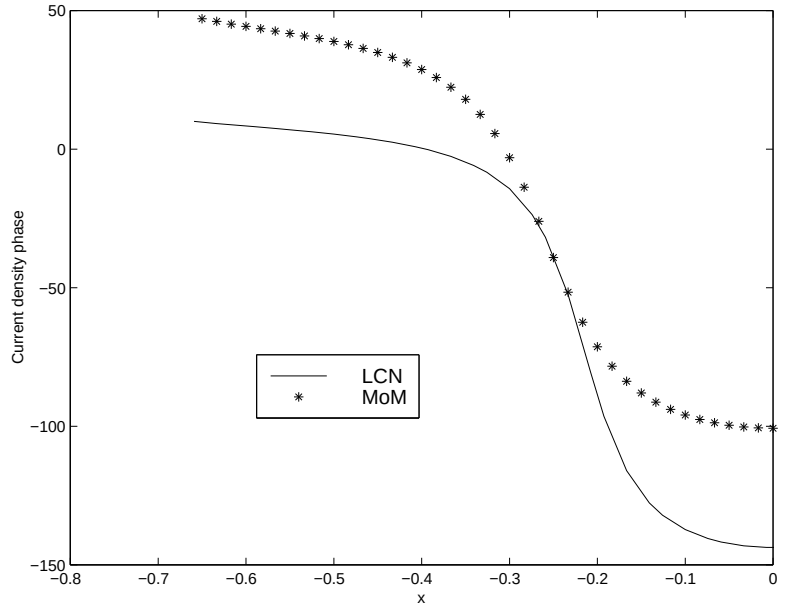

(b)

Figure 93: (a) The magnitude and (b) the phase of the co-pol component of the surface current density on a $4/3\lambda$ x $4/30\lambda$ strip in free space illuminated by a normally-incident uniform plane wave, along the centerline of the strip. The LCN result employed 20 cells. Half the strip is shown.

between the results, but still a measurable difference.

It should be noted that the current density obtained from the MoM representation exhibits a minimum in the center of the strip, while those of the LCN approach exhibit a uniform dependence for the 20-cell model and a linear transverse variation (with a minumum in the center) for the 40-cell model. The 40-cell LCN result yields current density values near the edge that are greater than those near the centerline, as would be expected due to the phenomenon of current crowding that leads to the edge singularity discussed above. In addition, the 40-cell LCN result is based on the current samples at the quadrature nodes nearest the centerline of the strip (not exactly at the centerline). Despite this fact, the difference between the MoM and LCN results is far more than would be expected due to sampling the current off the actual centerline.

For the next example, the transverse component of the current density is dropped from the LCN approach. The modified LCN approach is used with a 20-cell model, using cells of dimension h_x equal to 2/30 λ and h_y equal to 4/30 λ. The LCN procedure using a 3 by 2 representation for the co-pol component of the current density requires 6 unknowns per cell, or 120 unknowns overall. The magnitude and phase of the co-pol component of the surface current density on the strip are shown in Figures 95a and 95b. As was observed under similar conditions in Chapter 5, the results of the LCN approach (especially the phase) exhibit good agreement with the MoM results.

Similar results are observed when the modified LCN approach is used with a 40-cell model of the strip. Figures 96a and 96b show the magnitude and phase of the current on the centerline for this situation, when h_x is set to 2/30 λ and h_y is set to 2/30 λ. The LCN result requires 240 unknowns. This result shows good agreement between the methods, and it also shows that the modified LCN approach using the 40 cell model is sufficiently accurate.

The performance of the LCN procedure for the preceding examples is puzzling, because it is apparent that the observed error in the result is related to the presence of the cross-pol component of the current density in the model. The procedure can adjust the coefficients of the cross-pol current to zero, and would be expected to do so if that component of the

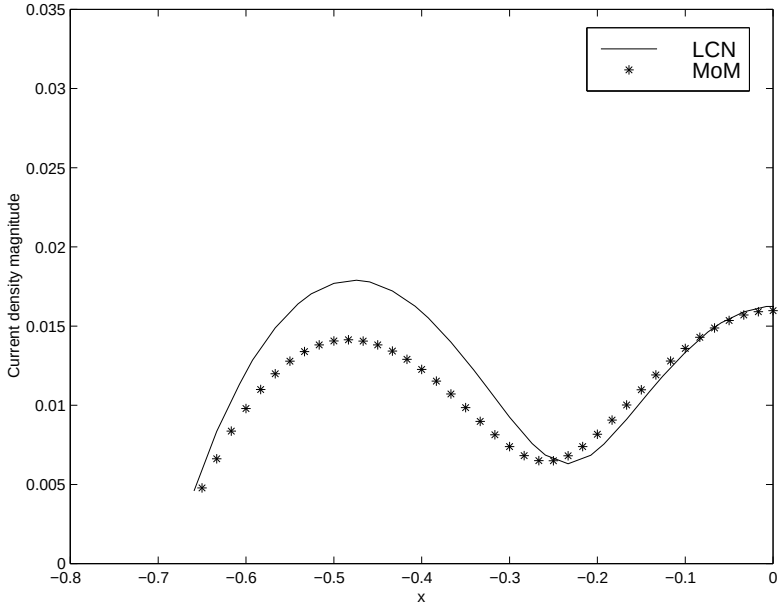

(a)

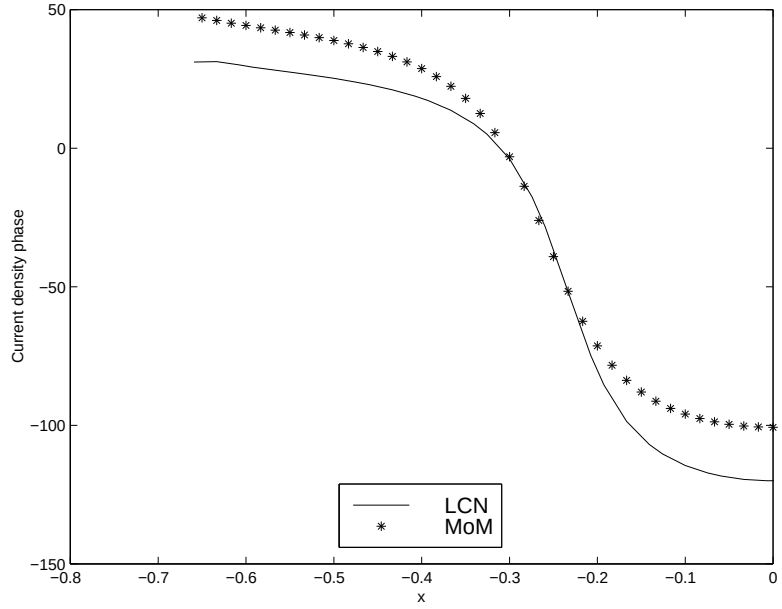

(b)

Figure 94: (a) The magnitude and (b) the phase of the co-pol component of the surface current density on a $4/3\lambda$ x $4/30\lambda$ strip when there are 40 cells used with the LCN approach. Half the strip is shown.

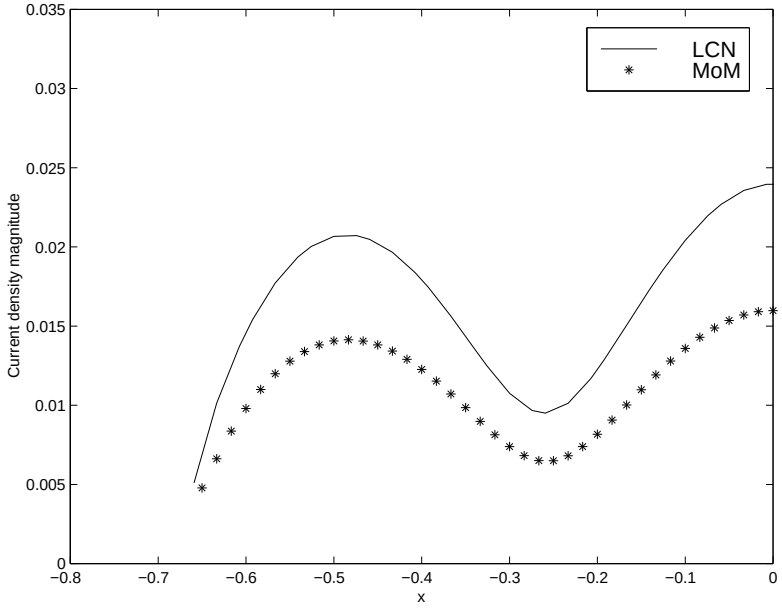

(a)

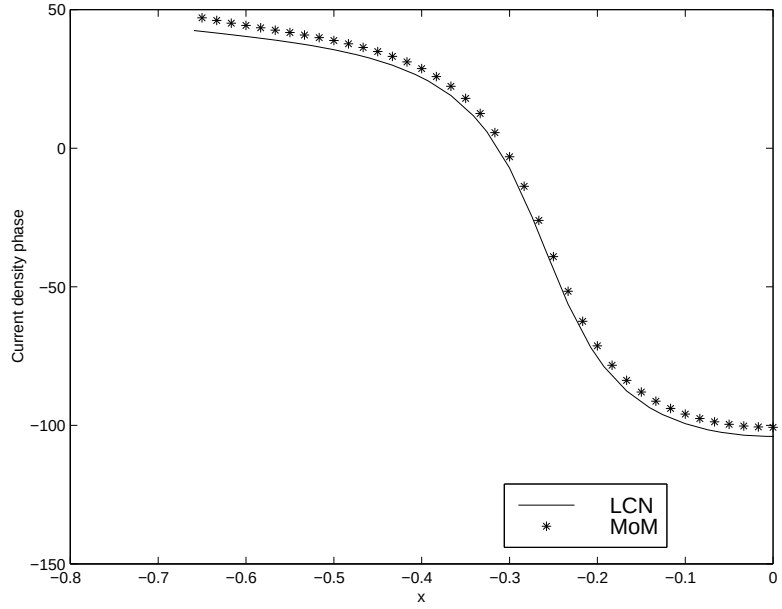

(b)

Figure 95: (a) The magnitude and (b) the phase of the co-pol component of the surface current density on a $4/3\lambda$ x $4/30\lambda$ strip. The 20-cell LCN result does not include the cross-pol current density. Half the strip is shown.

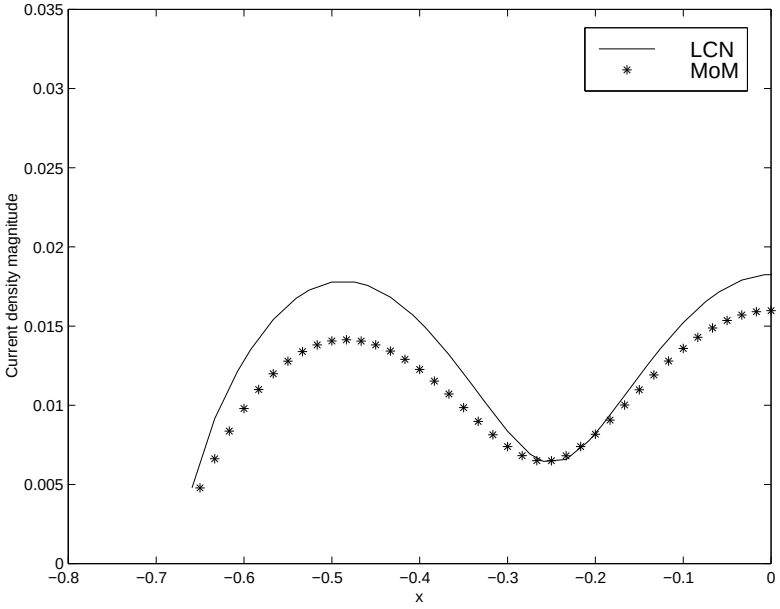

(a)

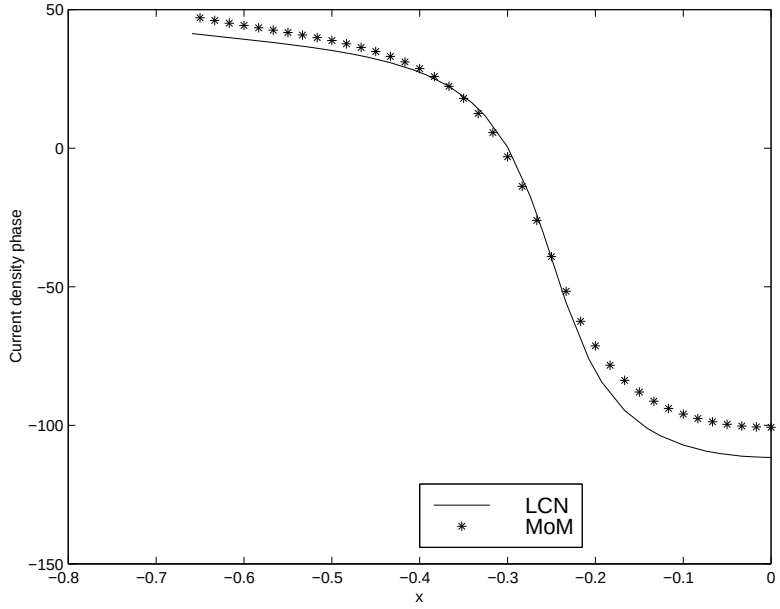

(b)

Figure 96: (a) The magnitude and (b) the phase of the co-pol component of the surface current density on a $4/3\lambda$ x $4/30\lambda$ strip. The 40-cell LCN result does not include the cross-pol current density. Half the strip is shown.

current is not needed for the solution. In this situation, the LCN approach is not producing coefficients of zero. In Chapter 5, it was postulated that the approach has difficulty with this situation due to the presence of the edge and the associated singularity in the current density. In order to investigate this postulate, a new representation was developed for use with LCN.

6.2 3 by 1 Representation Incorporating an Edge Singularity

The presence of the edge singularity in the current density along the strip suggests that a special basis function incorporating the edge singularity be considered. For convenience, consider a strip aligned along the x direction in free space. For such a strip in free space, the true current density behavior is known to exhibit a transverse dependence that, in the limit as the strip width becomes electrically small, is given by the function

$$\frac{1}{\sqrt{1-(y/h)^2}} \tag{107}$$

where h is the half-width of the strip. Consequently, a new LCN representation was developed that employed a quadratic representation for the x dependence of the current density and Eq. (107) for the y dependence. This representation, which is only under consideration for narrow strips, only incorporates an $x-$component of current density.

Since the y dependence is prescribed by the preceding function, the new LCN representation only requires 3 unknowns per cell. The implementation of the 3 by 1 approach requires a conversion to the use of a 1-point Jacobi quadrature rule in y in conjunction with a 3-point Gauss-Legendre rule in x. The local correction calculations must be modified to incorporate the singular function of y.

Results were generated using the 3 by 1 representation. It was determined that the size of the local correction footprint needed to be adjusted as the cell dimensions along x were reduced, and this was done (for example, 2 cells on each side of the source were included for a 20 by 1 cell discretization, while 5 cells on each side of the source cell were needed in the local correction footprint for a 40 by 1 cell discretization of the strip). Figures 97a and 97b show results for the 20 by 1 cell LCN discretization (60 unknowns) compared to the

MoM data, and Figures 98a and 98b show results for the 40 by 1 cell LCN discretization (120 unknowns). These LCN results exhibit far better agreement with the MoM data than the original 3 by 2 results presented earlier. The agreement is not perfect, however, and one might suppose that the difference between the LCN and MoM data in this case is due to the fact that the MoM data does not incorporate the edge singularity, and thus may not be as accurate as the 3 by 1 LCN results.

6.3 Condition Number Comparison

Table 1 summarizes the number of unknowns and the matrix condition numbers for the examples considered in this chapter. In addition, the table incorporates test runs based on the 3 by 3 polynomial complete representations originally considered in Chapter 4 for use with the LCN. LCN Results are presented for the 20-cell and 40-cell models of the strip. The matrix condition number is a measure of the sensitivity of a matrix to small changes in its entries. It is a number between 1.0 and infinity, with 1.0 being the desirable value. As the matrix condition number grows large, it is an indication that the system of equations representing the problem under consideration is less stable or less robust. From Table 1, it is easily observed that the 3 by 2 mixed-order LCN representation significantly reduces the condition number of the impedance matrix as compared to the polynomial-complete 3 by 3 LCN representation. The condition number often follows a trend similar to the number of unknowns (the order of the matrix). It can be observed from Table 1 that the use of the 3 by 2 representations with only the co-pol component of the current actually result in an *increase* of the condition number, despite the reduction in the number of unknowns. A significant decrease in the matrix condition number is realized with the 3 by 1 singular representation.

6.4 Conclusions

In this chapter, a new 3 by 1 representation was considered for use with the LCN procedure for modeling narrow strips. The new approach was investigated for a $4/3\lambda$ strip illuminated by a plane wave. For that problem, it appears to work well. The new representation also

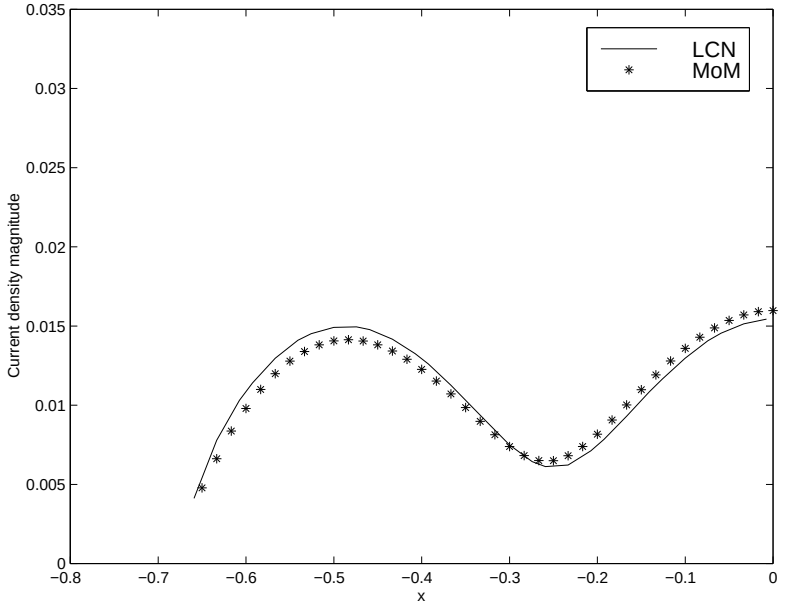

(a)

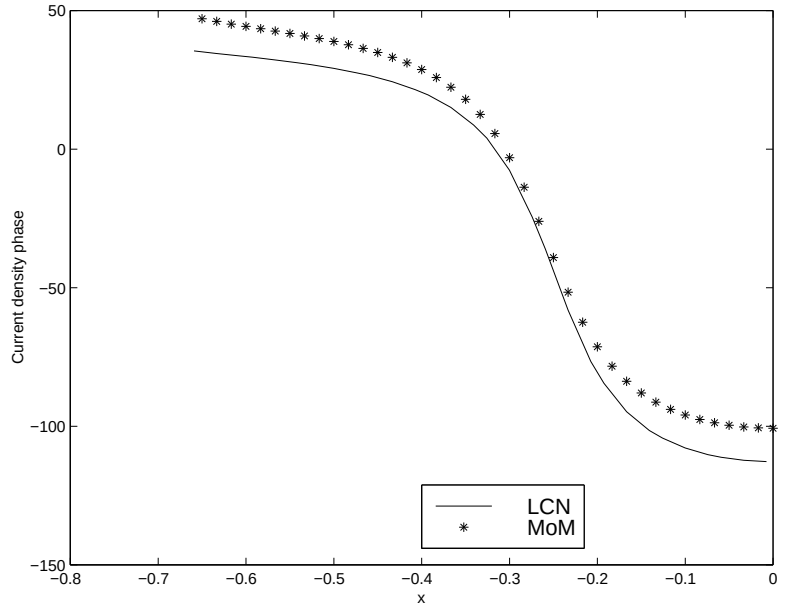

(b)

Figure 97: (a) The magnitude and (b) the phase of the co-pol component of the surface current density on a $4/3\lambda$ x $4/30\lambda$ strip in free space illuminated by a normally-incident plane wave. The 20-cell LCN result was obtained with the 3 by 1 singular representation. Half the strip is shown.

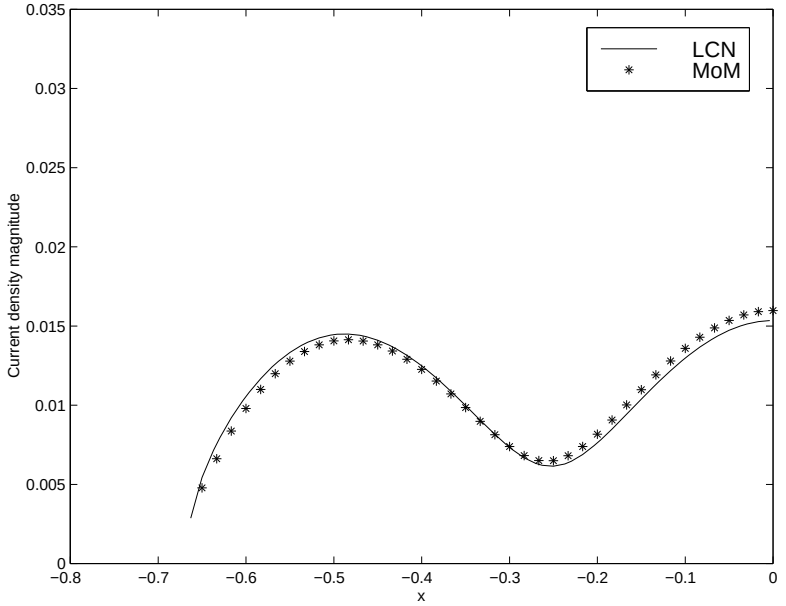

(a)

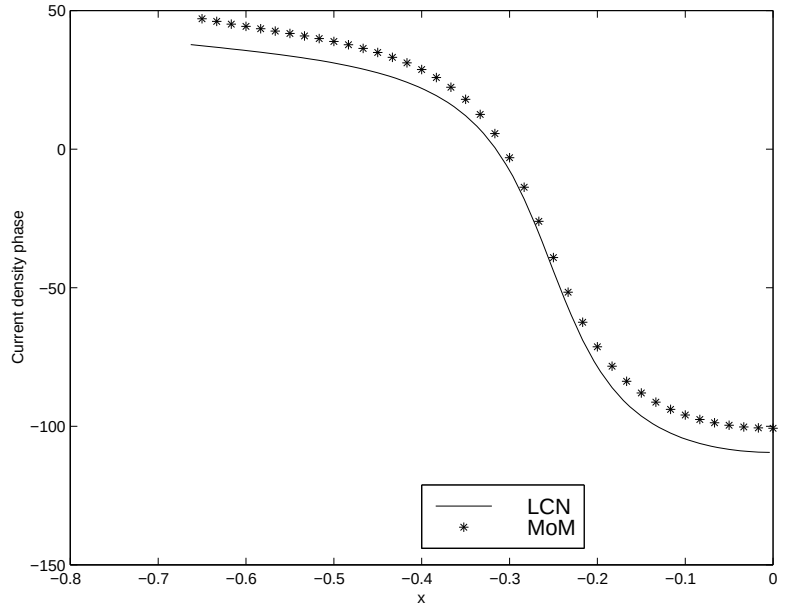

(b)

Figure 98: (a) The magnitude and (b) the phase of the co-pol component of the surface current density on a $4/3\lambda$ x $4/30\lambda$ strip in free space illuminated by a normally-incident plane wave. The 40-cell LCN result was obtained with the 3 by 1 singular representation. Half the strip is shown.

Table 1: Impedance matrix condition number comparisons

Method	number of unknowns per cell	number of unknowns	condition number
MoM	1.78	715	2791
LCN 3x3	18	360	3608
LCN 3x3	18	720	389560
LCN 3x2	12	240	369
LCN 3x2	12	480	479
LCN 3x2 no cross-pol component	6	120	582
LCN 3x2 no cross-pol component	6	240	1161
LCN 3x1	3	60	172
LCN 3x1	3	120	317

reduces the number of unknowns to 3 per cell, a reduction of a factor of 4 from the general 3 by 2 representation suggested in Chapter 4. This preliminary investigation bodes favorably for the use of a special LCN representation for narrow microstrip lines, a common structural feature of printed circuit geometries.

Although the preliminary results support the 3 by 1 approach, additional research should be carried out to determine if this idea will work in practice for narrow strips in planar, layered structures. In particular, the form of the edge singularity along conducting strips in the presence of a dielectric substrate may be different than the free-space form employed in this investigation. The behavior of the numerical results at a right-angle junction of strips or microstrip lines also needs to be studied.

CHAPTER VII

CONCLUSIONS

The objective of this work was to improve the existing electromagnetic modeling capabilities for application to printed circuit geometries.

A GPOF-based MoM solution of the mixed potential integral equation was developed primarily to provide a platform for comparison purposes. This approach is suitable for a multilayer environment, and can incorporate via modeling capabilities. S-parameter extraction is used to convert the currents and fields into useful circuit-based quantities. The GPOF implementation was previously developed by the author and colleagues Dr. M. I. Aksun and others at Bilkent University [10, 4, 15, 1, 30, 28].

Recent research has suggested that there may be advantages to the LCN discretization procedure, especially for problems where the Green's functions are expensive to compute and when higher-order representations are desired. For this reason, an LCN-based procedure for planar conductors in a multilayer structure was developed in this thesis. The relative efficiency and accuracy of the LCN and MoM procedures were also studied. In addition, a number of fundamental aspects of the LCN approach were investigated, including the use of mixed-order representations, representations incorporating edge singularities, and the use of nonconforming models.

Finally, the techniques were evaluated and employed for a number of structures representing electrical interconnects and devices in microelectronic packages. At the present time, it is not clear that the LCN procedure offers an advantage over MoM for this class of electromagnetic problem. In fact, it appears that the accuracy of the LCN method for planar layered media problems is difficult to guarantee. In the course of the investigation, however, several fundamental contributions to the development of the LCN approach were made.

7.1 Original Contributions

Several original contributions were made in the course of this thesis research. These are as follows:

- The use of the LCN approach for the analysis of layered media structures with the GPOF form of the Green's functions
- The use of mixed-order LCN representations for proper electric charge modeling
- The implementation of 3 by 2, 4 by 3, and 5 by 4 order representations
- The focus on the accuracy of the surface currents
- The demonstration that the LCN approach can be successful with nonconforming cell models
- The presentation of the impressed-current feed model and the associated de-embedding and S-parameter analysis in connection with the LCN procedure
- The use of a special edge singularity LCN representation for modeling narrow strips

7.2 Future Work

Due to the need to investigate and extend several fundamental aspects of the LCN procedure, the original goal of modeling realistic printed circuit structures with the LCN method was not achieved. This goal now appears within reach and should be pursued, by combining a special representation for narrow microstrip lines with the general mixed-order representations introduced in Chapter 4 for other conducting structures. Results can be generated for a number of microelectronic packaging applications, and compared with measured data obtained from structures designed and fabricated at the Georgia Tech Packaging Research Center to verify the numerical results.

The computational efficiency of the LCN method lies in the evaluation of the matrix entries. The indications are that both the MoM and the LCN approaches will require a large number of unknowns for the high accuracy modeling of realistic structures. Therefore,

the matrix solution time will dominate the overall performance of both techniques. Parallel programming appears to offer the best direction for reducing the solution time associated with solving the large system of equations.

There is considerable interest in the development of adaptive computational methods, where various estimates of the solution error are used to modify the model of the structure under consideration (h-refinement) or the order of the representation used with a fixed model (p-refinement). The LCN approach can easily incorporate p-refinement capabilities, and appears to be an ideal platform for exploring its use in electromagnetic analysis.

APPENDIX A

GENERALIZED PENCIL OF FUNCTION ALGORITHM

As mentioned in Chapter 2, the generalized pencil of function algorithm is used to approximate the spectral domain Green's functions with complex exponentials. Since application of the algorithm is an important step in approximating the Green's functions, it is given in this Appendix for convenience.

It is well known that the Prony method and it variants can be used to extract the poles [50, 51] of an EM system. The pencil of function (POF) method [26] is an alternate method to the Prony method to find the system poles. In the POF method, the poles are found from the solution of a generalized eigenvalue problem, whereas, the Prony method contains a two-step process where the first step involves the solution of a matrix equation and the second step involves finding the roots of a polynomial. The generalized pencil of function method, is a generalization to the POF method and it is used to estimate poles of an EM system from its transient response [24]. Compared to the Prony method, the GPOF method is more robust and less noise sensitive.

Now consider an EM transient signal which can be approximated as follows

$$y_k = \sum_{i=1}^{M} b_i \cdot e^{s_i \delta t k} \qquad k = 0, 1, \cdots, N-1 \tag{108}$$

where b_i are the complex residues, s_i are the complex poles, and δt is the sampling interval. In order to find the poles, one can use the following algorithm [24]:

1. As a first step, construct the following matrices,

$$Y_1 = [\mathbf{y_0}, \mathbf{y_1}, \cdots, \mathbf{y_{L-1}}] \tag{109}$$

$$Y_2 = [\mathbf{y_1}, \mathbf{y_2}, \cdots, \mathbf{y_L}] \tag{110}$$

where

$$\mathbf{y_i} = [y_i, y_{i+1}, \cdots, y_{i+N-L-1}]^T \tag{111}$$

here L is the pencil parameter and optimal choice of L is around $L = N/2$ [24].

2. Next, find a Z matrix as follows,

$$VD^{-1}U^H = \text{SVD}(Y_1) \tag{112}$$

$$Z = D^{-1}U^H Y_2 V \tag{113}$$

where SVD$(\cdot)$ and superscript H denote the singular value decomposition process and complex conjugate transpose of a matrix, respectively. The number of exponentials, M, is selected according to the significant singular values of the Y_1 matrix. Note that the matrices V, D, and U should be re-dimensioned according to the selected singular values.

3. Then, poles of the system are given by

$$s_i = \frac{\log z_i}{\delta t} \qquad\qquad i = 1, 2, \cdots, M \tag{114}$$

where z_i's are the eigenvalues of the Z matrix evaluated in step 2.

4. Finally residues are found from the least-squares solution of the following system

$$\begin{bmatrix} 1 & 1 & \cdots & 1 \\ z_1 & z_2 & \cdots & z_M \\ \vdots & \vdots & \cdots & \vdots \\ z_1^{N-1} & z_2^{N-1} & \cdots & z_M^{N-1} \end{bmatrix} \begin{bmatrix} b_1 \\ b_2 \\ \vdots \\ b_M \end{bmatrix} = \begin{bmatrix} y_0 \\ y_1 \\ \vdots \\ y_{N-1} \end{bmatrix} \tag{115}$$

APPENDIX B

GREEN'S FUNCTIONS IN THE SPECTRAL DOMAIN

All of the Green's functions, presented herein, are for the vector and scalar potentials. These are not defined uniquely in stratified media [15]. In other words, different sets of Green's functions for the vector and scalar potentials can be chosen to satisfy the same boundary conditions.

The spectral-domain Green's functions in the source layer for different kind of sources and orientations are obtained as follows [15]:

$$\tilde{G}^A_{xx} = \frac{\mu_i}{2jk_{z_i}}\left[e^{-jk_{z_i}|z-z'|} + A^e_h e^{jk_{z_i}(z-z')} + C^e_h e^{-jk_{z_i}(z-z')}\right] \tag{116}$$

$$\tilde{G}^A_{zx} = \frac{-\mu_i}{2jk_{z_i}}\left[\frac{k_x k_{z_i}}{k_\rho^2}\left(A^e_h + B^e_h\right)e^{jk_{z_i}(z-z')} + \frac{k_x k_{z_i}}{k_\rho^2}\left(D^e_h - C^e_h\right)e^{-jk_{z_i}(z-z')}\right] \tag{117}$$

$$\tilde{G}^{q_e}_x = \frac{1}{2j\epsilon_i k_{z_i}}\left[e^{-jk_{z_i}|z-z'|} + \frac{k_{z_i}^2 B^e_h + k_i^2 A^e_h}{k_\rho^2}e^{jk_{z_i}(z-z')} + \frac{k_i^2 C^e_h - k_{z_i}^2 D^e_h}{k_\rho^2}e^{-jk_{z_i}(z-z')}\right] \tag{118}$$

$$\tilde{G}^F_{xx} = \frac{\epsilon_i}{2jk_{z_i}}\left[e^{-jk_{z_i}|z-z'|} + A^m_h e^{jk_{z_i}(z-z')} + C^m_h e^{-jk_{z_i}(z-z')}\right] \tag{119}$$

$$\tilde{G}^F_{zx} = \frac{-\epsilon_i}{2jk_{z_i}}\left[\frac{k_x k_{z_i}}{k_\rho^2}\left(A^m_h + B^m_h\right)e^{jk_{z_i}(z-z')} + \frac{k_x k_{z_i}}{k_\rho^2}\left(D^m_h - C^m_h\right)e^{-jk_{z_i}(z-z')}\right] \tag{120}$$

$$\tilde{G}^{q_m}_x = \frac{1}{2j\mu_i k_{z_i}}\left[e^{-jk_{z_i}|z-z'|} + \frac{k_{z_i}^2 B^m_h + k_i^2 A^m_h}{k_\rho^2}e^{jk_{z_i}(z-z')} + \frac{k_i^2 C^m_h - k_{z_i}^2 D^m_h}{k_\rho^2}e^{-jk_{z_i}(z-z')}\right] \tag{121}$$

$$\tilde{G}^A_{zz} = \frac{\mu_i}{2jk_{z_i}}\left[e^{-jk_{z_i}|z-z'|} + A^e_v e^{-jk_{z_i}(z-z')} + B^e_v e^{jk_{z_i}(z-z')}\right] \tag{122}$$

$$\tilde{G}^{q_e}_z = \frac{1}{2j\epsilon_i k_{z_i}}\left[e^{-jk_{z_i}|z-z'|} + C^e_v e^{-jk_{z_i}(z-z')} + D^e_v e^{jk_{z_i}(z-z')}\right] \tag{123}$$

$$\tilde{G}^F_{zz} = \frac{\epsilon_i}{2jk_{z_i}}\left[e^{-jk_{z_i}|z-z'|} + A^m_v e^{-jk_{z_i}(z-z')} + B^m_v e^{jk_{z_i}(z-z')}\right] \tag{124}$$

$$\tilde{G}^{q_m}_z = \frac{1}{2j\mu_i k_{z_i}}\left[e^{-jk_{z_i}|z-z'|} + C^m_v e^{-jk_{z_i}(z-z')} + D^m_v e^{jk_{z_i}(z-z')}\right] \tag{125}$$

where the superscript A and F denote the electric and magnetic vector potentials, respectively, and q_e and q_m denote the electric and magnetic scalar potentials, respectively. The coefficients, $A_{h,v}^{e,m}$, $B_{h,v}^{e,m}$, $C_{h,v}^{e,m}$, and $D_{h,v}^{e,m}$ are functions of the generalized reflection coefficients, and are given [13, 15] as

$$A_h^{e,m} = \tilde{R}_{TE,TM}^{i,i+1} M_i^{TE,TM} \left[e^{-2jk_{z_i}(d_i - z')} + \tilde{R}_{TE,TM}^{i,i-1} e^{-2jk_{z_i} d_i} \right] \tag{126}$$

$$B_h^{e,m} = \tilde{R}_{TM,TE}^{i,i+1} M_i^{TM,TE} \left[e^{-2jk_{z_i}(d_i - z')} - \tilde{R}_{TM,TE}^{i,i-1} e^{-2jk_{z_i} d_i} \right] \tag{127}$$

$$C_h^{e,m} = \tilde{R}_{TE,TM}^{i,i-1} M_i^{TE,TM} \left[e^{-2jk_{z_i} z'} + \tilde{R}_{TE,TM}^{i,i+1} e^{-2jk_{z_i} d_i} \right] \tag{128}$$

$$D_h^{e,m} = \tilde{R}_{TM,TE}^{i,i-1} M_i^{TM,TE} \left[-e^{-2jk_{z_i} z'} + \tilde{R}_{TM,TE}^{i,i+1} e^{-2jk_{z_i} d_i} \right] \tag{129}$$

$$A_v^{e,m} = \tilde{R}_{TM,TE}^{i,i-1} M_i^{TM,TE} \left[e^{-2jk_{z_i} z'} + \tilde{R}_{TM,TE}^{i,i+1} e^{-2jk_{z_i} d_i} \right] \tag{130}$$

$$B_v^{e,m} = \tilde{R}_{TM,TE}^{i,i+1} M_i^{TM,TE} \left[e^{-2jk_{z_i}(d_i - z')} + \tilde{R}_{TM,TE}^{i,i-1} e^{-2jk_{z_i} d_i} \right] \tag{131}$$

$$C_v^{e,m} = \tilde{R}_{TM,TE}^{i,i-1} M_i^{TM,TE} \left[-e^{-2jk_{z_i} z'} + \tilde{R}_{TM,TE}^{i,i+1} e^{-2jk_{z_i} d_i} \right] \tag{132}$$

$$D_v^{e,m} = \tilde{R}_{TM,TE}^{i,i+1} M_i^{TM,TE} \left[-e^{-2jk_{z_i}(d_i - z')} + \tilde{R}_{TM,TE}^{i,i-1} e^{-2jk_{z_i} d_i} \right] \tag{133}$$

where

$$M_i^{TE,TM} = \left[1 - \tilde{R}_{TE,TM}^{i,i+1} \tilde{R}_{TE,TM}^{i,i-1} e^{-jk_{z_i} 2d_i} \right]^{-1} \tag{134}$$

$$\tilde{R}_{TE,TM}^{j+1,j} = \frac{R_{TE,TM}^{j+1,j} + \tilde{R}_{TE,TM}^{j,j-1} e^{-jk_{z_j} 2d_j}}{1 - R_{j,j+1} \tilde{R}_{TE,TM}^{j,j-1} e^{-jk_{z_j} 2d_j}} \tag{135}$$

Here R and $\tilde{R}$ are the Fresnel and generalized reflection coefficients [13] for which the subscripts TE and TM represent the polarization of the wave, and the superscripts show the layer numbers. The subscripts h and v represent the orientation of the source, horizontal and vertical, respectively, while the superscripts e and m denote the type of the source, electric and magnetic, respectively. It should be noted that the Green's functions for y-oriented dipoles can be obtained simply by setting $\tilde{G}_{yy}^{A,F} = \tilde{G}_{xx}^{A,F}$, $\tilde{G}_{zy}^{A,F}/k_y = \tilde{G}_{zx}^{A,F}/k_x$, and $\tilde{G}_y^{q_{e,m}} = \tilde{G}_x^{q_{e,m}}$.

When the observation layer is different from the source layer, the Green's functions are modified by using the appropriate boundary conditions and following iterative expressions [13]:

$$A_j^- = A_{j+1}^- \frac{T_{j+1,j} e^{-j\left(k_{z_{j+1}} - k_{z_j}\right)(z' + z_{i-j+1})}}{1 - R_{j,j+1} \tilde{R}_{j,j-1} e^{-jk_{z_j} 2d_j}} \tag{136}$$

$$A_j^+ = A_{j-1}^+ \frac{T_{j-1,j} e^{-j\left(k_{z_{j-1}} - k_{z_j}\right)(z_{i-j-1}+d_i-z')}}{1 - R_{j,j-1}\tilde{R}_{j,j+1} e^{-jk_{z_j}2d_j}} \tag{137}$$

where A_j^- and A_j^+ are the amplitudes of the down- and up-going waves, respectively, and T is the transmission coefficient. So, the field expressions in any layer can be obtained iteratively starting from the source layer.

Substituting (126), (127), (128) and (129) into (117), the following expression is obtained;

$$\begin{aligned}
\tilde{G}_{zx}^A \quad = \quad & -\frac{\mu_i}{2jk_{z_i}} \Bigg\{ \frac{k_x k_{z_i}}{k_\rho^2} \Big(\tilde{R}_{TE}^{i,i+1} M_i^{TE} \left[e^{-jk_{z_i}(2d_i - z' - z)} + \tilde{R}_{TE}^{i,i-1} e^{-jk_{z_i}(2d_i + z' - z)} \right] \\
& + \tilde{R}_{TM}^{i,i+1} M_i^{TM} \left[e^{-jk_{z_i}(2d_i - z' - z)} - \tilde{R}_{TM}^{i,i-1} e^{-jk_{z_i}(2d_i + z' - z)} \right] \Big) \\
& + \frac{k_x k_{z_i}}{k_\rho^2} \Big(\tilde{R}_{TM}^{i,i-1} M_i^{TM} \left[-e^{-jk_{z_i}(z+z')} + \tilde{R}_{TM}^{i,i+1} e^{-jk_{z_i}(2d_i + z - z')} \right] \\
& - \tilde{R}_{TE}^{i,i-1} M_i^{TE} \left[e^{-jk_{z_i}(z+z')} + \tilde{R}_{TE}^{i,i+1} e^{-jk_{z_i}(2d_i + z - z')} \right] \Big) \Bigg\}
\end{aligned} \tag{138}$$

Then, re-arranging the terms results in

$$\begin{aligned}
\tilde{G}_{zx}^A \quad = \quad & -jk_x \frac{\mu_i}{2jk_{z_i}} \frac{-jk_{z_i}}{k_\rho^2} \Bigg\{ e^{-jk_{z_i}(2d_i - z' - z)} \left(\tilde{R}_{TE}^{i,i+1} M_i^{TE} + \tilde{R}_{TM}^{i,i+1} M_i^{TM} \right) \\
& + e^{-jk_{z_i}(2d_i + z' - z)} \left(\tilde{R}_{TE}^{i,i+1} \tilde{R}_{TE}^{i,i-1} M_i^{TE} - \tilde{R}_{TM}^{i,i+1} \tilde{R}_{TM}^{i,i-1} M_i^{TM} \right) \\
& + e^{-jk_{z_i}(2d_i + z - z')} \left(\tilde{R}_{TM}^{i,i-1} \tilde{R}_{TM}^{i,i+1} M_i^{TM} - \tilde{R}_{TE}^{i,i-1} \tilde{R}_{TE}^{i,i+1} M_i^{TE} \right) \\
& + e^{-jk_{z_i}(z' + z)} \left(-\tilde{R}_{TE}^{i,i-1} M_i^{TE} - \tilde{R}_{TM}^{i,i-1} M_i^{TM} \right) \Bigg\}
\end{aligned} \tag{139}$$

Substituting (126), (127), (128) and (129) into (118), the following expression is obtained;

$$\begin{aligned}
\tilde{G}_x^{q_e} \quad = \quad & \frac{1}{2j\epsilon_i k_{z_i}} \Bigg\{ e^{-jk_{z_i}|z-z'|} \\
& + \frac{k_{z_i}^2}{k_\rho^2} \tilde{R}_{TM}^{i,i+1} M_i^{TM} \left[e^{-jk_{z_i}(2d_i - z' - z)} - \tilde{R}_{TM}^{i,i-1} e^{-jk_{z_i}(2d_i + z' - z)} \right] \\
& + \frac{k_i^2}{k_\rho^2} \tilde{R}_{TE}^{i,i+1} M_i^{TE} \left[e^{-jk_{z_i}(2d_i - z' - z)} + \tilde{R}_{TE}^{i,i-1} e^{-jk_{z_i}(2d_i + z' - z)} \right] \\
& + \frac{k_i^2}{k_\rho^2} \tilde{R}_{TE}^{i,i-1} M_i^{TE} \left[e^{-jk_{z_i}(z+z')} + \tilde{R}_{TE}^{i,i+1} e^{-jk_{z_i}(2d_i + z - z')} \right] \\
& - \frac{k_{z_i}^2}{k_\rho^2} \tilde{R}_{TM}^{i,i-1} M_i^{TM} \left[-e^{-jk_{z_i}(z+z')} + \tilde{R}_{TM}^{i,i+1} e^{-jk_{z_i}(2d_i + z - z')} \right] \Bigg\}
\end{aligned} \tag{140}$$

Then, re-arranging the terms results in

$$\tilde{G}_x^{q_e} \quad = \quad \frac{1}{2j\epsilon_i k_{z_i}} \Bigg\{ e^{-jk_{z_i}|z-z'|}$$

$$
\begin{aligned}
&+ \quad e^{-jk_{z_i}(2d_i-z'-z)}\left(\frac{k_{z_i}^2}{k_\rho^2}\tilde{R}_{TM}^{i,i+1}M_i^{TM}+\frac{k_i^2}{k_\rho^2}\tilde{R}_{TE}^{i,i+1}M_i^{TE}\right)\\
&+ \quad e^{-jk_{z_i}(2d_i+z'-z)}\left(-\frac{k_{z_i}^2}{k_\rho^2}\tilde{R}_{TM}^{i,i+1}\tilde{R}_{TM}^{i,i-1}M_i^{TM}+\frac{k_i^2}{k_\rho^2}\tilde{R}_{TE}^{i,i+1}\tilde{R}_{TE}^{i,i-1}M_i^{TE}\right)\\
&+ \quad e^{-jk_{z_i}(2d_i+z-z')}\left(-\frac{k_{z_i}^2}{k_\rho^2}\tilde{R}_{TM}^{i,i+1}\tilde{R}_{TM}^{i,i-1}M_i^{TM}+\frac{k_i^2}{k_\rho^2}\tilde{R}_{TE}^{i,i-1}\tilde{R}_{TE}^{i,i+1}M_i^{TE}\right)\\
&+ \quad e^{-jk_{z_i}(z'+z)}\left(\frac{k_{z_i}^2}{k_\rho^2}\tilde{R}_{TM}^{i,i-1}M_i^{TM}+\frac{k_i^2}{k_\rho^2}\tilde{R}_{TE}^{i,i-1}M_i^{TE}\right)\Bigg\} \qquad (141)
\end{aligned}
$$

Substituting (130) and (131) into (122), the following expression is obtained;

$$
\begin{aligned}
\tilde{G}_{zz}^{A} &= \frac{\mu_i}{2jk_{z_i}}\Bigg\{e^{-jk_{z_i}|z-z'|}+\tilde{R}_{TM}^{i,i-1}M_i^{TM}\left[e^{-jk_{z_i}(z+z')}+\tilde{R}_{TM}^{i,i+1}e^{-jk_{z_i}(z-z'+2d_i)}\right]\\
&+ \tilde{R}_{TM}^{i,i+1}M_i^{TM}\left[e^{-jk_{z_i}(2d_i-z-z')}+\tilde{R}_{TM}^{i,i-1}e^{-jk_{z_i}(z'-z+2d_i)}\right]\Bigg\} \qquad (142)
\end{aligned}
$$

Then, re-arranging the terms results in

$$
\begin{aligned}
\tilde{G}_{zz}^{A} &= \frac{\mu_i}{2jk_{z_i}}\Big\{e^{-jk_{z_i}|z-z'|}+\tilde{R}_{TM}^{i,i+1}M_i^{TM}e^{-jk_{z_i}(2d_i-z'-z)}+e^{-jk_{z_i}(z'+z)}\tilde{R}_{TM}^{i,i-1}M_i^{TM}\\
&+ \tilde{R}_{TM}^{i,i+1}\tilde{R}_{TM}^{i,i-1}M_i^{TM}e^{-jk_{z_i}(2d_i+z'-z)}+\tilde{R}_{TM}^{i,i-1}\tilde{R}_{TM}^{i,i+1}M_i^{TM}e^{-jk_{z_i}(2d_i+z-z')}\Big\} \qquad (143)
\end{aligned}
$$

Substituting (132) and (133) into (123), the following expression is obtained;

$$
\begin{aligned}
\tilde{G}_{z}^{q_e} &= \frac{1}{2jk_{z_i}\epsilon_i}\Bigg\{e^{-jk_{z_i}|z-z'|}+\tilde{R}_{TM}^{i,i-1}M_i^{TM}\left[-e^{-jk_{z_i}(z+z')}+\tilde{R}_{TM}^{i,i+1}e^{-jk_{z_i}(z-z'+2d_i)}\right]\\
&+ \tilde{R}_{TM}^{i,i+1}M_i^{TM}\left[-e^{-jk_{z_i}(2d_i-z-z')}+\tilde{R}_{TM}^{i,i-1}e^{-jk_{z_i}(z'-z+2d_i)}\right]\Bigg\} \qquad (144)
\end{aligned}
$$

Then, re-arranging the terms results in

$$
\begin{aligned}
\tilde{G}_{z}^{q_e} &= \frac{1}{2jk_{z_i}\epsilon_i}\Big\{e^{-jk_{z_i}|z-z'|}-\tilde{R}_{TM}^{i,i+1}M_i^{TM}e^{-jk_{z_i}(2d_i-z'-z)}-e^{-jk_{z_i}(z'+z)}\tilde{R}_{TM}^{i,i-1}M_i^{TM}\\
&+ \tilde{R}_{TM}^{i,i+1}\tilde{R}_{TM}^{i,i-1}M_i^{TM}e^{-jk_{z_i}(2d_i+z'-z)}+\tilde{R}_{TM}^{i,i-1}\tilde{R}_{TM}^{i,i+1}M_i^{TM}e^{-jk_{z_i}(2d_i+z-z')}\Big\} \qquad (145)
\end{aligned}
$$

APPENDIX C

EVALUATION OF THE INNER PRODUCTS IN MOM FORMULATIONS

In Chapter 3, the evaluation of the inner-products corresponding to the vertical metallizations is demonstrated on a typical inner-product term. In this appendix, the evaluations of the other inner-products containing integration operations on z and z' variables are given. It is assumed that $T_z^{l'} = T_z^{l'}(y,\, z) = T_z^{l'}(y)\, T_z^{l'}(z)$.

C.1 Evaluation of $\left\langle \frac{\partial}{\partial z} T_z^{l'},\; G_x^{q_e} * \frac{\partial B_x^m}{\partial x} \right\rangle$

This term contains integration and derivation with respect to z, and the inner product is written as follows

$$\begin{aligned} \left\langle \frac{\partial}{\partial z} T_{zm},\; G_x^{q_e} * \frac{\partial B_x^m}{\partial x} \right\rangle &= \iint dz\, dy\, \frac{\partial}{\partial z} T_z^{l'}(y,\, z) \\ &\quad \cdot \iint dx'\, dy'\, G_x^{q_e}(x - x',\, y - y',\, z) \frac{\partial}{\partial x'} B_x^m(x',\, y') \end{aligned} \tag{146}$$

At first, the spatial-domain Green's function in (146) is replaced with the spectral-domain Green's function by using (2) and then the integration with respect to z is considered:

$$\begin{aligned} F_x^{q_e} &\stackrel{\text{def}}{=} \int dz\, \frac{\partial}{\partial z} T_z^{l'}(z) \frac{1}{4\pi} \int_{SIP} dk_\rho\, k_\rho H_0^{(2)}(k_\rho \rho)\, \tilde{G}_x^{q_e}(k_\rho) \\ &= \frac{1}{4\pi} \int_{SIP} dk_\rho\, k_\rho H_0^{(2)}(k_\rho \rho) \int dz\, \frac{\partial}{\partial z} T_z^{l'}(z) \tilde{G}_x^{q_e}(k_\rho) \end{aligned} \tag{147}$$

where $\tilde{G}_x^{q_e}$ is given in (141). After evaluating the z integral, the inner-product (146) reduces to

$$\left\langle \frac{\partial}{\partial z} T_z^{l'},\; G_x^{q_e} * \frac{\partial B_x^m}{\partial x} \right\rangle = \int dy\, T_z^{l'}(y) \iint dx'\, dy'\, F_x^{q_e} \frac{\partial}{\partial x'} B_x^m(x',\, y') \tag{148}$$

by making the substitutions $x - x' = u$ and $y - y' = v$, the following expression is obtained

$$\left\langle \frac{\partial}{\partial z} T_z^{l'},\; G_x^{q_e} * \frac{\partial B_x^m}{\partial x} \right\rangle = \iint du\, dv\, F_x^{q_e} \int dy\, T_z^{l'}(y) \frac{\partial}{\partial x'} B_x^m(x - u,\, y - v) \tag{149}$$

where $x = x_i$.

C.2 Evaluation of $\left\langle \frac{\partial}{\partial x} T_x^m,\ G_z^{q_e} * \frac{\partial B_z^l}{\partial z} \right\rangle$

This term contains integration and derivation with respect to z, and the inner product is written as follows

$$\begin{aligned} \left\langle \frac{\partial}{\partial x} T_x^m,\ G_z^{q_e} * \frac{\partial B_z^l}{\partial z} \right\rangle &= \iint dx\, dy\, \frac{\partial}{\partial x} T_x^m(x,\, y) \\ &\quad \cdot \iint dz'\, dy'\, G_z^{q_e}(x - x',\, y - y',\, z') \frac{\partial}{\partial z'} B_z^l(y',\, z') \end{aligned} \tag{150}$$

At first, the spatial-domain Green's function in (150) is replaced with the spectral-domain Green's function by using (2) and then the integration with respect to z is considered:

$$\begin{aligned} F_z^{q_1} &\overset{\text{def}}{=} \int dz'\, \frac{\partial}{\partial z'} B_z^l(z') \frac{1}{4\pi} \int_{SIP} dk_\rho\, k_\rho H_0^{(2)}\left(k_\rho \rho\right) \tilde{G}_z^{q_e}\left(k_\rho\right) \\ &= \frac{1}{4\pi} \int_{SIP} dk_\rho\, k_\rho H_0^{(2)}\left(k_\rho \rho\right) \int dz'\, \frac{\partial}{\partial z'} B_z^l(z') \tilde{G}_z^{q_e}\left(k_\rho\right) \end{aligned} \tag{151}$$

where $\tilde{G}_z^{q_e}$ is given in (144). After evaluating the z' integral, the inner-product (150) reduces to

$$\left\langle \frac{\partial}{\partial x} T_x^m,\ G_z^{q_e} * \frac{\partial B_z^l}{\partial z} \right\rangle = \iint dx\, dy\, \frac{\partial}{\partial x} T_x^m(x,\, y) \int dy'\, F_z^{q_1} B_z^l\left(y'\right) \tag{152}$$

by making the substitutions $x - x' = u$ and $y - y' = v$, the following expression is obtained

$$\left\langle \frac{\partial}{\partial x} T_x^m,\ G_z^{q_e} * \frac{\partial B_z^l}{\partial z} \right\rangle = - \iint du\, dv\, F_z^{q_1} \int dy\, \frac{\partial}{\partial x} T_x^m(x' + u,\, y) B_z^l\left(y - v\right) \tag{153}$$

where $x' = x_i$.

C.3 Evaluation of $\left\langle \frac{\partial}{\partial z} T_z^{l'},\ G_z^{q_e} * \frac{\partial B_z^l}{\partial z} \right\rangle$

This term contains integration and derivation with respect to z and z', and the inner product is written as follows

$$\begin{aligned} \left\langle \frac{\partial}{\partial z} T_z^{l'},\ G_z^{q_e} * \frac{\partial B_z^l}{\partial z} \right\rangle &= \iint dz\, dy\, \frac{\partial}{\partial z} T_z^{l'}(y,\, z) \\ &\quad \cdot \iint dz'\, dy'\, G_z^{q_e}(x - x',\, y - y',\, z,\, z') \frac{\partial}{\partial z'} B_z^l(y',\, z') \end{aligned} \tag{154}$$

At first, the spatial-domain Green's function in (154) is replaced with the spectral-domain Green's function by using (2) and then the integrations with respect to z and z' are considered:

$$F_z^{q_2} \overset{\text{def}}{=} \iint dz\, dz'\, \frac{\partial}{\partial z} T_z^{l'}(z) \frac{1}{4\pi} \int_{SIP} dk_\rho\, k_\rho H_0^{(2)}\left(k_\rho \rho\right) \tilde{G}_z^{q_e}\left(k_\rho\right) \frac{\partial}{\partial z'} B_z^l(z')$$

$$= \frac{1}{4\pi}\int_{SIP} dk_\rho\, k_\rho H_0^{(2)}(k_\rho\rho) \iint dz\, dz'\, \frac{\partial}{\partial z} T_z^{l'}(z) \frac{\partial}{\partial z'} B_z^l(z') \tilde{G}_z^{q_e}(k_\rho) \tag{155}$$

where $\tilde{G}_z^{q_e}$ is given in (144). After evaluating the z and z' integrals, the inner-product (154) reduces to

$$\left\langle \frac{\partial}{\partial z} T_z^{l'},\ G_z^{q_e} * \frac{\partial B_z^l}{\partial z} \right\rangle = \int dy\, T_z^{l'}(y) \int dy'\, F_z^{q_2} B_z^l(y') \tag{156}$$

by making the substitution $y - y' = v$, the following expression is obtained

$$\left\langle \frac{\partial}{\partial z} T_z^{l'},\ G_z^{q_e} * \frac{\partial B_z^l}{\partial z} \right\rangle = -\int dv\, F_z^{q_2} \int dy\, T_z^{l'}(y) B_z^l(y - v) \tag{157}$$

where $x = x' = x_i$.

C.4 Evaluation of $\left\langle T_z^{l'},\ G_{zz}^A * B_z^l \right\rangle$

This term contains integration with respect to z and z', and the inner product is written as follows

$$\begin{aligned} \left\langle T_z^{l'},\ G_{zz}^A * B_z^l \right\rangle &= \iint dz\, dy\, T_z^{l'}(y,\, z) \\ &\quad \cdot \iint dz'\, dy'\, G_{zz}^A(x - x',\, y - y',\, z,\, z') B_z^l(y',\, z') \end{aligned} \tag{158}$$

At first, the spatial-domain Green's function in (158) is replaced with the spectral-domain Green's function by using (2) and then the integrations with respect to z and z' are considered:

$$\begin{aligned} F_{zz}^A &\overset{\text{def}}{=} \iint dz\, dz'\, T_z^{l'}(z) \frac{1}{4\pi} \int_{SIP} dk_\rho\, k_\rho H_0^{(2)}(k_\rho\rho)\, \tilde{G}_{zz}^A(k_\rho)\, B_z^l(z') \\ &= \frac{1}{4\pi} \int_{SIP} dk_\rho\, k_\rho H_0^{(2)}(k_\rho\rho) \iint dz\, dz'\, T_z^{l'}(z) B_z^l(z') \tilde{G}_{zz}^A(k_\rho) \end{aligned} \tag{159}$$

where $\tilde{G}_{zz}^A$ is given in (142). After evaluating the z and z' integrals, the inner-product (158) reduces to

$$\left\langle T_z^{l'},\ G_{zz}^A * B_z^l \right\rangle = \int dy\, T_z^{l'}(y) \int dy'\, B_z^l(x',\, y')\, F_{zz}^A \tag{160}$$

by making the substitution $y - y' = v$, the following expression is obtained

$$\left\langle T_z^{l'},\ G_{zz}^A * B_z^l \right\rangle = -\int dv\, F_{zz}^A \int dy\, T_z^{l'}(y) B_z^l(y - v) \tag{161}$$

where $x = x' = x_i$.

APPENDIX D

ANALYTICAL EVALUATIONS OF SOME INTEGRALS

In the various implementations of the MoM and LCN formulations discussed in previous chapters, the actual integrals are evaluated analytically for each term in a Taylor series expansion of the Green's function. The integrals involve the distance R defined as

$$R = \sqrt{u^2 + v^2 - \alpha^2} = \sqrt{u^2 + v^2 + c^2} \tag{162}$$

where α and c are complex constants. The following integrals arise in the evaluation:

$$\begin{aligned}
J_0 &= \int R\,du = \frac{1}{2}\left(Ru + (v^2+c^2)\ln(u+R)\right) \\
J_1 &= \int uR\,du = \frac{R^3}{3} \\
J_n &= \int u^n R\,du = \frac{u^{n-1}}{n+2}R^3 - \frac{n-1}{n+2}(v^2+c^2)J_{n-2} \\
K_0 &= \int \frac{1}{R}\,du = \ln(u+R) \\
K_1 &= \int \frac{u}{R}\,du = R \\
K_n &= \int \frac{u^n}{R}\,du = J_{n-2} - (v^2+c^2)K_{n-2} \\
I_0 &= \int \frac{1}{(u^2+c^2)R}\,du = \frac{1}{vc}\arctan\left(\frac{uv}{cR}\right) \\
I_1 &= \int \frac{u}{(u^2+c^2)R}\,du = \frac{\ln(R-v) - \ln(R+v)}{2v} \\
I_n &= \int \frac{u^n}{(u^2+c^2)R}\,du = K_{n-2} - c^2 I_{n-2} \\
L_0 &= \int \frac{1}{u^2+c^2}\,du = \frac{1}{c}\arctan\left(\frac{u}{c}\right) \\
L_1 &= \int \frac{u}{u^2+c^2}\,du = \frac{\ln(u^2+c^2)}{2} \\
L_n &= \int \frac{u^n}{u^2+c^2}\,du = \frac{u^{n-1}}{n-1} - c^2 L_{n-2} \\
M_n &= \int\int \frac{u^n}{R}\,dvdu = \frac{u^{n+1}\ln(v+R) - L_{n+2} + vI_{n+2}}{n+1}
\end{aligned}$$

Using the preceding quantities, the following integrals may be evaluated according to

$$
\begin{aligned}
\int\int \frac{u^n}{R}\,dvdu &= M_n \\
\int\int \frac{u^n v}{R}\,dvdu &= J_n \\
\int\int \frac{u^n v^2}{R}\,dvdu &= \frac{vJ_n - M_{n+2} - c^2 M_n}{2} \\
\int\int \frac{u^n v^3}{R}\,dvdu &= \frac{-2J_{n+2} + (v^2 - 2c^2)J_n}{3} \\
\int\int \frac{u^n v^4}{R}\,dvdu &= \frac{-3vJ_{n+2} + v(2v^2 - 3c^2)J_n + 3(M_{n+4} + 2c^2 M_{n+2} + c^4 M_n)}{8} \\
\int\int u^n v^m\,dvdu &= \frac{u^{n+1}}{n+1}\frac{v^{m+1}}{m+1} \\
\int\int u^n R\,dvdu &= \frac{vJ_n + M_{n+2} + c^2 M_n}{2} \\
\int\int u^n vR\,dvdu &= \frac{J_{n+2} + (v^2 + c^2)J_n}{3} \\
\int\int u^n v^2 R\,dvdu &= \frac{vJ_{n+2} + v(2v^2 + c^2)J_n - M_{n+4} - 2c^2 M_{n+2} - c^4 M_n}{8} \\
\int\int u^n v^3 R\,dvdu &= \frac{-2J_{n+4} + (v^2 - 4c^2)J_{n+2} + (3v^4 + v^2c^2 - 2c^4)J_n}{15} \\
\int\int u^n v^4 R\,dvdu &= \frac{-3vJ_{n+4} + 2v(v^2 - 3c^2)J_{n+2} + v(8v^4 + 2v^2c^2 - 3c^4)J_n}{48} \\
\int\int u^n v^m R^2\,dvdu &= \frac{u^{n+3}}{n+3}\frac{v^{m+1}}{m+1} + \frac{u^{n+1}}{n+1}\frac{v^{m+3}}{m+3} + c^2\frac{u^{n+1}}{n+1}\frac{v^{m+1}}{m+1} \\
\int\int u^n R^3\,dvdu &= \frac{5vJ_{n+2} + v(2v^2 + 5c^2))J_n + 3(M_{n+4} + 2c^2 M_{n+2} + c^4 M_n)}{8} \\
\int\int u^n vR^3\,dvdu &= \frac{J_{n+4} + 2(v^2 + c^2)J_{n+2} + (v^2 + c^2)^2 J_n}{5} \\
\int\int u^n v^2 R^3\,dvdu &= \frac{3vJ_{n+4} + (14v^3 + 6c^2 v)J_{n+2} + (v^3(8v^2 + 14c^2) + 3c^4 v)J_n}{48} \\
&\quad - \frac{3(M_{n+6} + 3c^2 M_{n+4} + 3c^4 M_{n+2} + c^6 M_n)}{48} \\
\int\int u^n v^3 R^3\,dvdu &= \frac{-2J_{n+6} + (v^2 - 6c^2)J_{n+4} + (8v^4 + 2v^2c^2 - 6c^4)J_{n+2}}{35} \\
&\quad + \frac{(5v^6 + 8v^4c^2 + v^2c^4 - 2c^6)J_n}{35} \\
\int\int u^n v^4 R^3\,dvdu &= \frac{v[-3J_{n+6} + (2v^2 - 9c^2)J_{n+4} + (24v^4 + 4v^2c^2 - 9c^4)J_{n+2}]}{128} \\
&\quad + \frac{v(16v^6 + 24v^4c^2 + 2v^2c^4 - 3c^6)J_n}{128} \\
&\quad + \frac{3(M_{n+8} + 4c^2 M_{n+6} + 6c^4 M_{n+4} + 4c^6 M_{n+2} + c^8 M_n)}{128} \\
\int\int u^n v^m R^4\,dvdu &= \frac{u^{n+1}}{n+1}\frac{v^{m+5}}{m+5} + 2\left(\frac{u^{n+3}}{n+3} + c^2\frac{u^{n+1}}{n+1}\right)\frac{v^{m+3}}{m+3}
\end{aligned}
$$

$$+\left(\frac{u^{n+5}}{n+5}+2c^2\frac{u^{n+3}}{n+3}+c^4\frac{u^{n+1}}{n+1}\right)\frac{v^{m+1}}{m+1}$$

APPENDIX E

LEGENDRE POLYNOMIALS AND GAUSSIAN QUADRATURE

We seek to represent the integral

$$\int_a^b f(x)\,dx \tag{163}$$

by the sum

$$\alpha_0 f(x_0) + \alpha_1 f(x_1) + \cdots + \alpha_n f(x_n) \tag{164}$$

where $x_0, x_1, \ldots, x_n$ are in the interval $[a, b]$. It is convenient to introduce the new independent variable u defined by the equivalent relations

$$\begin{aligned} u &= \frac{2x - (a+b)}{b-a} \\ x &= \frac{(b-a)u + (a+b)}{2} \end{aligned}$$

so that the interval $[a, b]$ corresponds to the interval $[-1, 1]$. The task is equivalent to the integration

$$\int_{-1}^{1} \phi(u)\,du = \frac{2}{b-a}\int_a^b f(x)\,dx \cong \alpha_0\phi(u_0) + \alpha_1\phi(u_1) + \cdots + \alpha_n\phi(u_n) \tag{165}$$

where $u_0, u_1, \ldots, u_n$ lie in the interval $[-1, 1]$. The procedure for determining the α_i and u_i is as follows. We determine the u_i as the roots of the polynomial equation

$$P_{n+1}(u) = 0 \tag{166}$$

where the Legendre polynomial of the degree n, $P_n(u)$ is defined by

$$P_n(u) = \frac{1}{2^n n!}\frac{d^n}{du^n}(u^2 - 1)^n \tag{167}$$

where n is a nonnegative integer and some of the polynomials are given as

$$P_0(u) = 1$$

$$
\begin{aligned}
P_1(u) &= u \\
P_2(u) &= \frac{3u^2-1}{2} \\
P_3(u) &= \frac{5u^3-3u}{2} \\
P_4(u) &= \frac{35u^4-30u^2+3}{8}
\end{aligned}
$$

Having found the u_i, the calculation of α_i is as follows

$$\alpha_k = \int_{-1}^{1} \omega_k(u)\, du \tag{168}$$

where

$$\omega_k(u) = \prod_{j=0(j\neq k)}^{n} \frac{u-u_j}{u_k-u_j} \tag{169}$$

The integral can be approximated by

$$\int_a^b f(x)\, dx \cong \frac{b-a}{2} \sum_{k=0}^{n} \alpha_k\, f\left(\frac{(b-a)u_k+(a+b)}{2}\right) \tag{170}$$

REFERENCES

[1] Aksun, M. I., "A robust approach for the derivation of closed-form Green's Functions," *IEEE Trans. on Microwave Theory Tech.*, vol. 44, pp. 651–658, May 1996.

[2] Aksun, M. I. and Mittra, R., "Derivation of closed-form Green's functions for a general microstrip geometry," *IEEE Trans. on Microwave Theory Tech.*, vol. 40, pp. 2055–2062, Nov. 1992.

[3] Aksun, M. I. and Mittra, R., "Spurious radiation from microstrip interconnects," *IEEE Trans. Electromagnetic Compat.*, vol. EMC-35, pp. 148–158, May 1993.

[4] Aksun, M. I., Çalışkan, F. and Gürel, L., "An efficient method for electromagnetic characterization of 2-D geometries in stratified media," *IEEE Trans. on Microwave Theory Tech.*, vol. 50, pp. 1264–1274, May 2002.

[5] Alatan, L., *Use of Computationally Efficient MoM in the Analysis and Design of Printed Structures.* PhD thesis, Middle East Technical University, Ankara, Turkey, June 1997.

[6] Alatan, L., Aksun, M. I., Mahadevan, K., and Birand, T., "Analytical evaluation of the MoM matrix elements," *IEEE Trans. on Microwave Theory Tech.*, vol. 44, pp. 519–525, April 1996.

[7] Atkinson, K. E., *A Survey of Numerical Methods for the Solution of Fredholm Integral Equations of the Second Kind.* Philadelphia: SIAM, 1976.

[8] Bahl, I. J., "MIC simulation column," *International Journal of Millimeter-Wave Computer-Aided Engineering*, vol. 5, pp. 131–132, March 1995.

[9] Benedek, P. and Silvester, P., "Equivalent capacitance of microstrip gaps and steps," *IEEE Trans. on Microwave Theory Tech.*, vol. MTT-20, pp. 729–733, November 1972.

[10] Çalışkan, F., "Efficient methods for electromagnetic characterization of 2-D geometries in stratified media," Master's thesis, Bilkent University, Ankara, Turkey, August 1997.

[11] Canino, L. F., Ottusch, J.J., Stalzer, M. A., Visher, J.L. and Wandzura, S. M., "Numerical solution of the Helmholtz equation in 2d and 3d using a high-order Nyström discretization," *Journal of Computational Physics*, vol. 146, pp. 627–663, 1998.

[12] Chandra, R. and Gupta, K. C., "Segmentation method using impedance matrices for analysis of planar microwave circuits," *IEEE Trans. on Microwave Theory Tech.*, vol. MTT-329, pp. 71–74, January 1981.

[13] Chew, W. C., *Waves and Fields in Inhomogeneous Media.* Van Nostrand Reinhold, 1990.

[14] Chow, Y. L., Yang, J. J., Fang, D. G. and Howard, G. E., "A closed-form spatial Green's function for the thick microstrip substrate," *IEEE Trans. on Microwave Theory Tech.*, vol. 39, pp. 588–592, March 1991.

[15] Dural, G. and Aksun, M. I., "Closed-form Green's functions for general sources and stratified media," *IEEE Trans. on Microwave Theory Tech.*, vol. 43, pp. 1545–1552, July 1995.

[16] Eleftheriades, G. V., and Mosig, J. R., "On the network characterization of planar passive circuits using the method of moments," *IEEE Trans. on Microwave Theory Tech.*, vol. 44, pp. 438–445, March 1996.

[17] Gardiol, F., *Microstrip Circuits*. New York: John Wiley & Sons, Inc., 1994.

[18] Gedney, S. D., "Application of the high-order Nyström scheme to the integral equation solution of electromagnetic interaction problems," in *IEEE International Symposium on Electromagnetic Compatibility*, pp. 289–294, August 2000, Washington, D.C.

[19] Glisson, A. W., Rao, S. M. and Wilton, D. R., "Physically-based approximation of electromagnetic field quantities," in *IEEE AP-S International Symposium*, pp. 78–81, 2002, San Antonio, TX.

[20] Gupta, K. C. and Sharma, P. C., "Segmentation and desegmentation techniques for the analysis of planar microstrip antennas," in *IEEE AP-S International Symposium*, 1981.

[21] Gürel, L., Sertel, K. and Şendur, I. K., "On the choice of basis functions to model surface electric current densities in computational electromagnetics," *Radio Science*, vol. 34, pp. 1373–1387, Nov.-Dec. 1999.

[22] Harrington, R. F., "Matrix methods for field problems," *Proceedings of IEEE*, vol. 55, pp. 136–149, Feb. 1967.

[23] Harrington, R. F., *Field Computation by Moment Methods*. The Macmillan Company, 1968.

[24] Hua, Y. and Sarkar, T. K., "Generalized pencil-of-function method for extracting poles of an EM system from its transient response," *IEEE Trans. on Antennas and Propagation*, vol. AP-37, pp. 229–234, Feb. 1989.

[25] Itoh, T., "Analysis of microstrip resonators," *IEEE Trans. on Microwave Theory Tech.*, vol. MTT-22, pp. 946–952, November 1974.

[26] Jain, V. K., Sarkar, T. K., and Weiner, D. D., "Rational modeling by pencil-of-function method," *IEEE Trans. on Acoust., Sppech, Signal Processing*, vol. ASSP-31, pp. 564–573, June 1983.

[27] Jin, J., *The Finite Element Method in Electromagnetics*. New York: John Wiley & Sons, Inc., 1993.

[28] Kinayman, N., *A Novel CAD Algorithm for the Analysis of Printed Geometries*. PhD thesis, Bilkent University, Ankara, Turkey, May 1997.

[29] Kinayman, N. and Aksun, M. I., "Comparative study of acceleration techniques for integrals and series in electromagnetic problems," *Radio Science*, vol. 30, pp. 1713–1722, Nov.-Dec. 1995.

[30] Kinayman, N. and Aksun, M. I., "Efficient use of closed-form Green's functions for the analysis of planar geometries with vertical connections," *IEEE Trans. on Microwave Theory Tech.*, vol. 45, pp. 593–603, May 1997.

[31] Kipp, R., and Chan, C. H., "Triangular-domain basis functions for full-wave analysis of microstrip discontinuties," *IEEE Trans. on Microwave Theory Tech.*, vol. 41, pp. 1187–1194, June/July 1993.

[32] Kunz, K. and Luebbers, R., *The Finite Difference Time Domain Method for Electromagnetics*. Boca Raton, FL: CRC press, 1993.

[33] Liu, G. and Gedney, S. D., "High-order Nyström solution of the volume EFIE for TM-wave scattering," *Microwave and Optical Technology Letters*, vol. 25, pp. 8–11, April 2000.

[34] Liu, G. and Gedney, S. D., "High-order Nyström solution of the volume EFIE for TE-wave scattering," *Electromagnetics*, vol. 21, pp. 1–14, January 2001.

[35] Lo, Y. T., Solomon, D. and Richads, W. F., "Theory and experiment on microstrip antennas," *IEEE Trans. on Antennas and Propagation*, vol. AP-27, pp. 137–145, March 1979.

[36] Mahadevan, K. and Auda, H. A., "Electromagnetic field of a rectangular patch of uniform and linear distributions of current," *IEEE Trans. on Antennas and Propagation*, vol. 37, pp. 1503–1509, Dec. 1989.

[37] Marple, S. L., *Digital Spectral Analysis with Applications*. Englewood Cliffs, NJ: Prentice-Hall, 1987.

[38] Michalski, K. A., "On the scalar potential of a point charge associated with a time-harmonic dipole in a layered medium," *IEEE Trans. on Antennas and Propagation*, vol. AP-35, pp. 1299–1301, November 1987.

[39] Michalski, K. A. and Zheng, D., "Electromagnetic scattering and radiation by surfaces of arbitrary shape in layered media, part I: theory," *IEEE Trans. on Antennas and Propagation*, vol. AP-38, pp. 335–344, March 1990.

[40] Mosig, J. R., "Arbitrarily shaped microstrip structures and their analysis with a mixed potential integral equation," *IEEE Trans. on Microwave Theory Tech.*, vol. MTT-36, pp. 314–323, February 1988.

[41] Naishadham, K. and Nuteson, T. W., "Efficient analysis of passive microstrip elements in MMICs," *International Journal of Millimeter-Wave Computer-Aided Engineering*, vol. 4, pp. 219–229, July 1994.

[42] Nyström, E. J., "Uber die praktische auflosung von integral-gleichungen mit anwendungen auf randwertaufgaben," *Acta Matha.*, vol. 54, pp. 185–204, 1930.

[43] Park, I., Mittra, R., and Aksun, M. I., "Numerically efficient analysis of planar microstrip configurations using closed-form Green's functions," *IEEE Trans. on Microwave Theory Tech.*, vol. 43, pp. 394–400, February 1995.

[44] Rautio, J. C., "A de-embedding algorithm for electromagnetics," *International Journal of Millimeter-Wave Computer-Aided Engineering*, vol. 1, no. 3, pp. 282–287, 1991.

[45] Rautio, J. C. and Harrington, R. F., "An electromagnetic time-harmonic analysis of shielded microstrip circuits," *IEEE Trans. on Microwave Theory Tech.*, vol. MTT-35, pp. 726–730, August 1987.

[46] Sarkar, T. K., Maricevic, Z. A., and Kahrizi, M., "An accurate de-embedding procedure for characterizing discontinuities," *International Journal of Millimeter-Wave Computer-Aided Engineering*, vol. 2, no. 3, pp. 135–143, 1992.

[47] Silvester, P. and Benedek, P., "Equivalent capacitance of microstrip open circuits," *IEEE Trans. on Microwave Theory Tech.*, vol. MTT-20, pp. 511–516, August 1972.

[48] Silvester, P. and Benedek, P., "Microstrip discontinity capacitances for right-angle bends, T-junctions, and crossings," *IEEE Trans. on Microwave Theory Tech.*, vol. MTT-21, pp. 341–346, May 1973.

[49] Sonnet Software Inc., "Em user's manual." 1995.

[50] Van Blaricum, M. L. and Mittra, R., "A technique for extracting the poles and residues of a system directly from its transient response," *IEEE Trans. on Antennas and Propagation*, vol. AP-23, pp. 777–781, November 1975.

[51] Van Blaricum, M. L. and Mittra, R., "Problem and solutions associated with Prony's method for processing transient data," *IEEE Trans. on Antennas and Propagation*, vol. AP-26, pp. 174–182, January 1978.

VITA

Fatma Çalışkan was born in Ankara, Turkey in 1973. In 1990, she graduated from Gazi High School, Ankara, Turkey. She received her bachelor of science degree in electrical and electronics engineering from Hacettepe University, Ankara, Turkey, in 1995. She graduated from Bilkent University, Ankara, Turkey, with a master of science degree also in electrical and electronics engineering in 1997. From 1995 through 1998, she worked as a research and teaching assistant in Bilkent University.

In 1998, she enrolled in Georgia Institute of Technology as a Ph.D. student and graduate research assistant. Her Ph.D. studies were funded by Packaging Research Center, Georgia Institute of Technology, Atlanta, GA. During her Ph.D. study, she also conducted an internship with Texas Instruments, Dallas, Texas, in the summer of 2001. She expects to receive her Ph.D. degree in electrical and computer engineering from the Georgia Institute of Technology, Atlanta, Georgia, in the summer of 2004.